

RADC-TR-89-121, Vol II (of two)
In-House Report
June 1989

FILE COPY

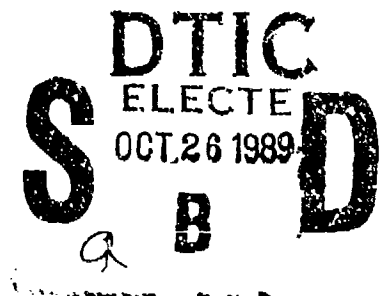


PROCEEDINGS OF THE 1988 ANTENNA APPLICATIONS SYMPOSIUM

Paul Mayes, et al

AD-A213 815

Sponsored by
ELECTROMAGNETIC SCIENCES DIVISION
ROME AIR DEVELOPMENT CENTER
HANSCOM AFB, BEDFORD MASS. 01731
AIR FORCE SYSTEMS COMMAND



APPROVED FOR PUBLIC RELEASE; DISTRIBUTION UNLIMITED.

ROME AIR DEVELOPMENT CENTER
Air Force Systems Command
Griffiss Air Force Base, NY 13441-5700

89 10 26 098

This report has been reviewed by the RADC Public Affairs Office (PA) and is releasable to the National Technical Information Service (NTIS). At NTIS it will be releasable to the general public, including foreign nations.

RADC TR-89-121, Vol II (of two) has been reviewed and is approved for publication.

APPROVED:



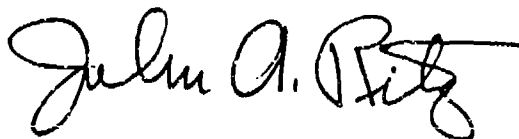
ROBERT J. MAILLOUX
Chief, Antennas and Components Division
Directorate of Electromagnetics

APPROVED:



JOHN K. SCHINDLER
Director of Electromagnetics

FOR THE COMMANDER:



JOHN A. RITZ
Directorate of Plans and Programs

DESTRUCTION NOTICE - For classified documents, follow the procedures in DOD 5200.22-M, Industrial Security Manual, or DOD 5200.1-R, Information Security Program Regulation. For unclassified limited documents, destroy by any method that will prevent disclosure of contents or reconstruction of the document.

If your address has changed or if you wish to be removed from the RADC mailing list, or if the addressee is no longer employed by your organization, please notify RADC (EEAS) Hanscom AFB MA 01731-5000. This will assist us in maintaining a current mailing list.

Do not return copies of this report unless contractual obligations or notices on a specific document requires that it be returned.

Unclassified

SECURITY CLASSIFICATION OF THIS PAGE

REPORT DOCUMENTATION PAGE

1a. REPORT SECURITY CLASSIFICATION Unclassified			1b. RESTRICTIVE MARKINGS		
2a. SECURITY CLASSIFICATION AUTHORITY			3. DISTRIBUTION/AVAILABILITY OF REPORT Approved for public release; Distribution unlimited		
2b. DECLASSIFICATION/DOWNGRADING SCHEDULE					
4. PERFORMING ORGANIZATION REPORT NUMBER(S) RADC-TR-89-121 Volume II			5. MONITORING ORGANIZATION REPORT NUMBER(S)		
6a. NAME OF PERFORMING ORGANIZATION Rome Air Development Center		6b. OFFICE SYMBOL (if applicable) EEAS		7a. NAME OF MONITORING ORGANIZATION	
6c. ADDRESS (City, State, and ZIP Code) Hanscom AFB Massachusetts 01731-5000			7b. ADDRESS (City, State, and ZIP Code)		
8a. NAME OF FUNDING / SPONSORING ORGANIZATION		8b. OFFICE SYMBOL (if applicable)		9. PROCUREMENT INSTRUMENT IDENTIFICATION NUMBER	
8c. ADDRESS (City, State, and ZIP Code)			10. SOURCE OF FUNDING NUMBERS		
			PROGRAM ELEMENT NO. 62702F	PROJECT NO. 4600	TASK NO. 14
			WORK UNIT ACCESSION NO. 01		
11. TITLE (Include Security Classification) Proceedings of the 1988 Antenna Applications Symposium					
12. PERSONAL AUTHOR(S)					
13a. TYPE OF REPORT In-house Final		13b. TIME COVERED FROM 9/21/88 TO 9/23/88		14. DATE OF REPORT (Year, Month, Day) 1989 June	
15. PAGE COUNT 306					
16. SUPPLEMENTARY NOTATION VOLUME I CONSISTS OF PAGES 1 THROUGH 291; VOLUME II CONSISTS OF PAGES 293 THROUGH 590					
17. COSATI CODES			18. SUBJECT TERMS (Continue on reverse if necessary and identify by block number)		
FIELD	GROUP	SUB-GROUP	Antennas, Microstrip, Multibeam Antennas		
			Satellite Antennas, Reflector Array Antennas		
			Broadband Antennas, HF, VHF, UHF		
19. ABSTRACT (Continue on reverse if necessary and identify by block number)					
<p>The Proceedings of the 1988 Antenna Applications Symposium is a collection of state-of-the-art papers relating to phased array antennas, multibeam antennas, satellite antennas, microstrip antennas, reflector antennas, HF, VHF, UHF and various other antennas.</p>					
20. DISTRIBUTION/AVAILABILITY OF ABSTRACT <input type="checkbox"/> UNCLASSIFIED/UNLIMITED <input type="checkbox"/> SAME AS RPT <input type="checkbox"/> DTIC USERS			21. ABSTRACT SECURITY CLASSIFICATION Unclassified		
22a. NAME OF RESPONSIBLE INDIVIDUAL John Antonucci			22b. TELEPHONE (Include Area Code) (617) 377-3549		22c. OFFICE SYMBOL



Accession For	
NTIS GRA&I	<input checked="checked" type="checkbox"/>
DTIC TAB	<input type="checkbox"/>
Unannounced	<input type="checkbox"/>
Justification	
By _____	
Distribution/	
Availability Codes	
Dist	Avail and/or Special
A-1	

CONTENTS

- * Keynote: "Antennas: Our Eyes and Ears on the World," John Kraus,
Ohio State University, Columbus, OH

WEDNESDAY, 21 SEPTEMBER 1988

SESSION I

RADIATING ELEMENTS

1. "Semi-Conductor Dipole: Possible Radiating Element for
Microwave/Millimeter Wave Monolithic Integrated Circuits
(MIMIC)," P. D. Patel 1
2. "Experimental Design and Performance of Endfire and Conformal
Flared Slot (Notch) Antennas and Applications to Phased Arrays:
An Overview of Development," M. J. Povinelli 27
3. "Power Handling Printed Sub-Array for Wide Bandwidth Scanning
Antenna Array," P. Pons, L. Maury and S. Dutheil 53

* NOT INCLUDED IN THIS VOLUME

Contents

4.	"Printed Circuit Antenna Designs," D. A. Mullinix and P. M. Proudfoot	71
* 5.	"Log-Periodic Slot Antenna With Meanderline Feeder," S. C. Kuo and C. G. Roberts	-
6.	"A Study of the Propagation and Radiation Characteristics of Tape Helical Structures," A. F. Peterson, B. Greene and R. Mittra	105

SESSION II

ARRAYS

7.	"Advanced Architecture for a Monopulse Active Aperture Array," P. D. Hrycak, A. C. Sullivan and G. E. Evans	133
8.	"Broadband MMIC T/R Module/Subarray Performance," D. Brubaker, D. Scott, S. Ludvik, M. Lynch, H. H. Chung, W. Foy and S. Y. Peng	157
9.	"Array Trade-Off Study Using Multilayer Parasitic Subarrays," A. Zaman, R. Q. Lee and R. Acosta	187
10.	"A K-Band MMIC Active Phased Array Antenna," C. Donn, A. E. Bollesen and S. H. Wong	199
11.	"Sidelobe Reduction via Multi-Aperture Microwave Systems," S. M. Watson, J. P. Mills and D. H. Stone	225
* 12.	"Low Sidelobe, Short, Highly Producible Microstrip Array," R. Chew	-
13.	"Dual-Polarized, Common-Aperture Monopulse Antenna," R. Kliger, R. Mariano, N. Sa and J. Toth	255

THURSDAY, 22 SEPTEMBER 1988

SESSION III

MICROSTRIP ANTENNAS

14.	"Improved Bandwidth Microstrip Antenna Array," S. Sanzgiri, B. Powers, Jr., and J. Hart	277-
15.	"Broadbanding Techniques for Microstrip Patch Antennas - A Review," K. C. Gupta	293

* NOT INCLUDED IN THIS VOLUME

Contents

16.	"Characteristics of Electromagnetically Coupled Rectangular Patch Antennas With Overlaying Parasitic Elements," R. Q. Lee and K. F. Lee	323
17.	"The Annular Sector Microstrip Antenna Mounted on Planar and Conical Surfaces," D. C. Thompson and C. A. Balanis	337
18.	"Mode Purity of Rectangular Patch Antennas With Post and Aperture Excitations," H. K. Smith and P. E. Mayes	363
19.	"Circular Polarization From Stacked Microstrip Patches," A. Adrian and D. H. Schaubert	377
20.	"Analysis of the Annular-Ring-Loaded Circular-Disk Microstrip Antenna," Z. Nie, W. C. Chew and Y. T. Lo	391

SESSION IV

SYSTEM ANALYSIS AND MEASUREMENT

21.	"Design and Economic Considerations for Broad Band Phased-Array Elements," G. J. Monser	413
22.	"A Large Multibeam Lens Antenna for EHF SATCOM," J. P. Montgomery, D. L. Runyon and J. A. Fuller	431
23.	"Measured Antenna Performance of an EHF Hybrid Scan Array Antenna for MILSATCOM Applications," J. F. Pedersen	461
24.	"Technique to Measure Large Antenna Arrays," P. Franchi and H. Tobin	485
25.	"Mathematical Model of a Large Aperture Focusing Antenna," T. B. Smerczynski, N. Marchand and G. Smith	505
26.	"Analytical Approximation of a Distorted Reflector Surface Defined by a discrete Set of Points," R. Acosta and A. Zaman	525
27.	"The Flexible Adaptive Spatial Signal Processor," R. N. Smith, A. M. Greci, S. A. Carollo, D. Jackson and E. Toughlian	539

* NOT INCLUDED IN THIS VOLUME

Contents

FRIDAY, 23 SEPTEMBER 1988

SESSION V

THEORY AND EXPERIMENT

- * 28. "Asymmetric Ridge Waveguide Radiating Element for a Scanned Array," H. Shnitkin, J. Green and P. Bertalan
- 29. "A Rapid, Accurate Test Method for Measuring Electrical Phase Length," G. J. Monser 557
- 30. "2-D Microwave Imaging of Aircraft," B. D. Steinberg 571
- * 31. "Application of Method of Moments to Dual Polarization Finite Array Antennas," E. Conaty
- * 32. "Broadband, Low Sidelobe, Zero Height, Slotted Circular Disk Antenna," K. Alemu

* NOT INCLUDED IN THIS VOLUME

PREFACE

The Antenna Applications Symposium, held at the University of Illinois, Robert Allerton Park, was cosponsored by Rome Air Development Center's Electromagnetics Directorate (RADC/EEAA), Hanscom AFB, MA and the University of Illinois' Electromagnetics Laboratory under contract F19628-88-M-0015. Professor John Mayes of UI was the symposium chairman. John Antonucci of RADC/EEA was the symposium manager for the Air Force.

BROADBANDING TECHNIQUES FOR MICROSTRIP PATCH ANTENNAS - A REVIEW

K.C. Gupta
Department of Electrical and Computer Engineering
University of Colorado
Boulder, CO 80309-0425

Abstract

The need for development of wideband microstrip patch antennas has been very well recognized. This article is a review of various techniques attempted for increasing the bandwidth of microstrip patches. These include multiple resonator configurations (with patches located on the same plane as well as multiple-layered substrate geometries) and wideband impedance matching network approach. Various results reported in the literature are discussed and areas for continued research efforts are identified.

1. INTRODUCTION

Narrow bandwidth available from printed microstrip patches has been recognized as one of the most significant factors limiting the widespread applications of this class of antennas. The operating bandwidth of a single linearly polarized patch antenna is limited by its input VSWR (or reflection loss) and is inversely proportional to the Q-factor of the patch resonator. Typical values for the fractional bandwidth are 2 to 4%. Over the last decade, several attempts have been made for improving the bandwidth of microstrip patches. This article is a review of various techniques employed for broadband design of microstrip antenna elements and arrays and attempts to present a comparison of the results reported.

Various techniques used to increase the bandwidth of microstrip patch antennas may be classified as follows: (i) Decreasing the Q-factor of the patch by increasing the substrate height and lowering the dielectric constant. (ii) Use of multiple resonators located in one plane. (iii) Use of multilayer configurations with multiple resonators stacked vertically. (iv) Use of impedance matching networks.

These techniques are discussed in Sections 2 through 5. Special considerations for the bandwidth of circularly polarized patches are discussed in Section 6. Finally, bandwidth considerations for arrays of microstrip patches are contained in Section 7. Comparison of various approaches and concluding remarks are contained in the last section.

Bandwidth Definitions

Since the bandwidth (BW) of linearly polarized single microstrip patches is usually limited by the reflection loss at the input terminal, the commonly used definition for BW of the microstrip patches is *the frequency range over which the input VSWR is less than certain specified value s* . Usually s is taken equal to 2 but certain specifications choose $s = 1.5$. Thus one has to be careful while comparing bandwidths quoted in different reports.

A concept of *radiation bandwidth* for microstrip antennas has been introduced in [1]. The radiation BW is defined as the frequency range over which the radiated power is within 3 dB of the incident power and the radiation pattern is essentially the same. The second part of this definition can be made more specific by quantifying the allowed variations in the radiation pattern (for example in beam direction, beam width, or the sidelobe level). This definition is more comprehensive as the radiated power is reduced

because of the input reflection as well as by other factors such as changes in voltage distribution along the edges of the patch.

2. BANDWIDTH OF SINGLE PATCH ANTENNAS

Input impedance and the impedance bandwidth of a microstrip patch antenna may be computed using its transmission line model or the cavity model. If we represent the resonant patch in terms of a parallel L-C-G network, its input admittance Y_{in} can be written as

$$Y_{in} = G(1 + 2jQ \Delta f/f_0) \quad (1)$$

where $Q = \omega C/G$ and Δf is the deviation from the center frequency f_0 . Bandwidth BW defined for input VSWR to be better than s is given [2] by

$$BW = \frac{s-1}{Q\sqrt{s}} \quad (2)$$

For $s=2$, and substituting for Q in terms of energy stored and power radiated we can write

$$BW = \frac{\sqrt{2}h G_e}{\pi c \sqrt{\epsilon_{re}} \epsilon_0 b_e} \quad (3)$$

where G_e is the edge conductance, h is the substrate thickness, b_e is the effective width and ϵ_{re} the effective dielectric constant of the equivalent microstrip line. From (3), we note that the BW increases linearly with increase of h . Also, BW increases when ϵ_r (and hence ϵ_{re}) is reduced. Recognizing that the edge conductance for a patch width b is given by [3],

$$G_e = \frac{1}{120} \frac{b}{\lambda_0} \quad \text{for } b/\lambda_0 \gg 1 \quad (4)$$

and

$$G_0 = \frac{1}{90} (b/\lambda_0)^2 \quad \text{for } b/\lambda_0 \ll 1$$

we find the fractional bandwidth BW increases with the operating frequency f_0 .

Typical variation of BW with h/λ is depicted in [4] whereas variation with frequency is shown in [2]. Computations agree with the measured values. As pointed out in [3], bandwidths up to 15% can be obtained at the expense of an increase in the antenna height to about 0.1 wavelengths. However, such thick substrates are not desirable or practical because of the following reasons: (i) For probe-fed patches, an increase in the substrate thickness causes an increase in the probe inductance which, in turn, creates input matching problems. (ii) For microstrip-fed patches, increased substrate thickness causes an increase junction reactance, which creates spurious radiation as well as the input match problems. (iii) Thick substrates are not well suited for microstrip circuitry used for signal distribution and phase shifting networks fabricated on the same substrate. (iv) Thick substrates make it mechanically difficult to have antenna arrays conformal to curved surfaces (of aircraft, space craft, missiles, etc.). (v) Many of the analysis and design techniques used (cavity model, etc.) become inaccurate for thick substrates.

Decrease in the BW of microstrip antenna by decreasing the substrate thickness h , or decreasing the width b , or by decreasing the length a (by increasing ϵ_r) is consistent with the general relationship between the Q and volume of small antennas [5]

A useful formula for bandwidth of microstrip patches is given by Munson [6] as

$$BW = 4f^2 \left(\frac{t}{1/32} \right) \quad (5)$$

where BW is the bandwidth in MHz (for $VSWR < 2$), f is the operating frequency in GHz, and t is the thickness in inches.

Non-rectangular Shaped Patches

Bandwidths available from circular microstrip patches [7] are of the same order as those available from rectangular or square shaped antennas. The two other geometries which have been shown to yield wider bandwidths are: circular ring [8] and square ring [9] microstrip antennas. As pointed out in [8], TM_{11} mode of the annular ring is a poor radiator but TM_{12} mode of the ring yields a bandwidth about two times larger than the bandwidth of a circular disk. The bandwidths for the rectangular patch and for the rectangular ring patch are compared in [9], and in a typical case ($\epsilon_r = 2.50$, $h = 0.159$ cm, and $f = 1080$ MHz), the ring has a BW value 1.63 times that of the rectangular patch. Qualitative reasons for improved bandwidth are the same in two cases. For ring geometries, energy storage underneath the patch is smaller but the power radiated from the radiating edges is about the same.

3. SINGLE-SUBSTRATE MULTIPLE-RESONATOR CONFIGURATIONS

Use of multiple resonant patches located in the same plane (on the top surface of a single substrate) has been explored by several investigators [10-16]. The key idea in these configurations is that the stagger tuned coupled resonators can yield wider frequency response in the same way as obtained in the case of multi-stage tuned amplifier circuits.

In [10], two narrow conducting strips are placed close (~ 2.5 to 3.0 times the substrate thickness) to the non-radiating edges of a rectangular patch (Fig. 1). Bandwidth of 5% ($VSWR < 2$, $f_0 = 350$ MHz, on 1.27 cm thick silicone fiberglass

substrate) was obtained experimentally. Coupling of parasitic patches to the radiating edges of a rectangular patch has been described in [11]. In this case, the parasitic patches are $\lambda/4$ long (shorted at the far ends, as shown in Fig. 2) and therefore the locations of the radiating apertures do not change. A bandwidth 2.12 times that of a single open patch ($f_0 = 1.275$ MHz, $\epsilon_r = 2.5$, $h = 3.18$ mm, $VSWR < 2$) has been reported. The characteristics of this configuration have been explained in terms of an antiphase mode of a pair of coupled resonators and it is shown that the bandwidth improvement is independent of the coupling capacitance.

Multiport network analyses of multiresonator configurations (Fig. 3 a,b and c) with additional patches gap coupled to the radiating edges, to the non-radiating edges, or to all the four edges of a probe-fed central patch are reported in [12] and [13]. Coupling gaps are modeled by multiport capacitive networks and two-dimensional analysis (segmentation method) is used to evaluate input impedance as well as the voltage distributions around the edges. Bandwidth ($VSWR < 2$) of the five-resonator configuration (Fig. 3c) has been evaluated theoretically and experimentally to be 6.7 times that of a single patch on the same substrate ($\epsilon_r = 2.55$, $h = 0.318$ cm, and $f_0 = 3.16$ GHz, $BW = 25.8\%$). Alternative multiport configurations wherein the additional resonators are not gap-coupled but connected to the central patch through small sections of microstrip lines (as shown in Fig. 4) have been discussed in [14]. Again multiport network modeling and planar analysis is employed and experimental verifications are reported. For the 5-patch configuration (Fig. 4(c)), a bandwidth improvement of 7.36 times over that for a single patch ($VSWR < 2$, $\epsilon_r = 2.55$, $h = 0.318$ cm, $f_0 = 3.18$ GHz, $BW = 24\%$) have been reported.

Another interesting multi-patch antenna configuration is described in [15]. This configuration consists of 4 triangular patches as shown in Fig. 5. The central patch A is probe fed, the lower patch B is gap coupled, and the other two patches C and D are coupled by short sections of microstrip lines. The design was optimized by experimental iterations. A bandwidth (VSWR < 2) of 11.3% ($\epsilon_r = 2.55$, $h = 1.6$ mm, $f_0 = 3.19$ GHz) which is 5.4 times the bandwidth of a single rectangular patch antenna has been reported. Over this bandwidth, the 3 dB beamwidth varies from 55° to 72° in the E-plane and 40° to 70° in the H-plane. The cross-pol level is better than 14 dB in the H-plane and 12 dB in the E-plane. Analysis and design of this type of antenna may also be carried out by the multiport network modelling approach discussed for multiresonator rectangular patches in [12-14]. Such antennas may find use in applications where a wide bandwidth is required but some variations in radiation characteristics over the bandwidth range may be tolerated.

There are two problems associated with the use of the multiresonator configurations described above: (i) larger area requirement and consequent difficulty in using these configurations as array elements, and (ii) variations of the radiation pattern over the impedance bandwidth of the configuration.

A modification of the multiresonator patches (for avoiding the above-mentioned two problems) is described in [16]. This configuration (shown in Fig. 6) is a modification of the non-radiating-edges coupled resonator configuration (shown in Fig. 3b). Six narrow patches are coupled through capacitive gaps. Their lengths are equal but widths are different. The configuration was designed by experimental iterations. Measured bandwidth (VSWR < 2) equal to 10 times that of a single patch of the same overall area has been reported ($\epsilon_r = 2.2$, $h = 0.8$ mm, $f_0 \sim 875$ MHz, BW $\sim 6\%$). Since the size of this multiresonator configuration is compact, the radiation pattern is consistently good over

the bandwidth. Measured radiation patterns at 854 MHz and 897 MHz support this contention. Information regarding variation of gain over the bandwidth is not available in [16]. Analysis and design procedures for this type of antenna have not been reported so far. Of course, the multiport network modeling approach used for 3-patch configuration of Fig. 3b can be extended to the six-patch configuration also. An alternative approach is to model the multiple-resonator patch as a section of a multiple coupled microstrip line, and to construct a coupled-line model (similar to the transmission line model for a single patch). This concept of coupled-line model as applicable to a two-resonator configuration is discussed in [1]. Certainly, multiple-resonator configuration with narrow patches coupled along non-radiating edges, is an antenna configuration for which further detailed investigations are recommended.

4. MULTIPLE-RESONATOR CONFIGURATIONS WITH PATCHES STACKED VERTICALLY

In this approach, two or more layers of dielectric substrates are used. Resonant patches are located on the top of each of the substrate layers and are stacked vertically. Two-layer configurations are most common, although three dielectric layers (and three patches) have also been used. The two patches may be identical (same size) or of slightly different sizes (and hence resonant at slightly different frequencies). When the patches have unequal dimensions, two different arrangements are possible. Smaller patches can be located on the top layer (Fig. 7a) or the larger patch can be placed on the top (Fig. 7b). Both of these arrangements have been used. When the smaller patch is on the top, edges of both the smaller and the larger patches become the sources of radiation with the effective aperture shifting from the bigger patch to the smaller patch as the frequency of operation is increased. On the other hand, when the larger patch is on the top (and the

smaller patch below), the boundary of the upper patch constitutes the radiating aperture. The lower patch helps in the broadband excitation of the upper patch, and is termed as the feeder patch. Of course, two patches can have identical dimensions in which case the distinction between the feeder and the radiator patches disappears and the two functions are merged together. In most of these two-patch configurations, the lower patch is fed via a probe or a microstrip line. Two different ways of excitations of the upper patch are available. We can use a vertical probe passing through a hole in the lower patch and making contact to the upper patch. Alternatively capacitive coupling between the patches is used to excite the upper patch.

Double layer two-patch configurations were initially used for dual frequency microstrip antennas [10,17]. Wide bandwidth application was reported by Hall et al in [18] wherein two-layer and three-layer configurations are described. In these designs, the lower substrate layer is alumina ($\epsilon_r = 9.8$, $h = 0.625$ mm) where the feed line and the associated circuitry is fabricated. The second and third layers are polyguide ($\epsilon_r = 2.32$, $h = 1.59$ mm) where the resonant radiating patches are fabricated (see Fig. 8 a and b). Bandwidths of 13% and 18% (return loss > 10 dB, $f_0 \sim 10.6$ GHz) were measured for two-layer and three-layer configurations respectively. For comparison, bandwidth of a single layer patch on alumina substrate is only 1.1%, while that on polyguide is about 6.6%. This technique of capacitively-coupled stick-on antennas is well suited for certain applications where the antenna may be regarded as an additional component in the transmitter/receiver circuits.

There have been several reports of two layer antennas with an air-gap in between the two layers. In the configuration described in [19], the lower patch has a smaller size and acts as a feeder resonator. Out of the various configurations presented, S-band

circular disc configuration has a bandwidth of 15% ($VSWR < 2.0$, air-gap thickness not specified). For the configuration reported in [20], a low ϵ_r dielectric foam material is used to separate the two patches. For a spacing of 0.572 cm, a 17.3% BW ($VSWR < 1.92$, 3.85-4.58 GHz) is reported. The lower patch is smaller in size and is fed by a probe or a microstrip line. The element has been used in 4x4 array of circularly polarized patches (two feed points on each patch). An investigation of the two layer antenna performance as a function of the air-gap spacing is discussed in [21].

An experimental study of vertically stacked triangular patches is reported in [22]. Both dual frequency and broadband operation are described. For two identical equilateral triangular patches fabricated on dielectric layers (with $\epsilon_r = 2.55$ and thickness 1.6 mm) separated by a foam thickness of 5.0 mm, a bandwidth of 17.46% ($VSWR < 2$, $f_0 = 3.61$ GHz) has been reported. For comparison, the bandwidth of the same two-patch configuration with zero foam thickness is only 2.5%.

All of the vertically-stacked multiple resonator configurations discussed above have been designed by experimental iterations. However, analyses of such configurations based on equivalent transmission line model [23] as well as based on full-wave spectral domain approach [24,25] have been reported recently. In [23], the transmission line model analysis of a two-layer rectangular patch is described. The upper patch is smaller, and the region common to both the patches is modeled as a coupled line section. Conceptually, the approach is similar to that described in [26] for a suspended patch antenna excited by an electromagnetically coupled inverted microstrip feed. For the configuration described in [23], a BW of 13.5% ($f_0 = 13$ GHz, $VSWR < 2$, lower and upper substrates have $h = 0.8$ mm and $\epsilon_r = 2.55$) has been reported. For comparison the bandwidth for a single patch is only 4.46%.

Hankel transform domain analysis of two-layer circular patch configuration reported in [24,25] is an extension of the analysis of a single layer open circular microstrip radiating structure discussed in [27]. Complex resonant frequencies of the unloaded two-patch configuration are found by solving the equivalent transverse transmission line circuits for TE and TM components in the Hankel transform plane. Basis functions chosen for current distribution take into account the edge condition. Green's functions in spectral (Hankel transform) domain are in algebraic form. Coefficients of the immittance matrix are obtained via complex integration in the spectral domain. Equating coefficients determinant to zero yields complex resonance frequencies. Input VSWR characteristic is obtained by using natural complex frequencies computed and an equivalent circuit model. Radiation patterns are computed without inverting the Hankel transform current distribution. Numerical resonant frequency and VSWR variation are shown to be in good agreement with the experimental data ($\epsilon_r = 2.55$, $f \sim 2.4$ -2.8 GHz, dielectric layers 1.6 mm thick, air spacing between layers 10.0 mm, lower patch radius 20.8 mm, upper patch radius 21.0 mm).

Vertically stacked multi-resonator configurations are the most widely used broadband microstrip antenna elements. But, convenient practical design and analysis procedures are not available so far. Analytical treatments based on the extension of cavity and multiport network models are likely to be developed in the near future.

5. IMPEDANCE MATCHING NETWORKS FOR BROAD-BAND MICROSTRIP ANTENNAS

Approaches for widebanding of microstrip antennas discussed so far are based on either the concept of decreasing the resonator Q-factor, or on the concept of coupled multiresonator circuits. An entirely different approach makes use of wideband impedance

matching networks to reduce the reflection loss at the input of the resonant patch antenna. It is an obviously natural solution from microwave circuit designers' point of view. However, a very small number [28-32] of microstrip antenna designers have looked upon the broadbanding problem from this angle.

As pointed out in [28,29,32], the maximum bandwidth obtainable by using an impedance matching network can be calculated by using Fano's broadband matching theory [33]. Treating the microstrip patch antenna as a parallel resonant circuit (as discussed in Sec. 2), it can be shown the input impedance bandwidth BW is given by

$$BW = \frac{1}{Q} \sqrt{\left\{ \left(\frac{s}{GZ_0} - 1 \right) (s-1) / s \right\}} \quad (6)$$

where G is the shunt conductance in the parallel resonant network and Z_0 is the characteristic impedance of the input transmission line. When $Z_0 = 1/G$, the relation (6) reduces to (2) of Section 1. However, one can find a value of Z_0 that will maximize the BW in (6) and this is given by

$$Z_{0 \text{ optimum}} = \frac{2}{G(s + 1/s)} \quad (7)$$

For this optimum value of Z_0 , the optimum BW is given by

$$BW_{\text{opt.}} = \frac{1}{Q} \sqrt{\left\{ \frac{s^2 - 1}{2s} (s-1) \right\}} \quad (8)$$

For the usual value of $s=2$, $BW_{\text{opt.}}$ given by (8) is about 1.2 times the bandwidth given by (2). It implies that if we do not insist on a perfect match at the center frequency, the

frequency range over which the input VSWR is less than 2 can be increased by about 20%. This is consistent with Fano's theory [33] according to which maximum BW over which a parallel resonant circuit can be matched for a $VSWR < s$, is given by [28],

$$BW_{max} = \frac{1}{Q} \frac{\pi}{\ln \{ (s+1)/(s-1) \}} \quad (9)$$

Comparing the values given by (9) with those given by (2), it can be shown that a bandwidth improvement by a factor of 4.04 can be obtained (for $s = 2$) by designing a perfect impedance matching network.

Experimental results reported in [28] point out a bandwidth improvement by a factor of 3.9 (3 GHz, BW = 10%, $s = 1.9$) by using a shielded microstrip matching network consisting of two resonator elements etched on the same substrate as the patch. Configuration reported in [29], on the other hand, makes use of the feed probe inductance (occurring in a thick substrate coaxial-fed microstrip antenna element) as a part of impedance matching network. A series capacitance located at the top end of the probe (Kapton layer shown in Fig. 9) forms a series resonant circuit which is used for broadband matching of the parallel resonant circuit constituted by the resonant patch antenna. Experimental results show a marked improvement in the return loss (~ 11.3 GHz, $\epsilon_{r1} = 1.06$, $h_1 = 1.6$ mm, $\epsilon_{r2} = 3.3$ mm, $h_2 = 0.15$ mm) but bandwidth improvement data is not reported in [29].

Another wideband circular disc antenna making use of a series resonant circuit (feed probe inductance being a part of the series resonance) is described in [30]. The matching network (details not given) was optimized using CAD techniques and interfaced directly with a triplate array feed network. For a 6 mm radius patch ($\epsilon_r = 2.2$, $h = 3.2$ mm) a

bandwidth of 35% of $VSWR < 1.5$ has been reported. Radiation patterns over the whole band (7 to 10.5 GHz) shows little variation. Gain is about 6 dBi.

A forthcoming paper by Pues and Van de Capelle [32] describes in detail the transmission-line matching network design for broadband microstrip antennas.

A single stub impedance matching technique for increasing the bandwidth of an electromagnetically coupled microstrip patch (Fig. 10) is discussed in [31]. In this case, the input impedance of the electromagnetically coupled patch was measured by a network analyzer and component values for a network model (a capacitance in series with a parallel RLC) were obtained by a computer-aided model fitting procedure. A stub circuit was then designed to match to this load. A bandwidth of 13% ($VSWR < 2$, 3.375 GHz to 3.855 GHz, $\epsilon_{r1} = \epsilon_{r2} = 2.2$, and $d_1 = d_2 = 0.158$ cm) was thus obtained.

As evident from the above discussions, broadband impedance matching networks provide a really effective means of increasing the usable bandwidth of microstrip antennas. A combination of this technique with the other approaches discussed earlier would perhaps lead to the optimum configuration for wide bandwidth microstrip patches.

Electromagnetically Coupled Microstrip Patches

The example of broadband patch discussed above (described in [31]) makes use of an electromagnetic coupled patch (Fig. 10) consisting of two dielectric layers. The feeding microstrip line is printed on the lower layer and the patch is on the top of the upper dielectric layer. Such a coupling arrangement is frequently used in printed microstrip antennas [18, 26, 35-37]. Electromagnetically coupled patches are preferred as the feeding microstrip line network and other circuitry are located on a thinner (and possibly higher ϵ_r if desired) substrate and the radiating resonant patch is fabricated on the thicker and low ϵ_r layer.

Electromagnetically coupled patches are very convenient from the broadbanding point of view also. Impedance matching networks may be located on the lower layer underneath the patch without requiring additional substrate area. Also the capacitive coupling between the patch and the microstrip line constitutes a series capacitance which can be utilized as a component of the impedance matching network.

Some of these considerations are implicit in the bandwidth enhancement method for electromagnetically coupled strip dipoles discussed in [36]. In this paper, it is demonstrated that if parasitic metallic strips are incorporated in the structure either coplanar and parallel to the embedded microstrip line open-end, or between the transmission line and microstrip dipole, then substantial bandwidth enhancement can be obtained.

6. BANDWIDTH CONSIDERATIONS FOR CIRCULARLY POLARIZED PATCHES

Two different design philosophies are used for circularly polarized (CP) microstrip patches. One of these makes use of the two spatially orthogonal modes of a square or a circular patch. These two modes (each of them giving rise to a linearly polarized radiation when excited independently) are fed through two orthogonally located feeds by two signals which are equal in magnitude but are in phase quadrature. The bandwidth of these two-feed circularly polarized antennas is the same as that for the corresponding linearly polarized antennas, and all the broadbanding techniques discussed above are applicable to this class of circularly polarized antennas also. Reference [38] is an example where two vertically stacked circular resonator configuration is used to obtain a wide-band circularly polarized patch. A branch line hybrid is used to split the incoming signal for two orthogonally located feeds. A bandwidth of 13% ($VSWR < 1.5$) is obtained when the two patches (fabricated on $\epsilon_r = 2.55$, 1.6 mm thick dielectric layers) are separated by air gap of

$0.08 - 0.09 \lambda_0$. The radius of the upper patch is 1.0 to 1.1 times that of lower patch (frequency ~ 2.4 to 2.8 GHz).

The second design approach used for circularly polarized patches does not require a signal splitting network and makes use of only a single feed patch. There are several configurations [39-42] based on this approach. All of these configurations make use of two spatially orthogonal modes of the patch. The resonance frequencies of these two modes are made slightly different from each other. The patch is fed at a frequency in between these two resonances and the feed location is selected such that the two modes are excited equally. Since the resonance frequency of one of the modes is lower than the signal frequency and that of the other mode is higher than the signal frequency, a proper selection of frequencies causes the two modes to be excited 90° out of phase. Thus the conditions for a CP radiation are met.

The bandwidth of the single feed CP patches is limited not by the input VSWR (as is the case for linearly polarized patches), but by the degradation of the axial ratio as one moves away from the center design frequency. However, an analysis based on the cavity model [43] shows that the required separation between the two resonance frequencies and hence the axial ratio bandwidth is inversely proportional to the Q-factor of the patch.

A comparison of the axial-ratio bandwidths for various CP patches, given in [40], shows that the square ring configuration has a wider bandwidth (5.2%, axial ratio < 6 dB, $f = 3.0$ GHz, $\epsilon_r = 2.50$, and $h = 0.159$ cm) as compared to crossed strip, almost square patch, corner chopped square patch, and a square patch with a diagonal slot configurations. Another wideband single feed CP configuration is annular ring with an ear configuration discussed in [42]. In this case, TM_{12} mode is used and higher bandwidth is

obtained for small ratios of the outer to inner radii of the ring. A 6% bandwidth (axial ratio < 6 dB, $\epsilon_r = 2.52$, $h = 0.159$ cm, $f \sim 4.5$ GHz) is reported.

As discussed in Section 2, rectangular ring and circular ring patches provide the maximum impedance bandwidth among the single-layer, single-resonator patch configurations. Thus it is not surprising to note that these two configurations also provide the maximum axial ratio bandwidth when used as single-feed CP configurations.

7. BROAD-BAND MICROSTRIP ARRAY CONFIGURATIONS

As the individual microstrip patches exhibit antenna gains of the order of 4-6 dB only, they are frequently used in linear and two-dimensional array configurations. As a general rule, arrays of broadband microstrip patches yield wide bandwidth. This is illustrated in [38] where 4x4 array of broadband patches is shown to yield 8.5% bandwidth (VSWR < 1.5 , gain > 18.8 dBi, efficiency $> 62\%$, SLL < -22 dB) at 2.6 GHz using the broadband CP patches discussed earlier.

Specially designed broadband configurations for linear arrays have also been reported [44,45]. The configuration discussed in [44] is a series fed linear array of rectangular elements. The individual elements of this array are two-port rectangular patches. For two-port patches, the VSWR bandwidth depends not only on the patch but also on the power transmitted to the output port. Thus much wider impedance bandwidths are available in series-fed array. The design reported in [44] has a bandwidth of 40% (VSWR ≤ 2) and a gain of ~ 10 dB at x-band. The configuration employs a double section non-uniform antenna (Fig. 11) having a length equal to about $5.0 \lambda_{\max}$ and consisting of two rows, spaced about $1.5 \lambda_{\max}$, each of seven radiating patches.

The application of the log-periodic technique to the series-fed electromagnetically coupled overlaid-patch array has been discussed in [45]. A k- β analysis of microstrip

arrays is reported and indicates that the microstrip patch is not an optimum element for log-periodic arrays and that elements connected directly to the feed line result in the arrays having a limited bandwidth. The addition of the series capacitance to the patch equivalent circuit, implemented by electromagnetic coupling, allows an optimum to be approached. Log-periodic overlaid patch array design (Fig. 12) has been reported to have a 4:1 bandwidth with an input return loss of 8 dB, a gain of 8 dBi and a 30° backfire beam whose beamwidth varies from 63 to 32 degrees across the band. In spite of limitations on the ultimate BW obtainable, this design certainly extends the useful application areas of microstrip antennas.

8. CONCLUDING REMARKS

Various techniques used for increasing the bandwidth of microstrip patch antennas have been reviewed. It is pointed out that the consideration of the *impedance bandwidth* alone is not sufficient for broadband microstrip antennas, and a concept of *radiation bandwidth* is introduced.

It has been discussed (in Sec. 2) that the Q-factors of the resonant patches can be decreased and hence their bandwidths can be increased by increasing the height of the dielectric substrates. The problems associated with thick substrates are: increased reactance of the feed junction, and the radiation from the microstrip circuits included on the same substrate. These difficulties may be overcome by using electromagnetically coupled patches with feed network and associated circuitry on the lower (and thinner) substrate. There is a need to develop design procedures for electromagnetically coupled patches based on the extension of cavity model or multiport network model.

Among the three other approaches used for obtaining wider bandwidth, more attention needs to be directed to the application of wideband impedance matching

network approach discussed in Sec. 5. The only difficulty with this method is the need for larger substrate area required for incorporating the matching network. Again, the use of electromagnetically coupled patches should prove very useful since the matching network can be incorporated at the lower level, possibly underneath the patch itself. Further research efforts need to be pointed in this direction.

Between the two different methods of constructing multiresonator coupled patch configurations, the two-layer configuration with vertically-stacked patches requires smaller area and does not suffer much from pattern degradation with frequency. This configuration is used frequently but most of the designs are carried out by experimental iterations. Convenient models and analysis procedures need to be developed so that the design and optimization of these configurations can be carried out more systematically. Among the various configurations with multiple patches on the same layer, the configuration with the six narrow patches coupled along the non-radiating edges [15] has yielded the most promising results. Further research leading to analysis and design of this type of geometry is desirable. A multiple coupled microstrip line model, proposed recently for two patches coupled along the non-radiating edges [1], appears to be a reasonable approach for this purpose.

The search for an "ideal" wideband printed microstrip antenna is still on. Perhaps a combination of various approaches discussed in this review would lead to an optimum broadband configuration. We can look forward to continued research in this area.

REFERENCES

1. Gupta, K.C. and B. Bandhauer, "Coupled microstrip antennas for wider bandwidth", Proc. Symp. Antenna Technology Applied Electromagnetics, Univ. of Manitoba (Winnipeg, Canada), Aug. 10-12, 1988.
2. Derneryd, A.G. and A.G. Lind, "Extended analysis of rectangular microstrip resonator antennas", IEEE Trans. Antennas Propagat., vol. AP-27, pp. 846-849, Nov. 1979.
3. James, J.R., P.S. Hall and C. Wood, Microstrip Antenna Theory and Design, Peter Peregrinus Ltd. (UK), 1981, p. 88.
4. Derneryd, A.G. and I. Karlsson, "Broadband microstrip antenna element and array", IEEE Trans. Antennas Propagat., vol. AP-29, no. 1, Jan. 1981, pp. 140-142.
5. Wheeler, H.A., "Fundamental limitations of small antennas", Proc. IRE, vol. 35, pp. 1479-1484, Dec. 1947.
6. Munson, R.E., "Microstrip Antennas", chapter 7 in Antenna Engineering Handbook, 2nd Edition, Ed. R.C. Johnson and H. Jasik, McGraw-Hill Book Co., 1984, pp. 7.1-7.28.
7. Derneryd, A.G., "The circular microstrip antenna element", Proc. International Conf. Antennas and Propagat., Nov. 1978, London, pp. 307-311.
8. Chew, W.C., "A broadband annular-ring microstrip antenna", IEEE Trans. Antennas Propagat., vol. AP-30, no. 5, Sept. 1982, pp. 918-922.
9. Palanisamy, V. and R. Garg, "Rectangular ring and H-shaped microstrip antennas - Alternatives to rectangular patch antennas", Electronics Letters, vol. 21, no. 19, Sept. 1985, pp. 874-876.

10. Schaubert, D.H. and F.G. Farrar, "Some conformal, printed circuit antenna design",
Proc. Workshop Printed Circuit Antenna Techn., Oct. 1979, New Mexico State Univ., Las Cruces (NM), pp. 5.1-5.21.
11. Wood, C., "Improved bandwidth of microstrip element using parasitic elements",
Proc. IEE, vol. 127, Pt. H, 1980, pp. 231-234.
12. Kumar, G. and K.C. Gupta, "Broad-band microstrip antennas using additional resonators gap-coupled to the radiating edges", IEEE Trans. Antennas Propagat., vol. AP-32, Dec. 1984, pp. 1375-1379.
13. Kumar, G. and K.C. Gupta, "Non-radiating edges and four-edges gap-coupled with multiple resonator, broadband microstrip antennas", IEEE Trans. Antennas Propagat., vol. AP-33, 1985, pp. 173-178.
14. Kumar, G. and K.C. Gupta, "Directly coupled multiple resonator wideband microstrip antennas", IEEE Trans. Antennas Propagat., vol. AP-33, 1985, pp. 588-595.
15. Bhatnagar, P.S., et al., "Hybrid edge, gap and directly coupled triangular microstrip antenna", Electronics Letters, vol. 22, no. 16, 31 July 1986, pp. 853-855.
16. Aanandan, C.K. and K.G. Nair, "Compact broadband microstrip antennas",
Electronics Letters, vol. 22, no. 20, pp. 1064-1065, 1986.
17. Long, S.A. and M.D. Walton, "A dual-frequency stacked circular disk antenna",
IEEE Trans. Antennas Propagat., vol. AP-27, March 1979, pp. 270-273.
18. Hall, P.S., C. Wood and C. Garrett, "Wide bandwidth microstrip antennas for circuit integration", Electronics Letters, vol. 15, 1979, pp. 458-459.
19. Sabban, A., "A new broadband stacked two-layer microstrip antenna", 1983 IEEE AP-S Int. Symp. Antennas Propagat. Digest, pp. 63-66.

20. Chen, C.H., et al., "Broadband two-layer microstrip antenna", 1984 IEEE AP-S Int. Symp. Antennas Propagat. Digest, vol. 2, pp. 251-254.
21. Lee, R.Q., et al., "Characteristics of a two-layer electromagnetically coupled rectangular patch antenna", Electronics Letters, vol. 23, no. 20, 1987, pp. 1070-1072.
22. Bhatnagar, P.S., et al., "Experimental study of stacked triangular microstrip antennas", Electronics Letters, vol. 22, no. 16, 1986, pp. 864-865.
23. Dubest, G., G. Beauquet, J. Hocquencourt, and G. Bonnet, "Patch antenna bandwidth increase by means of a director", Electronics Letters, vol. 22, pp. 1345-1347, 1986.
24. Araki, K., H. Ueda and M. Takahashi, "Hankel transform domain analysis of complex resonant frequencies of double-tuned circular disc microstrip resonators/radiators", Electronics Letters, vol. 21, no. 7, 28 March 1985, pp. 277-279.
25. Araki, K., et al., "Numerical analysis of circular disc microstrip antennas with parasitic elements", IEEE Trans. Antennas Propagat., vol. AP-34, Dec. 1986, pp. 1390-1394.
26. Zang, Q., Y. Fukuoka and T. Itoh, "Analysis of a suspended patch antenna excited by an electromagnetically coupled inverted microstrip feed", IEEE Trans. Antennas Propagat., vol. AP-33, 1985, pp. 895-899.
27. Araki, K. and T. Itoh, "Hankel transform domain analysis of open circular microstrip radiating structures", IEEE Trans. Antennas Propagat., vol. AP-29, no. 1, Jan. 1981, pp. 84-89.

28. Pues, H.W. and A.R. Van de Capelle, "Wideband impedance-matched microstrip resonator antennas", IEEE Second Inter. Conf. on Antennas and Propagat., Pt. 1, 1981, pp. 402-405.
29. Fong, F.S., H.F. Pues and M.J. Withers, "Wideband multilayer coaxial-fed microstrip antenna element", Electronics Letters, vol. 21, 1985, pp. 497-498.
30. Griffin, J.M. and J.R. Forest, "Broadbanding circular disc microstrip antenna", Electronics Letters, vol. 18, no. 6, 1982, pp. 266-269.
31. Pozar, D.M. and B. Kaufman, "Increasing the bandwidth of a microstrip antenna by proximity coupling", Electronics Letters, vol. 23, no. 8, April 1987, pp. 368-369.
32. Pues, H.G. and A.R. Van de Capelle, "An impedance-matching technique for increasing the bandwidth of microstrip antennas", to be published.
33. Fano, R.M., "Theoretical limitations on the broadband matching of arbitrary impedances", Jour. Franklin Institute, vol. 249, no. 1-2, pp. 57-83 and 139-154, Jan.-Feb. 1950.
34. Oltman, H.G. and D.A. Huebner, "Electromagnetically coupled microstrip dipoles", IEEE Trans. Antennas Propagat., vol. AP-29, 1981, pp. 151-157.
35. Katehi, P.B. and N.G. Alexopoulos, "On the modeling of electromagnetically coupled microstrip antennas - The printed strip dipole", IEEE Trans. Antennas Propagat., vol. AP-32, no. 11, Nov. 1984, pp. 1179-1185.
36. Katehi, P.B., et al., "A bandwidth enhancement method for microstrip antennas", IEEE Trans. Antennas Propagat., vol. AP-35, Jan. 1987, pp. 5-12.
37. Rivera, J. and T. Itoh, "Analysis of a suspended patch antenna excited by an inverted microstrip line", Electromagnetics, vol. 3, nos. 3-4, July-Dec. 1983, pp. 289-298.

38. Hori, T. and N. Nakajima, "Broadband circularly polarized microstrip array antenna with coplanar feed", Electronics and Commun. in Japan, Part I, vol. 69, no. 11, 1986, pp. 76-83.
39. Sharma, P.C. and K.C. Gupta, "Analysis and optimized design of single feed circularly polarized microstrip antennas", IEEE Trans. Antennas Propagat., vol. AP-31, 1983, pp. 949-955.
40. Palanisamy, V. and R. Garg, "Analysis of circularly polarized square ring and cross strip microstrip antennas", IEEE Trans. Antennas Propagat., vol. AP-34, no. 11, Nov. 1986, pp. 1340-1346.
41. Suzuki, Y., et al., "Circularly polarized radiation from singly fed equilateral triangular microstrip antennas", IEE Proc., vol. 134, Pt. H, 1987, pp. 194-198.
42. Bhattacharyya, A.K. and L. Shafai, "A wider band microstrip antenna for circular polarization", IEEE Trans. Antennas Propagat., vol. AP-36, no. 2, Feb. 1988, pp. 157-163.
43. James, J.R., P.S. Hall and C. Wood, Microstrip Antenna - Theory and Design, Peter Peregrinus, 1981, pp. 201-204.
44. Dong, W.R. and D.L. Sengupta, "A class of broadband patch microstrip traveling wave antennas", IEEE Trans. Antennas Propagat., vol. AP-32, 1984, pp. 98-100.
45. Hall, P.S., "Multioctave bandwidth log-periodic microstrip antenna array", IEE Proc., vol. 133, Pt. H, no. 2, April 1986, pp. 127-136.

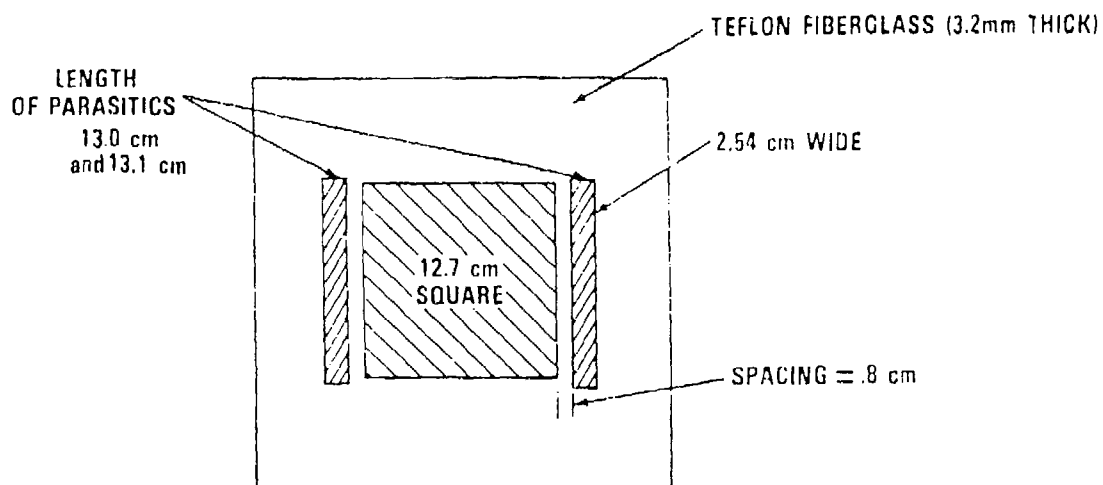


Fig. 1 A rectangular patch antenna with parasitically coupled strips [10].

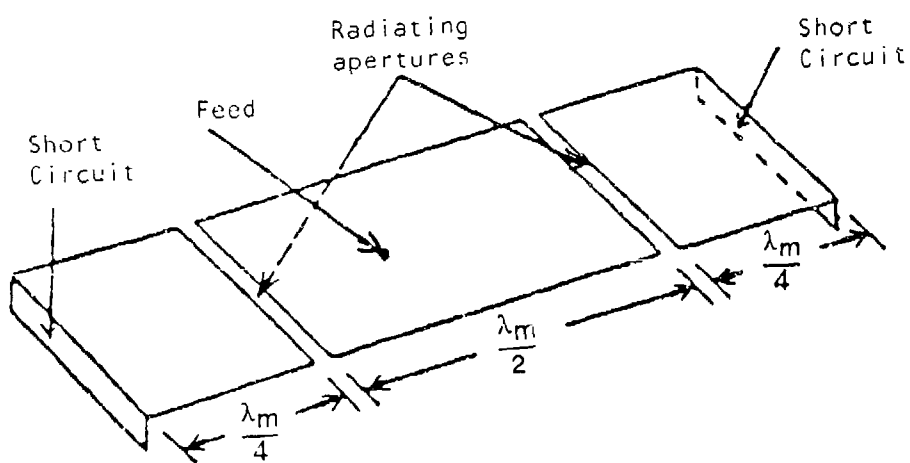


Fig. 2 A rectangle with two $\lambda/4$ shorted patches coupled to the non-radiating edges [11].

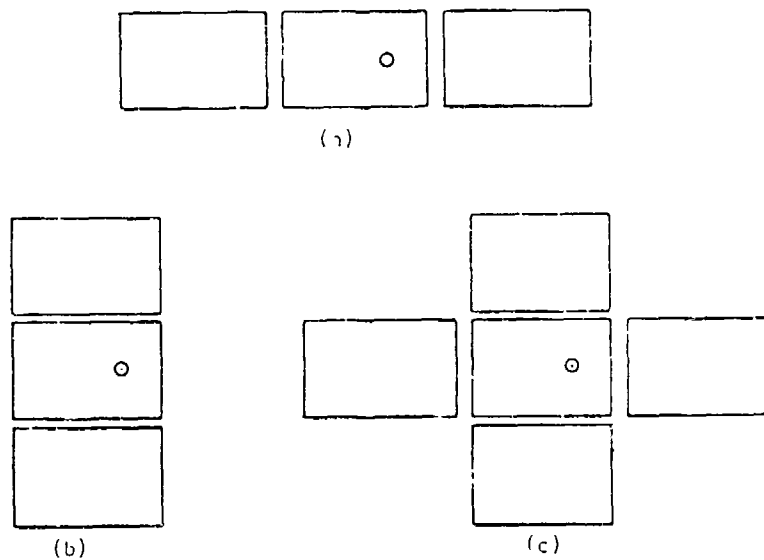


Fig. 3 (a) Radiating-edges gap-coupled microstrip antenna [12];
 (b) Non-radiating edges gap-coupled microstrip antennas [13]; and
 (c) Four-edges gap-coupled microstrip antenna [13].

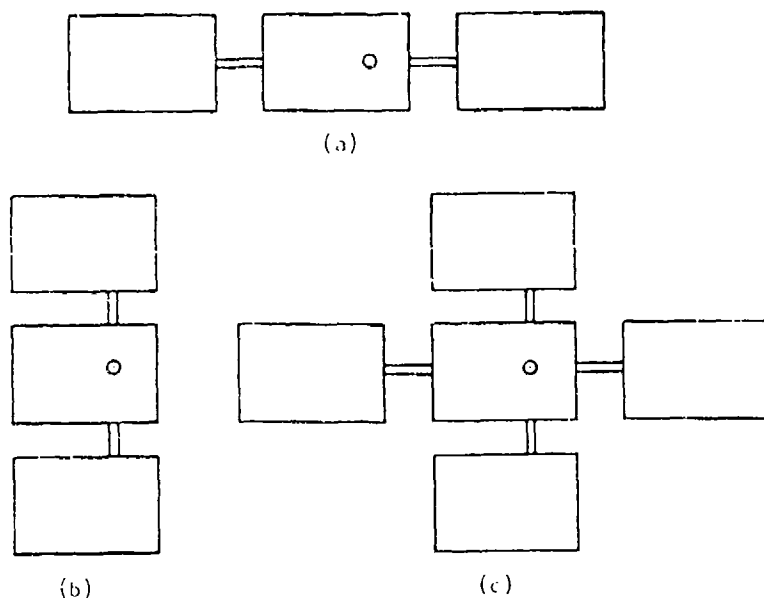


Fig. 4 (a) Radiating-edges directly-coupled microstrip antenna [14];
 (b) Non-radiating edges directly-coupled microstrip antenna [14] and
 (c) Four-edges directly-coupled microstrip antenna [14].

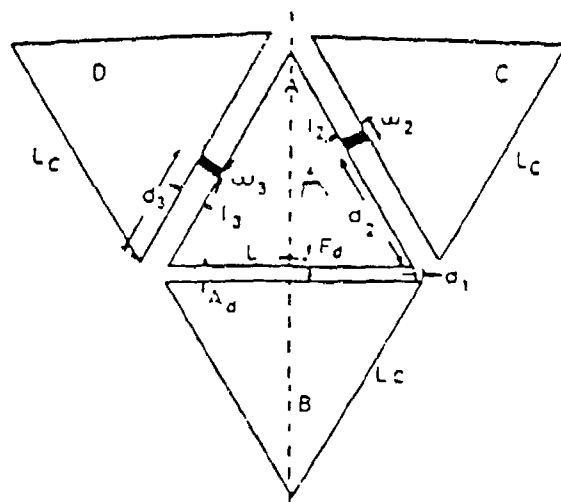


Fig. 5 A multiresonator microstrip antenna using four triangular patches [15].

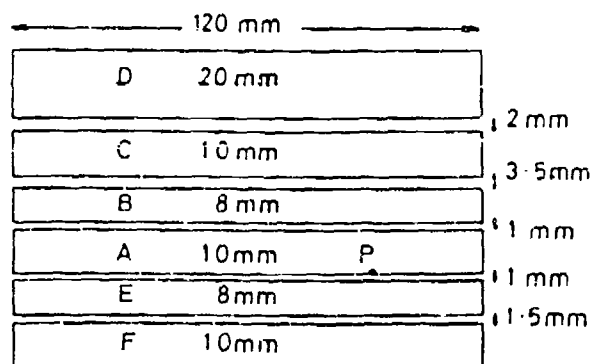
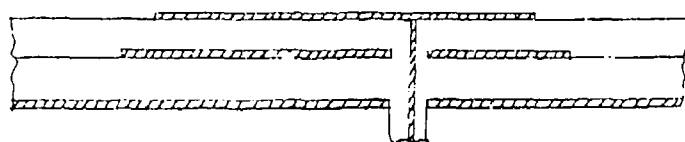
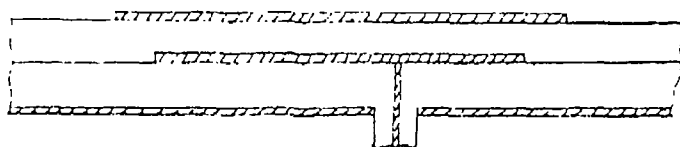


Fig. 6 A multiresonator microstrip antenna using six narrow patches coupled at the non-radiating edges [16].



(a)



(b)

Fig. 7 (a) Two-patch two-layer antenna with smaller patch located on the top layer.
 (b) Two-patch two-layer antenna with larger patch located on the top layer.

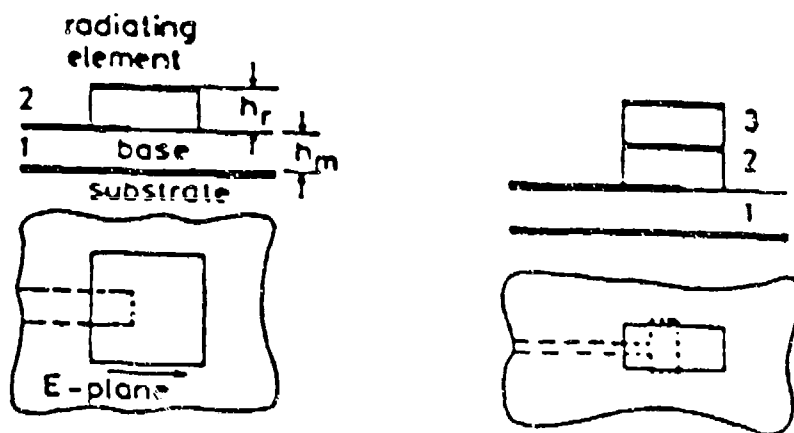


Fig. 8 (a) and (b) Examples of wideband microstrip antennas for circuit integration [18].

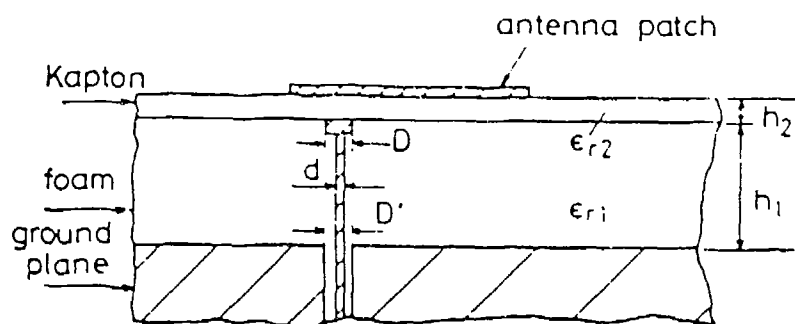


Fig. 9 A microstrip antenna with a series L-C network used for wideband impedance matching [29].

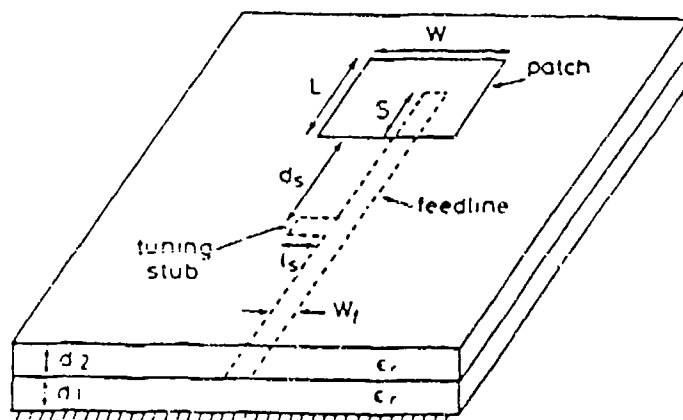


Fig. 10 A single stub impedance matching technique for increasing the bandwidth of an electromagnetically coupled microstrip patch [31].

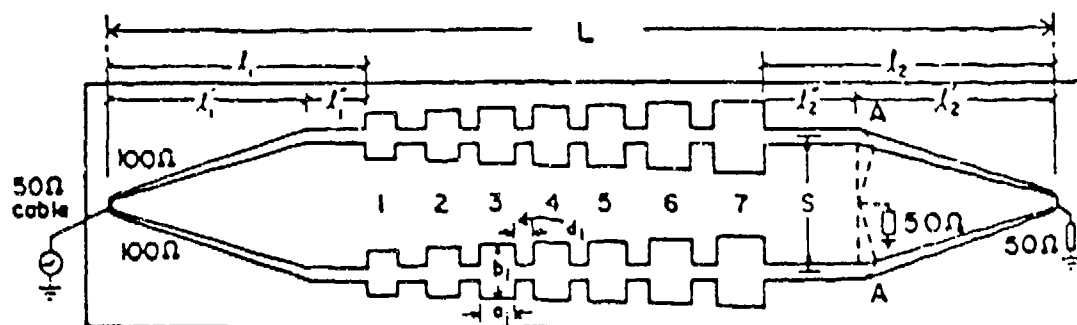


Fig. 11 Double-section wideband series-linear array of microstrip patches [44].

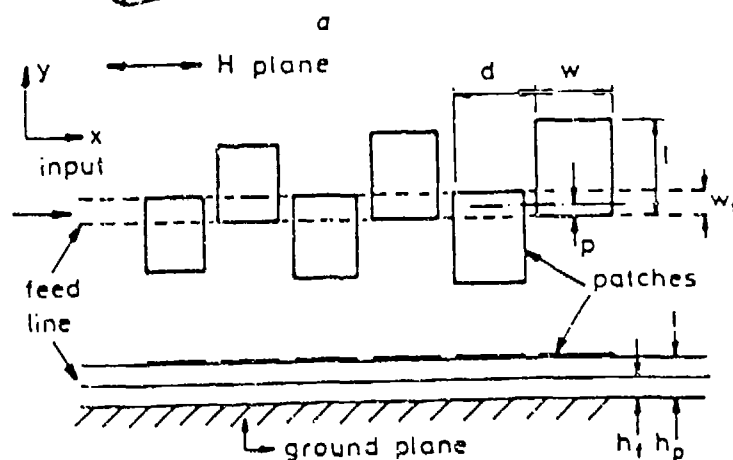
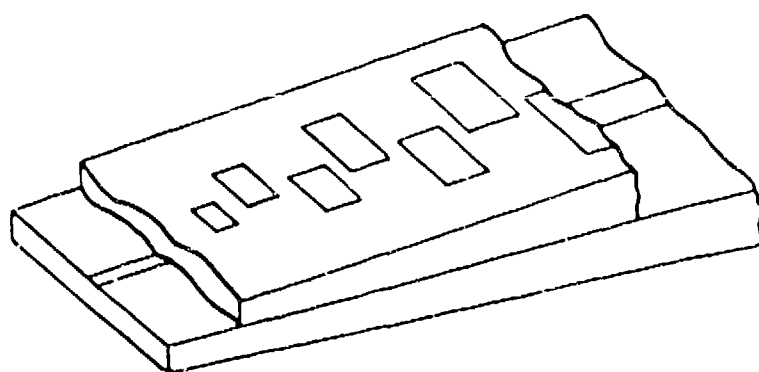


Fig. 12 A log-periodic overlaid array of electromagnetically coupled microstrip patches [45].

CHARACTERISTICS OF ELECTROMAGNETICALLY COUPLED RECTANGULAR PATCH
ANTENNAS WITH OVERLAYING PARASITIC ELEMENTS

by

R. Q. Lee

NASA Lewis Research Center
Cleveland, OH 44135

K. F. Lee

Department of Electrical Engineering
The University of Toledo
Toledo, OH 43606

ABSTRACT

The characteristics of electromagnetically coupled patch (EMCP) antennas consisting of a driven rectangular element in the bottom and identical parasitic elements on the top have been investigated experimentally. The antenna was excited at the resonant frequency of the TM_{01} mode with teflon spacers to vary the spacings between the antenna layers. Experimental results indicate that, for the two-layer EMCP antenna, the characteristics can be separated into three regions depending on the spacings between the driven and parasitic layers. Significant improvement in bandwidth is possible

only in region 1, and high gain with about one percent bandwidth is achievable in region 3. Region 2 generally has poor radiation characteristics and is therefore not suitable for antenna applications. For the three-layer EMCP antenna operated in the high gain region 3, experimental results show that the overlaying parasitic elements can enhance the gain (db) and reduce the beamwidth of the antenna by a factor of two or better.

INTRODUCTION

Microstrip antennas are known to have narrow bandwidth and low gain. In recent years, research on bandwidth improvement utilizing parasitic element has been extensive and significant results have been made. By coupling coplanar parasitic elements to a fed patch antenna, a bandwidth five times as large as that of a single patch has been reported [1]. The problem of gain enhancement has received disproportionately little attention in the literature. A method to increase the gain of printed circuit antennas using superstrates has been proposed by N. G. Alexopoulos et al [2]. This method requires the use of a superstrate with either very large dielectric constant ϵ or permeability μ . The practicality of this method depends on the availability of such materials. In a recent article, it was demonstrated that by placing closely spaced parasitic elements in the same plane of a driven patch, substantial enhancement of the gain was obtained [3]. It appears that, as in the case of bandwidth, parasitic elements play an important role in enhancing the gain of a microstrip patch.

This paper reports an experimental investigation of a two-layer and a three-layer EMCP antennas. Although the two-layer geometry has been studied by several investigators [4, 5], the emphasis of previous studies was on bandwidth improvement, and the spacing, s , between antenna layers seldom exceeded 0.15λ (λ = dielectric wavelength).

In a recent study [6] of a two-layer EMCP antenna with air spacing, it has been established that, depending on the spacing, s , the antenna characteristics can be divided into three regions: significant improvement in bandwidth is possible only in region 1, and high gain is achievable in region 3. Region 2 generally has poor radiation characteristics and is therefore not suitable for antenna applications. The high gain region begins at approximately 0.3λ (.61cm) and is accompanied by a narrow bandwidth of 1-2%. It is therefore reminiscent of a Yagi antenna. In this paper, results for the characteristics of a two-layer and a three-layer EMCP antennas with teflon spacers separating the antenna layers are presented. The three-layer EMCP antenna with two overlaying parasitic directors was designed to operate in the high gain region.

EXPERIMENTAL RESULTS

The microstrip patch used in our experiment is shown in Fig. 1a. The patch with dimensions $a=1.5$ cm and $b=1.0$ cm is fabricated on Cufilon substrate with $\epsilon_r=2.17$ and thickness 0.025 cm (10 mil). The

two-layer EMCP antenna consisting of an overlaying parasitic element and a driven patch is shown in Fig. 1b. The driven patch was excited with a coaxial probe at the resonant frequency of the TM_{01} mode. In the experiment, the spacing between antenna layers was incremented in multiples of 0.381 mm (15 mil) using teflon spacers. For each spacing, s , the E and H-plane patterns and the swept frequency response were measured. From these, the resonant frequency as well as the antenna gain can be estimated. The estimated gains computed from the formula [7]

$$\text{Gain (db)} \sim 10 \log \left(\frac{26000}{HP_E^\circ HP_H^\circ} \right)$$

are found to agree to within ± 0.6 db of the measured values. The characteristics for the case of 10 mil substrates for both driven and parasitic patches are summarized in Table-1. As in the case with air separation, the antenna characteristics can be divided into three regions: region 1 ($0 \leq s \leq 0.114$ cm) exhibits a double-humped response characteristics with an estimated gain of about 7 db; region 2 ($0.305 \leq s \leq 0.381$ cm) has "abnormal" radiation patterns while region 3 ($s > 0.61$ cm) exhibits "normal" pattern shapes and has an estimated gain of about 11 db. Representative patterns for each region are shown in Fig. 2.

To evaluate the concept of gain enhancement using parasitic directors, a three-layer EMCP antenna with two identical rectangular parasitic patches was tested. The EMCP antenna was designed with proper spacings, s , for operation in the high gain region. For comparison purpose, antenna gain, radiation patterns and swept frequency response of a single microstrip patch and a two-layer EMCP antenna were also measured. The experimental results are given in Table 2. Based on these results, the following comments can be made:

- a) The presence of parasitic directors reduces the 3 db beamwidth of both the E and H-plane patterns. The 3 db beamwidth of the E-plane is reduced from 103° to 45° with one parasitic director and to 30° with two parasitic directors, while the 3 db beamwidth of the H-plane is reduced from 70° to 50° to 35° respectively. The E and H-plane patterns are shown in Figures 3 and 4.
- b) As indicated in the swept frequency measurement in Fig. 5, the parasitic directors reduce the resonant frequency from 10.12 GHz for the single patch to 10.06 GHz for the two-layer and to 10.02 GHz for the three-layer EMCP antennas.
- c) The spacings for operating in the high gain region are 0.35λ for the two-layer; 0.35λ and 0.47λ for the three-layer antennas.

d) Antenna gains were measured using the image method under mismatched conditions [8]. The measured gain for the single patch is 4.7 db compared to 8.4 db for the two-layer and 10.6 db for the three-layer EMCP antennas. It appears that further increase in gain is possible with additional directors.

CONCLUSION

In conclusion, experimental results for a two-layer and a three-layer EMCP antennas have been presented. In addition to the large bandwidth region at $s \leq .114$ Cm, a high gain region is found at $s > 0.3 \lambda$. For the three-layer EMCP antenna operated in the high gain region, the parasitic directors enhance the gain of a rectangular patch antenna from 4.7 db to 10.6 db, and reduce the 3 db beamwidth from 103° to 30° for the E-plane and from 70° to 35° for the H-plane. The three-layer EMCP antenna exhibits similar characteristics as a Yagi antenna with over 10 db gain and with about 1-2% bandwidth.

REFERENCES

1. G. Kumar and K. C. Gupta, "Broad-band Microstrip Antennas Using Additional Resonators Gap-coupled to the Radiating Edges", IEEE Trans. AP-32, No. 12, 1984 pp. 1375-1379.

2. N. G. Alexopoulos and D. R. Jackson, "Fundamental Superstrate (Cover) effects on Printed Circuit Antennas", IEEE Trans. AP-32, 1984 pp. 807-816.
3. R. Q. Lee, R. Acosta and K. F. Lee, "Radiation Characteristics of Microstrip Array With Parasitic Elements", Electronics Lett., Vol. 23, 1987 pp. 835-837.
4. A. Sabin, "A New Broadband Stacked Two-layer Microstrip Antenna", IEEE AP-S Int. Sym. Digest, 1983, pp. 63-66.
5. C. H. Chen, A. Tubintseff and R. M. Sorbello, "Broadband Two-layer Microstrip Antenna", IEEE AP-S Int. Sym. Digest, 1984, pp. 251-254.
6. R. Q. Lee, K. F. Lee and J. Bobinchak, "Characteristics of a Two-layer Electromagnetically Coupled Rectangular Patch Antenna", Electronics Lett., Vol. 23, 1987, pp. 1070-1072.
7. W. L. Stutzman and G. A. Thiele, "Antenna Theory and Design", John Wiley & Sons, 1981, p. 397.
8. R. Q. Lee and M. F. Baddour, "Absolute Gain Measurement of Microstrip Antennas Under Mismatched Conditions", Electronics Lett. Vol. 24, 1988, pp. 521-522.

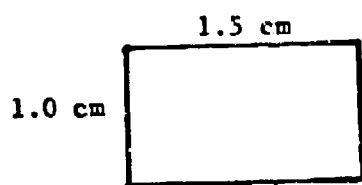
Table 1. Characteristics of a rectangular EMCP antenna with teflon separation: $a=1.5\text{cm}$, $b=1.0\text{cm}$, $\epsilon_r=2.17$, $t_1=t_2=0.0254\text{cm}$.

Spacing s (cm)	f_{01} (GHz)	Pattern shape	3 dB beamwidth (deg.)	Estimated gain (dB)	Bandwidth* (%/°)
0.000	10.3	normal	88 x 65	6.6	7.1
0.038	10.8	normal	78 x 65	7.1	3.0
0.076	10.5	normal	82 x 65	6.9	1.7
0.114	10.5	normal	78 x 65	7.1	1.5
0.305	10.3	abnormal	-	-	-
0.343	10.2	abnormal	-	-	-
0.381	10.2	abnormal	-	-	-
0.610	10.1	normal	40 x 50	11.1	1.0
0.648	10.1	normal	40 x 55	10.7	1.0
0.762	10.0	normal	40 x 50	11.1	1.0
Single patch	10.2	normal	110 x 70	5.3	2.3

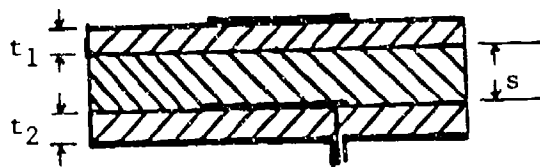
*Range of frequencies for which the real part of the impedance is greater than one-half of its value at resonance.

Table 2. Characteristics of a rectangular electro-magnetically coupled patch antenna with $a=1.5$ cm, $b=1.0$ cm

Antenna Types	Single Patch	Two-layer	Three-layer
3 db beamwidth (E-plane)	103°	45°	30°
3 db beamwidth (H-plane)	70°	50°	35°
Gain (db)	4.7	8.4	10.6
Freq. (GHz)	10.12	10.06	10.02
Element Spacings	---	0.35λ	0.35λ 0.47λ



(a)



(b)

Fig. 1 Geometry of (a) rectangular microstrip patch and (b) two-layer EMCP antenna.

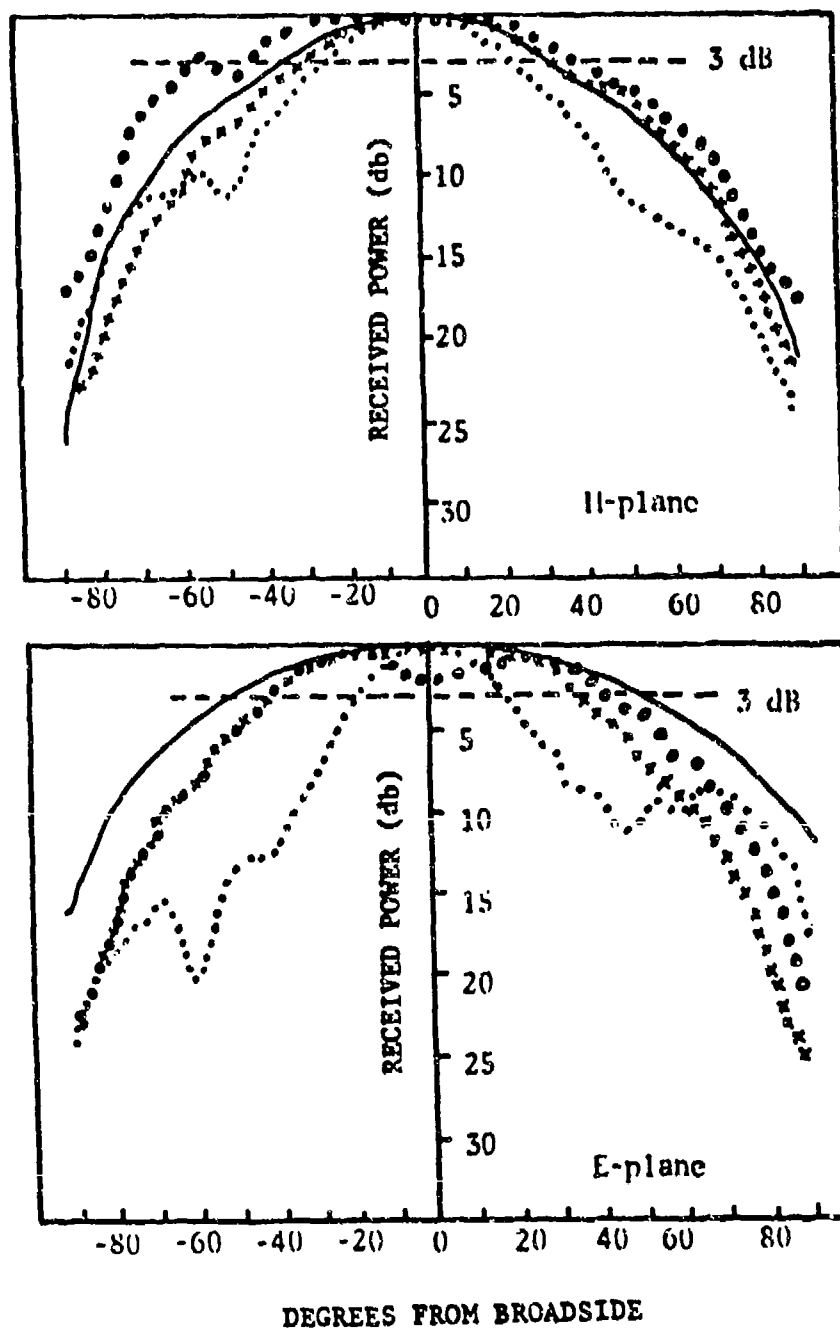


Fig. 2 Patterns of a rectangular EMCP antenna with teflon separation: $a=1.5$ cm, $b=1.0$ cm, $\epsilon_r=2.17$, $t_1=t_2=0.0254$ cm.

—————	single patch
xxxxxxxxx	$s=0.038$ cm (region 1)
ooooooooo	$s=0.305$ cm (region 2)
.....	$s=0.648$ cm (region 3)

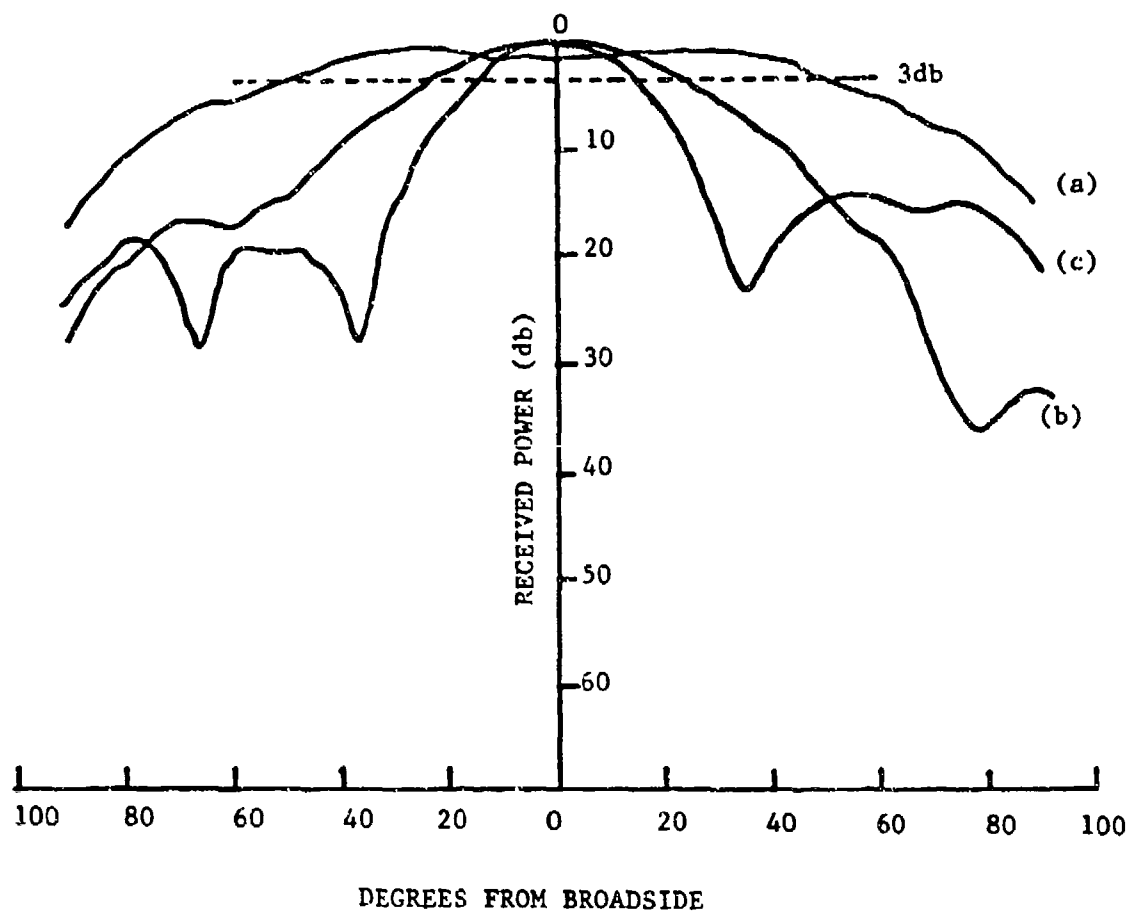


Fig. 3 E-plane patterns for (a) single patch, (b) two-layer EMCP antenna and (c) three-layer EMCP antenna.

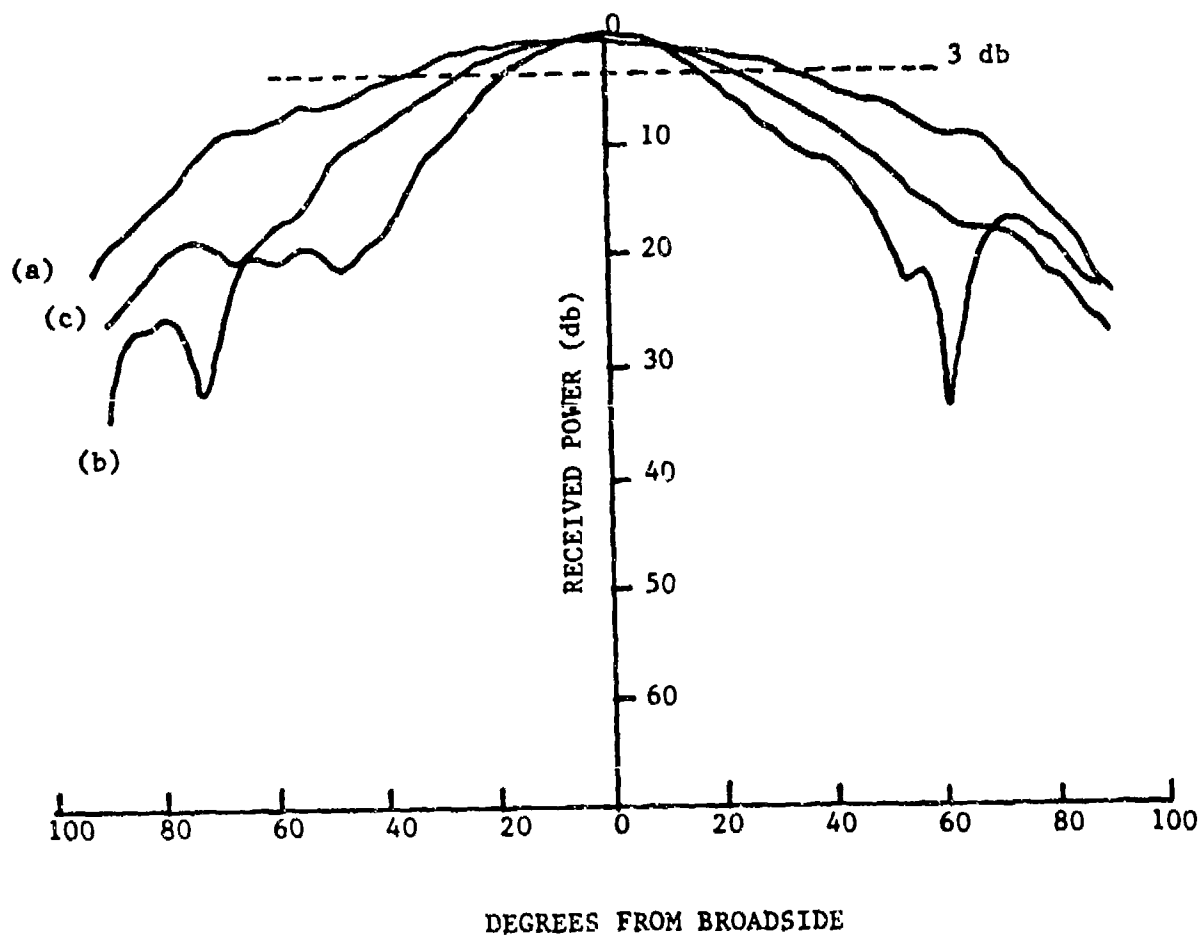


Fig. 4 H-plane patterns for (a) single patch, (b) two-layer EMCP antenna and (c) three-layer EMCP antenna.

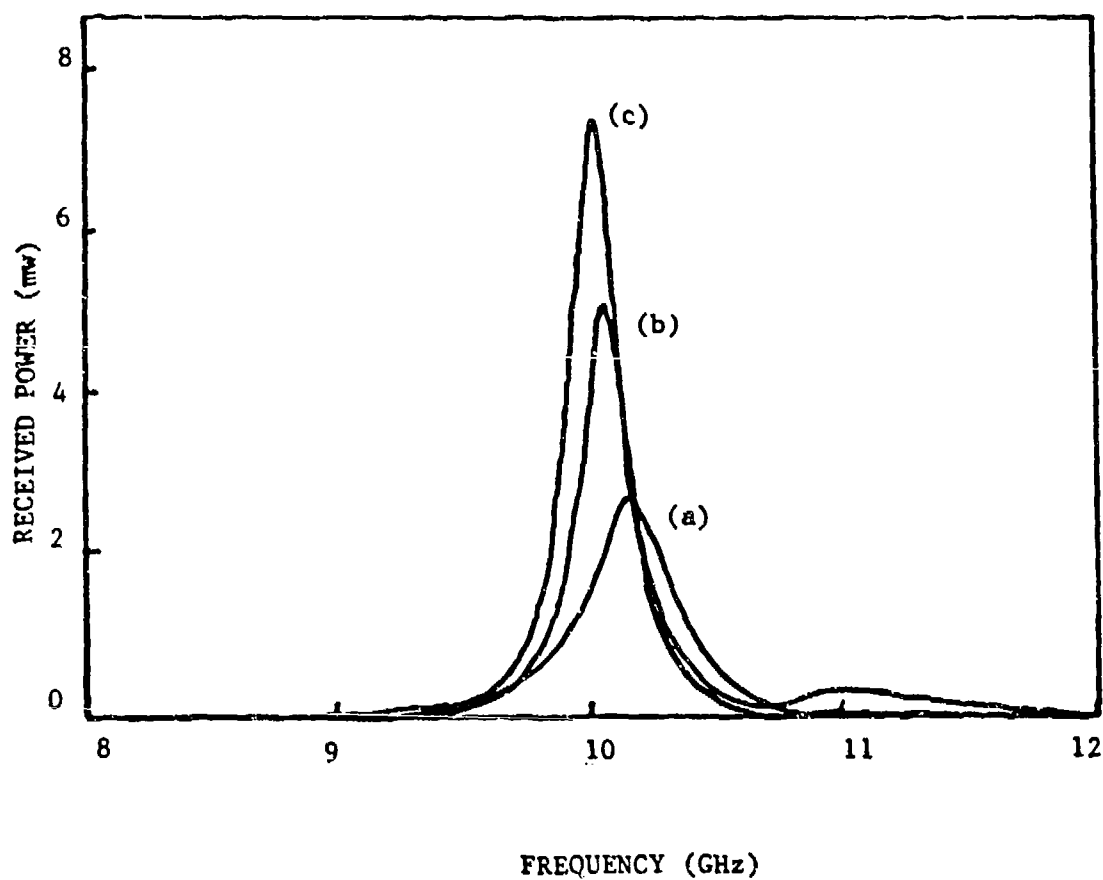


Fig. 5 Swept frequency measurement of (a) single patch, (b) two-layer EMCP antenna and (c) three-layer EMCP antenna.

**THE ANNULAR SECTOR MICROSTRIP ANTENNA
MOUNTED ON PLANAR AND CONICAL SURFACES**

David C. Thompson
Motorola, Inc., Government Electronics Group
Scottsdale, Arizona 85252

Constantine A. Balanis
Department of Electrical and Computer Engineering
Arizona State University
Tempe, Arizona 85287

ABSTRACT:

When a microstrip antenna is mounted on a conical surface, the planar element geometry which conforms to that of the cone is the annular sector element. This paper presents analytical and experimental results for the annular sector microstrip antenna when mounted on both planar and conical surfaces. The cavity model is applied to analyze the resonant frequency, input impedance, and radiation patterns of the element on a planar surface. This theory is then expanded upon and applied to the design of elements mounted on conical surfaces. Experimental pattern characteristics of the element mounted on a conical surface are presented, for both the TM_{01} and TM_{11} modes. A set of design curves has been developed to provide a practical means of designing the annular sector element based upon the specified mode and resonant frequency.

1.0 INTRODUCTION:

The microstrip antenna has proven to be a very useful element in many applications, because it may be designed in a variety of geometric shapes, and it can be conformally mounted on flat and curved surfaces. Extensive analysis has been done for the more commonly

used microstrip antenna geometries, including the rectangle, square, and the circular disk¹⁻³. However, when a patch element is conformally mounted on a conical surface, the geometrical constraints require that the annular sector shape be used. On a planar surface, the annular sector element is defined as shown in Figure 1. Although some analysis has been done for this element in the planar configuration^{4,5}, very little work has been reported in the literature regarding analysis and practical considerations for the design of such an element mounted on conical surfaces.

This paper applies the cavity model theory to determine the resonant frequency, polarization, input impedance, and radiation patterns for the planar annular sector element. This theory is extended to the design of elements on conical surfaces by projecting the dimensions of the conical structure onto a planar surface, using the cavity model to design elements on this equivalent planar surface, and computing the element dimensions as projected onto the cone.

2.0 THEORY:

The cavity model theory was originally developed by Y. T. Lo et al¹ for application to a wide variety of

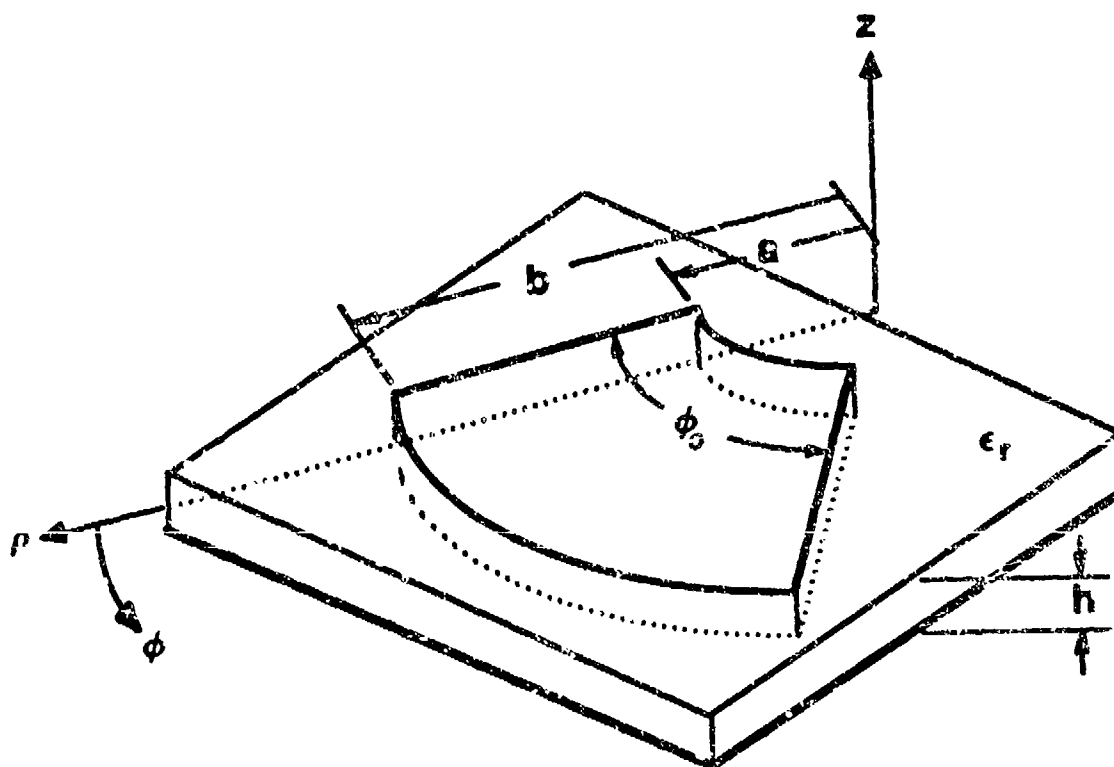


FIGURE 1:
ANNULAR SECTOR MICROSTRIP ANTENNA,
PLANAR ELEMENT CONFIGURATION

canonical shaped elements. Basically, this theory models the microstrip patch element as a cavity bounded by electric conductors on the top and bottom, and magnetic conductor walls on all sides. Restricting the analysis to that of a "thin" substrate allows the field components to be modelled as constant along the z-axis, with the E-field in the cavity oriented along the z-axis (TM^z). By applying the appropriate boundary conditions in a cylindrical coordinate system, this theory may be applied specifically to the annular sector element.

Using such a cavity model, a series of (TM) modal solutions may be obtained. Since this element is analyzed in the cylindrical coordinate system, the solutions are expressed in terms of circumferential field variations as TM_{pq} modes, with the subscripts defined as:

p = number of circumferential field variations
(p = 0, 1, 2, ...)

q = the qth radial root for a given p
(q = 1, 2, 3, ...)

To focus on the practical applications for this element, the analysis presented here shall concentrate on the design of two specific modes, the TM₀₁ and TM₁₁ modes. The fundamental difference between these two

modes is that their internal field distributions, and thus their radiation patterns, are polarized on orthogonal axes. As shown in Figure 2, the E-field has a radial component (E_ρ) for the TM_{01} mode, and a circumferential component (E_ϕ) for the TM_{11} mode. This provides a great deal of flexibility when implementing the annular sector element in specific design applications.

2.1 Resonant Frequency

The resonant frequency is computed by analyzing the internal field structure of the element, subject to the appropriate boundary conditions. The solution is derived in terms of a wave function ψ_{pq} : ($E_z = -j\omega\mu\psi_{0q}$)

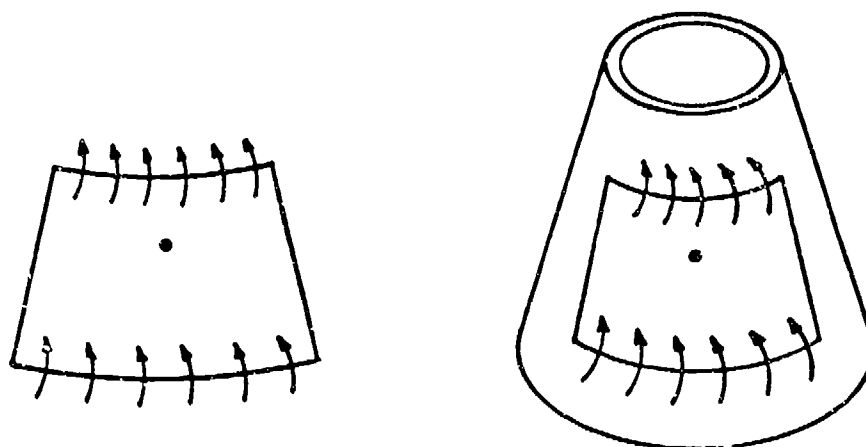
$$\psi_{pq} = [A_1 J_m(k\rho) + B_1 Y_m(k\rho)] \cos(m\phi) \quad (1)$$

where J_m and Y_m are Bessel functions of the first and second kind, respectively, of order m . Applying the boundary conditions on the electric and magnetic fields leads to a characteristic equation:

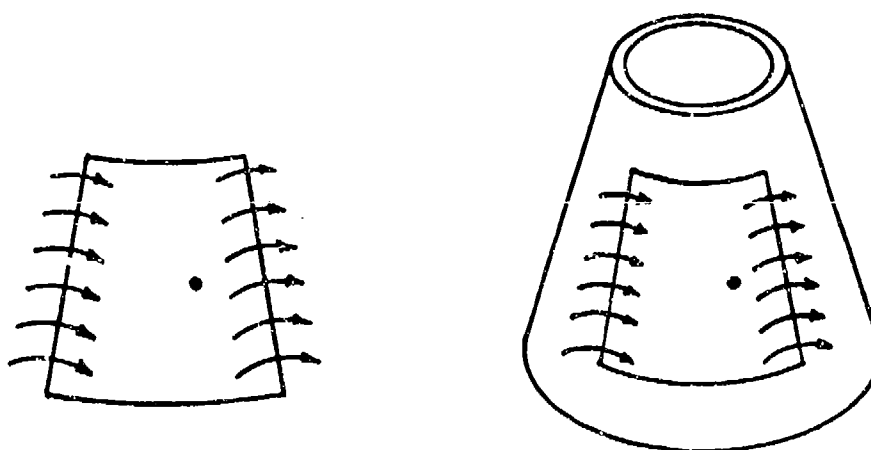
$$J'_m(ka)Y'_m(kb) - J'_m(kb)Y'_m(ka) = 0 \quad (2)$$

$$m = p\pi/\phi_0, \quad p = 0, 1, 2, \dots$$

Any annular sector element design must satisfy (2).



(a) TM_{01} MODE (E_ρ)



(b) TM_{11} MODE (E_ϕ)

FIGURE 2: ANNULAR SECTOR E-FIELD DISTRIBUTIONS

Thus, given the physical dimensions (a , b , and ϕ_0) of the element, the resonant frequency may be computed by solving (2) for k , where $k = 2\pi f\sqrt{\mu_0\epsilon_0\epsilon_r}$. However, many design problems specify the frequency of operation, and desire to determine the element dimensions. This can be accomplished best by casting (2) in another form. Let us express the characteristic equation (2) as follows:

$$\frac{Y_m'(ka)}{J_m'(ka)} = \frac{Y_m'(kb)}{J_m'(kb)} \quad (3)$$

In this form, the solution is obtained for a given frequency (which fixes k) and angle ϕ_0 (which fixes m) by determining the inner (a) and outer (b) radii that satisfy the equation.

The practical application of this may be seen by plotting $Y_m'(kr)/J_m'(kr)$ vs kr for the desired modes. The resultant graphical solutions provide a set of design tools for determining the dimensions of an annular sector element. The characteristic curves for the TM_{01} mode are shown in Figure 3. Note that the solutions for the TM_{01} mode are independent of the sector angle ϕ_0 . A set of TM_{11} mode solutions are shown in Figure 4 for a number of sector angles ranging

ANNULAR SECTOR PATCH ANTENNA

TM 01 MODE SOLUTIONS, FOR ANY ANGLE ϕ_0

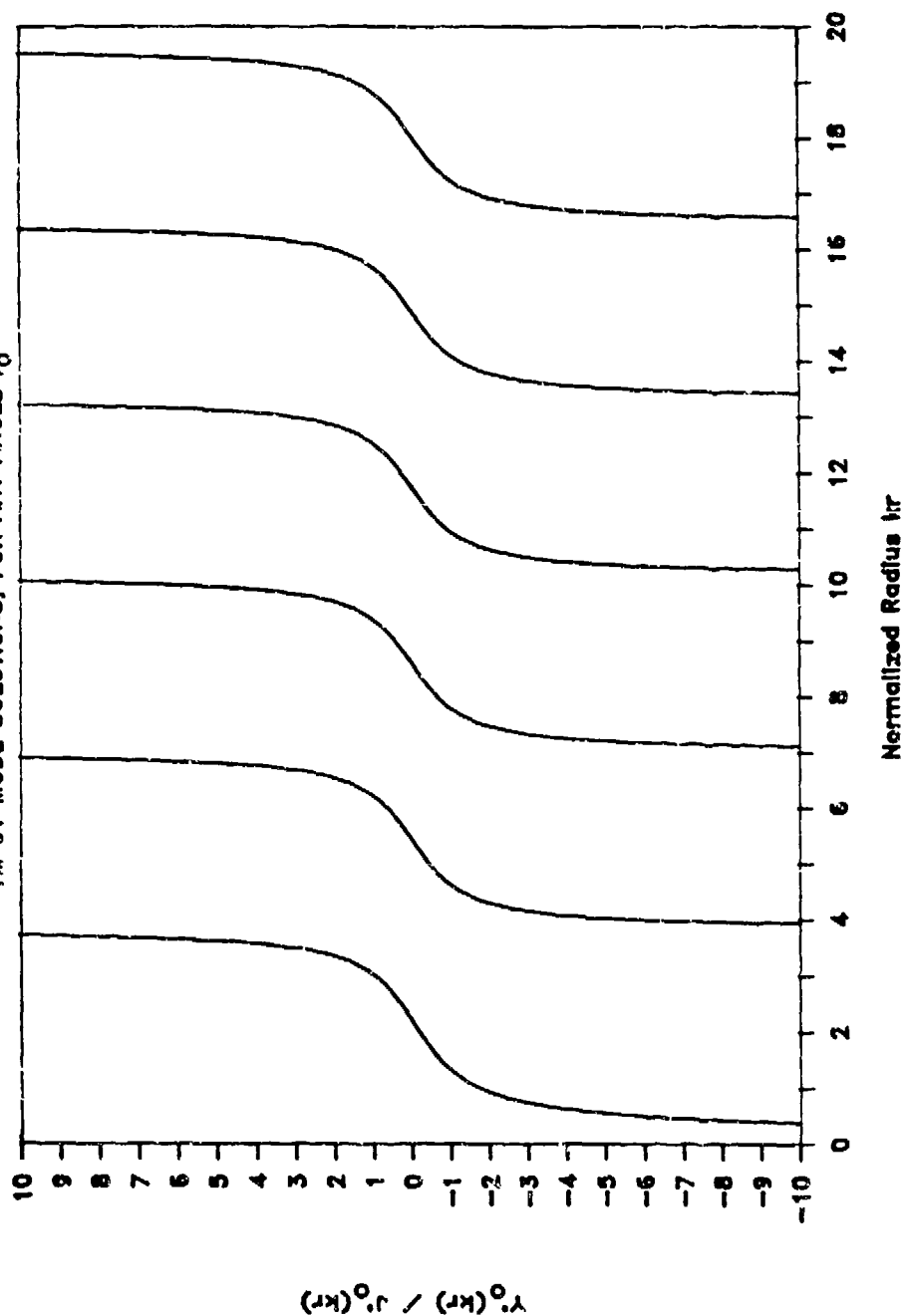


FIGURE 3: DESIGN CURVES FOR TM₀₁ MODE

ANNULAR SECTOR PATCH ANTENNA

TM₁₁ MODE SOLUTIONS

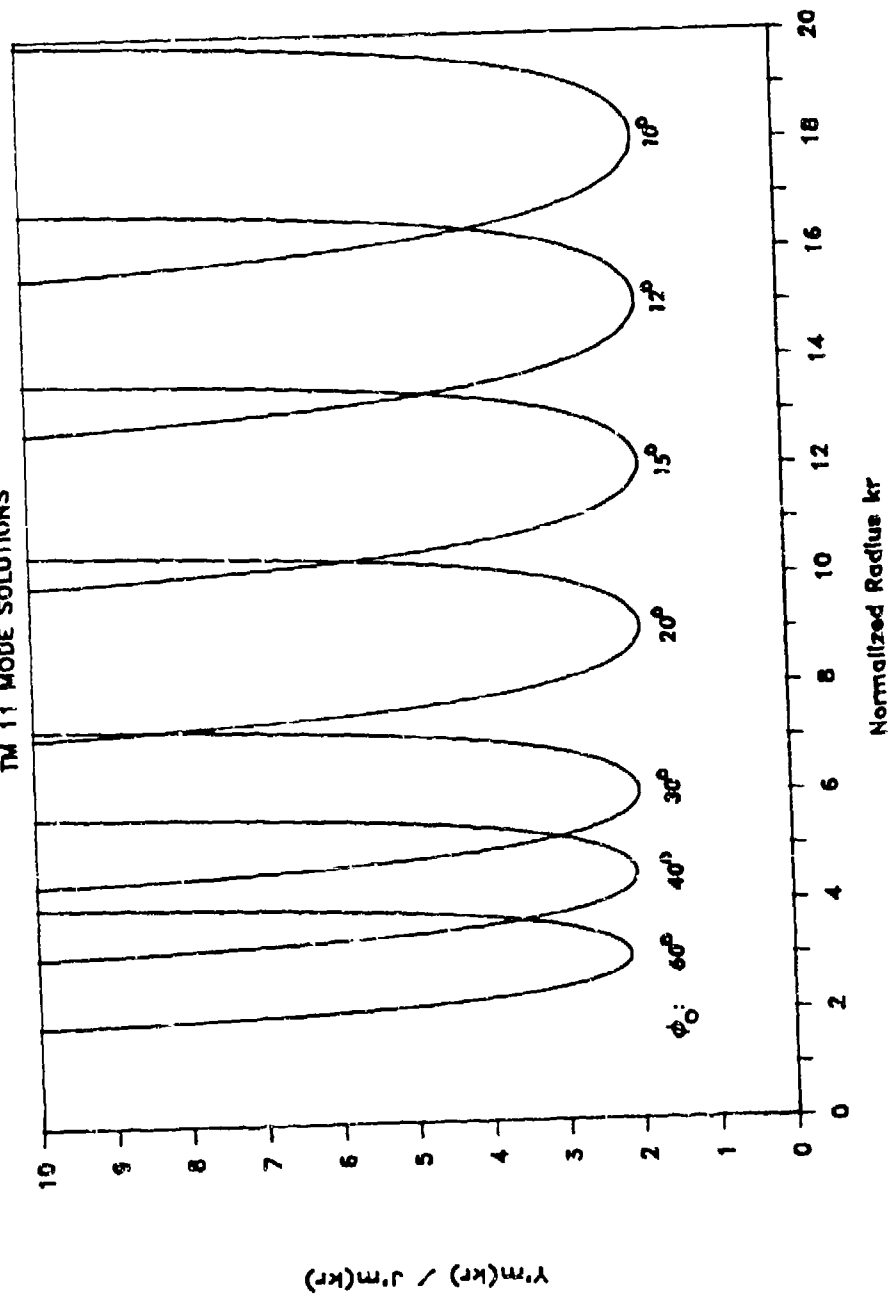


FIGURE 4: DESIGN CURVES FOR TM_{11} MODE

from 10 to 60 degrees. These design curves are applied by choosing the desired sector angle ϕ_0 , and finding two points, ka and kb , which have equal values on the vertical axis.

The dimensions calculated with this method do not account for the fringing fields which extend beyond the physical dimensions on the radiating edges. Thus, to maintain resonance at a given frequency, the element dimensions must be adjusted to compensate for the fringing effects. Formulas have been developed for various element shapes^{2,6,7}. For the annular sector element the microstrip line open circuit formula⁸ was modified to fit more closely with the measured data:

$$\Delta l = 0.412h \frac{(\epsilon_r + 0.300) (W_{eff}/h + 0.264)}{(\epsilon_r - 0.258) (W_{eff}/h + 0.800)} \quad (4)$$

Thus, (4) has modified the original formulation by using the relative dielectric constant ϵ_r , rather than an effective dielectric constant. This method was found to provide a more accurate prediction of the resonant frequency, similar to observations made by others using different element shapes⁶. W_{eff} is an effective element width, defined below.

Using Δl , the physical dimensions of the element may be adjusted to account for the fringing effects.

The resonant length of the element depends upon the selected mode. Shown in Figure 2, the TM_{01} resonant length is on the radial axis, whereas the TM_{11} resonant length is on the angular axis. Thus, the element corrections to account for fringing in these two modes are derived as:

TM_{01} Mode:

$$W_{eff} = \frac{a + b}{2} \phi_0 \quad (5a)$$

$$a' = a + \Delta l \quad (5b)$$

$$b' = b - \Delta l \quad (5c)$$

$$\phi'_0 = \phi_0 \quad (5d)$$

TM_{11} Mode:

$$W_{eff} = b - a \quad (6a)$$

$$a' = a \quad (6b)$$

$$b' = b \quad (6c)$$

$$\phi'_0 = \phi_0 - \frac{4\Delta l}{a + b} \quad (6d)$$

The primed variables in (5) and (6) represent the corrected physical dimensions of the element after accounting for the fringing. (Note: angular variables are expressed in radians.)

2.2 Input Impedance

The cavity model may be used to calculate the patch input impedance using a coax probe feed. However, the initial model must be modified to account for the feed location in the cavity, and to properly include the power loss due to radiation and dissipation mechanisms. Basically, the input impedance is proportional to the E-field, as given by:

$$Z_{in} = \frac{V}{I} = \frac{hE_z}{I} = hE_z \Big|_{I=1 \text{ amp}} \quad (7)$$

Thus, the probe feed is modelled as a 1 amp current source located at (ρ_f, ϕ_f) . To account for this discontinuity, the analysis was modified to an inhomogeneous problem using a technique of mode matching. This technique allows the patch element to be divided into two homogeneous regions, each of which satisfies the source-free boundary conditions. The sum of these modes are then matched to the source discontinuity. The wave function ψ_{pq} given by (1) is expanded about the boundary at $\rho = \rho_f$:

$$\psi_{pq}^1 = \sum_{p=0}^{\infty} [A_p^1 J_m(k\rho) + B_p^1 Y_m(k\rho)] \cos(m\phi) \quad (a < \rho < \rho_f) \quad (8a)$$

$$\psi_{pq}^2 = \sum_{p=0}^{\infty} [A_p^2 J_m(k\rho) + B_p^2 Y_m(k\rho)] \cos(m\phi) \quad (\rho_f < \rho < b) \quad (8b)$$

The wave functions in (8) were expanded in a series form to include the reactive impedance contributions from all higher order modes. These formulations were solved by enforcing field continuity between the two regions. Thus, the input impedance solution was derived and found to agree with that by Ou⁴:

$$Z_{in} = j\frac{\omega\mu\pi h}{\phi_0} \sum_{p=0}^{\infty} \left\{ \frac{[J_m(k\rho_f)Y'_m(ka) - J'_m(ka)Y_m(k\rho_f)]}{[J'_m(kb)Y'_m(ka) - Y'_m(kb)J'_m(ka)]} \right. \\ \left. \cdot [Y'_m(kb)J_m(k\rho_f) - J'_m(kb)Y_m(k\rho_f)] \frac{\cos^2(m\phi_f)}{1 + \delta_{0p}} \right\} \quad (9)$$

where $\delta_{0p} = 1$ for $p = 0$, and 0 for $p \neq 0$. However, (9) does not yet account for the power losses due to radiation (P_{rad}), and dissipation in the dielectric (P_d) and copper plating (P_c). Richards, et al⁹ developed an effective loss tangent δ_{eff} , equal to $1/Q$ of the cavity:

$$\delta_{eff} = \frac{1}{Q} = \frac{P_{rad} + P_d + P_c}{2 W_e} \quad (10)$$

Thus, the power terms¹ and the stored electric energy W_e ¹⁰ are computed and used to develop this effective loss tangent. This term for δ_{eff} is then used to express the wave number k as a complex quantity:

$$k_{\text{eff}} = 2\pi f \sqrt{(1 - j\delta_{\text{eff}})\mu_0\epsilon_0\epsilon_r} \quad (11)$$

Finally, the complex wave number in (11) is substituted into (9) to provide an accurate model for computing the input impedance of the annular sector element.

2.3 Radiation Patterns

The radiation characteristics of this element were computed using the equivalence principle. The electric fields at all edges of the element may be derived from (8) where $E_z = -j\omega\mu\psi_{pq}$. Huygen's principle was then applied to obtain the equivalent magnetic current densities on each of the cavity walls:

$$\mathbf{M} = -2\hat{n} \times \hat{a}_z E_z \quad (12)$$

By integrating these magnetic currents along the four edges of the element, the far-field radiation patterns were computed. However, to account for the edge effects of the finite substrate ground plane, the Geometric Theory of Diffraction (GTD)¹¹ was applied.

The radiation pattern theory was again applied only to the annular sector element mounted on a planar surface, although recent work has been done to develop theory for evaluation of pattern characteristics on more complex conformal surfaces¹².

3.0 EXPERIMENTAL RESULTS:

The theory developed for the planar annular sector patch was applied to design both TM_{01} and TM_{11} planar elements. Furthermore, to verify the application of this theory to antenna design on conformal surfaces, the planar dimensions were used to compute equivalent element dimensions as projected onto a cone. The cone structure fabricated for these tests had a 30° apex angle and was truncated at both ends, as indicated in Figure 2. The antennas were fabricated on a 0.062" thick substrate with a dielectric constant $\epsilon_r = 2.2$. The design frequency was chosen as $f_0 = 2.5$ GHz.

The characteristic equation (3) and fringing terms (4)-(6) were used to compute the element dimensions. However, when optimizing the input impedance, it was observed that the impedance formula (9) provided a more accurate prediction of the resonant frequency.

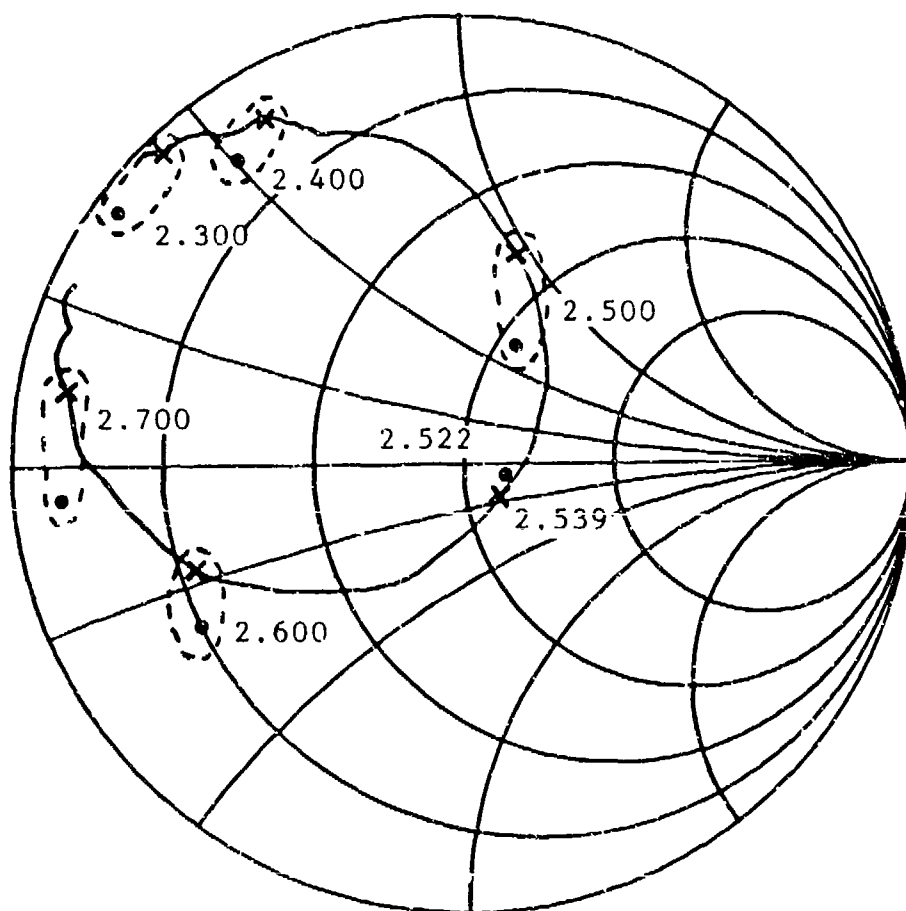
The resonant frequency measurements are compared with theory in Table 1 for each of the element designs. The resonant frequency was defined as the frequency which has the minimum VSWR, or optimum impedance match.

TABLE 1: RESONANT FREQUENCY:
MEASURED vs. THEORETICAL

Element Description	Measured (GHz)	Theoretical Using Eq. (3) (% error)	Theoretical Using Eq. (9) (% error)
TM ₀₁ Planar	2.539	2.500 (1.5%)	2.522 (0.7%)
TM ₀₁ Conical	2.527	2.500 (1.1%)	2.522 (0.2%)
TM ₁₁ Planar	2.535	2.500 (1.4%)	2.521 (0.6%)
TM ₁₁ Conical	2.452	2.500 (1.9%)	2.521 (2.8%)

The input impedance was optimized by applying (9), and locating the feed point to maximize the 2:1 VSWR bandwidth. The measured and theoretical impedance of the four antenna elements are shown in Figures 5-8. As can be seen, the agreement is generally good, with the exception of the TM₀₁ conical element in Figure 6. This element has good agreement for the resonant frequency, but shows a discrepancy in the impedance magnitude, which is believed to be caused by the close proximity of the patch radiation edges to the truncated cone edges.

The radiation patterns were measured for the TM₀₁ and TM₁₁ conical annular sector elements, and are shown



— experimental

• • theoretical

FIGURE 5:

INPUT IMPEDANCE FOR TM_{01} PLANAR ELEMENT

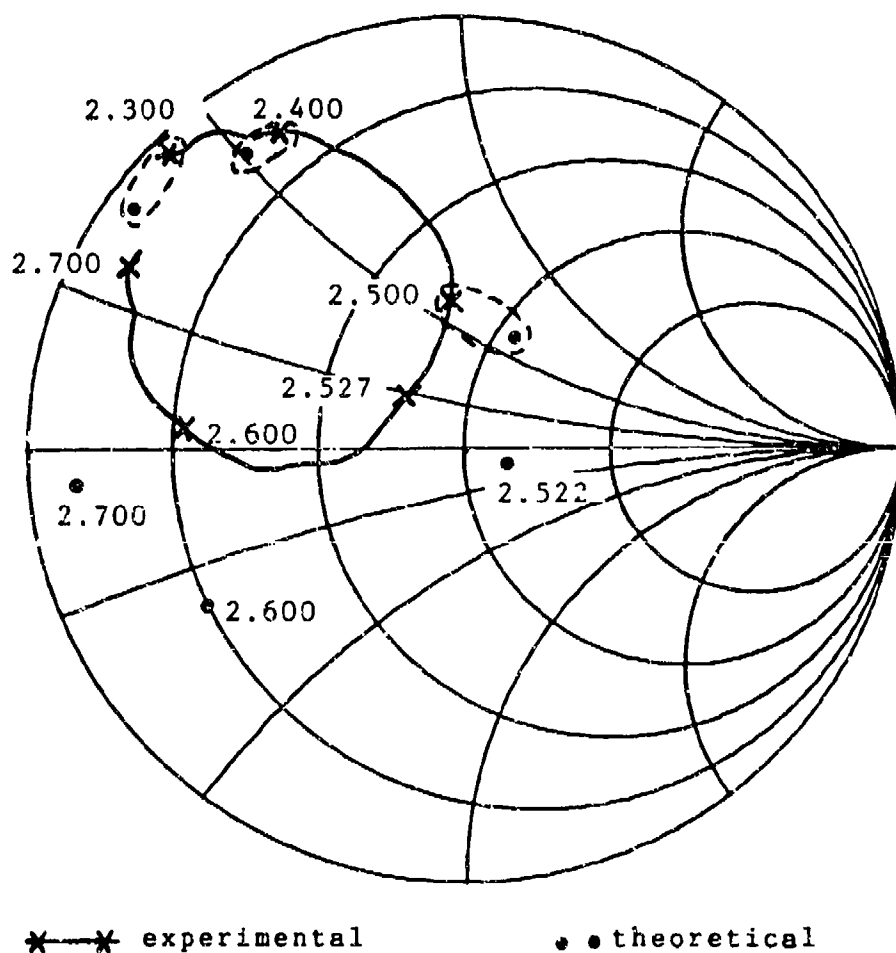
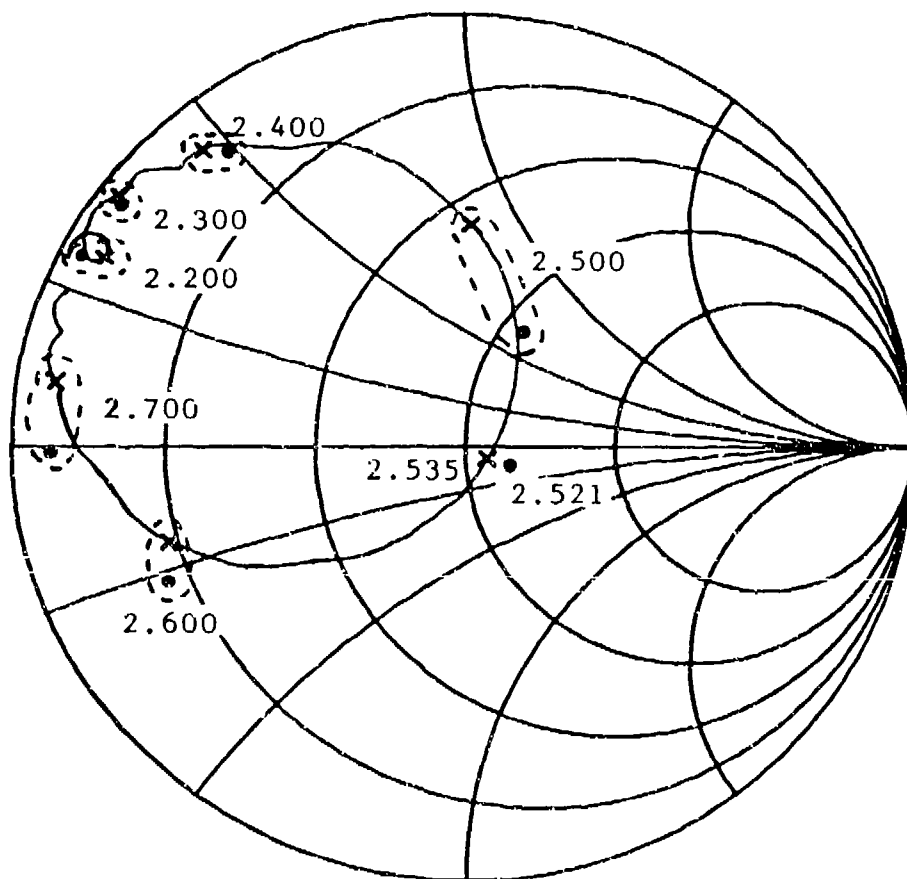


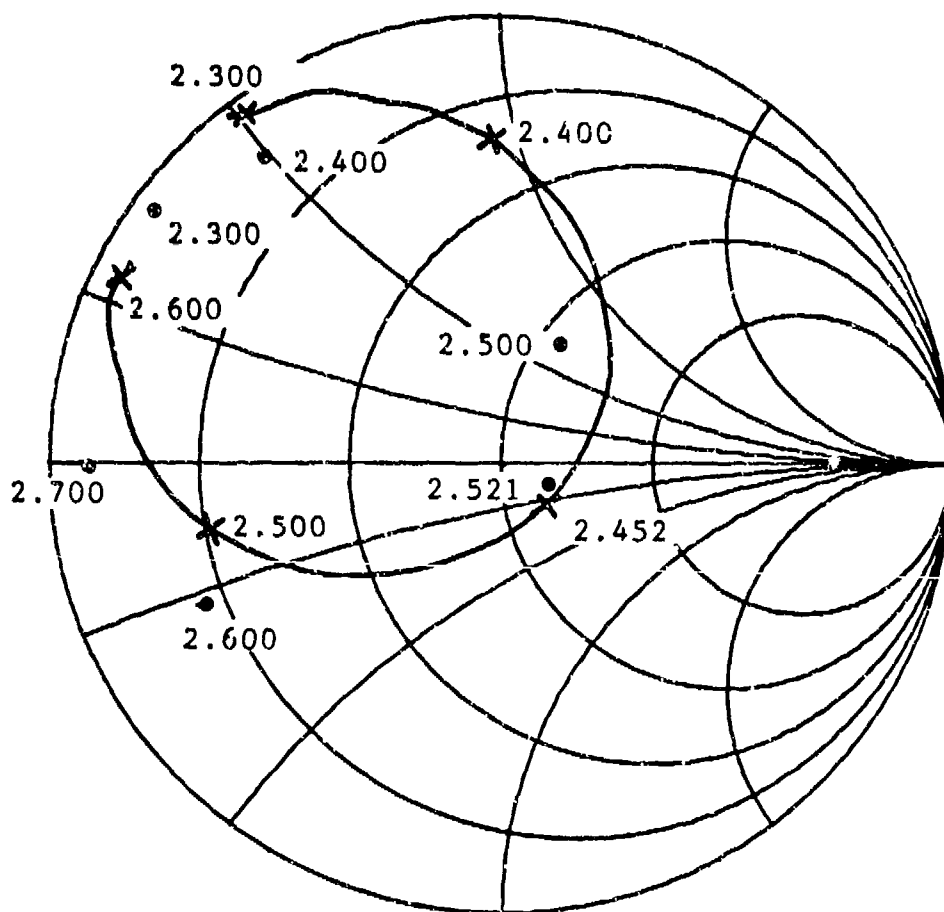
FIGURE 6:
 INPUT IMPEDANCE FOR TM_{01} CONICAL ELEMENT



— experimental

• • theoretical

FIGURE 7:
INPUT IMPEDANCE FOR TM_{11} PLANAR ELEMENT



— experimental

••theoretical

FIGURE 8:

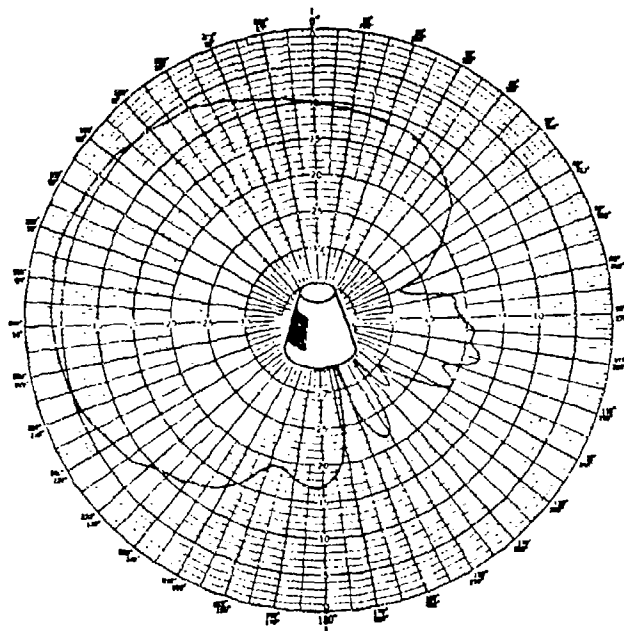
INPUT IMPEDANCE FOR TM_{11} CONICAL ELEMENT

in Figures 9 and 10, respectively. The pattern characteristics for these two elements are summarized in Table 2:

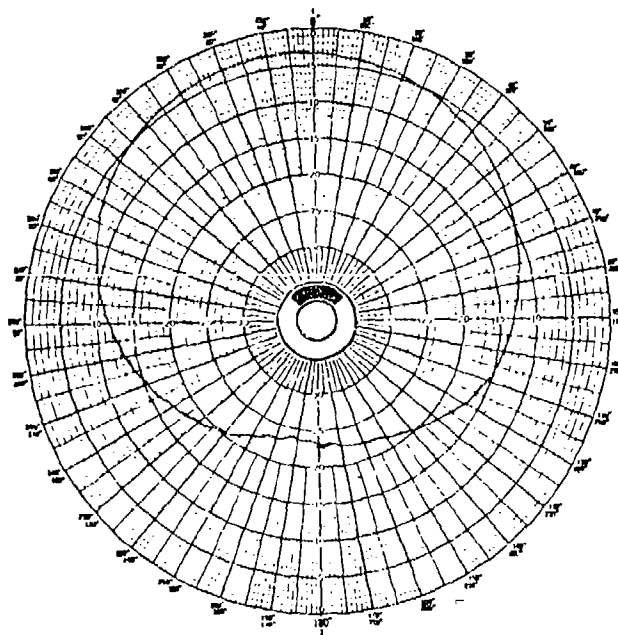
TABLE 2: MEASURED RADIATION PATTERN CHARACTERISTICS
FOR CONICAL MOUNTED ANNULAR SECTOR ELEMENTS

Element Description	E-Plane HPBW	H-Plane HPBW	Peak Gain (dBi)
TM ₀₁ Mode	90 Deg.	94 Deg.	6.8 dBi
TM ₁₁ Mode	86 Deg.	75 Deg.	5.5 dBi

One discrepancy to be noted is that the TM₀₁ patterns have an H-plane half-power beamwidth (HPBW) which is wider than the E-plane HPBW. Although this is not typical for a planar microstrip antenna, it may be explained by referring to Figure 2(a), observing that the radiating edges of this element are conformally curved around the circumference of the cone, and thus radiating over a wider azimuth range than a planar element. Overall, the radiation patterns indicate that the annular sector element may provide good coverage when mounted on a conical surface.

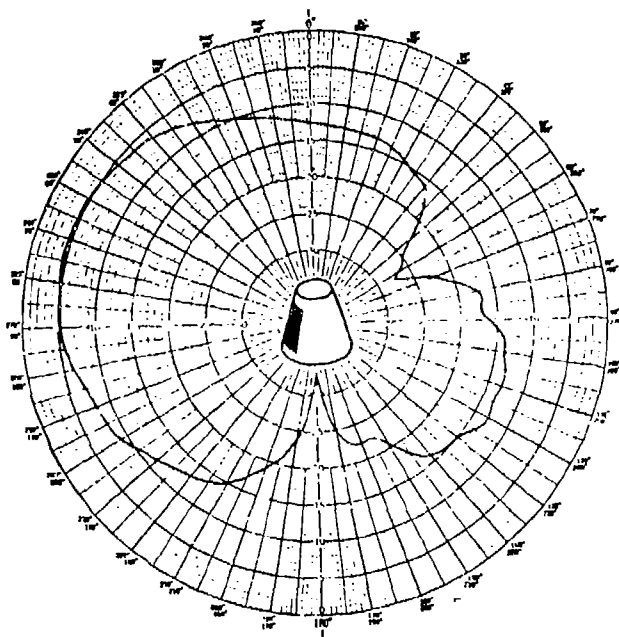


(a) ELEVATION PLANE (E-PLANE)

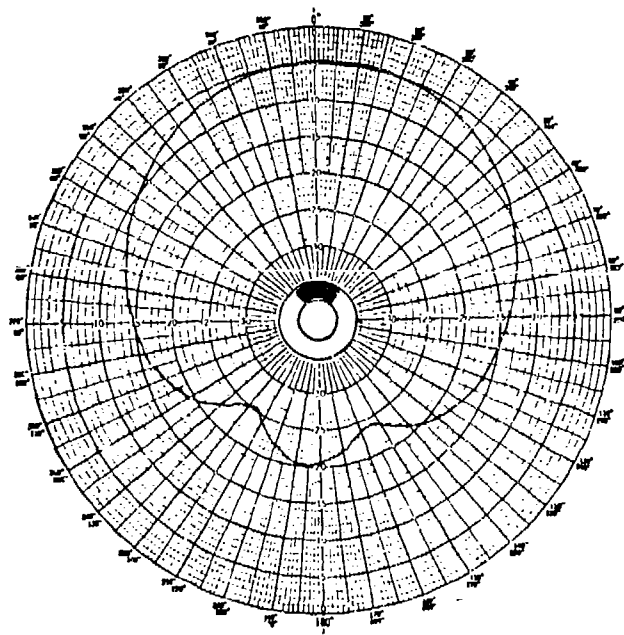


(b) AZIMUTH PLANE (H-PLANE)

FIGURE 9: TM_{01} CONICAL ELEMENT RADIATION PATTERNS



(a) ELEVATION PLANE (H-PLANE)



(b) AZIMUTH PLANE (E-PLANE)

FIGURE 10: TM_{11} CONICAL ELEMENT RADIATION PATTERNS

4.0 CONCLUSIONS AND FURTHER APPLICATIONS:

This paper has applied the cavity model theory to analyze the annular sector patch on planar and conical surfaces. To provide a practical design method, a set of design curves was presented for the TM_{01} and TM_{11} modes. Accurate formulas were developed to properly account for the edge fringing. Experimental results confirmed the accuracy of the planar element theory when applied to the design of elements on conical surfaces.

Further applications being pursued are the use of annular sector elements in the design of conical microstrip arrays, and the extension of this theory to the design of circular polarized (CP) elements.

5.0 ACKNOWLEDGEMENTS:

Motorola, Inc. is acknowledged for the support of this research investigation.

REFERENCES:

1. Lo, Y.T., Solomon, D., and Richards, W.F. (1979) Theory and experiment on microstrip antennas, IEEE Trans. Antennas Propagat. AP-27 (No. 2):137-145.
2. Long, S.A. and Shen, L.C. (1977) The circular disc, printed circuit antenna, IEEE Antennas Propagat. Int. Symp. Digest pp. 100-103.
3. Howell, J.Q. (1975) Microstrip antennas, IEEE Trans. Antennas Propagat. AP-23 (No. 1):90-93.
4. Ou, J.D. (1981) Theoretical and experimental analysis of annular, annular sector, and circular sector printed-circuit antennas, M.S. thesis, Dept. Elec. Eng. Univ. Houston, TX.
5. Richards, W.F., Ou, J.D., and Long, S.A. (1984) A theoretical and experimental investigation of annular, annular sector, and circular sector microstrip antennas, IEEE Trans. Antennas Propagat. AP-32 (No. 8):864-867.
6. Garg, R. and Long, S.A. (1988) An improved formula for the resonant frequencies of the triangular microstrip patch antenna, IEEE Trans. Antennas Propagat. AP-36 (No. 4):570.
7. Bahl, I.J. and Bhartia, P. (1980) Microstrip Antennas, Artech House, Dedham, MA, p. 46.
8. Hammerstad, E.O. (1975) Equations for microstrip circuit design, Proc. 5th European Microwave Conf. pp. 268-272, paper presented in Hamburg, W. Germany
9. Richards, W.F., Lo, Y.T., and Harrison, D.D. (1979) Improved theory for microstrip antennas, Electronics Letters 15 (No. 2):42-44.
10. Harrington, R.F. (1961) Time-Harmonic Electromagnetic Fields, McGraw-Hill, New York, pp. 22-24, 74-76.
11. Keller, J.B. (1962) Geometrical theory of diffraction, J. Opt. Soc. Am. 52 (No. 2):116-130.
12. Clark, V.A. and Lo, Y.T. (1987) Conformal microstrip antennas. Paper presented at Antenna Applications Symposium, Allerton Park, IL.

MODE PURITY OF RECTANGULAR PATCH ANTENNAS WITH POST AND APERTURE EXCITATIONS

H. K. Smith and P. E. Mayes
Electromagnetics Laboratory
Department of Electrical and Computer Engineering
University of Illinois
Urbana, Illinois

Abstract

Microstrip patch antennas offer many attractive features which include low profile, low cost, conformability, compactness, and light weight. Even the inherent high quality factor of these antennas can be advantageous if a narrow band of operation is desired.

The microstrip patch antenna can be excited by various methods such as slot line, coplanar waveguide, microstrip line, apertures, and posts. Each of the methods above has advantages and disadvantages in the areas of fabrication, spurious radiation, feed network/antenna design, and input impedance. It is the focus of this paper to investigate the post feed and aperture coupling methods of excitation for identical rectangular microstrip patches of various aspect ratios. Comparison between the two feeds will center around the issue of mode purity, in this case, the 0,1 mode.

To experimentally detect the excitation of modes other than the 0,1 mode, properties of the far-field radiation, in particular, cross-polarization in the principal planes, will be used.

Introduction

For linear polarization, it is usually desirable that the microstrip patch antenna be excited in a single mode. Associated with the desired mode is a particular radiation pattern. Any additional modes which are excited by the feed mechanism may result in additional radiation which is likely to be undesirable. Hence, some types of degradation of the dominant mode radiation pattern can be attributed to spurious modes of the patch.

One detrimental effect of mode contamination is a rise in the cross-polarization levels. For a rectangular microstrip patch antenna operating in the 0,1 mode, the cross-polarization in the principal planes is, theoretically, zero. Here we use Ludwig's second definition [1] for cross-polarization and define E_ϕ as the co-pol component and E_θ as cross-pol component for the H-plane. In the E-plane, the reverse is true. E_θ becomes the co-pol component and E_ϕ becomes the cross-pol component. For the 0,1 mode, cross-polarization in either principal plane can be attributed to the excitation of additional modes.

Oberhart and Lo previously studied the cross-polarization of rectangular patch antennas. In their study, the cavity model theory [4] for the rectangular microstrip patch antenna was employed to determine a $|E_{cpol}|/|E_{xpol}|$ ratio for a given feed location and various aspect ratios ranging from 1.00 to 2.11. R. C. Hansen also discusses the cross-polarization of square, rectangular, and circular microstrip patches [5]. Rectangular patches were the subject of investigation by Huynh, Lee, and Lee [6] in which the cavity model theory was used to determine relative co-pol to cross-pol levels as a function of not only aspect ratios but also feed position, substrate thickness, and relative permittivity of the substrate supporting the patch.

The scope of this paper is to compare the purity of the 0,1 mode for identical rectangular microstrip patch antennas where one is excited by a post and the other is excited by an rectangular aperture. This comparison will be conducted for various aspect ratios ranging from 1.5 to 3.5 for both feed types.

Construction and Measurements

The geometries of the two patch antennas are shown in Figures 1 and 2. The post-fed patch (Figure 1) consists of a copper rectangle of appropriate dimensions which is supported 2mm above a ground plane by Rohacell, a low loss, low permittivity foam ($\epsilon_r = 1.071$ and a loss tangent of .00156). The post, which is the center conductor of .085 coaxial cable, is located at ($x=0.0\text{mm}$, $y=10.0\text{mm}$). The post at this position will couple strongly into the electric field of the 0,1 mode, less strongly to that of other modes.

The aperture-fed patch (Figure 2) is configured identically. However, instead of the post feed, a rectangular aperture (.5mm by 20mm) is cut in the ground plane. This aperture is located at ($x=0.0\text{mm}$, $y=25.0\text{mm}$) and will couple strongly to the magnetic field of the 0,1 mode but will not couple to as many higher order modes as the post because of its symmetric location. A microstrip line which runs along the underside of the ground plane separated by a 1/16" of Rexolite 2200 dielectric is used to excite the slot.

Scattering parameters were measured on a HP8510 Network Analyzer to determine the exact resonant frequency of the 0,1 mode. Both Through-Line-Reflect calibration and a standard 3-term calibration were used for error correction.

At the appropriate resonant frequencies, far-field radiation patterns were taken for both polarizations in both principal planes and one diagonal plane. The measurements were conducted on a 20' by 20' ground plane range. The receiver used was a Scientific Atlanta model which has a 40 dB dynamic range. Great care was taken to ensure proper orientation of the microstrip patch antenna and the alignment of the receiving horn antenna.

Results and Discussion

The original dimensions of the rectangular patches were $a = 175\text{mm}$ by $b = 50\text{mm}$ which gives an aspect ratio of 3.5. The aspect ratios of the patches were varied from 3.5 to 1.5 in 0.5 increments by merely trimming the "a" dimension (while keeping the "b" dimension constant). Although the cavity model theory predicts the 0,1 resonance to be

3.00 GHz, due to the presence of the fringing fields at the edge of the patch, the actual resonance frequency is depressed. The amount by which the "resonant frequency" is perturbed is also a function of aspect ratio. In addition to the effect of the fringing fields, the resonant frequency of the aperture-fed patch is decreased because of the presence of the slot. Scattering parameters were measured to determine the exact 0,1 resonant frequency. Far-field radiation patterns were measured at the exact resonant frequency. Although far-field data was measured in both principal planes and in one diagonal plane, the most meaningful data was gathered in the H-plane.

Figure 3 shows the H-plane far-field radiation patterns for 1.5 aspect ratio rectangular patches fed both by post and aperture. The cross-polarization component E_θ is relatively non-existent for the aperture-fed patch. However for the post-fed patch, cross polarization levels as high as -23 dB are observed. The shape of the E_θ pattern suggests that the 2,0 mode is being slightly excited. Nothing unusual is noted for the E_ϕ component except for a ripple in the pattern at zenith which is believed to be the result of multiple scattering.

Data for the 2.0 aspect ratio patches are presented in Figure 4. In the post-fed patch, the 2,0 mode presence can clearly be detected in the pattern for the E_θ component. This is expected since the cavity model theory predicts that the 0,1 and 2,0 modes have the same resonant frequency at this aspect ratio. Again the cross-polarization level for the aperture-fed patch is considerably lower, with peaks in the neighborhood of -35 dB.

As the aspect ratio is increased to 2.5 (Figure 5), the aperture-fed patch is again well behaved with respect to cross-polarization performance. However in the case of the post-fed patch, the cross-polarization, with peaks at the -23 dB level, still indicate the presence of the 2,0 mode. The co-polarization component, E_ϕ , begins to show side lobes at $\theta = 70^\circ$ that are 33 dB down. These side lobes result from the extreme length of the principal radiating magnetic current.

At aspect ratio of 3.0 (Figure 6), curiously enough, both post and aperture feeds produce almost non-existent cross-polarization. The E_ϕ component of the post-fed patch shows that the side lobe is now well defined and levels are now peaked at $\theta = 60^\circ$ and have risen to the -20 dB level. Side lobes also begin to appear in the aperture-fed patch at the -31 dB level for $\theta = 70^\circ$.

The final aspect ratio measured was 3.5 (Figure 7). The E_ϕ component for both the aperture and post feeds show that the side lobe level is around -23 dB and that the side lobes are not as well defined as in the case of the post-fed patch of aspect ratio 3.0. The E_θ component of the post-fed patch reveals that the 4,0 mode is being excited. The cross-polarized field for the aperture-fed patch peaks around the -35 dB level.

Conclusion

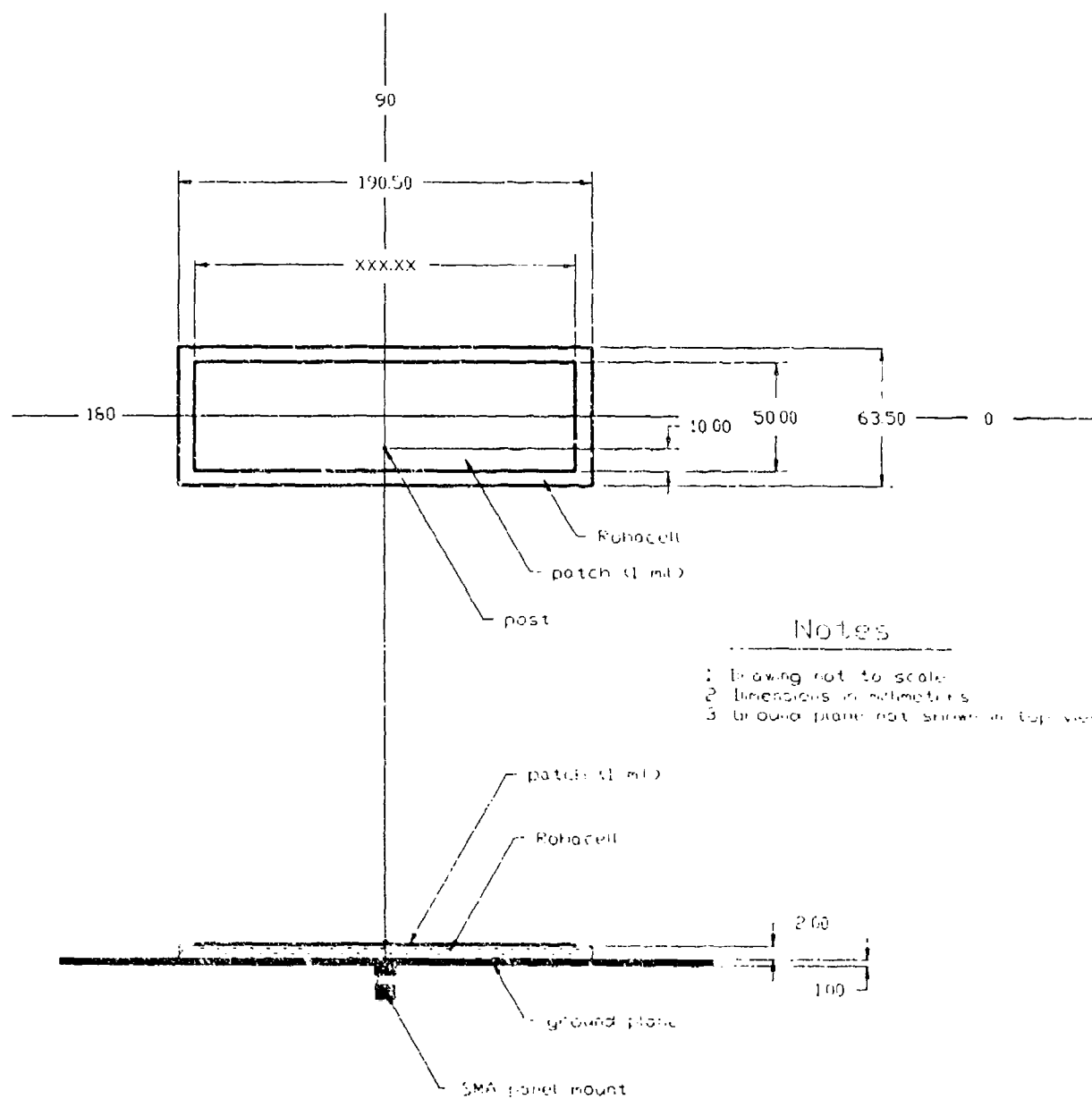
It has been shown that one aperture feed produces a purer 0,1 mode excitation than a particular post feed over a variety of aspect ratios for rectangular patch antennas. Only one aperture dimension was investigated and no attempt was made to vary the input impedance by manipulation of the feeds. It is quite certain that the mode purity resulting from the aperture excitation is a function of both aperture feed dimension and position.

References

- [1] Lugwig, A. C., "The definition of cross polarization," IEEE Trans. Antenna Propagat., vol. AP-21, no. 1, pp 116-119, Jan. 1973.
- [2] Oberhart, M. L., Lo, Y. T., and Lee, R. Q. H., "Cross polarization considerations for microstrip antenna array modules," Proc. of 1985 Antenna Applications Symposium at Allerton Park, University of Illinois, Urbana, IL.
- [3] Oberhart, M. L., Lo, Y. T., and Lee, R. Q. H., "New simple feed network for an array module of four microstrip elements," Electronics Letters, vol. 23, no. 9, pp. 436-437, April 23, 1987.
- [4] Richards, W. F., Lo, Y. T., and Harrison, D. D., "An improved theory for microstrip antennas and applications," IEEE Trans. Antennas Propagat., vol. AP-21, no. 1, pp. 38-46, Jan. 1981.
- [5] Hansen, R. C., "Cross polarization of microstrip patch antennas," IEEE Trans Antennas Propagat., vol. AP-35, no. 6, pp. 731-732, June 1987.
- [6] Huynh, T., Lee, K. F., and Lee, R. Q., "Cross polarization of rectangular patch antennas," Proc. of the 1988 IEEE AP-S International Symposium, vol. II, pp. 708-711, Syracuse, New York, June 1988.

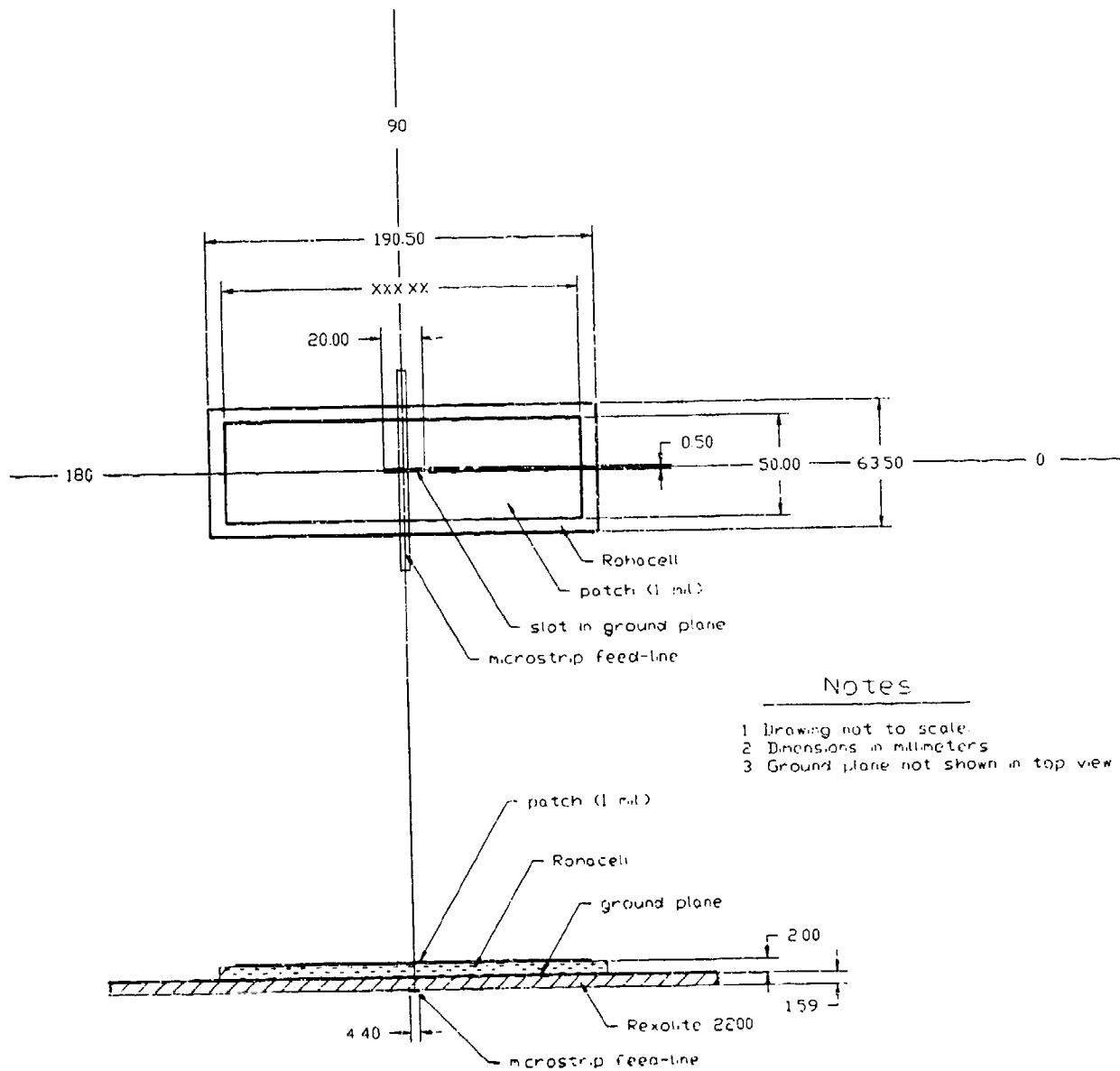
Acknowledgment

The authors would like to thank Paul Hoover and James Gentle for their help toward the completion of this work.



Post-fed patch

Figure 1 Geometry of the post-fed rectangular patch.

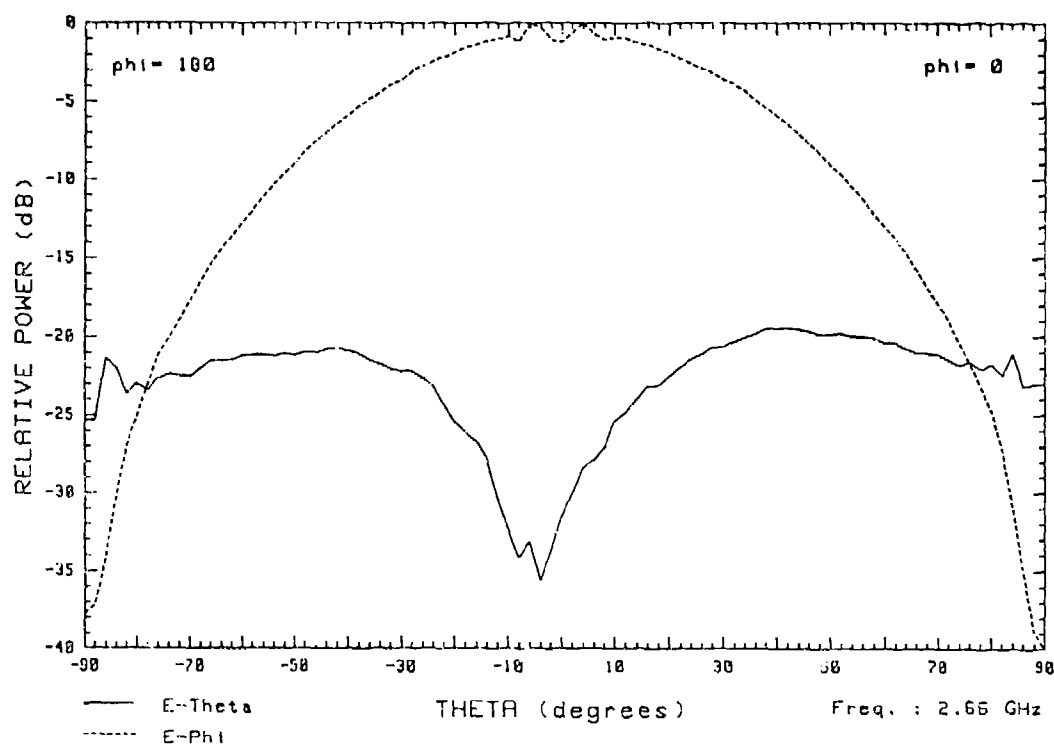


Aperture-fed patch

Figure 2 Geometry of the aperture-fed rectangular patch.

1.5 ASPECT RATIO POST-FEED H-PLANE

9



1.5 ASPECT RATIO APERTURE-FEED H-PLANE

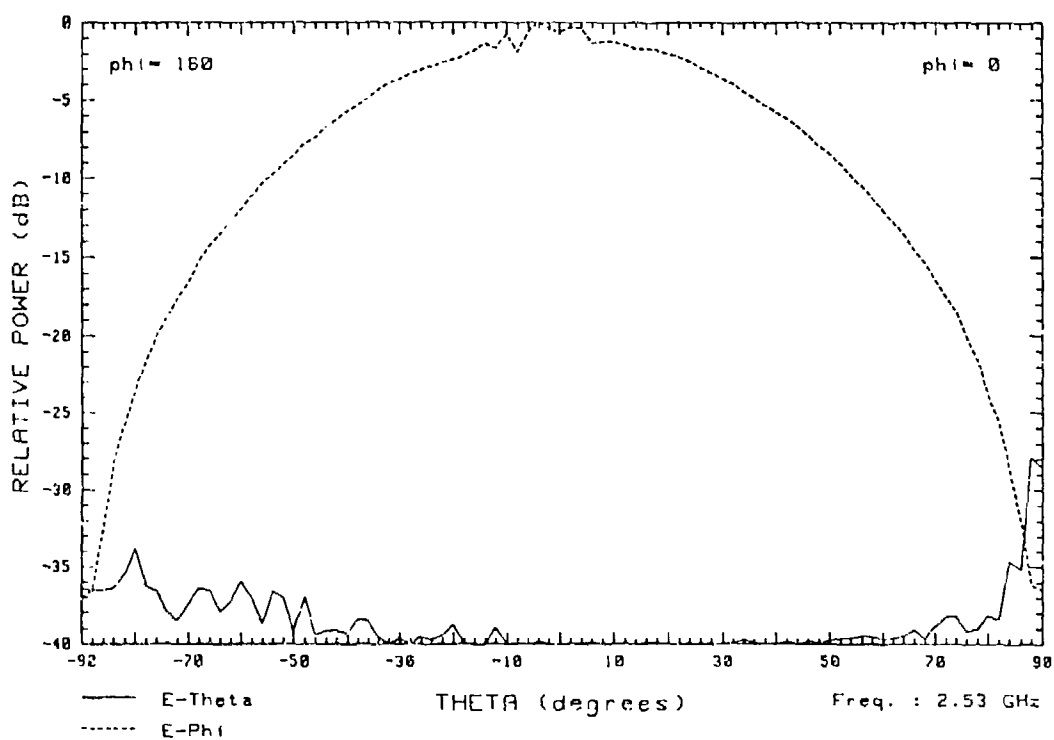
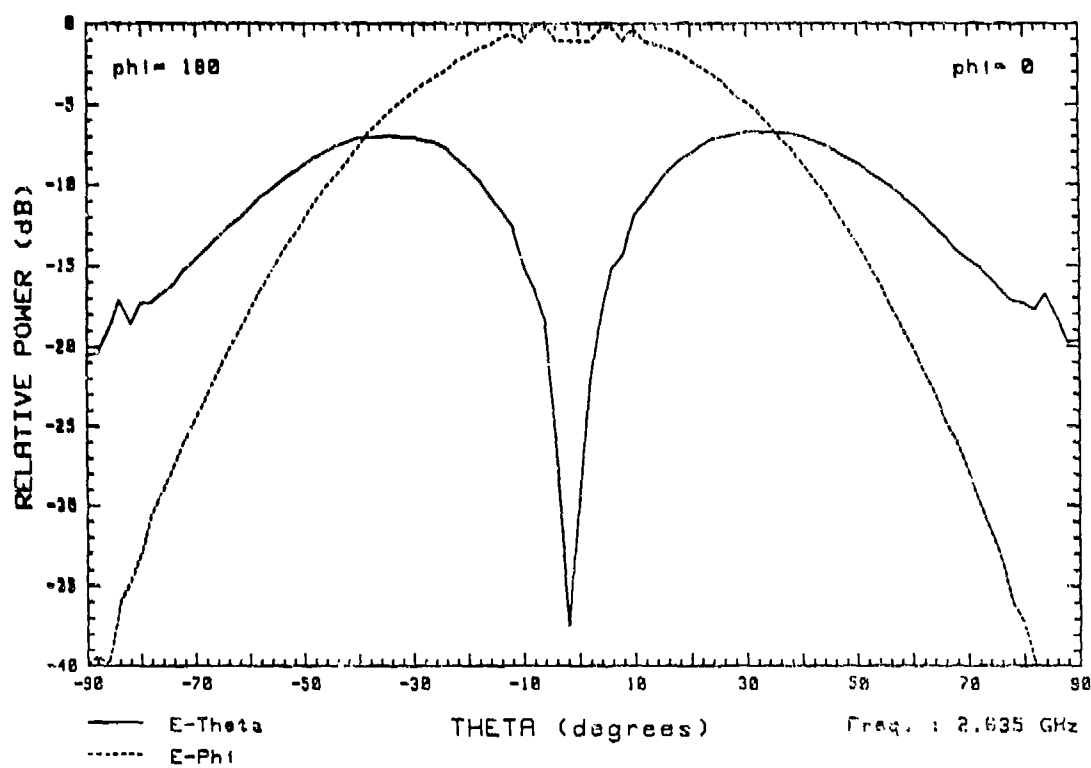


Figure 3 H-plane of both the post-fed and aperture-fed rectangular patches of aspect ratio 1.5.



2.0 ASPECT RATIO APERTURE-FEED H-PLANE

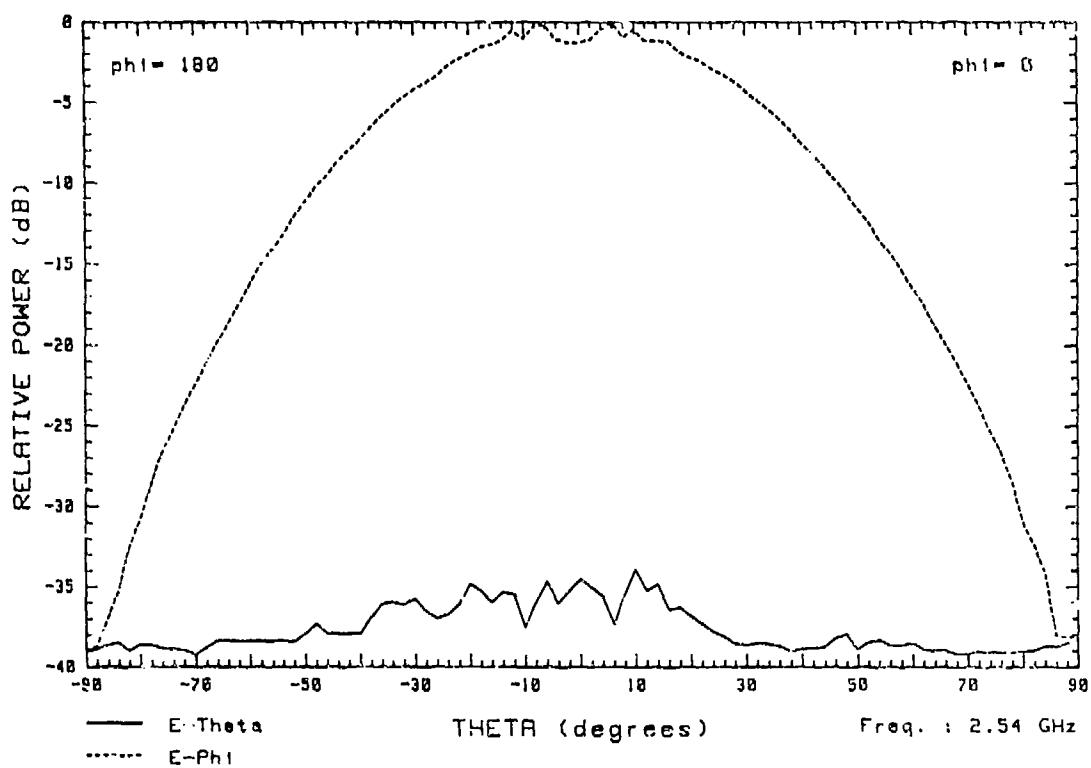
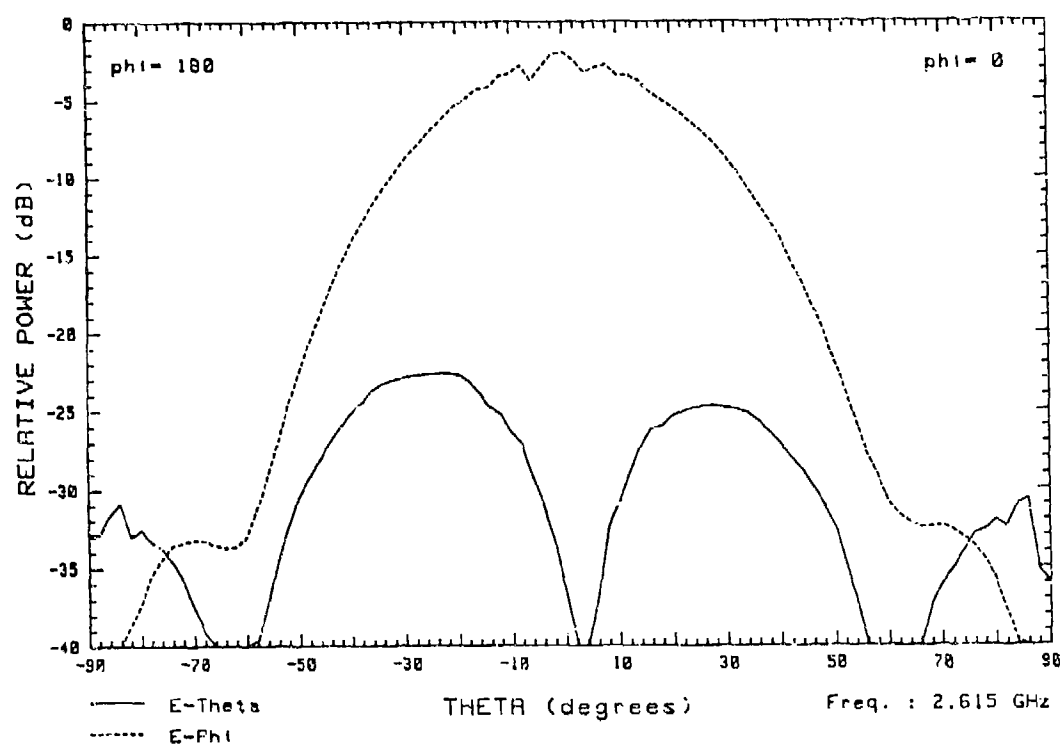


Figure 4 H-plane of both the post-fed and aperture-fed rectangular patches of aspect ratio 2.0.

2.5 ASPECT RATIO POST-FEED H-PLANE

11



2.5 ASPECT RATIO APERTURE-FEED H-PLANE

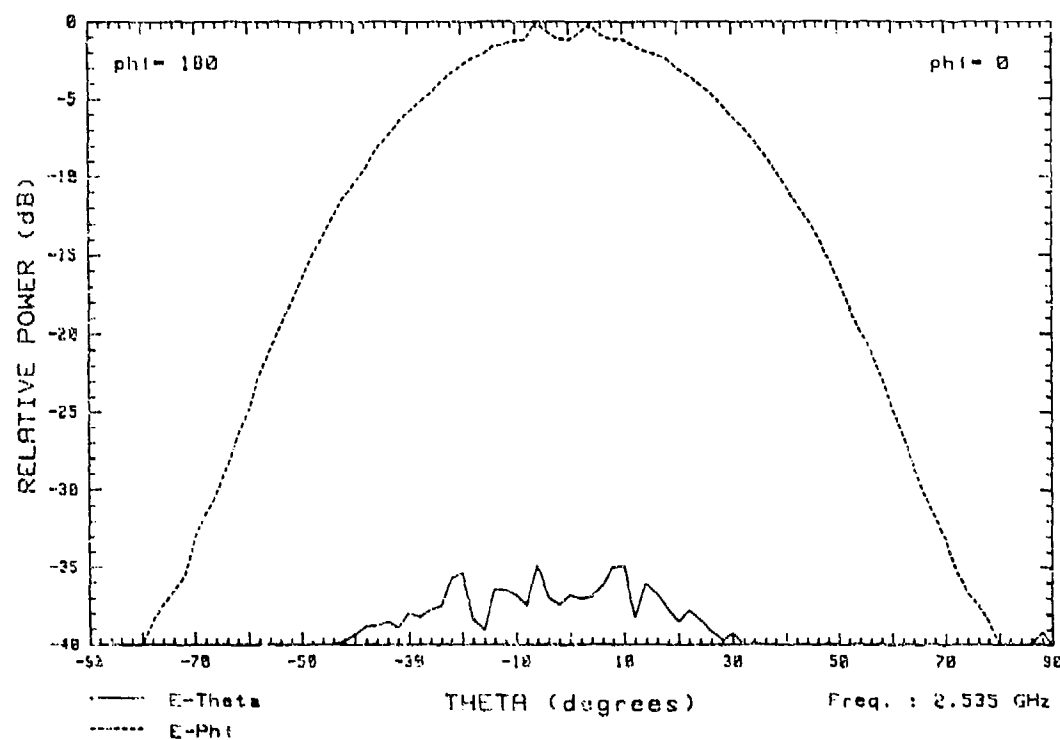
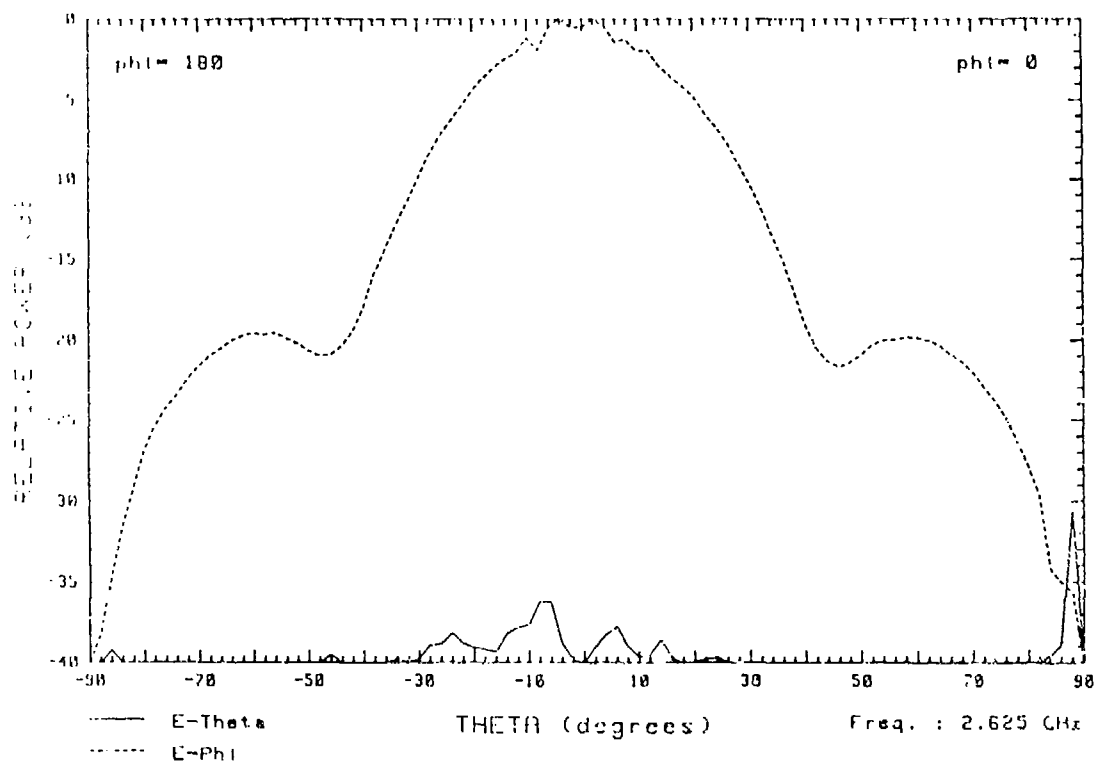


Figure 5 H-plane of both the post-fed and aperture-fed rectangular patches of aspect ratio 2.5.

3.0 ASPECT RATIO POST-FEED H-PLANE

12



3.0 ASPECT RATIO APERTURE-FEED H-PLANE

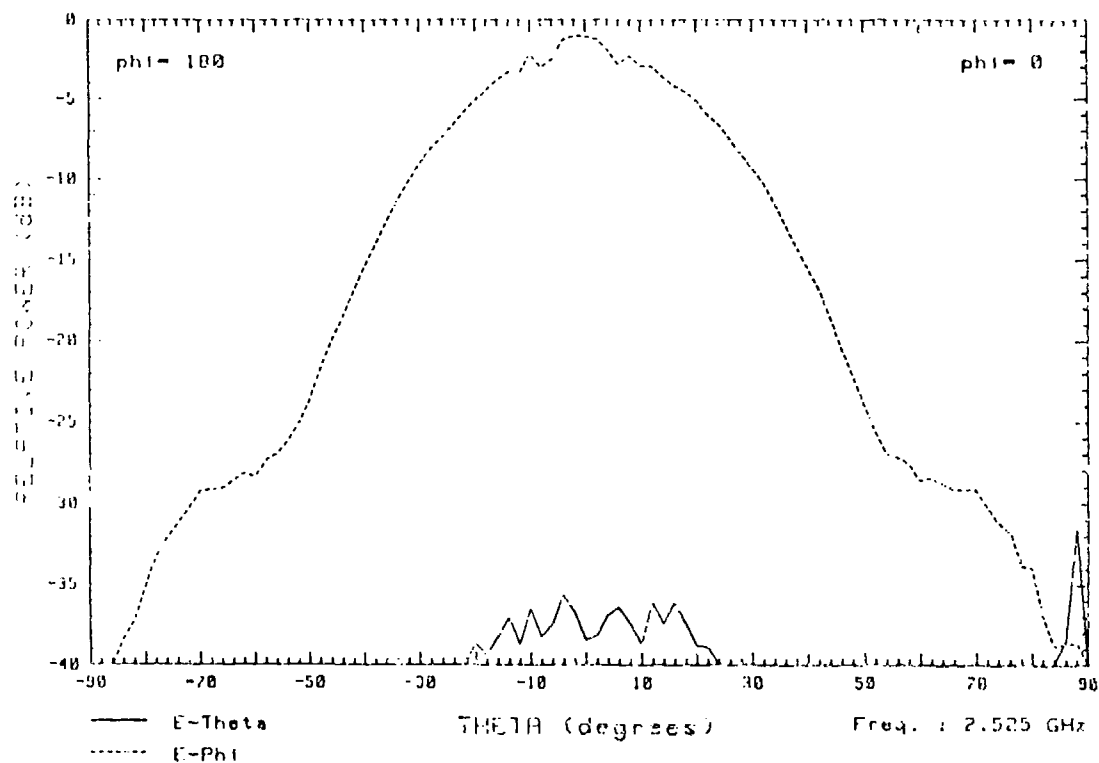


Figure 6 H-plane of both the post-fed and aperture-fed rectangular patches of aspect ratio 3.0.

CIRCULAR POLARIZATION FROM STACKED MICROSTRIP PATCHES

by

Andrew Adrian

Texas Instruments

McKinney, Texas

Daniel H. Schaubert

University of Massachusetts

Amherst, Massachusetts

ABSTRACT

A novel method of achieving circularly polarized radiation with rectangular microstrip patches is described. In this geometrical arrangement, two stacked microstrip patches are orthogonally polarized. The bottom patch acts as a partial ground plane for the top patch, and the top patch does not significantly affect the radiation from the bottom patch. Energy is coupled to the top patch via a diagonal aperture in the center of the bottom patch while the entire system is fed by a single excitation of the bottom patch. This excitation can consist of any suitable feed for a microstrip patch. In this case, a probe feed was utilized. Circularly polarized radiation then occurs when the aperture is tuned for 3 dB coupling with a 90 degree phase shift.

(Fig. 1a). Consequently, the top patch does not significantly affect the radiation of the bottom patch, and the bottom patch acts as a partial ground plane for the top patch.

2.2 Excitation

Only the bottom patch needs an external excitation. This can be implemented as any suitable microstrip patch antenna feed. In the case that is being described here, a probe was utilized. Consequently, the top patch is excited by energy that is coupled through the aperture from the bottom patch (Fig. 2).

The aperture itself is centered on the bottom patch. However, its major axis is oriented on a 45 degree angle to both patches. In order to achieve circularly polarized radiation, the aperture must be tuned for 3 dB coupling with a 90 degree phase shift. This can be accomplished by adjusting the aperture size and its exact shape.

3.0 EXPERIMENTAL RESULTS

3.1 Geometry

An experimental prototype of the ACSCEP was fabricated with two layers of 0.062 inch thick Rogers R/T Duroid 5880 which has a dielectric permittivity of 2.20. Dimensions of the exact geometry are

displayed in Fig. 3. Amplitude and phase tuning of the aperture resulted in its unique shape.

3.2 Center Frequency

The operating center frequency of the element is 3.470 GHz where its return loss is 6.8 dB. This is evident from the cusp in the Smith Chart and return loss plots of the ACSCPP (Fig. 4) as well as the measurements of axial ratio over frequency (Table 1). A spin-linear radiation pattern that was taken in the E-plane of the bottom patch at 3.470 GHz is illustrated in Fig. 5. The axial ratio at this frequency is 1.8 dB.

3.3 Bandwidth

The operating bandwidth of this element is limited by its axial ratio. Below 3.450 GHz and above 3.490 GHz, the axial ratio is greater than 3 dB (Table 1). This resulted in a 3 dB axial ratio bandwidth of 1.01 %. From measurements of the relative radiated power of each patch in the stack and the axial ratio of the combined patches, the phase shift through the aperture was calculated (Table 1). From Table 1 it is evident that at the low end of the element's frequency band, a poor phase shift through the aperture contributes to the poor axial ratio there. Conversely, on the other end of the band, a poor power

split limits the axial ratio bandwidth.

The antenna tested here has been compared to a single patch with a diagonal slot for circular polarization (Kerr) [1]. The Kerr antenna was fabricated on a substrate of the same dielectric permittivity as the ACSCPP. Conversely, the substrate was 0.128 inch thick in order to have the same overall thickness as the ACSCPP. This was felt to be the most fair comparison of antenna bandwidths. However, the ACSCPP require that only the bottom patch be fed, which means the feed probe or microstrip feedline corresponds to a substrate one-half the total antenna thickness. This can be very important for wide bandwidth antennas on thick substrates where feed inductance and/or radiation can cause severe problems.

The 3 dB axial ratio bandwidth of the Kerr antenna was optimized to a value of 1.46 %, which is greater than the prototype ACSCPP. However, the ACSCPP may be capable of greater bandwidth if an optimized design is developed. This development can utilize the following interdependent parameters to obtain the most desirable performance:

- Bottom patch width
- Aperture size and shape
- Top patch width
- Substrate thicknesses and permittivities.

During the development of the prototype ACSCPP, it was

found that the resonant frequencies of the top and bottom patches are affected differently by changes in the aperture size. Therefore, trial and error design is tedious and an analysis of the element would be very beneficial.

4.0 CONCLUSION

This paper has documented a proof of concept design for ACSCPP. The input return loss was 6.8 dB, and the 3 dB axial ratio bandwidth was 1.01 %. Improving the input match in this case can probably be accomplished by moving the feed probe closer to a radiating edge of the bottom patch. The additional distance between the aperture and the probe may also result in an easier tuning procedure. Gains in axial ratio bandwidth may be possible by optimizing the aperture for an improved amplitude and phase coupling profile. Furthermore, use of the ACSCPP requires feeding only the bottom patch. This may be advantageous for antennas on very thick substrates (as when wide bandwidth is desired).

Finally, the ACSCPP may have a potential which has yet to be investigated. Since the radiators are stacked, materials with different dielectric permittivities and/or thicknesses can be used for each layer of the fabrication. This could provide a means

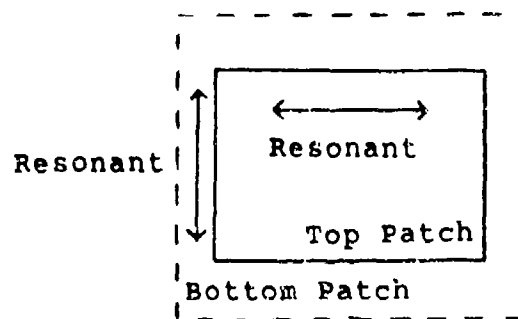
for obtaining dual frequency circular polarization with a single element or circular polarization at one frequency and linear at one or two others. This would require resonating the patches in both linear directions.

ACKNOWLEDGMENT

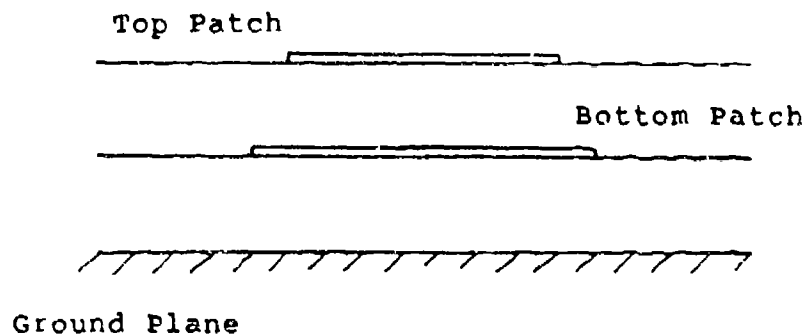
This work was supported by the General Electric Company Electronics Laboratory, Syracuse, NY.

REFERENCES

- [1] Kerr, J. L. (1978) Microstrip Polarization Techniques. Paper presented at the Antenna Applications Symposium, Monticello, Illinois.

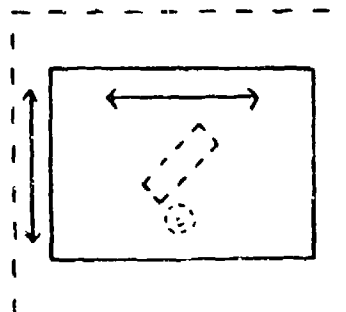


(a)

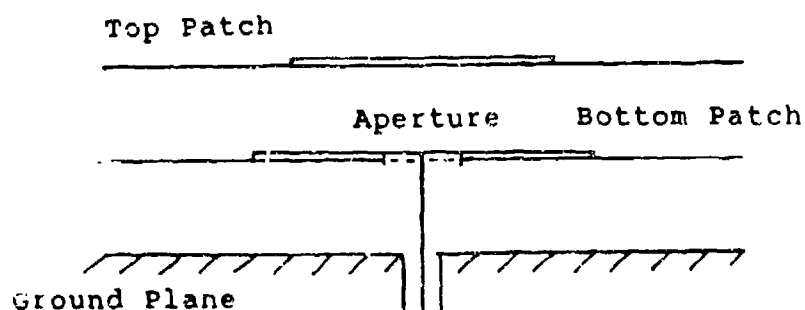


(b)

Figure 1 (a) Top and (b) side views of stacked, orthogonally polarized microstrip patches.

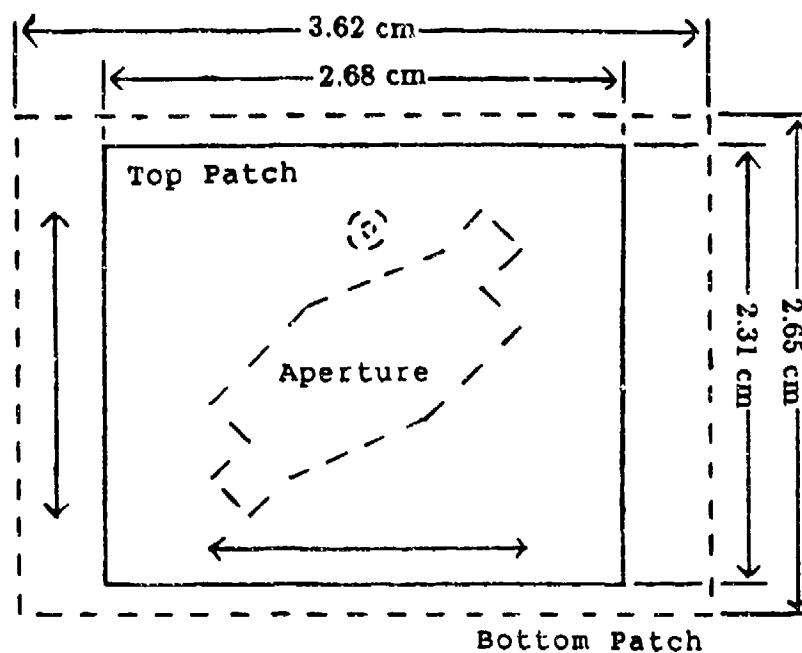


(a)

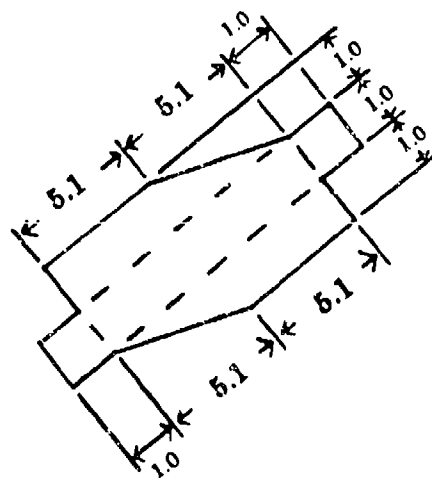


(b)

Figure 2 (a) Top and (b) side views of stacked, orthogonally polarized microstrip patches with an aperture coupled top patch.



(a)



(b)

Figure 3 Dimensions of the prototype ACSCPP. The (a) patches are dimensioned in cm and the (b) aperture is labeled in mm.

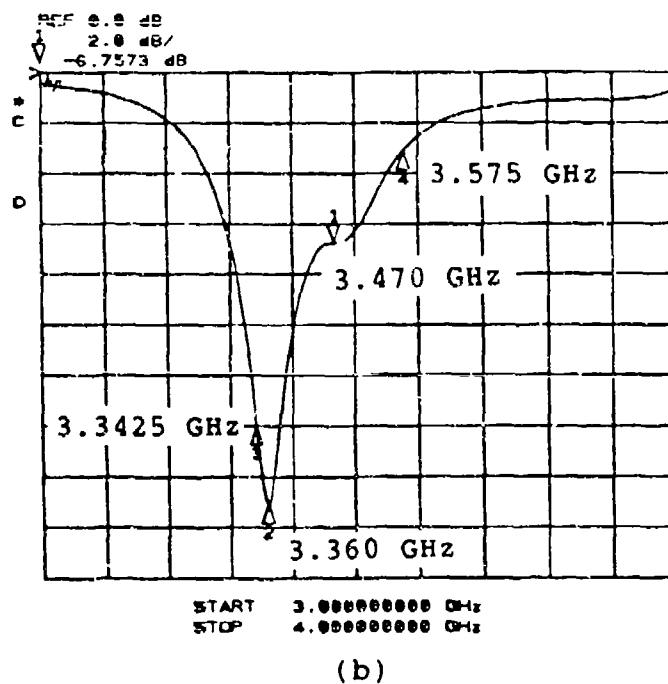
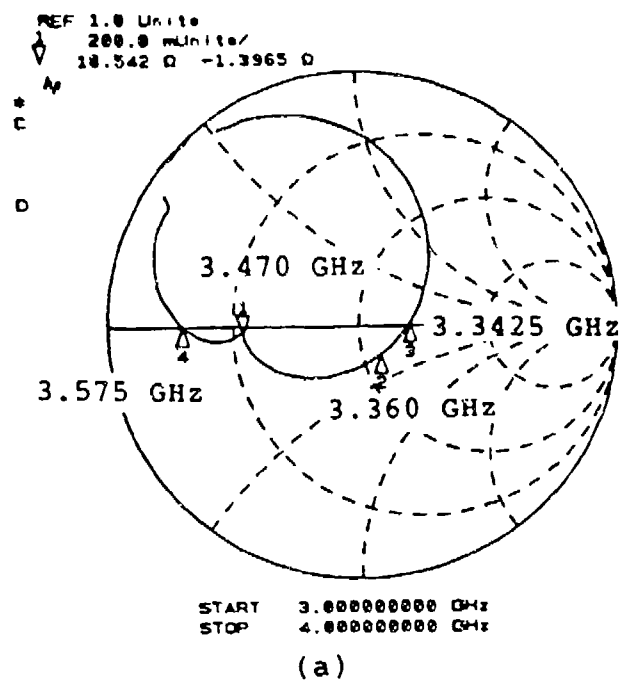


Figure 4 (a) Input impedance and (b) $|S_{11}|$ of the ACSCPP.

Table 1

Frequency (GHz.)	Relative Gain of Top Patch (dB)	Relative Gain of Bottom Patch (dB)	Ratio of Bottom Patch Gain to Top Patch Gain (dB)	Relative C.P. Gain (dB)	Axial Ratio (dB)	Calculated Phase Shift (deg.)
3.450	-1.3	-1.3	0.0	-0.6	3.6	67
3.455	-1.2	-0.9	0.3	-0.3	2.9	71
3.460	-1.0	0.0	1.0	-0.3	2.4	76
3.465	-1.6	-0.7	0.9	-1.2	2.0	78
3.470	-2.2	-1.1	1.1	-1.0	1.8	81
3.475	-3.2	-1.5	1.7	-1.4	1.8	86
3.480	-3.4	-1.7	1.7	-1.7	2.0	97
3.485	-3.7	-1.7	2.0	-1.6	2.6	101
3.490	-3.6	-0.6	3.0	-1.0	3.2	97

Table 1 Calculated phase shift between the top and bottom patches of the ACSCPP from relative power and axial ratio measurements with a coherent receiver.

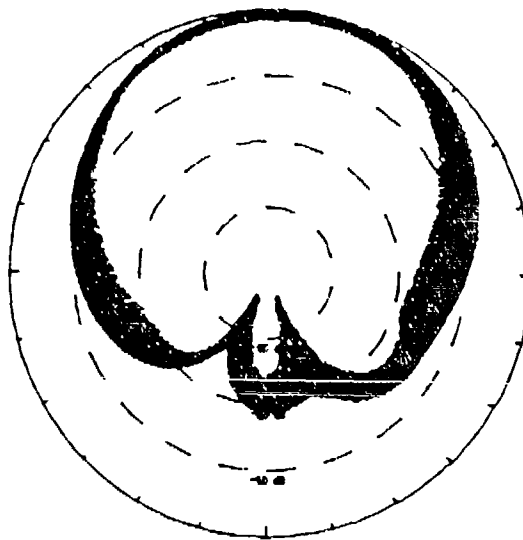


Figure 5 Far-field, spin-linear pattern of the ACSCPP at 3.470 GHz. The scale is 10 dB per division.

Analysis of the Annular-Ring-Loaded Circular-Disk Microstrip Antenna[†]

Z. Nie, W. C. Chew and Y. T. Lo

Electromagnetics Laboratory
Department of Electrical and Computer Engineering
University of Illinois
Urbana, IL 61801

Abstract

A rigorous analysis of the natural resonance frequencies and input impedance characteristics of an annular-ring-loaded (ARL) circular-disk microstrip antenna is presented. Using vector Hankel transforms (VHT), the problem is formulated in terms of vector dual-integral equations. Galerkin's method is then used to solve the equations to obtain the resonance frequencies and the current distributions on the conductive patches arising from a probe excitation. Due to the singular nature of the current distribution, the singularity subtraction method has been used to accelerate the convergence of basis function expansions. Experiments for determining resonance frequencies and input impedance characteristics of an ARL circular-disk microstrip antenna with various substrate thicknesses have been made. The theoretical results are in good agreement with the experiment data even when the electrical thickness of the substrate is 0.1 wavelength. It is shown that this theory can be used to analyze some microstrip antennas with an electrically thick substrate and mutual coupling between conductive patches or between the patch and the feed of a microstrip antenna.

I. Introduction

In recent years, microstrip antennas have aroused great interest in both theoretical research and engineering applications due to their low profile, light weight, conformal structure, and ease in fabrication and integration with solid-state devices. Because of the inherent narrow bandwidth of microstrip antennas, many attempts have been made to improve their frequency characteristics. In general, there are two efficient approaches to broaden the bandwidth of the microstrip antennas, i.e., by increasing the substrate thick-

[†] This research is supported by a grant from National Science Foundation NSF ECS 85-25891 plus a grant from TRW.

ness and by combining several patches with similar resonance frequencies on the same or different layers of an antenna structure.

Unfortunately, some popular analysis methods for microstrip antennas in the past, such as the cavity model method, are no longer valid in the above cases because these methods do not consider the effects of surface waves and fringing fields at the edge of the patch. They cannot be used to model easily the mutual coupling between conductive patches or between the patch and the feed. Some efforts have been made to analyze the above problems [1]-[3]; most of these used the exact Green's functions and spectral domain moment formulation. Due to the limitations of computer resources, the numerical results for the antennas with the thickness greater than 0.054 wavelength have not been given in [1]. In [2], an artificial approximation for edge extension has been used as a correction because the analysis in [2] was still based on a cavity model even though the substrate was electrically thick. The analysis in [3] did not consider the singular nature of the current at the feed region.

In this paper, the annular-ring loaded (ARL) circular-disk microstrip antenna with mutual coupling between the ring and the disk has been analyzed in the spectral domain by using the vector Hankel transform (VHT). First we study the natural resonance frequencies of the ARL circular-disk antenna. The problem is formulated in terms of a set of vector dual integral equations. Galerkin's method is then used to convert the integral equation into a system of linear algebraic equations. The natural resonances can be found by searching for the zeroes of the coefficient matrix. Good agreement between theoretical results and experiment data has been obtained. Next, the problem of an ARL circular-disk microstrip antenna excited by a probe is studied. Due to the singular nature of the current distribution on the conductive patch, the singularity subtraction method has been used to accelerate the convergence of the basis function expansion. The induced EMF method is used to calculate the input impedance of the probe-excited antenna at the ground plane of the antenna. Good agreement has been found between the numerical results and measured data even for substrate thicknesses up to 0.1 wavelength.

II. Integral Equations for the ARL Disk Antenna

Using the vector Hankel transform (VHT) formulation [1,4,5,7,8], the vector dual integral equations for the ARL disk antenna shown in Figure 1

are given by

$$\mathbf{e}_n(\rho) = \int_0^\infty dk_\rho k_\rho \bar{\mathbf{H}}_n(k_\rho \rho) \cdot \bar{\mathbf{G}}(k_\rho) \cdot \mathbf{K}_n(k_\rho) = 0, \quad \rho < a_1, \quad a < \rho < b, \quad (1)$$

$$\kappa_n(\rho) = \int_0^\infty dk_\rho k_\rho \bar{\mathbf{H}}_n(k_\rho \rho) \cdot \mathbf{K}_n(k_\rho) = 0, \quad a_1 < \rho < a, \quad \rho > b, \quad (2)$$

where

$$\mathbf{e}_n(\rho) = \begin{bmatrix} E_{\rho n}(\rho)/\cos n\phi \\ -E_{\phi n}(\rho)/\sin n\phi \end{bmatrix} \quad (3)$$

is related to the n -th harmonic of the electric field,

$$\kappa_n(\rho) = \begin{bmatrix} -K_{\rho n}(\rho)/\cos n\phi \\ K_{\phi n}(\rho)/\sin n\phi \end{bmatrix} \quad (4)$$

is related to the n -th harmonic of the current on the ring and the disk,

$$\mathbf{K}_n(k_\rho) = \begin{bmatrix} K_{n1}(k_\rho) \\ K_{n2}(k_\rho) \end{bmatrix} \quad (5)$$

is the VHT of the current $\kappa_n(\rho)$ on the ring and the disk,

$$\bar{\mathbf{H}}_n(k_\rho \rho) = \begin{bmatrix} J'_n(k_\rho \rho) & \frac{n}{k_\rho \rho} J_n(k_\rho \rho) \\ \frac{n}{k_\rho \rho} J_n(k_\rho \rho) & J'_n(k_\rho \rho) \end{bmatrix} \quad (6)$$

is the kernel of the vector Hankel transform, and

$$\bar{\mathbf{G}}(k_\rho) = \begin{bmatrix} \frac{k_z}{2\omega\epsilon}(1 - R^{TM}) & 0 \\ 0 & \frac{\omega\mu}{2k_z}(1 + R^{TE}) \end{bmatrix} \quad (7)$$

is the dyadic Green's function for the ρ and ϕ components of the current in the VHT spectral space.

In the above, R^{TM} and R^{TE} are generalized reflection coefficients for TM and TE waves, respectively. They can be expressed as

$$R^{TE, TM} = \frac{R_{01}^{TE, TM} + R_{12}^{TE, TM} e^{2ik_{1z}d}}{1 + R_{01}^{TE, TM} R_{12}^{TE, TM} e^{2ik_{1z}d}}. \quad (8)$$

For a dielectrical substrate backed by a PEC ground plane,

$$R_{01}^{TE} = \frac{\mu_1 k_z - \mu k_{1z}}{\mu_1 k_z + \mu k_{1z}} = \frac{k_z - k_{1z}}{k_z + k_{1z}}, \quad R_{12}^{TE} = -1, \quad (9)$$

$$R_{01}^{TM} = \frac{\epsilon_1 k_z - \epsilon k_{1z}}{\epsilon_1 k_z + \epsilon k_{1z}}, \quad R_{12}^{TM} = 1. \quad (10)$$

Therefore, we obtain

$$R^{TM} = \frac{i\epsilon_1 k_z \cos k_{1z}d - \epsilon k_{1z} \sin k_{1z}d}{i\epsilon_1 k_z \cos k_{1z}d + \epsilon k_{1z} \sin k_{1z}d}, \quad (11)$$

$$R^{TE} = \frac{ik_z \sin k_{1z}d + k_{1z} \cos k_{1z}d}{ik_z \sin k_{1z}d - k_{1z} \cos k_{1z}d}, \quad (12)$$

where

$$k_z = (k^2 - k_\rho^2)^{\frac{1}{2}}, \quad k_{1z} = (k_1^2 - k_\rho^2)^{\frac{1}{2}}, \\ k^2 = \omega^2 \mu \epsilon, \quad k_1^2 = \omega^2 \mu_1 \epsilon_1 = \omega^2 \mu \epsilon_1, \quad (13)$$

and d is the substrate thickness. Equations (1) and (2) are the consequence of imposing the mixed boundary conditions on the conductive patches at the plane $z = 0$, namely,

$$\mathbf{e}_n(\rho) = 0, \quad \rho < a, \quad \text{and} \quad a < \rho < b \quad (z = 0), \quad (14)$$

$$\kappa_n(\rho) = 0, \quad \text{outside the patches} \quad (z = 0) \quad (15)$$

where \mathbf{e}_n and κ_n are given by equations (1) and (2), respectively.

III. Selection of Basis Functions

In equations (1) and (2), the current distribution $\kappa_n(\rho)$ or its VHT $K_n(k_\rho)$ is unknown. We can solve for the unknowns using Galerkin's method. To do this, we expand the unknown current in terms of a basis set. An orthogonal and complete set of eigenfunctions derived from the current distributions of the modes of a magnetic-wall cavity is used to expand the currents on the patches.

The current on the annular ring corresponding to the field of a TM_{nm} mode of a magnetic wall cavity is [7]

$$\kappa_n(\rho) = \begin{cases} A_m \psi_{nm}(\rho) & a \leq \rho \leq b \\ 0 & \text{elsewhere} \end{cases}, \quad (16)$$

where

$$\psi_{nm}(\rho) = \left[\frac{\psi'_n(\beta_{nm}\rho/a)}{\frac{na}{\beta_{nm}\rho} \psi_n(\beta_{nm}\rho/a)} \right], \quad (17)$$

and

$$\psi_n(\beta_{nm} \frac{\rho}{a}) = J_n(\beta_{nm} \frac{\rho}{a}) N'_n(\beta_{nm}) - J'_n(\beta_{nm}) N_n(\beta_{nm} \frac{\rho}{a})$$

$$\psi'_n(\beta_{nm}\frac{b}{a}) = \psi'_n(\beta_{nm}) = 0.$$

β_{nm} is determined from $\psi'_n(\beta_{nm}c) = 0$ where $c = b/a$. The VHT of $\kappa_n(\rho)$ in equation (16) can be derived as

$$\mathbf{K}_n(k_\rho) = A_m \boldsymbol{\psi}_{nm}(k_\rho) \quad (18)$$

where

$$\boldsymbol{\psi}_{nm}(k_\rho) = \begin{bmatrix} \frac{\beta_{nm}}{(\beta_{nm}/a)^2 - k_\rho^2} Y'_{nm}(k_\rho) \\ \frac{na}{k_\rho \beta_{nm}} Y_{nm}(k_\rho) \end{bmatrix}, \quad (19)$$

$$Y_{nm}(k_\rho) = \psi_n(\beta_{nm}c) J_n(k_\rho b) - \psi_n(\beta_{nm}) J_n(k_\rho a), \quad (20)$$

$$Y'_{nm}(k_\rho) = c \psi_n(\beta_{nm}c) J'_n(k_\rho b) - \psi_n(\beta_{nm}) J'_n(k_\rho a), \quad (21)$$

where $c = b/a$. The current distribution on the circular disk corresponding to the field of the TM_{nl} mode of a magnetic wall cavity can be written as [8]

$$\kappa_n(\rho) = \begin{cases} C \xi_{nl}(\rho) & \rho \leq a_1 \\ 0 & \rho > a_1 \end{cases}, \quad (22)$$

where

$$\xi_{nl}(\rho) = \begin{bmatrix} \frac{J'_n(\gamma_{nl}\rho/a_1)}{\frac{na_1}{\gamma_{nl}\rho} J_n(\gamma_{nl}\rho/a_1)} \end{bmatrix}. \quad (23)$$

The VHT of $\mathbf{K}(\rho)$ in equation (22) is given by

$$\mathbf{K}_n(k_\rho) = C \boldsymbol{\xi}_{nl}(k_\rho) \quad (24)$$

where

$$\boldsymbol{\xi}_{nl}(k_\rho) = \begin{bmatrix} \frac{\gamma_{nl}}{(\gamma_{nl}/a_1)^2 - k_\rho^2} J_n(\gamma_{nl}) J'_n(k_\rho a_1) \\ \frac{na_1}{\gamma_{nl} k_\rho} J_n(k_\rho a_1) \end{bmatrix} \quad (25)$$

and the eigenvalue γ_{nl} can be determined from $J'_n(\gamma_{nl}) = 0$.

For completeness, we have to include the currents corresponding to the TE modes of the magnetic-wall cavity. The current on the annular ring corresponding to the field of the TE_{np} mode can be written as [7]

$$\kappa_n(\rho) = \begin{cases} B_p \phi_{np}(\rho) & a \leq \rho \leq b \\ 0 & \text{elsewhere} \end{cases} \quad (26)$$

where

$$\phi_{np}(\rho) = \begin{bmatrix} \frac{na}{\alpha_{np}\rho} \phi_n(\alpha_{np}\rho/a) \\ \phi'_n(\alpha_{np}\rho/a) \end{bmatrix} \quad (27)$$

and

$$\phi_n(\alpha_{np}\rho/a) = J_n(\alpha_{np}\rho/a)N_n(\alpha_{np}) - J_n(\alpha_{np})N_n(\alpha_{np}\rho/a) \quad (28)$$

The eigenvalue α_{np} is determined by $\phi_n(\alpha_{np}c) = 0$. The VHT of $\kappa_n(\rho)$ in equation (26) can be derived to be:

$$\mathbf{K}_n(k_\rho) = B_p \phi_{np}(k_\rho) \quad (29)$$

where

$$\phi_{np}(k_\rho) = \left[\frac{0}{k_\rho^2 - (\alpha_{np}/a)^2} Z_{np}(k_\rho) \right] \quad (30)$$

and

$$Z_{np}(k_\rho) = c\phi'_n(\alpha_{np}c)J_n(k_\rho b) - \phi'_n(\alpha_{np})J_n(k_\rho a). \quad (31)$$

For the circular disk, the current corresponding to the field of the TE_{nq} mode is [8]

$$\kappa_n(\rho) = \begin{cases} D_q \eta_{nq}(\rho) & \rho \leq a_1 \\ 0 & \text{elsewhere} \end{cases} \quad (32)$$

where

$$\eta_{nq}(\rho) = \left[\frac{\frac{na_1}{\chi_{nq}\rho} J_n(\chi_{nq}\rho/a_1)}{J'_n(\chi_{nq}\rho/a_1)} \right]. \quad (33)$$

The eigenvalue χ_{nq} is determined by $J_n(\chi_{nq}) = 0$, and is the q -th root of the equation. The VHT of $\kappa_n(\rho)$ in equation (32) can be written as

$$\mathbf{K}_n(k_\rho) = D_q \eta_{nq}(k_\rho) \quad (34)$$

where

$$\eta_{nq}(k_\rho) = \left[\frac{0}{k_\rho^2 - (\chi_{nq}/a_1)^2} J'_n(\chi_{nq}) J_n(k_\rho a_1) \right]. \quad (35)$$

A complete set of vector basis functions approaching the current distribution on the antenna patches then can be written as

$$\kappa_n(\rho) = \begin{cases} \sum_{m=1}^M A_m \psi_{nm}(\rho) + \sum_{p=1}^P B_p \phi_{np}(\rho) & a \leq \rho \leq b \\ \sum_{l=1}^L C_l \xi_{nl}(\rho) + \sum_{q=1}^Q D_q \eta_{nq}(\rho) & \rho \leq a_1 \\ 0 & \text{elsewhere} \end{cases} \quad (36)$$

and the VHT of $\kappa_n(\rho)$ in equation (36) is

$$\mathbf{K}_n(k_\rho) = \sum_{m=1}^M A_m \psi_{nm}(k_\rho) + \sum_{p=1}^P B_p \phi_{np}(k_\rho) + \sum_{l=1}^L C_l \xi_{nl}(k_\rho) + \sum_{q=1}^Q D_q \eta_{nq}(k_\rho). \quad (37)$$

Substituting equation (37) into (1), we obtain

$$\begin{aligned} & \sum_{m=1}^M A_m \int_0^\infty k_\rho dk_\rho \bar{H}_n(k_\rho \rho) \cdot \bar{G}(k_\rho) \cdot \psi_{nm}(k_\rho) \\ & + \sum_{p=1}^P B_p \int_0^\infty k_\rho dk_\rho \bar{H}_n(k_\rho \rho) \bar{G}(k_\rho) \cdot \phi_{np}(k_\rho) \\ & + \sum_{l=1}^L C_l \int_0^\infty k_\rho \cdot dk_\rho \bar{H}_n(k_\rho \rho) \cdot \bar{G}(k_\rho) \cdot \xi_{nl}(k_\rho) \\ & + \sum_{q=1}^Q D_q \int_0^\infty k_\rho dk_\rho \bar{H}_n(k_\rho \rho) \cdot \bar{G}(k_\rho) \cdot \eta_{nq}(k_\rho) = 0. \end{aligned} \quad (38)$$

It can be shown from the derivation of $\mathbf{K}_n(k_\rho)$ that equation (2) is satisfied automatically. Therefore, we need only to solve equation (38) to obtain the natural resonance frequencies of the microstrip antennas.

IV. Characteristic Equation for Eigenmodes

Equation (38) can be converted to a matrix equation by applying the testing functions in Galerkin's method. Multiplying equation (38) by $\rho \phi_{ni}^t(\rho)$, $\rho \phi_{nj}^t(\rho)$, $\rho \xi_{nk}^t(\rho)$ and $\rho \eta_{nt}^t(\rho)$, respectively, and integrating with respect to ρ from 0 to ∞ for $i = 1, \dots, M$, $j = 1, \dots, P$, $k = 1, \dots, L$, $t = 1, \dots, Q$, and using Parseval's Theorem for the vector Hankel transform [4], equation (38) became a system of $M + P + L + Q$ linear algebraic equations and can be written in the following matrix form

$$\begin{bmatrix} \bar{A}^{\psi\psi} & \bar{A}^{\psi\phi} & \bar{A}^{\psi\xi} & \bar{A}^{\psi\eta} \\ \bar{A}^{\phi\psi} & \bar{A}^{\phi\phi} & \bar{A}^{\phi\xi} & \bar{A}^{\phi\eta} \\ \bar{A}^{\xi\phi} & \bar{A}^{\xi\phi} & \bar{A}^{\xi\xi} & \bar{A}^{\xi\eta} \\ \bar{A}^{\eta\psi} & \bar{A}^{\eta\phi} & \bar{A}^{\eta\xi} & \bar{A}^{\eta\eta} \end{bmatrix} \begin{bmatrix} A \\ B \\ C \\ D \end{bmatrix} = 0 \quad (39)$$

where

$$A_{ij}^{\alpha\beta} = \int_0^\infty dk_\rho k_\rho \alpha_{ni}^t(k_\rho) \cdot \bar{G}(k_\rho) \cdot \beta_{nj}(k_\rho). \quad (40)$$

where α and β can be either ψ , ϕ , ξ or η . Due to reciprocity, the matrix in equation (39) is symmetric or $A_{ij}^{\alpha\beta} = A_{ji}^{\beta\alpha}$. In the above, the superscript t implies transpose. In order for the system of equations (39) to have a nontrivial solution, its determinant must vanish. Denoting the determinant in equation (39) by $D(\omega)$, we can conclude easily that the natural resonance frequencies ω_i of the microstrip antenna must satisfy the following equation

$$D(\omega_i) = 0. \quad (40a)$$

In general, the roots of equation (40) are complex with a negative imaginary part, indicating damping due to radiation loss.

V. Input Impedance of the Probe Excited Antenna

In order to find the input impedance of the ARL circular-disk microstrip antenna excited by a probe as shown in Figure 2, we have to consider the excitation problem [1]. In this case, the electric field on the patches is not only due to the current on the patch, but also due to the current on the probe. To determine the transverse electric field on the patches due to a vertical probe with a finite radius embedded in the dielectric substrate, we have to find the field in the substrate due to the probe first. Using the dyadic Green's function formalism, we can express the z -component of the electric field in the substrate due to the probe as [1, 5]

$$E_{1z}^P = -\frac{Il}{4\pi\omega\epsilon} \int_0^\infty dk_\rho \frac{k_\rho^3}{k_{1z}} \text{sinc}\left(\frac{k_{1z}l}{2}\right) e^{\pm ik_{1z}(z+\frac{d}{2})} J_0(k_\rho\rho) J_0(k_\rho R) \\ z > -\frac{d-l}{2} \quad \text{or} \quad z < -\frac{d+l}{2} \quad (41)$$

where R , l and I are radius, length, and assumed uniform current of the probe in the z -direction, respectively, as shown in Figure 2. The function $\text{sinc}(x) = \sin(x)/x$.

Using the transmission and reflection properties of the electromagnetic waves in a stratified medium [6], we can find the field in the upper-half space from equation (41). For a probe location at $\rho = \hat{x}b'$, using the addition theorem we can express the field in terms of a series of Bessel functions. Then, the transverse components of the electric field in the upper-half space due to the probe can be derived from E_z yielding

$$E_s^P = \begin{bmatrix} E_{\rho n}^P \\ E_{\phi n}^P \end{bmatrix} = \begin{bmatrix} e_{\rho n}^P \cos n\phi \\ -e_{\phi n}^P \sin n\phi \end{bmatrix}, \quad (42)$$

and

$$\mathbf{e}_n^p = \begin{bmatrix} e_{\phi_n}^p \\ e_{\phi_n}^p \end{bmatrix} = \int_0^\infty dk_\rho k_\rho \cdot \bar{\mathbf{H}}_n(k_\rho \rho) \cdot \mathbf{S}_n(k_\rho) \quad (43)$$

where

$$\mathbf{S}_n(k_\rho) = \begin{bmatrix} i \frac{k_\rho}{k_p} P_n(k_\rho) \\ 0 \end{bmatrix}, \quad (44)$$

$$P_n(k_\rho) = -\frac{Id}{4\pi\omega\epsilon} \frac{k_\rho^2}{k_{1z}} \text{sinc} \left[\frac{k_{1z}d}{2} \right] \left[\frac{1 + R_{12}^{TM} e^{ik_{1z}d}}{1 - R_{10}^{TM} R_{12}^{TM} e^{2ik_{1z}d}} \right] \cdot X_{10}^{TM} e^{ik_{1z}d} J_0(k_\rho R) J_n(k_\rho b') (2 - \delta_{0n}), \quad (45)$$

where δ_{nm} is the Kronecker delta function and $X_{10}^{TM} = 1 + R_{10}^{TM}$.

When the ARL circular-disk antenna is being excited by a probe, the current distribution on the disk in the vicinity of the probe has a singularity due to the singular nature of the field around the probe, which results in slow convergence. Therefore, the current $J_S^S(\rho)$ of a lossy magnetic wall cavity under a probe excitation is added to the regular current distribution $J_S^R(\rho)$ on the patch to accelerate the convergence [5] and the VHT of $J_S^S(\rho)$ can be found in closed form as [1,5]

$$\mathbf{K}_n^S(k_\rho) = -\frac{I}{2\pi} (2 - \delta_{0n}) \left\{ J_0(k_{1z}R) \frac{J_n(k_{1z}b')}{J_n'(k_{1z}a)} \left[\frac{\frac{k_{1z}}{k_p^2 - k_{1z}^2} J_n'(k_\rho a)}{-\frac{n J_n(k_\rho a)}{k_{1z} k_\rho a}} \right] - \left[\frac{\frac{k_p J_0(k_p R) J_n(k_p b')}{k_p^2 - k_{1z}^2}}{0} \right] \right\}, \quad (46)$$

where k_{1z} is the wavenumber of the dielectric medium in the magnetic wall cavity and can be written as

$$k_{1z} = (1 + i\alpha) \frac{\gamma_{nm}}{a_1} \quad (47)$$

where α is a positive loss factor. The expression in (46) consists of both the singular term and the reflected wave term. Since we are only interested in the singular term in (46), we can choose α to increase the loss such that the reflected wave term is unimportant. Considering the excitation condition and using the singularity subtraction, we can rewrite equation (1) as

$$\int_0^\infty dk_\rho k_\rho \bar{\mathbf{H}}_n(k_\rho \rho) \cdot \bar{\mathbf{G}}(k_\rho) \cdot [\mathbf{K}_n^R(k_\rho) + \mathbf{K}_n^S(k_\rho)] + \int_0^\infty dk_\rho k_\rho \bar{\mathbf{H}}_n(k_\rho \rho) \cdot \mathbf{S}_n(k_\rho) = 0 \quad (48a)$$

or

$$\begin{aligned} \int_0^\infty dk_\rho k_\rho \bar{H}_n(k_\rho \rho) \cdot \bar{G}(k_\rho) \cdot K_n^R(k_\rho) \\ = - \int_0^\infty dk_\rho k_\rho \bar{H}_n(k_\rho \rho) \cdot [S_n(k_\rho) + \bar{G}(k_\rho) \cdot K_n^S(k_\rho)]. \end{aligned} \quad (48b)$$

Using Galerkin's method, performing operations similar to those given in Section IV, we obtain a system of linear algebraic equations. Solving the matrix equation, the current distribution on the patches and then the z-component of the total field \mathbf{E} in the substrate can be determined. Therefore, the input impedance of the antenna under a probe excitation can be derived by using the induced EMF method [9]

$$Z_{in} = - \int_V \mathbf{E} \cdot \mathbf{J} dV / I^2 \quad (49)$$

The above is a variational expression for Z_{in} . The input impedance expression in terms of the current distribution both on the patches and on the probe can be derived from equation (49) as

$$\begin{aligned} Z_{in} = \frac{1}{4\pi\omega\epsilon_1} \int_0^\infty dk_\rho \cdot \frac{k_\rho}{k_{1z}} J_0^2(k_\rho R) \left\{ \frac{2}{ik_{1z}} \left[\frac{2e^{ik_{1z} \frac{d}{2}} k_\rho^2 \sin(\frac{k_{1z}d}{2})}{k_{1z}} - k_{1z}^2 d \right] \right. \\ \left. + \frac{4k_\rho^2}{k_{1z}^2} \frac{\sin^2(\frac{k_{1z}d}{2}) e^{ik_{1z}d}}{1 - R_{10}^{TM} R_{12}^{TM} e^{2ik_{1z}d}} [R_{10}^{TM} + R_{12}^{TM} + 2R_{10}^{TM} R_{12}^{TM} e^{ik_{1z}d}] \right\} \\ + \sum_n \frac{1}{2i\omega\epsilon_1 I} \int_0^\infty dk_\rho k_\rho^2 [K_{n1}^S(k_\rho) + K_{n1}^R(k_\rho)] \\ \frac{e^{ik_{1z}d} - 1}{ik_{1z}} [1 + R_{12}^{TM} e^{ik_{1z}d}] \left[\frac{1 + R_{12}^{TM}}{1 + R_{12}^{TM} e^{2ik_{1z}d}} \right] J_0(k_\rho R) J_n(k_\rho b'), \end{aligned} \quad (50)$$

where the subscript $n1$ denotes the first elements of vectors \mathbf{K}_n^S , \mathbf{K}_n^R . The vector \mathbf{K}_n^R , which corresponds to the regular part of the current distribution on the disk, is obtained by solving the integral equation (48b) using Galerkin's method. It is given by

$$\mathbf{K}_n^R = \sum_{m=1}^M A_{nm} \psi_{nm}(k_\rho) + \sum_{l=1}^L C_{nl} \xi_{nl}(k_\rho). \quad (51)$$

VI. Results and Discussions

In this paper the vector integral equations are solved using Galerkin's method. As in other problems solved with this method, the convergence of the solution has to be considered. Furthermore, to enhance the accuracy of the numerical calculation, the integral paths are deformed to avoid the singularities near the real axis. The oscillatory property of the integrand and the convergence of the infinite integral have to be evaluated *a priori* to select a suitable numerical integral method and appropriate truncation points for the infinite integrals. The singularity subtraction method has been used to accelerate the convergence of the integral with a singular current distribution. The slowly decaying parts of the integral in equation (50) have been subtracted out and evaluated in close form.

The numerical analysis for natural resonance frequencies in this paper are the same as those in Figure 3 of [7] when $L = 0$ and $Q = 0$ (for the case of an annular-ring antenna) or as those in Figure 3 of [8] when $M = 0$ and $P = 0$ (for the case of a circular-disk antenna). This is because the above are the special cases of ARL circular-disk microstrip antennas.

As shown in the theoretical analysis and the experiment, ARL circular disk microstrip antennas have dual resonance frequencies, which can be used to broaden the bandwidth of the antenna. In general, one resonance is higher than the natural resonance of the annular ring antenna, and the other resonance is lower than the natural resonance of the circular-disk antenna. The difference depends on the mutual coupling (odd and even) between the two patches; therefore, it depends on the geometrical configuration of the microstrip antenna and the dielectric constant of the substrate. Figure 3 shows the dual resonance frequencies as the function of the substrate thickness. An appropriate excitation condition is important to obtain the dual resonance frequencies.

Figure 4 shows the resonance frequencies and the bandwidth of two ARL circular-disk microstrip antennas with different patch sizes as a function of substrate thickness. It can be shown that the resonance frequencies decrease and the bandwidths increase as the thickness of the substrate increases. The numerical results are in good agreement with experiment data even when the substrate thickness increases to 0.1 wavelength.

Figures 5-7 show the input impedance characteristics of the ARL circular-disk microstrip antenna with various electrical thicknesses as a function of frequencies. In Figure 5 the electrical thickness of the antenna substrate is $d = 0.054\lambda_c$; M , P , L , Q , the number of the basis functions for current distribution on the patches, are 2,1,2,1, respectively. The agreement between theoretical results and experimental data is excellent.

Figure 6 shows the input impedance of the antenna with electrical thickness $d = 0.07\lambda_e$. The numbers of the basis functions for the current on the patches are the same as in Figure 5. The results of the induced EMF method still agree well with the experiment data. The impedance locus shift between the induced EMF method and experiment data is the effect of the edge extension caused by the fringing field at the edge of the patches. This fringing field effect is caused by singular charge distribution near the edge; hence, more basis functions are required to approximate this fringing field effect. Therefore, the resonances obtained by numerical calculation with an insufficient number of basis functions tend to be higher than that obtained from the experiment. The thicker the substrate, the more significant the fringing field effect, therefore, the greater the shift between the locus obtained from the theory and experiment for a given number of basis functions.

Figure 7 shows the input impedance of the antenna with electrical thickness $d = 0.1\lambda_e$. The number of the basis functions of the TM mode for current distribution on the circular disk is increased to 8 ($L = 8$) to account for the fringing field effect. A very good agreement between the numerical and the experimental results has been achieved. Increasing the number of basis functions for the circular disk rather than for the annular ring is because the dominant resonance is coming from the disk rather than the ring.

Figure 8 shows the input impedance locus for $L=2$ and $L=8$ when the electrical thickness $d = 0.1\lambda_e$. The edge extension caused by the fringing field at the edge of the patch cannot be neglected, and more basis functions of the TM modes have to be chosen to account for the fringing field effect when the substrate is electrically thick.

It can be shown from the above discussion that the theory in this paper can be used to analyse the characteristics of microstrip antennas, especially the antennas with mutual coupling between patches, which are difficult to analyse with some popular methods such as the cavity model method. Furthermore, this theory, when applied to the analysis of the microstrip antennas with an electrically thick substrate, gives results of resonances and input impedances in good agreement with experimental data if we use more basis functions of the TM modes to account for the fringing field effect. However, much more computer resources are required in such a case. It is also shown from the numerical analysis that the effect of the probe on the resonances is much less than the effect of the fringing field of the patch when the microstrip antenna is electrically thick. We have not used any artificial correction on the theory for the good agreement with measurement results. The uniform-probe-current assumption does not affect the input impedance appreciably because the input impedance is dominated by the disk current, even for antennas with electrically thick substrates.

References

- [1] W. C. Chew and J. A. Kong, "Analysis of circular microstrip disk antenna with thick dielectric substrate", *IEEE Trans. Antennas Propagat.*, v. AP-29, pp. 68-76, Jan. 1981.
- [2] M. Davidovitz and Y. T. Lo, "Input impedance of a probe-fed circular microstrip antenna with thick substrate," *IEEE Trans. Antennas Propagat.*, v. AP-34, pp. 905-911, July 1986.
- [3] S. M. Wright and Y. T. Lo, "Efficient analysis of infinite microstrip antenna arrays on electrically thick substrates", *RADC-TR-86-8 Final Technical Report*, Rome Air Development Center, University of Illinois, March 1986. ADA169011
- [4] W. C. Chew and T. M. Habashy, "The use of vector transform in solving some electromagnetic scattering problems", *IEEE Trans. Antennas Propagat.*, v. AP-34, pp. 871-879, July 1986.
- [5] W. C. Chew, *Mixed Boundary Value Problems in Microstrip and Geophysical Probing Applications*, Ph. D. dissertation, Massachusetts Inst. Technol., Cambridge, 1980.
- [6] J. A. Kong, *Theory of Electromagnetic Waves*. New York: Wiley, 1975.
- [7] S. M. Ali, W. C. Chew and J. A. Kong, "Vector Hankel transform analysis of annular-ring microstrip antenna," *IEEE Trans. Antennas Propagat.*, v. AP-30, pp. 637-644, July 1982.
- [8] W. C. Chew and J. A. Kong, "Resonance of nonaxial symmetric modes in circular microstrip disk antenna", *J. Math. Phys.*, v. 21, n. 10, pp. 2590-2598, Oct. 1980.
- [9] E. C. Jordan and K. G. Balmain, *Electromagnetic Waves and Radiating Systems*. Prentice Hall: New Jersey, 1968.

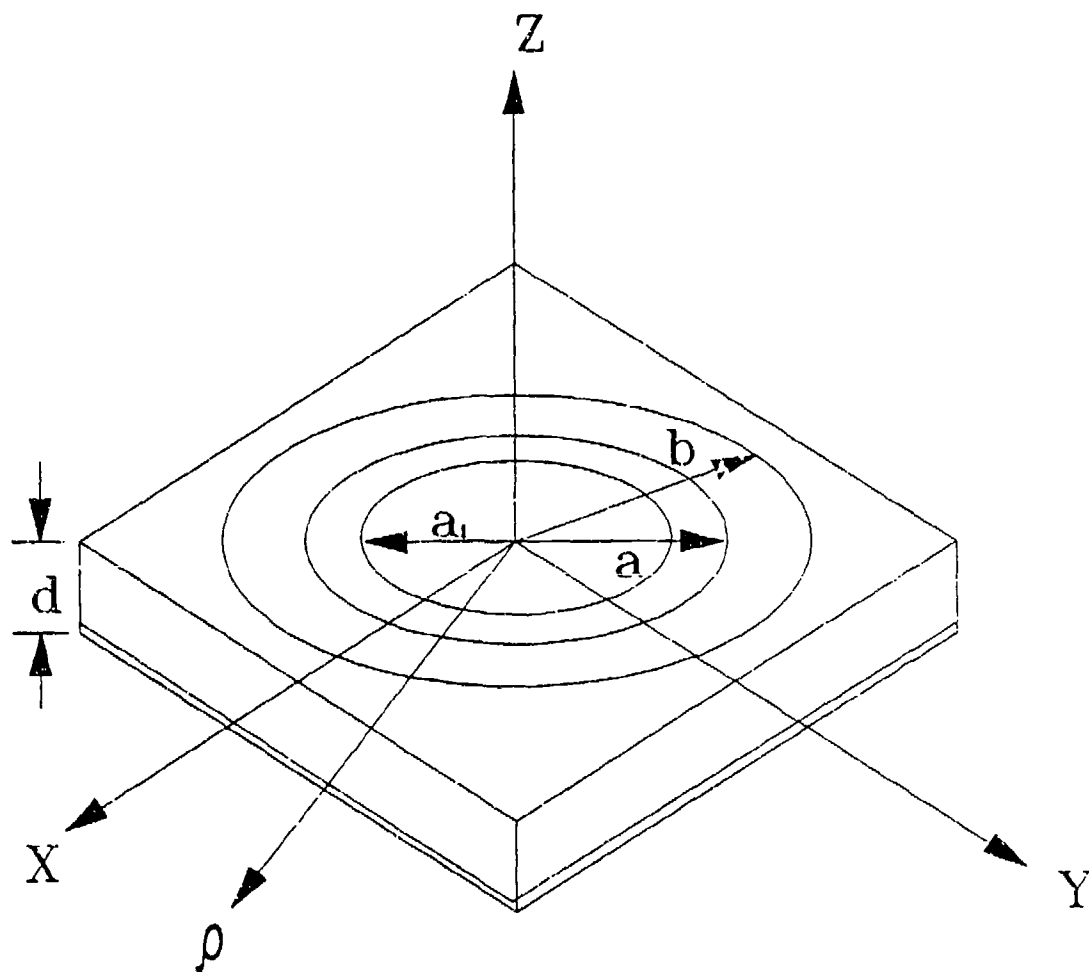


Fig.1 Geometrical configuration of annular-ring loaded circular disk antenna

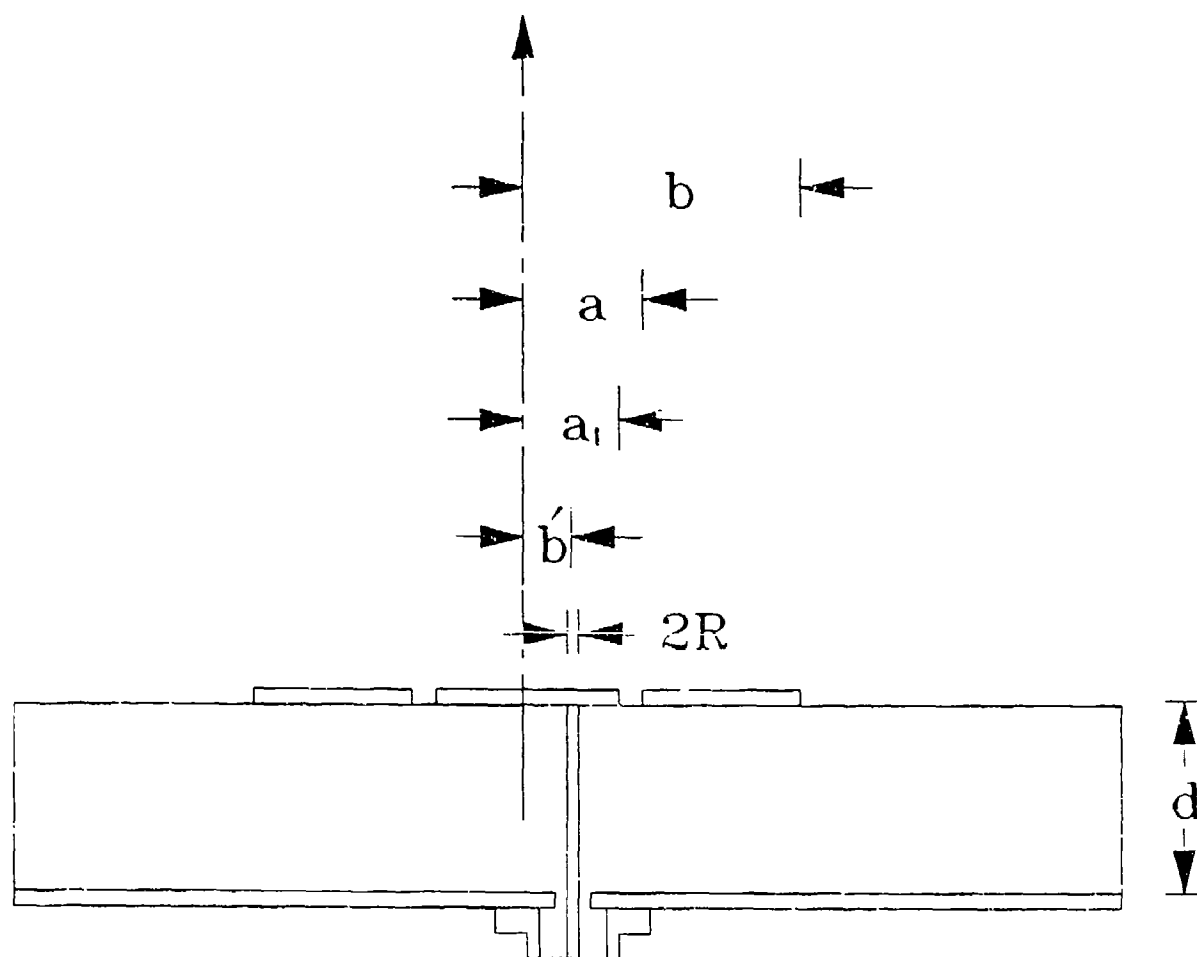


Fig.2 ARL circular-disk microstrip antenna excited by a probe

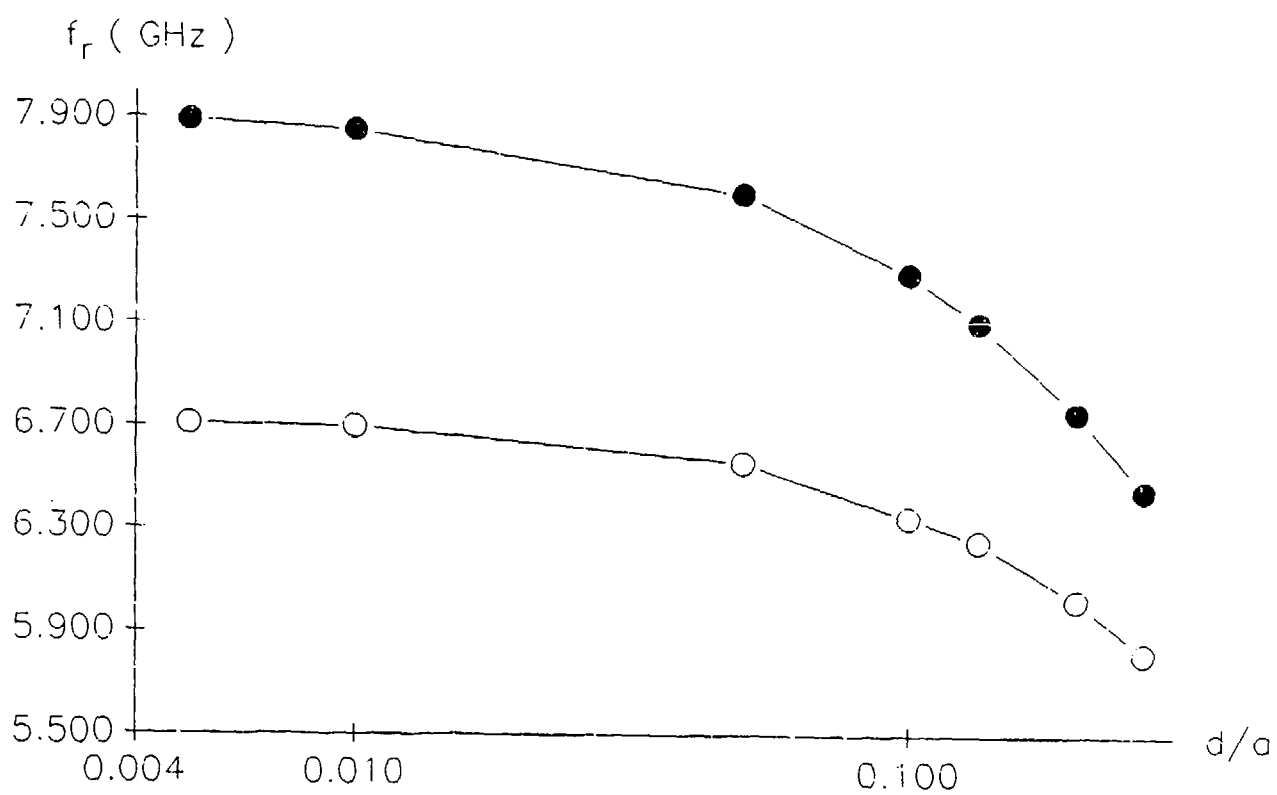


Fig.3. Higher and lower resonance frequencies of the ARL circular disk microstrip antenna; $a=1.2\text{cm}$, $b=2.0a$, $a_1=0.67a$, $\epsilon_r=2.65$.

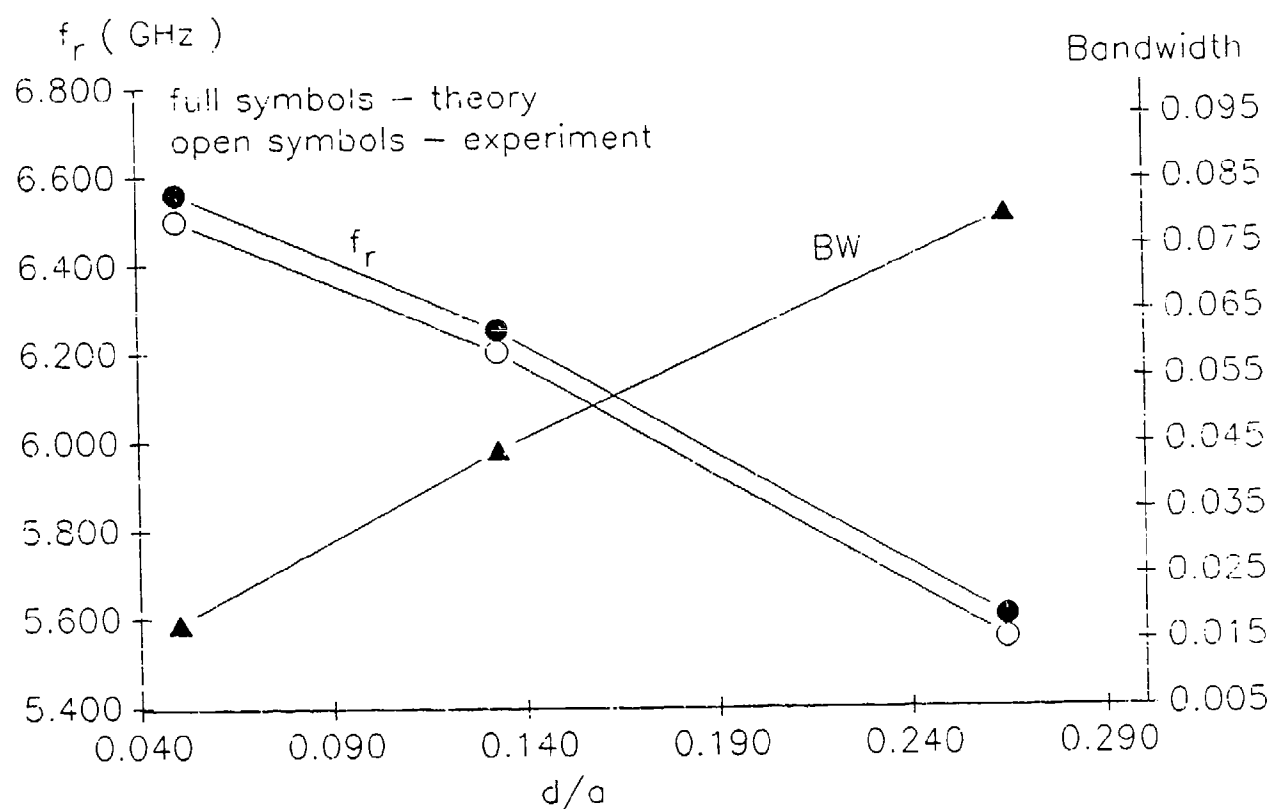


Fig.4a. Resonance frequency shift as a function of d , where $a=1.2\text{cm}$, $b=2.0a$, $a_1=0.67a$, $\epsilon_r=2.65$.

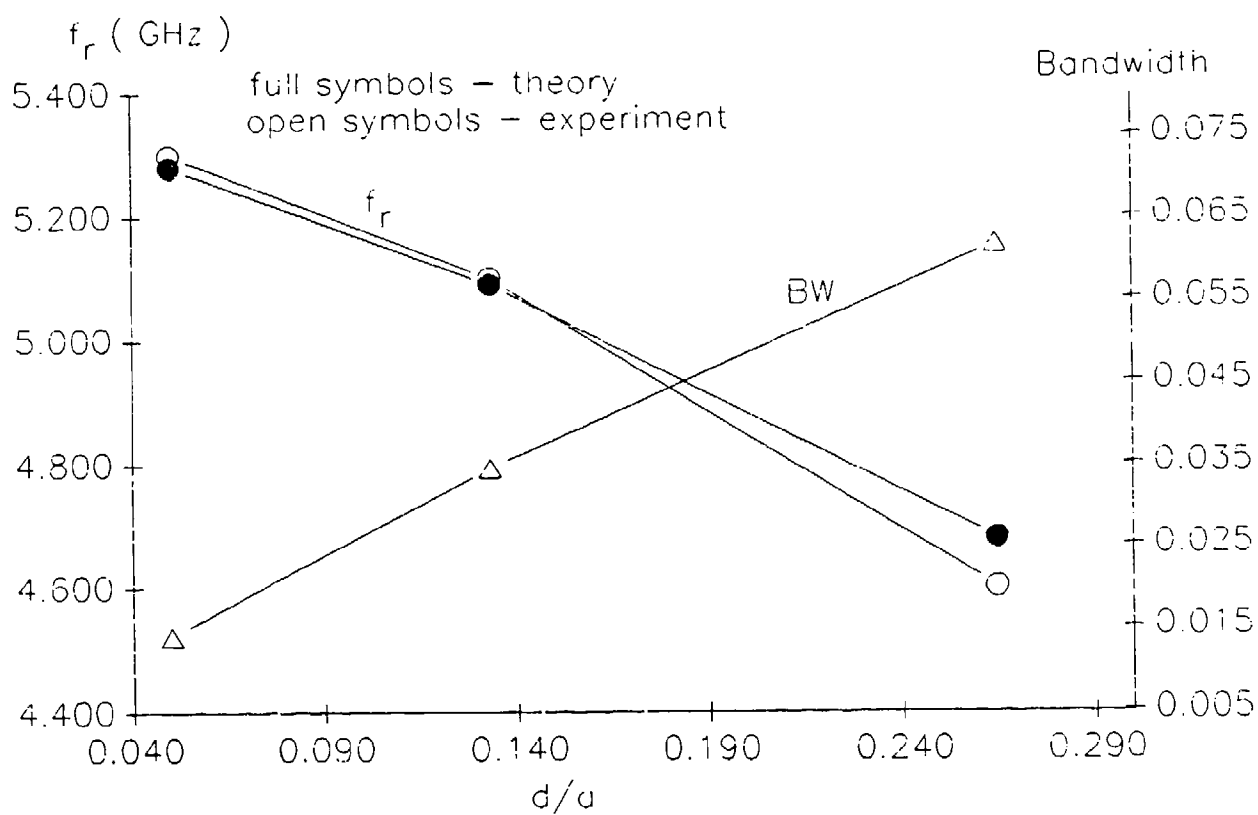


Fig.4b. Resonance frequency shift as a function of d , where $a=1.2\text{cm}$, $b=2.0a$, $a_1=0.83a$, $\epsilon_r=2.65$.

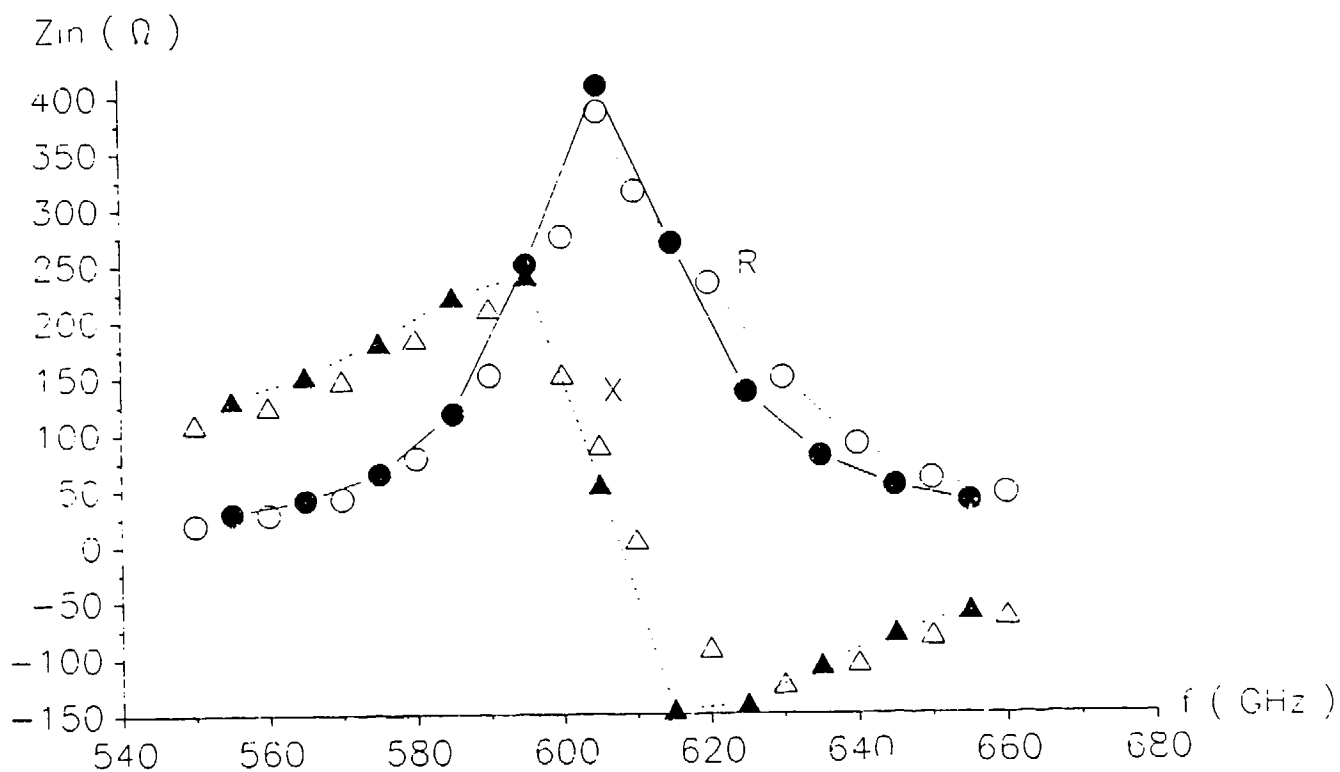


Fig.5. Comparison of experiment and theory for input impedance, where $d=0.054$ wavelength. full symbols - theory. open symbols - experiment.

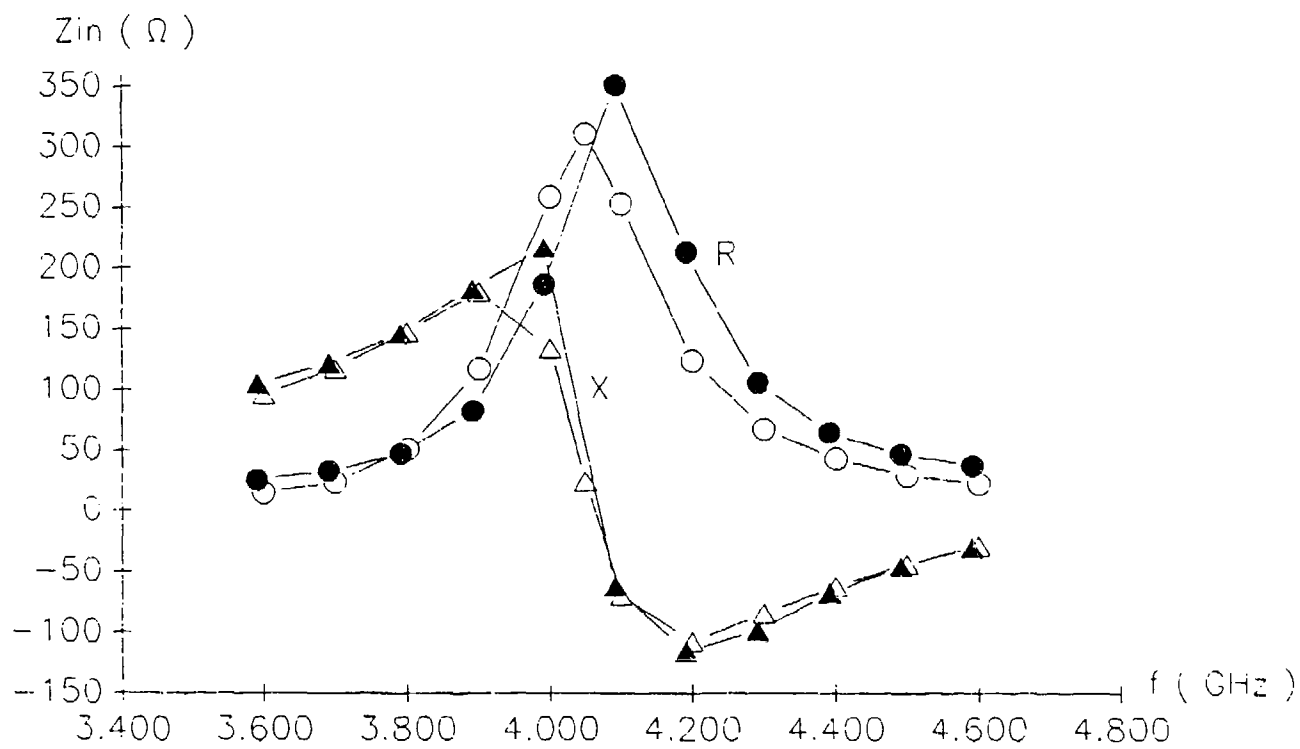


Fig.6. Comparison of experiment and theory for input impedance, where $d=0.07$ substrate wavelength, full symbols — theory, open symbols — experiment.

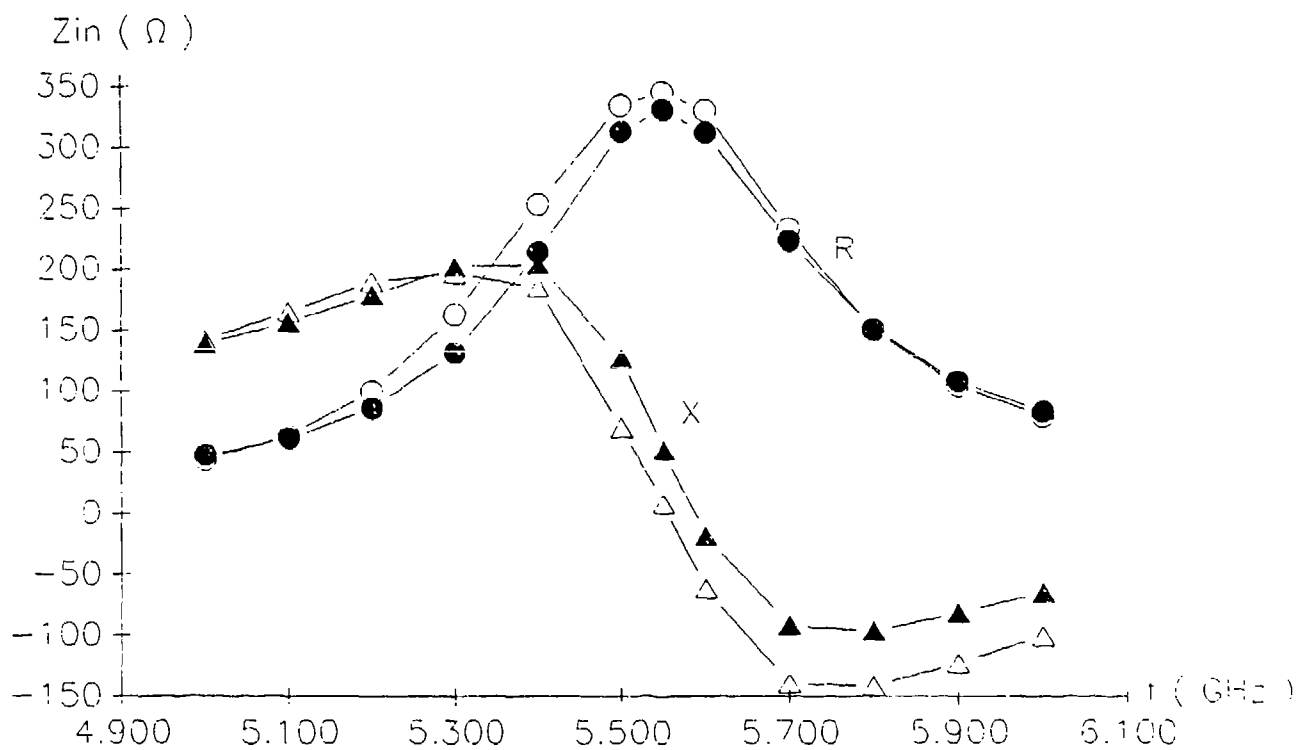


Fig.7. Comparison of experiment and theory for input impedance, where $d=0.1$ substrate wavelength, full symbols — theory, open symbols — experiment.

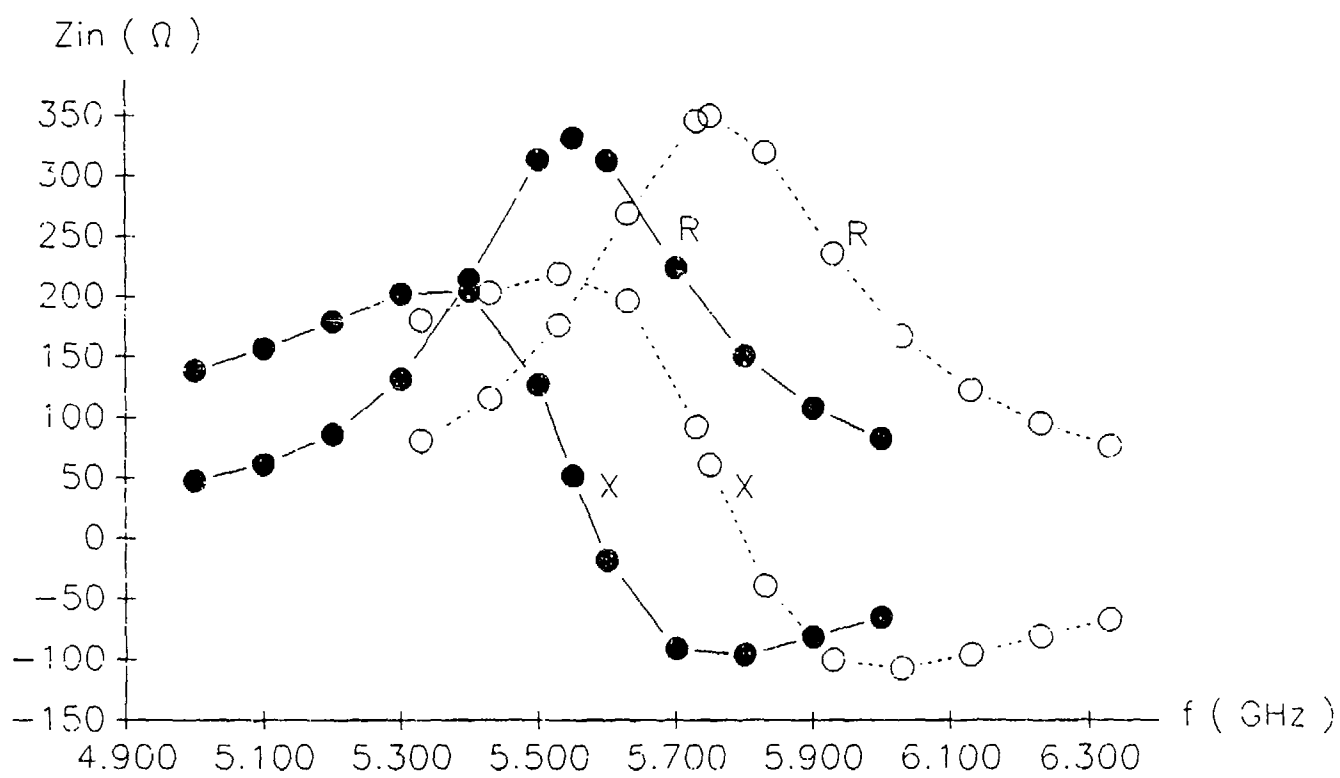


Fig.8. Fringing field effect. full symbols - 8 basis functions for current on disk patch, open symbols - 2 basis functions for current on disk patch.

DESIGN AND ECONOMIC CONSIDERATIONS FOR BROADBAND PHASED-ARRAY ELEMENTS

Presented to
Antenna Applications Symposium
USAF/University of Illinois

Presented by
George J. Monser
Consulting Engineer

23 September 1988

DESIGN AND ECONOMIC CONSIDERATIONS FOR BROADBAND PHASED-ARRAY ELEMENTS

George J. Monser

1.0 INTRODUCTION

Today's technology and economy demand that the arrays function over multi-octaves and that the cost per element be small. This talk addresses both needs. Three stages of linear-array development are presented. Stage 1, where the consideration was for a linearly-polarized array. Stage 2, where the consideration was to extend the array to include an orthogonal polarization. The final stage describes areas of consideration for maximizing the array bandwidth.

2.0 STAGE 1 DESIGN CONSIDERATIONS

In forming a linear array, as depicted in Figure 1, two dimensions are important. The element dimension d , which is aligned with the array, is fixed by the highest frequency of intended operation. If d exceeds $1/2$ wavelength, secondary lobes will appear when the beam is scanned beyond about 30° from boresight. For a variety of reasons, system requirements generally impose a limit on the formation of secondary lobes so that the dimension d is approximately $\lambda/2$ where λ is the wavelength corresponding to the uppermost frequency. The dimension H , perpendicular to the array, represents a free dimension in linear array design limited only by the minimum field-of-view (FOV) orthogonal to the array. The FOV in degrees is given approximately by $51 (\lambda/H)$, where λ is the free-space wavelength and H is the height both in consistent measurement units (i.e., inches, CMs, etc.).

Once H is chosen, the space per array element for interior element design is set for the depth or length of the array element are generally limited by the installation space. Where space is a premium, such as in tactical aircraft, sufficient depth for an optimum design may not exist.

Figure 2 shows an array element cell of a phased-array with dimensions H and d . Both H and d are determined by the highest frequency of operation. For example, if the highest frequency corresponds to 0.65 inches in wavelength and

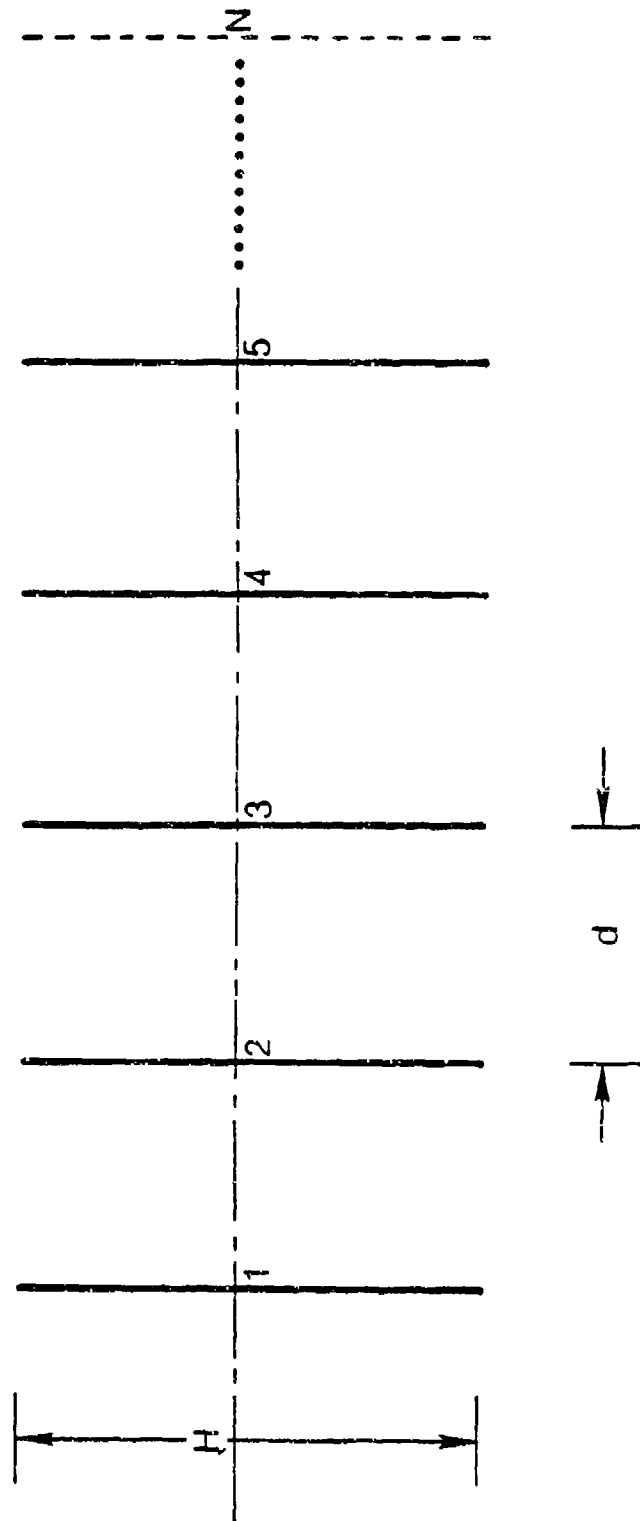


Figure 1. Linear Array

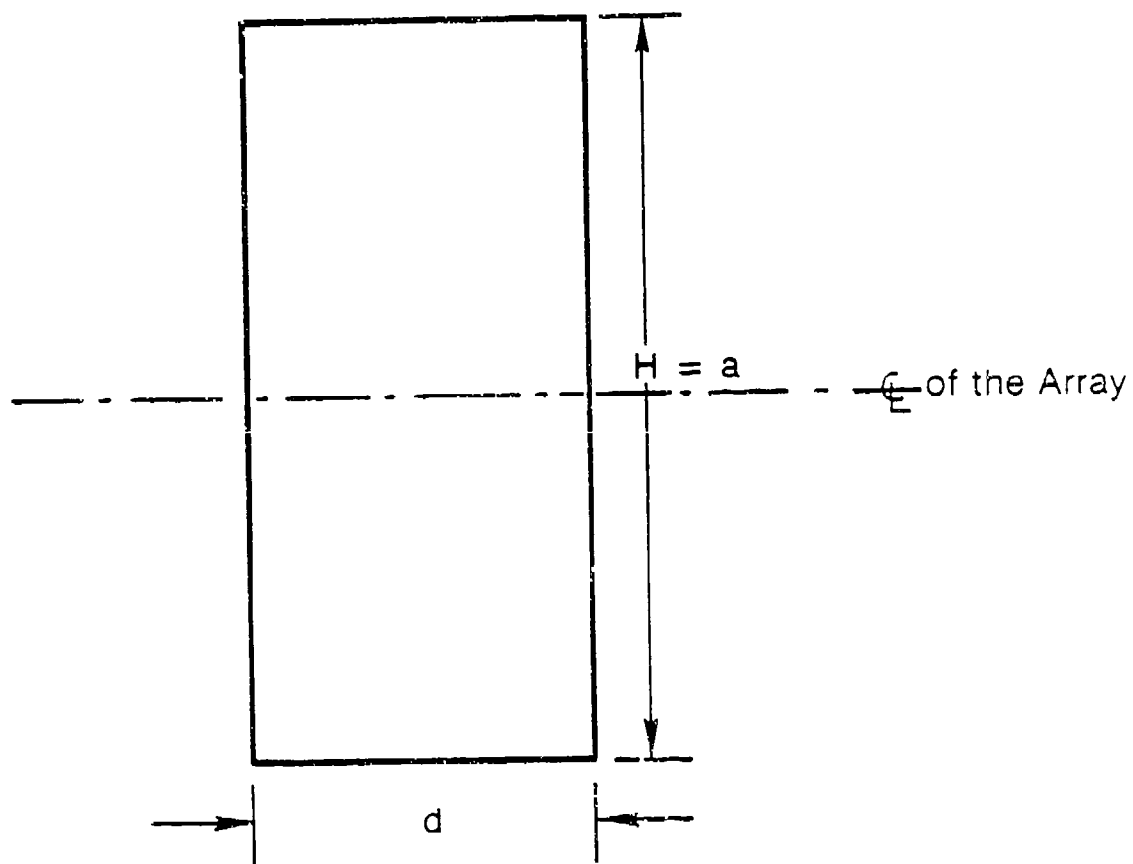


Figure 2. Element Dimensions

a FOV of 30° is required, then from equation (1), $H = 1.105$ inches, and from the $(1/2)\lambda$ requirement, $d = 0.325$ inches. Thus, the array element dimensions for this application are fixed (1.105×0.325 inches).

If a bit of the grating lobe is allowed to exist, a slightly larger d can be used. If the FOV is re-defined, from say the half-power limits to the $1/3$ power limits, then a slightly larger H is permitted. In any case, both dimensions are established.

3.0 STAGE 2 DESIGN CONSIDERATIONS

With the array-element real estate established, it is necessary to look for array elements that can be fit within these constraints of Figure 2, and which are economical to produce. A horn within which ridges can be placed to yield a $3/1$ bandwidth was selected as one candidate element. Mechanical tolerance and performance studies were conducted to support the use of cast elements for the final design. For the other candidate element, it was visualized that an array of printed notches, with one board per array element, offered an economical and broadband solution. In addition, the simplest solution for integrating the printed notches in the horn array would consist of replacing a section of each horn wall with the printed notch board. The notches radiate primarily from the step discontinuity near the aperture plane so that they would function effectively and so would the horns for the walls necessary for propagating the TE_{10} mode would be nearly intact except for the small notches.

Photographs of these elements are shown in Figure 3. Since gain versus frequency is most important, each element was first tested as an isolated element. Results are given in Figure 4. In this figure, the results are plotted versus the critical design dimension expressed as a fraction of a wavelength. In both cases, the critical dimension is H for the notches aligned with the a dimension of the horn (see Figure 2). To achieve the extended band for the horn element it is necessary to place ridges, as shown, inside the array element. The ridges lower the cut-off frequency of the horn. Without ridges, the cut-off frequency corresponds to a wavelength equal to $(2 \times a)$. With ridges, the cut-off wavelength can be increased significantly, to at least

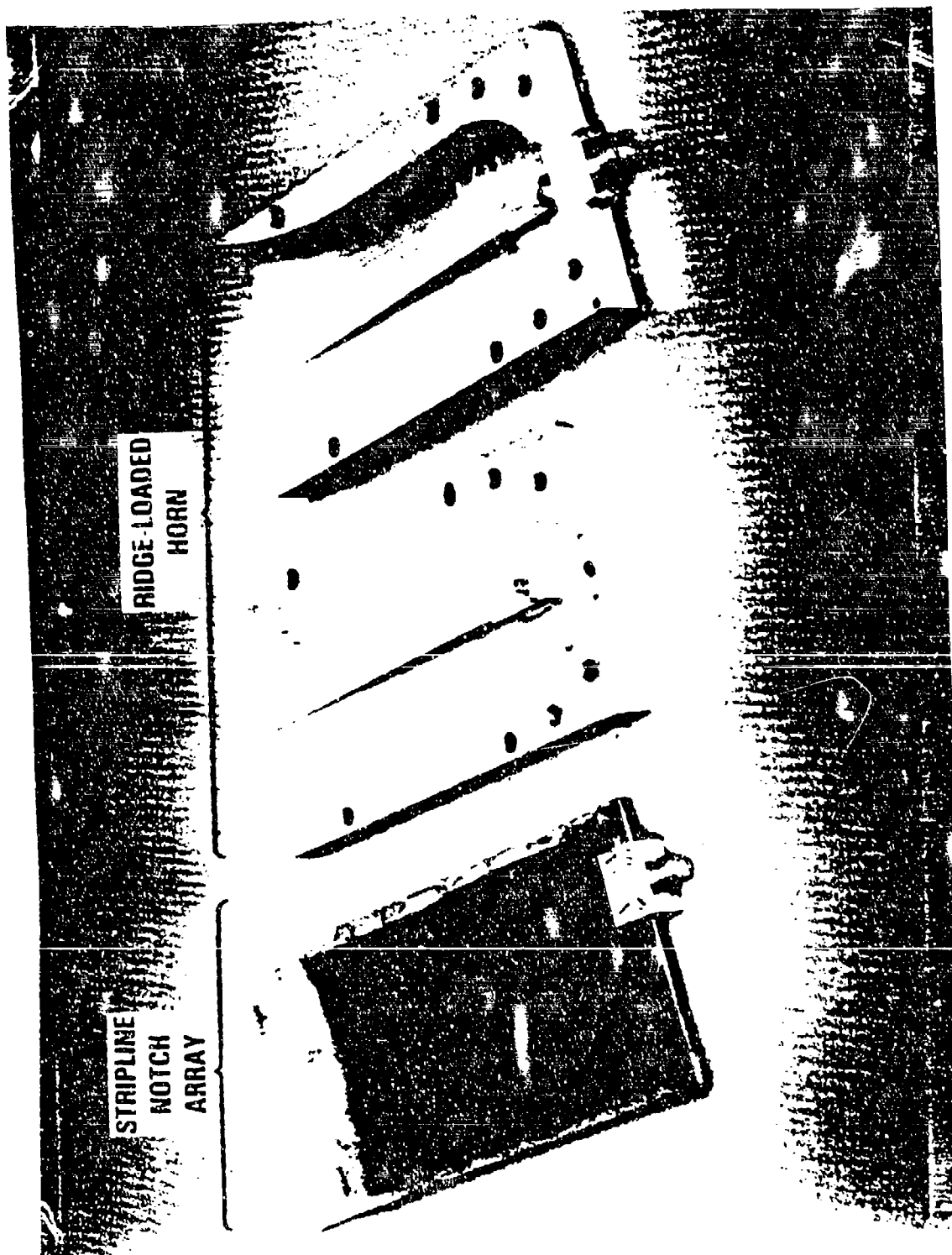


Figure 3. Photographs of Elements

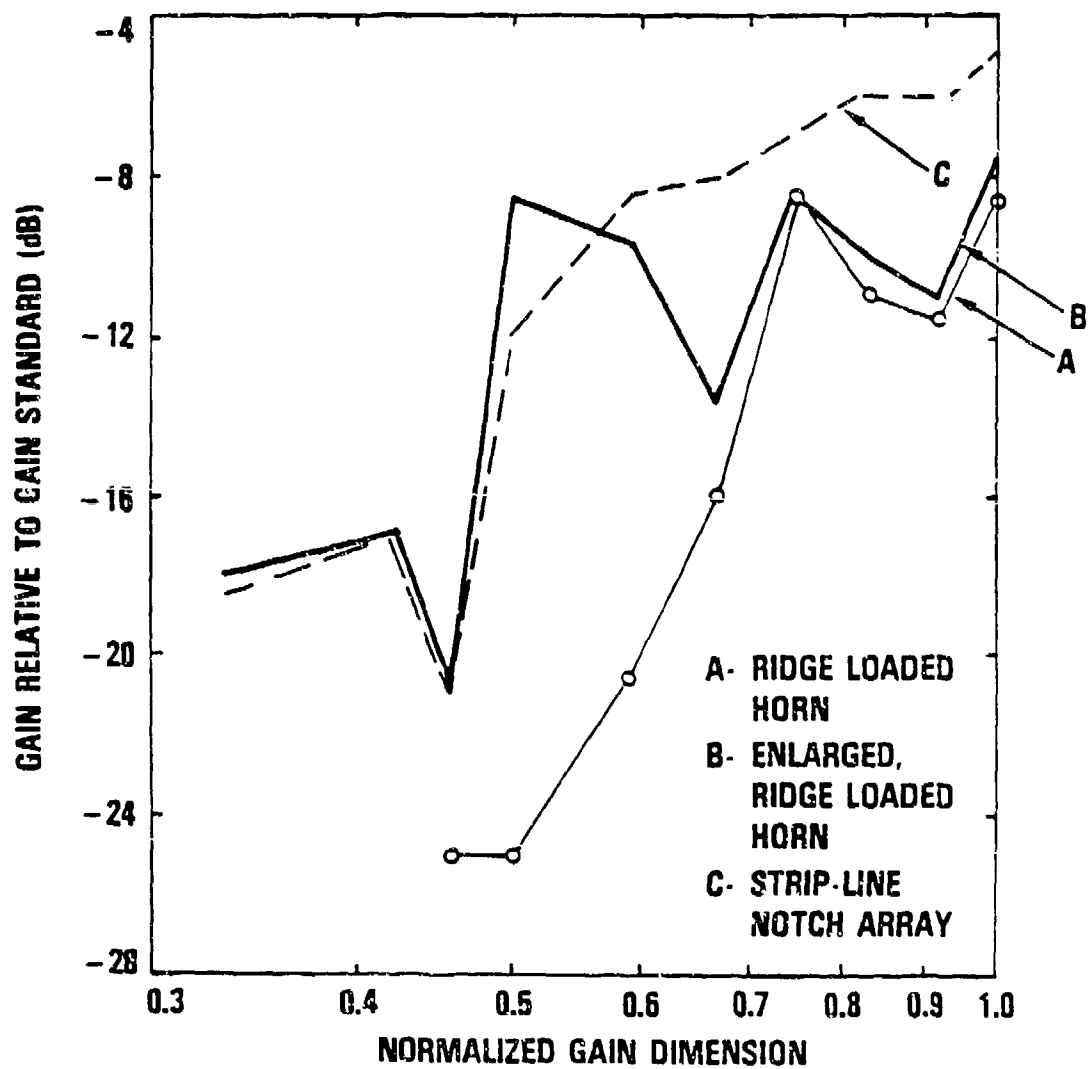


Figure 4. Isolated Element Gains

(3 x a), resulting in a lower useable frequency as frequency and wavelength are inversely related. A further point should be made and that is, while the H or a dimension is fixed at the aperture, by the minimum FOV, inside the horn the a dimension is selected to achieve the low frequency limit of operation (i.e., 4 GHz) and at the same time avoiding higher order waveguide modes. Should this occur a lowering of the uppermost frequency would result.

Having selected the elements, an array was constructed consisting of both types of elements interlaced so that two polarizations could be transmitted or received by the array. One polarization is intercepted or formed by the horn elements, parallel to the array, and the other polarization, perpendicular to the array is intercepted or formed by the notch elements. A photograph of this array is shown in Figure 5.

4.0 PERFORMANCE TESTS

Having constructed the array, array element VSWR was first measured, as it determines element efficiency. Here it is important to note that the VSWR of concern is that realized when all array elements are simultaneously driven. This is referred to as the active VSWR as contrasted to the passive VSWR measured on a single element in the array with all other elements terminated or loaded. In this design it was found that at the lower frequencies the passive VSWR for the horn elements predicted efficiencies on the order of 50 percent. However, from active VSWR values closer to 80 percent result. Active match can be found by measuring the passive reflection coefficient and the coupling coefficients from all elements to element under test, with all quantities expressed as complex values or phasors. The inset box (see Figure 6) shows how active match is found. There, it may be observed that for the horn element the passive reflection partially cancels the coupled energy resulting in a low active reflection coefficient and good active VSWR. However, for the notch elements the vectors do not cancel to the same extent. For this element, the lowest passive reflection is achieved by design and the resulting coupling and active VSWR tolerated.

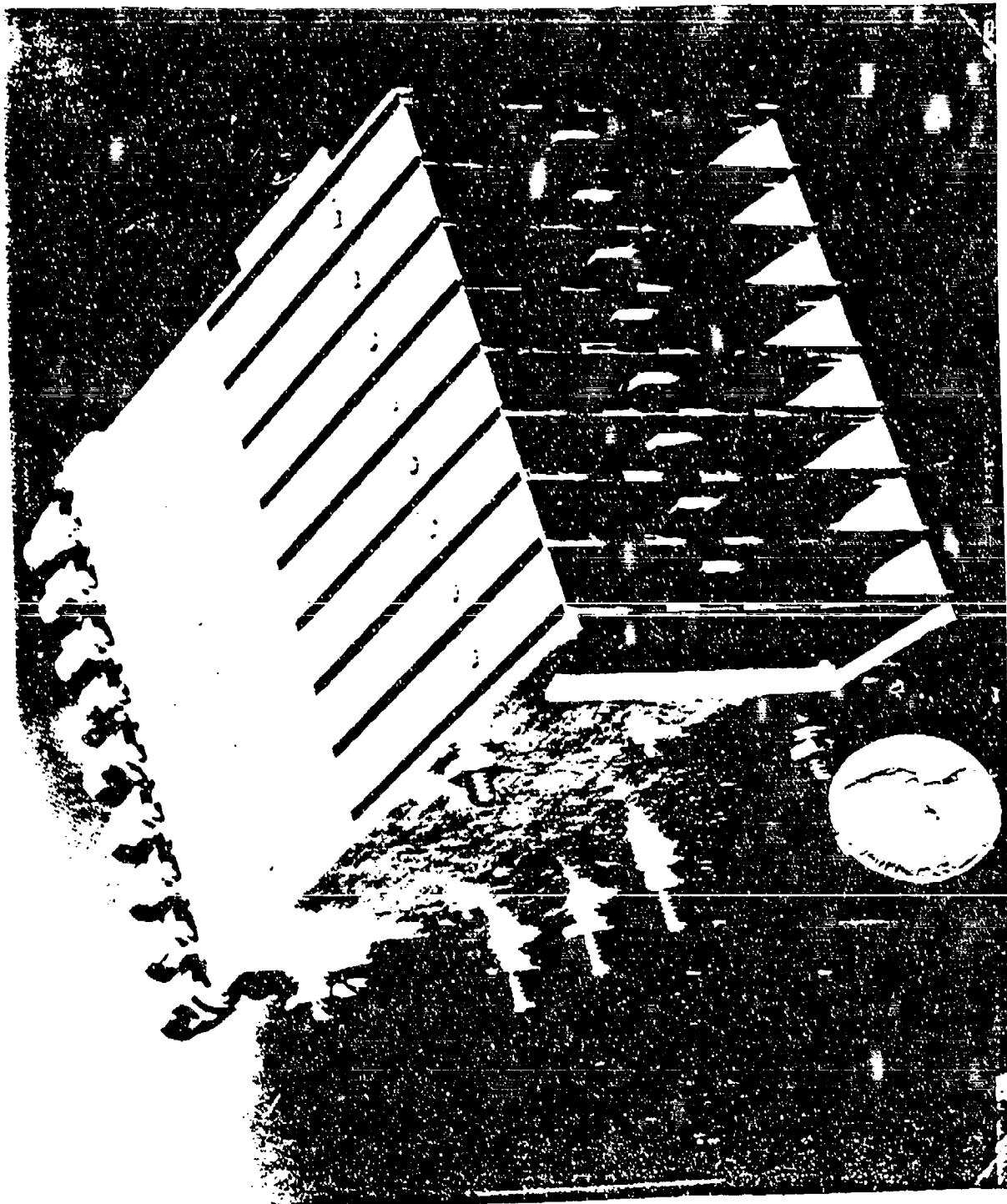


Figure 5. Photograph of Finished Array

1



•

CASE NO. 2: PHASORS FOR S/L NO. 5, 0° SCAN, F=6.5 GHz

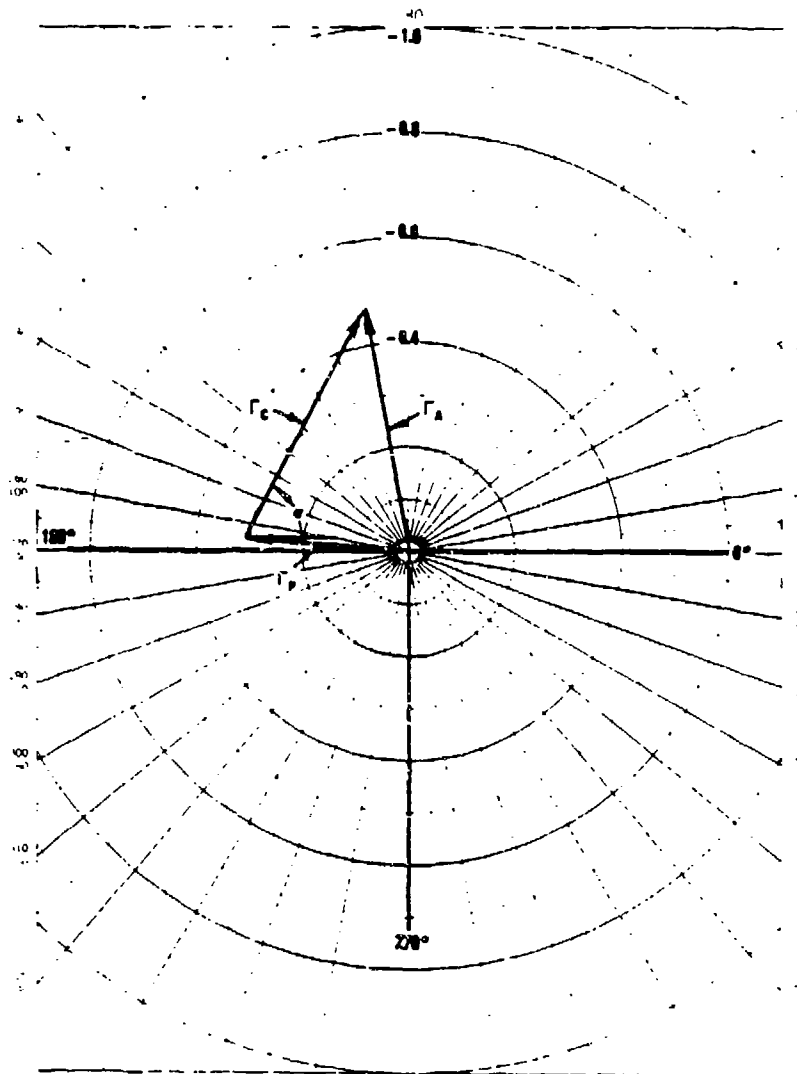


Figure 6b. Phasor Relationships (Striplines)

Once these VSWR determinations were complete, gains for all elements were checked over the full frequency band to assure continuous coverage. Typical swept-gain plots are given in Figure 7. There, it can be seen that none of the elements had drop-outs in gain over the full band from 5 to 18 GHz (i.e., continuous coverage).

Pattern coverage for each type of element is given in Figures 8 and 9. In Figure 8, coverage in the array-plane at mid-band is shown to exceed 100° between half-power points (i.e., -3 dB points on the patterns). Thus, when all elements of the array are driven with phasing set to steer the beam, good scan characteristics should result over a 100° sector (i.e., $\pm 50^\circ$ from bore-sight). Figure 9 shows the coverage orthogonal to the array exceed 30° for half power limits (i.e., -3 dB points on the patterns).

5.0 COST ANALYSIS

Production costs for each type of array element were estimated. Excluding one-time tooling costs for each element, it was determined that each array element (both polarizations) could be manufactured for well under \$100. For example, the cost of cast horn elements was \$10. Adding \$10 per element for "touch labor" in assembly and \$25 for production test yields a total cost under \$50.

6.0 CONCLUDING REMARKS

This talk has described the design of an economically-producible dual-polarized array capable of 4/1 bandwidth for both polarizations and 6/1 bandwidth for the printed-notch array.

Recent investigative efforts have indicated that the bandwidth for the horn elements can possibly be extended to cover a 6/1 band.

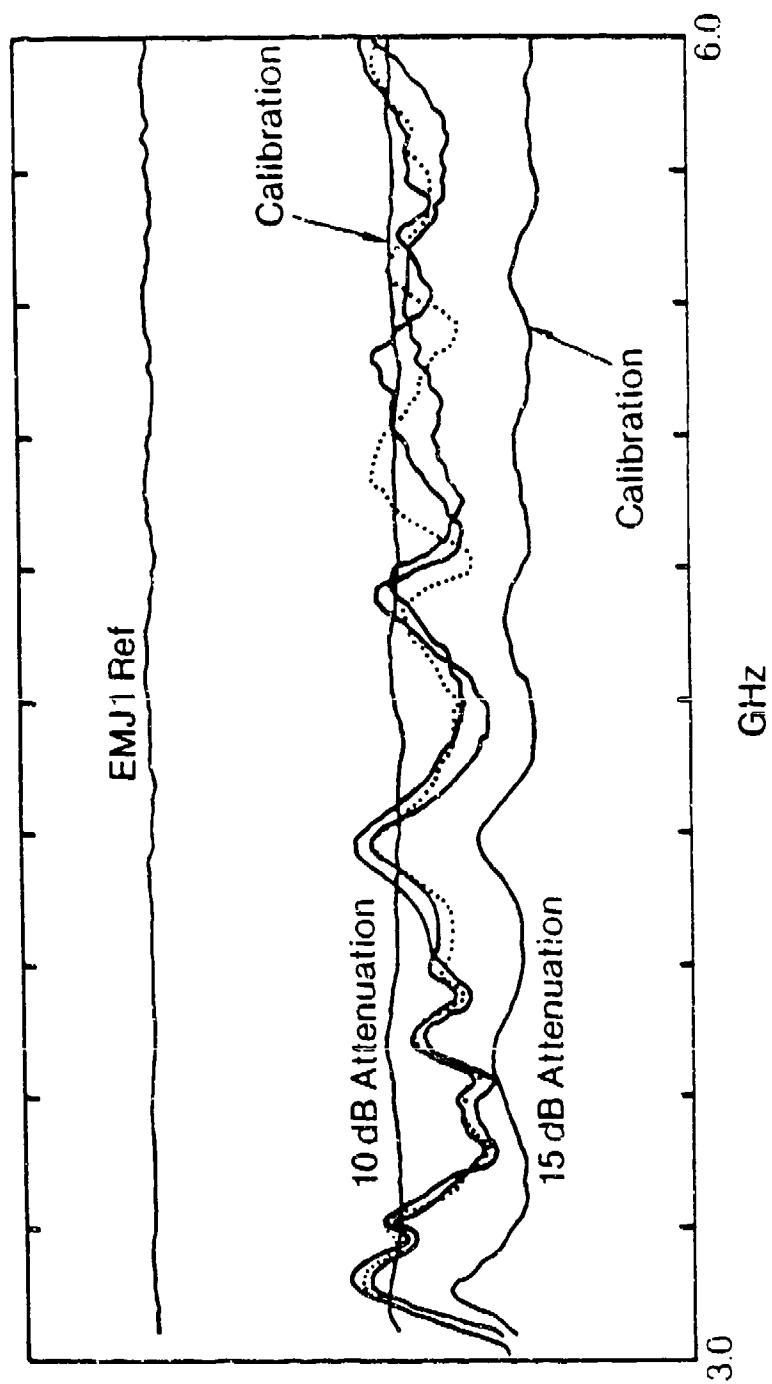


Figure 7a. Lower Band Swept Gain

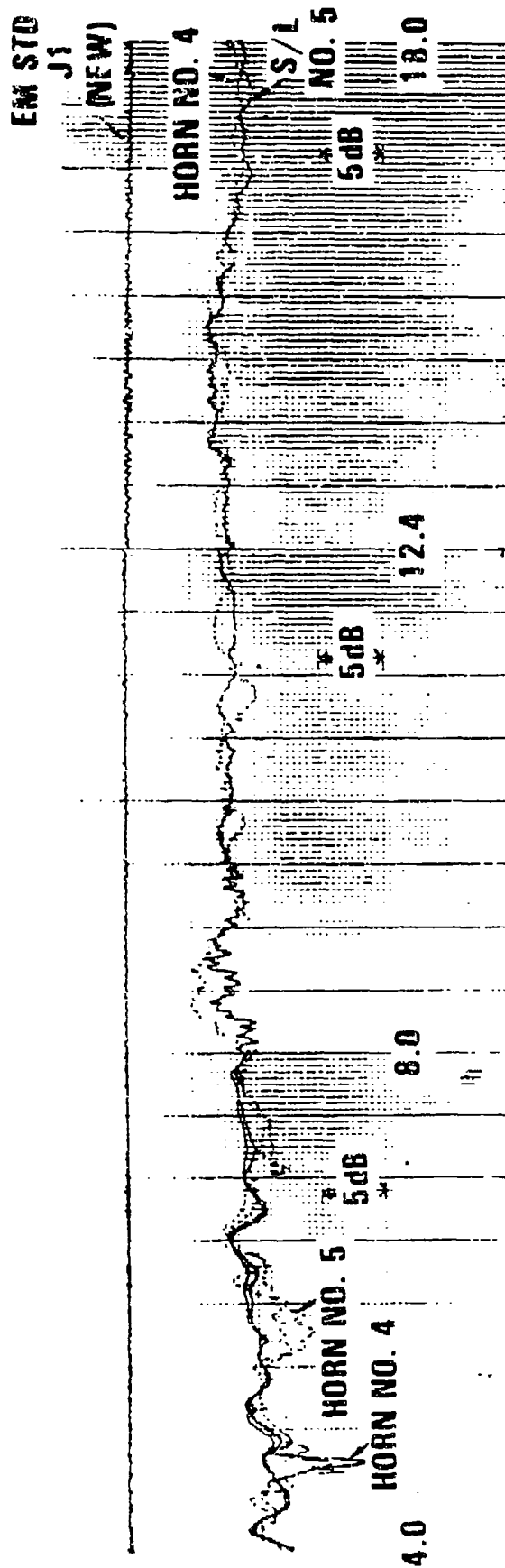


Figure 7b. Swept Gain Full Band
(Vertical and Horizontal Polarizations)

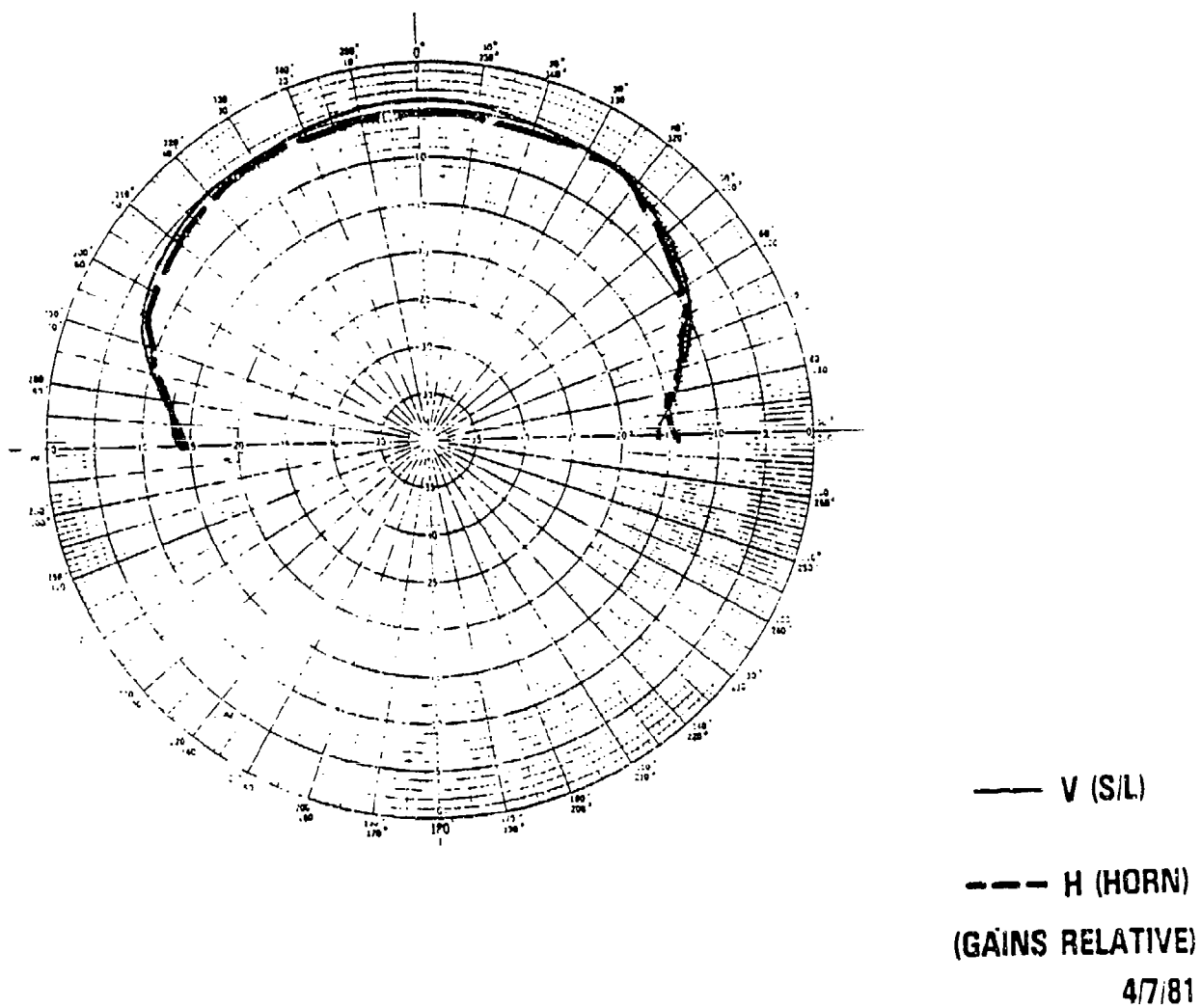


Figure 8. Coverage in Array Plane at Mid-Band

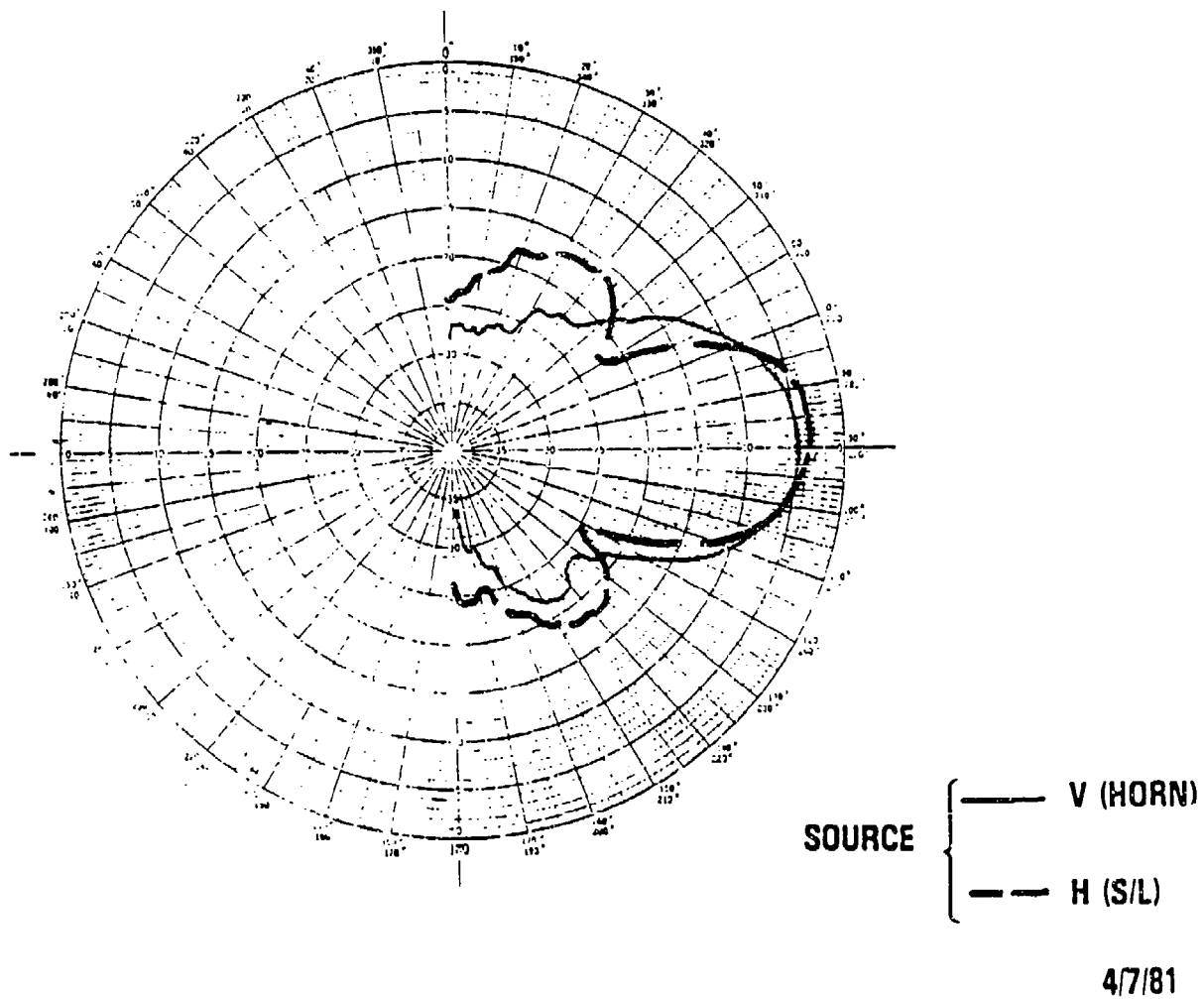


Figure 9. Orthogonal Coverage (Elevation)
 at Mid-Band

ACKNOWLEDGEMENT

I especially want to acknowledge Mr. Al Roy and Mr. Brian Lopez for their many contributions during the development.

Raytheon holds the patents on this antenna and a disclosure has been submitted on the new horn.

A LARGE MULTIBEAM LENS ANTENNA FOR EHF SATCOM

J. P. Montgomery, D. L. Runyon, and J. A. Fuller
Electromagnetic Sciences, Inc.
Norcross, Georgia 30092

ABSTRACT

Development of very large, satellite based, multiple beam antennas (MBAs) using extremely high frequencies (EHF) for satellite communications (SATCOM) is the subject of this paper. Very large MBAs having *several hundred beams* is a significant increase in the complexity of an MBA by today's standards. The main issue to be resolved is whether the beamforming network (BFN) required for such an MBA can be implemented in a practical manner. The paper is extracted from a more complete report [Montgomery, Runyon, and Fuller, 1988] recently published and presents strong support for the feasibility of these large MBAs.

Two primary approaches to realizing the BFN are examined: (1) a *constrained BFN* using interleaved switch networks with an adaptive combining network, and (2) a *space fed array* consisting of modules capable of precision phase and amplitude control. Consideration is given to the addition of solid state low noise amplifiers for uplink antennas, however, nulling requirements place stringent requirements on these components. Both approaches are compared with regard to: gain and noise temperature, adaptive nulling, power requirements, weight and size, complexity and cost, reliability, and robustness.

Common to either MBA approach is the use of a large, high performance, zoned dielectric lens and the use of feed clusters to obtain improved scanning and sidelobe performance.

1. INTRODUCTION

The use of EHF for SATCOM is expected to grow substantially over the next decade. EHF frequencies allow more user channels while accommodating wide band users. EHF frequencies also permit high efficiency antennas with narrow beamwidths, high gain, and low sidelobes with minimal size and weight penalties — ideal for satellite based systems. These antenna characteristics are well suited for minimizing the adverse effects of spatially distributed jammers both with and without the use of adaptive nulling networks.

Electronic scanning of an MBA is accomplished by the electronic control of the BFN. The critical EHF components such as switches and phase shifters which comprise the BFN typically utilize ferrite technology which is capable of achieving low insertion losses with low switching powers while maintaining the reliability required for satellite applications. Typically, the BFN uses power from one or more antenna feed ports, by controlling switch matrices and variable power combiners, to move the active port centroid in the focal region of either a reflector or lens to provide an electronically agile beam.

This paper considers antennas with component beams having a 0.5° half power beamwidth. Depending on the beam spacings, this beamwidth implies approximately 700-900 beams within the earth field-of-view (FOV). By utilizing a high performance dielectric lens with component beam clusters, the MBA has considerable flexibility in controlling the secondary pattern characteristics over the entire earth FOV while also permitting high performance adaptive nulling.

2. LEAM FORMING METHODS

Two techniques for the realization of the large MBA are examined: (1) a traditional, *constrained BFN* using seven interlaced switch trees (refer Figure 1) with a seven port variable power combiner (VPC) and phasing network; and (2) a space fed array comprised of precision phase and amplitude control modules at each port - and denoted as a *beam port array* (refer Figure 2). The interlaced switch tree is only used with the constrained BFN. The beam port array achieves the same excitation flexibility with a fundamentally different technique.

Beam Geometry

A hexagonal beam geometry is assumed for both techniques. Figure 3 illustrates the hexagonal geometry and defines the *two beam crossover* and the *triple crossovers* (i.e., three beam crossovers). A fundamental design parameter for either method is the number of beams required. Table 1 illustrates the number of beams within the circular earth FOV

TABLE 1. *Hexagonal Beam Parameters*

Number of Beams	Beam Spacing ¹
7	7.44782°
19	4.13131
37	2.97913
61	2.27156
91	1.86195
127	1.56149
265	1.06397
685	0.64764
769	0.60761
859	0.57291

¹ Assumes earth radius = 8.6°

and their spacing when the earth radius passes through the triple crossover of the hexagonal grid. In order to determine the beamwidths of the component beams, the concept of *minimum gain* for a *switched beam* system is used. The minimum gain of a switched beam system occurs at the *triple crossover point* and is related to the two beam crossover angle as shown in Figure 3. The minimum gain (relative to peak) approximately determines the two beam crossover (relative to peak) and the beamspacing to beamwidth ratio by using a Gaussian beam model. Table 2 illustrates these quantities for a parameter range of interest. The final crossover levels are chosen by *maximizing the minimum gain*.

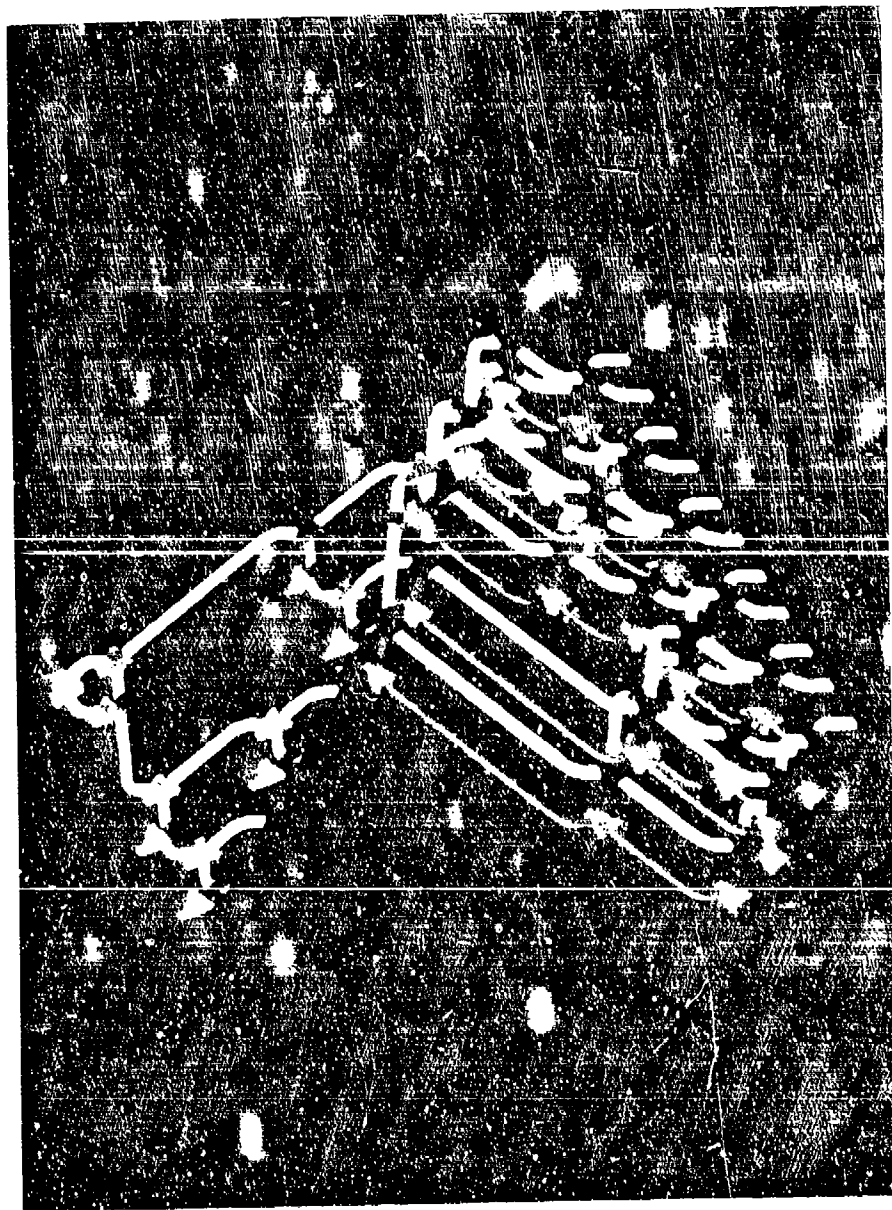


Figure 1. Switch Trees for Constrained BFN

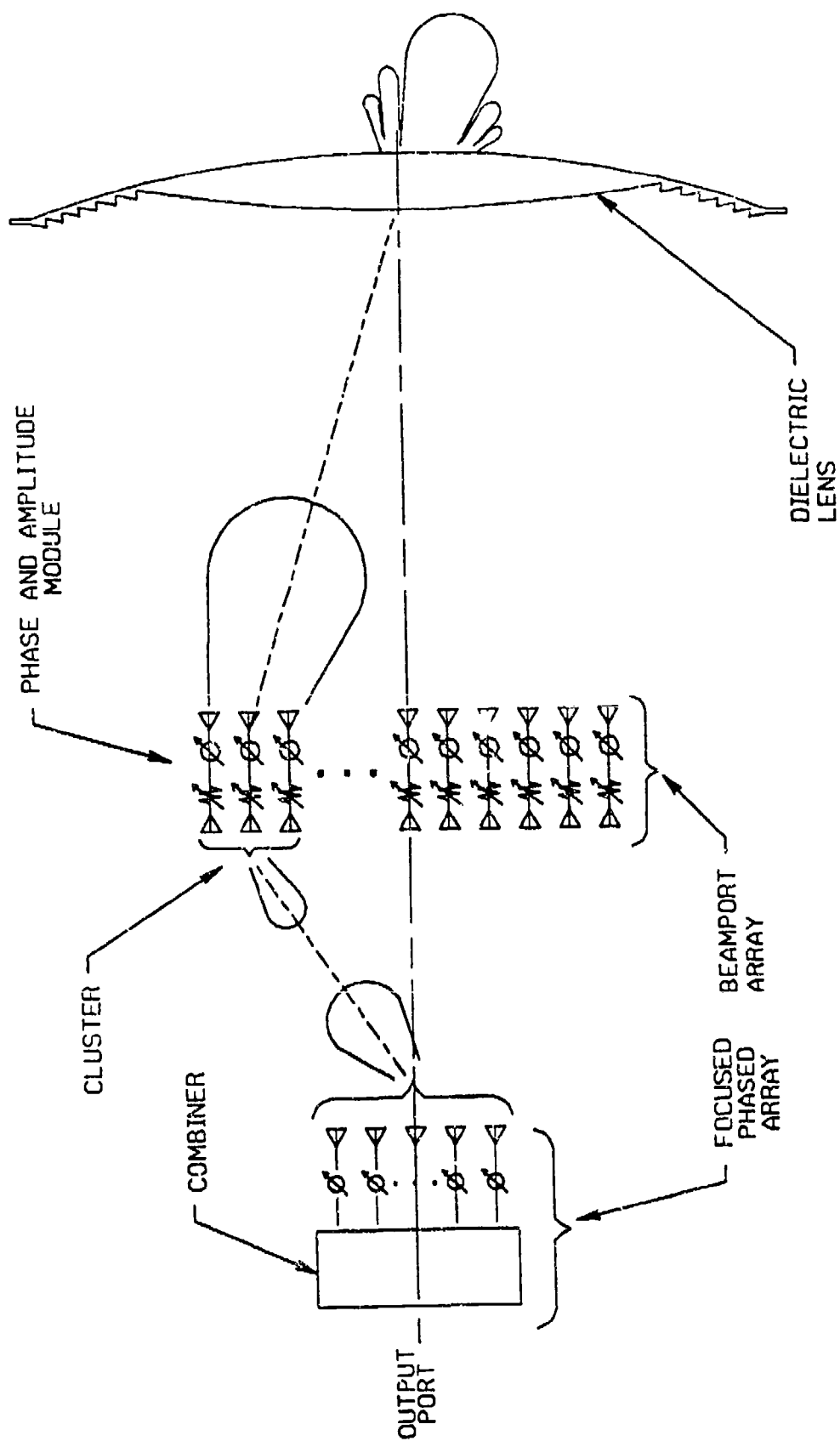


Figure 2. Beam Port Array Concept

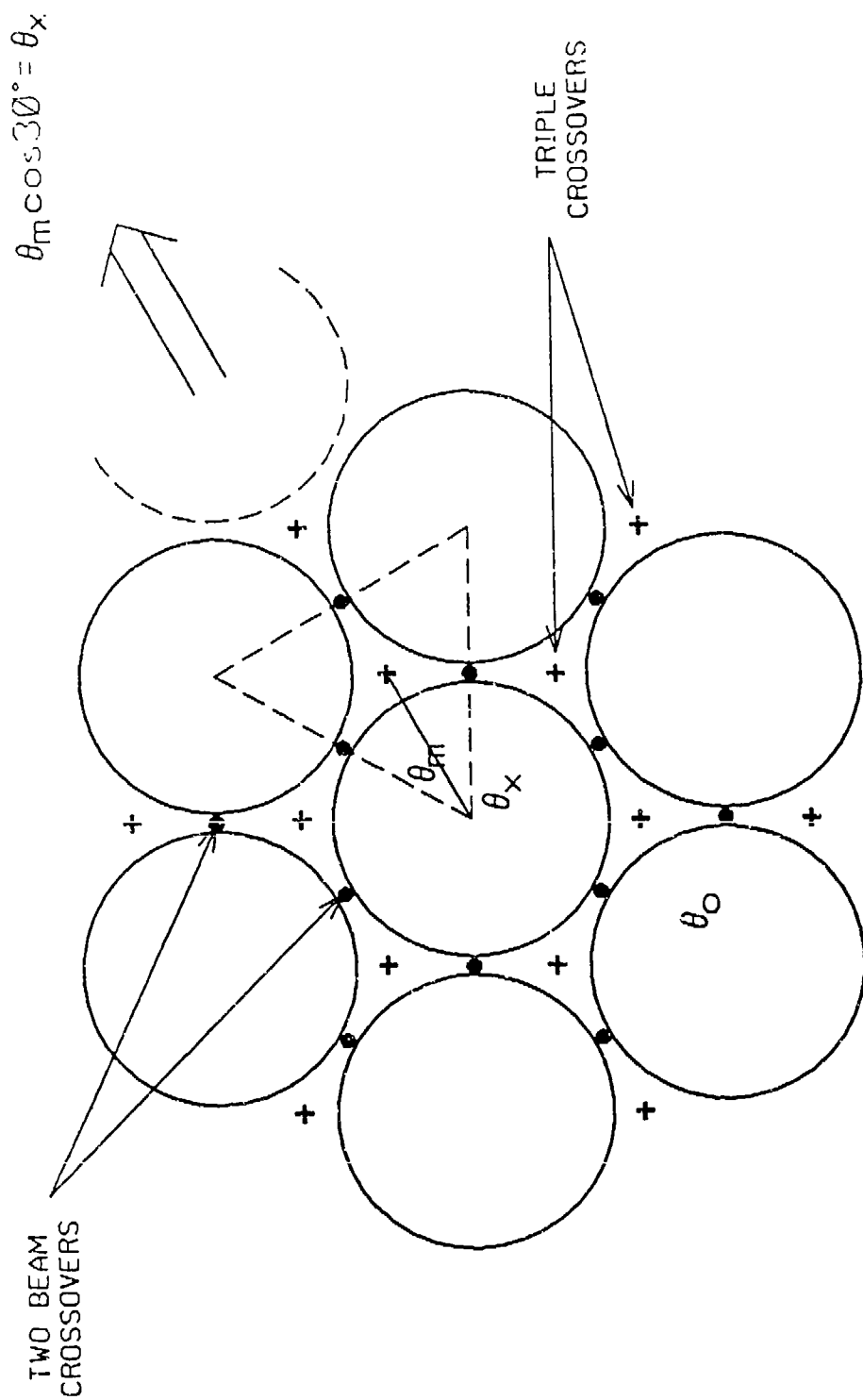


Figure 3. Double and Triple Crossover Points

TABLE 2. *Beam Crossover Parameters*

Two Beam Crossover	Triple Crossover	Beam Spacing/ Beamwidth
-2.25 dB	-3.00 dB	0.866
-3.00	-4.00	1.000
-4.00	-5.33	1.155
-5.00	-6.67	1.291
-5.50	-7.33	1.354
-6.00	-8.00	1.414

A proper determination of the minimum gain requires the consideration of the effects of the finite feed horn spacing on the spillover loss and taper efficiency. Figure 4 illustrates the minimum gain as a function of the two beam crossover level for the case of 685 and 859 beams. The solid and dotted curves are the result of an approximate analysis while the discrete data represent the results of a more complete lens ray tracing analysis using a conical horn pattern with finite wall thickness. The reduced gain of the ray tracing solution in comparison to the approximate result is a consequence of: (1) the nonsymmetric conical horn pattern, (2) a finite feed horn wall thickness, and (3) lens ohmic loss and reflection. The minimum gain derived with either analysis is maximum when the crossover level is approximately 5.5 dB below the peak. This value is lower than the 3 dB which is commonly used. However, note that the gain in the vicinity is slowly varying; for example, a 4 dB crossover results in approximately a 0.4 dB gain reduction. Furthermore, there are frequently added considerations (e.g. nulling or low sidelobe cluster excitations) which can favor the use of higher crossover levels. Nevertheless, a 5.5 dB two beam crossover level is used for both beam forming methods studied.

Constrained BFN

Figure 5 illustrates the port designation pattern of the seven interlaced switch networks in the central region of a large constrained BFN. Each of the switch networks is observed to have a hexagonal periodicity which is related to the fundamental port-to-port spacing. More importantly, this geometry permits *planar switch networks* for each of the seven interlaced networks. This is more easily seen in Figure 6 (also Figure 1), which illustrates the port designations for an 859 port constrained BFN and the planar row and column connections for the number 4 port. The row-to-row spacing of the planar networks is found to be: $\Delta_r = 0.32733 s$, where s is the port-to-port spacing. A typical row-to-row spacing is 0.190 inch and accommodates EHF switch heights and permits the use of standard height waveguide. The port-to-port spacing (typically 1.538 inch) within each planar network easily permits the use of added switches at each port for increased isolation. Figure 7 illustrates one of the row networks for the 859 port feed. Because of the periodicity, each network is similar to all others and only differ by which ports are deleted. For the 859 port feed, the basic building block network is a 16:1 binary divider. If a port of the binary network is not required for a particular row, it is omitted. It is assumed that the number

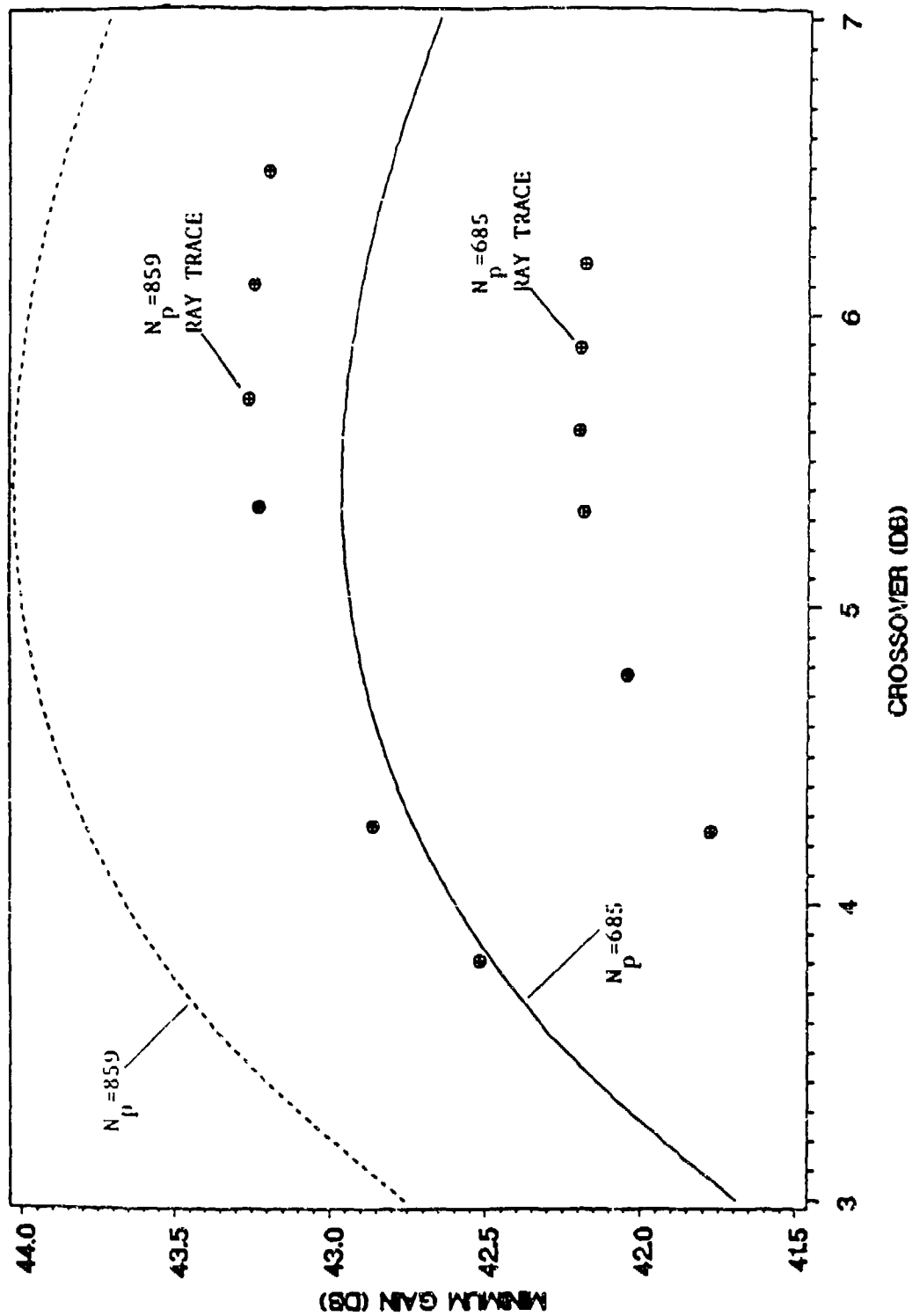
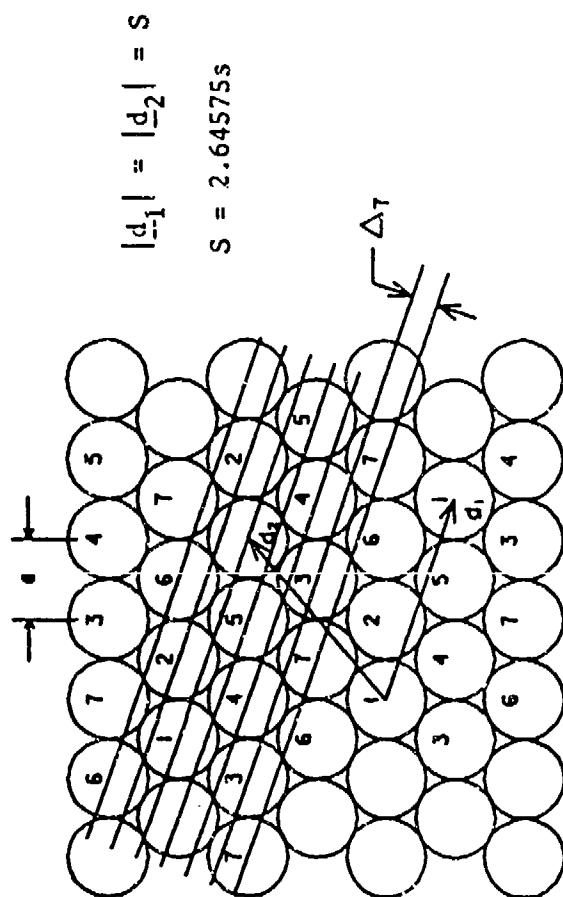


Figure 4. Minimum Gain vs. Crossover Loss



$$|d_1| = |d_2| = S$$

$$S = 2.64575s$$

Figure 5. Seven Port Constrained BFN Layout Pattern

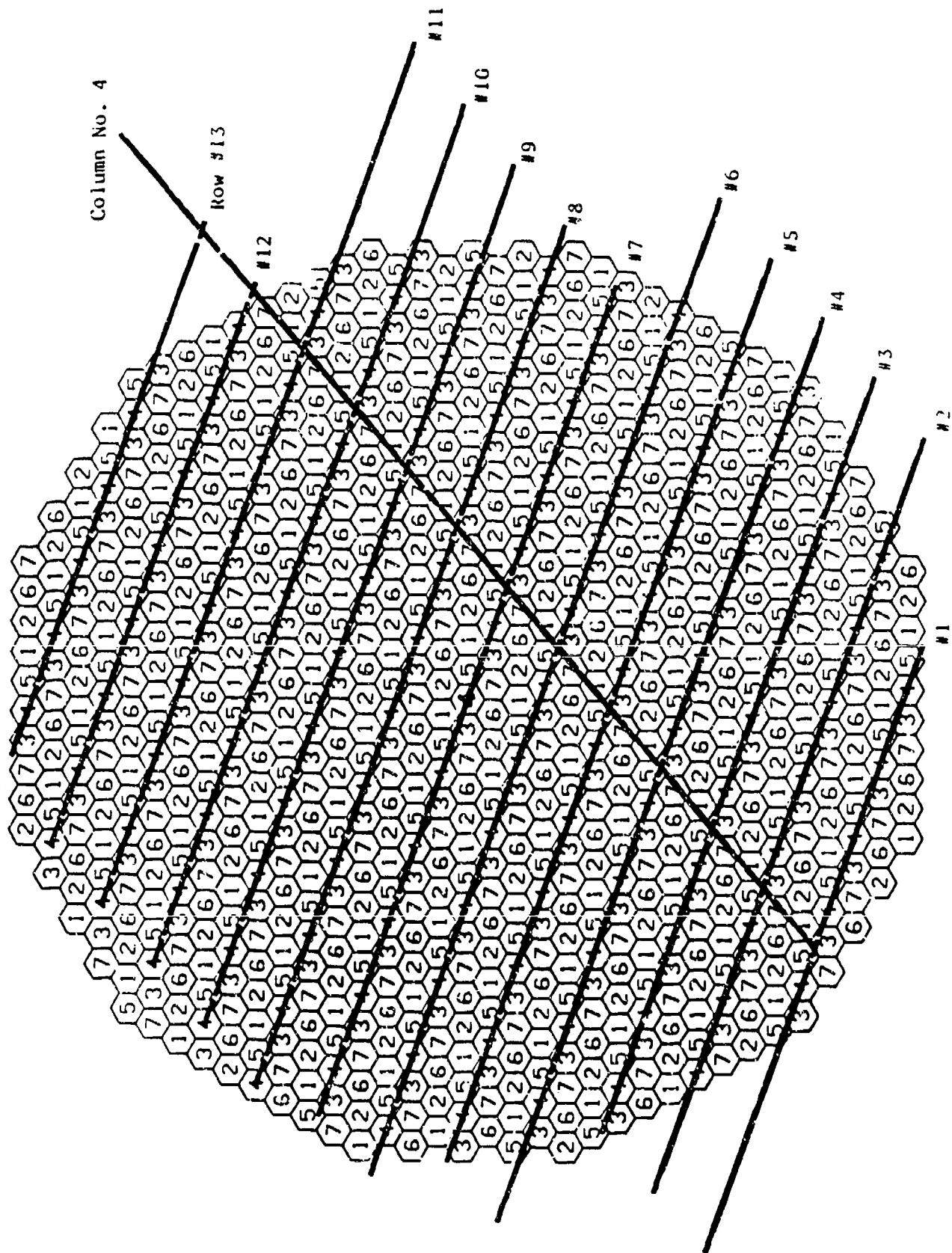


Figure 6. Row and Column Switch Tree Connections for 859 Port MBA

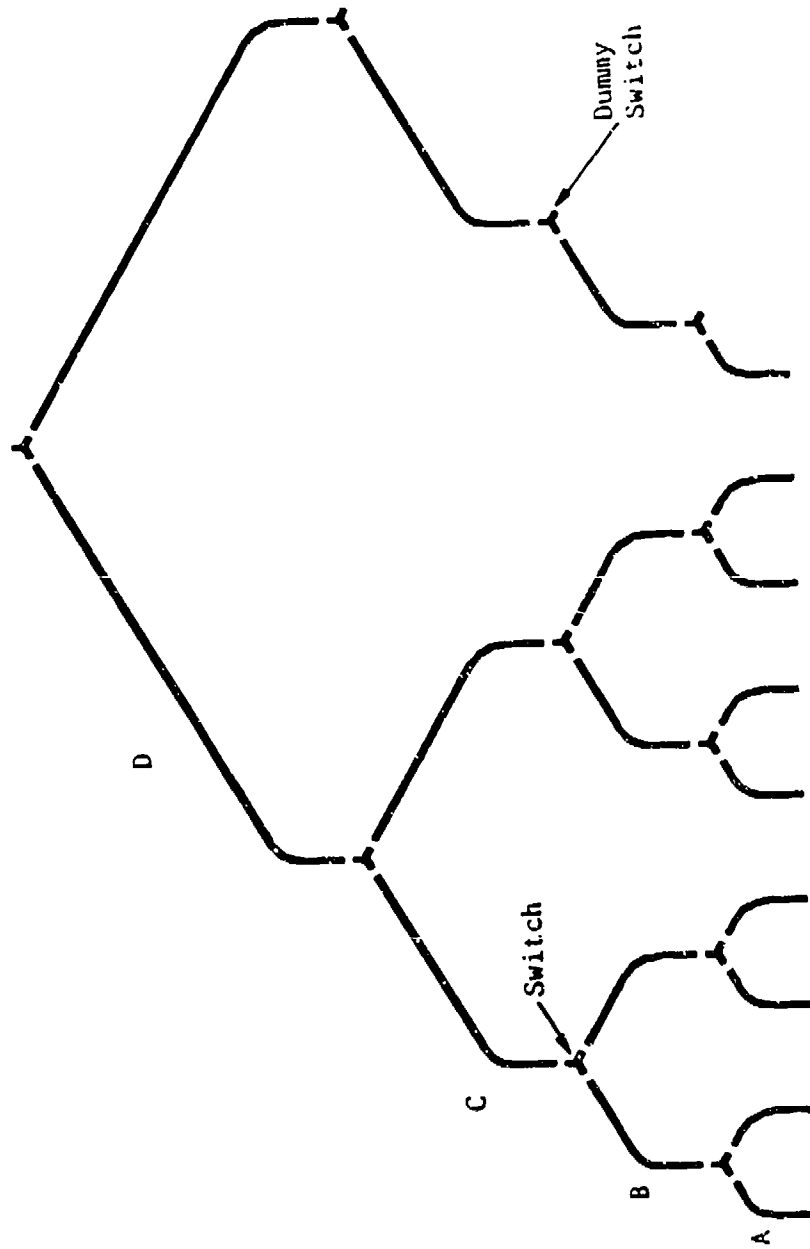


Figure 7. Typical Row Switch Matrix for 859 Port MBA

of switches in any path is a constant in order to facilitate port phase tracking over the frequency and temperature ranges of interest. This requires the use of *dummy switches* as shown in Figure 7. Figure 7 also illustrates that the number of unique part types is small even with a discrete implementation; although, the quantities of each type may be large. Techniques for an *integrated network assembly* are available and include: flangeless switch housings, drop-in switches, or an integrated housing such as shown in Figure 8. Indeed, the fabrication of large BFNs depends on using techniques such as these to render the method practical.

The element of the constrained BFN which ultimately permits the flexibility afforded by feed clusters is the variable power combiner and phasing network as shown in Figure 9a. The network is comprised of two types of components: VPCs and 360° phase shifters. The VPC is realized by utilizing hybrids and phase shifters as shown in Figure 9b. The phase shifters for the VPC need only have a differential electrical length of 90° (for the mixed hybrids) or 180° (for like hybrids). The requirements of the network are normally dictated by the adaptive nulling properties and would indicate phase errors should be less 1° and amplitude errors less than 0.1 dB. These type of errors certainly indicate high performance components.

Beam Port Array

The beam port array (BPA) is a fundamentally different feed from the constrained feed. The BPA illustrated in Figure 2 is space fed by a focused phased array which is capable of creating a localized illumination in the the BPA aperture. The centroid of the illumination can be varied and hence results in beam scanning. In order to provide the same cluster control as the constrained BFN, the BPA uses phase and amplitude modules (PAMs) at each element. The PAMs are realized by using a variable power combiner (VPC) with an internal termination of the isolation port. The phase control is achieved by using 360° phase shifters in contrast to the 90° or 180° phase shifters normally used in VPC networks. The BPA offers a potential advantage for eliminating the waveguide switch networks and the VPC networks of the constrained BFN.

Beam port array concepts have been examined previously by Tang and Winter [1973]. Tang and Winter used a focused phased array in conjunction with a constrained lens in both the feed region and the radiating aperture. In contrast to the present study, Tang and Winter used half wavelength element spacings for both the focused phased array and the feed constrained lens; furthermore, Tang and Winter utilized nonplanar surfaces in order to maximize the illumination efficiencies. This previous antenna design should be contrasted with the present embodiment, where the port-to-port spacing of the BPA is approximately two wavelengths. Furthermore, the goal of the present design is to use *planar interfaces* on either side of the BPA with compensating cluster amplitude and phase weights. Additionally, a phase and amplitude module is utilized at each element instead of a simple constraining transmission line connection. These nontrivial differences are intended ultimately to reduce the system cost.

Figure 10 illustrates a single phase and amplitude module utilizing ferrite components and includes the feed horns and a circular polarizer. Figure 11 illustrates a 37 port subarray of these phase and amplitude modules using planar interfaces and indicates the apparent simplicity of the method.

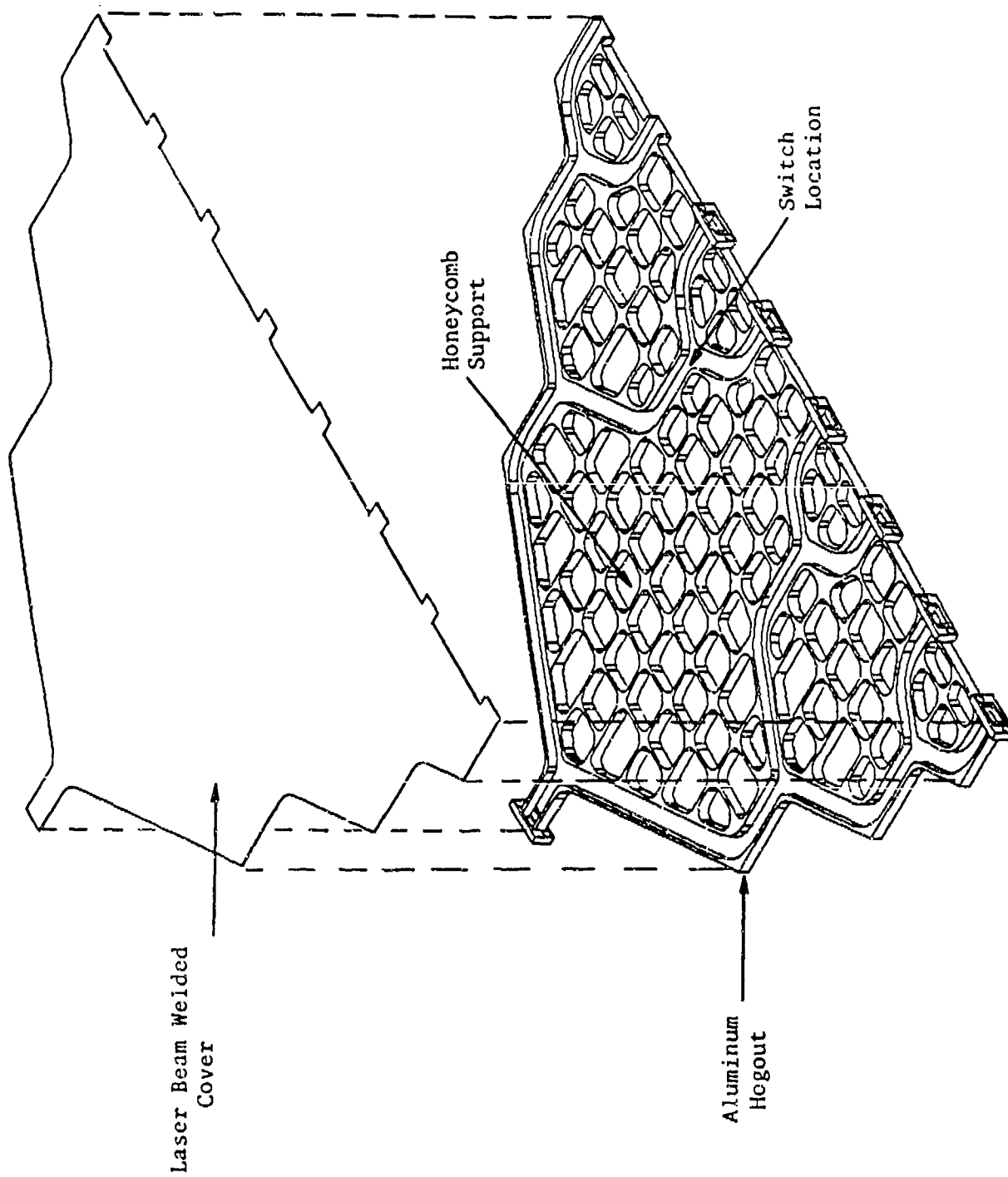
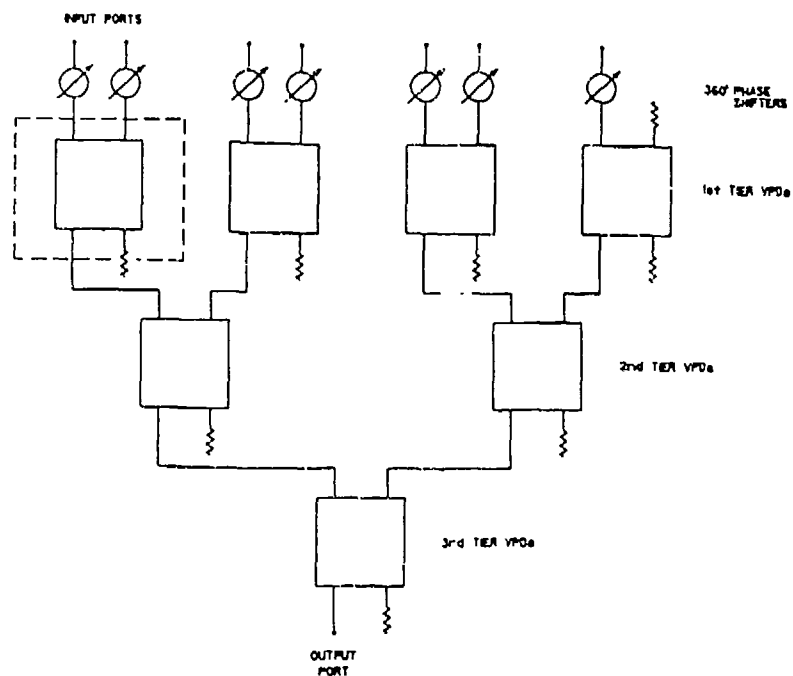
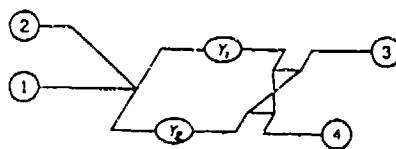


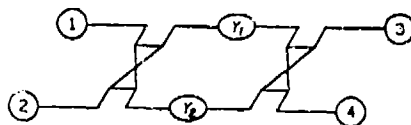
Figure 8. Integrated Planar Switch Matrix



(a) Network Schematic



(a) MIXED HYBIROS



(b) LIKE HYBIROS

(b) Variable Power Combiner Configurations

Figure 9. Seven Port Amplitude and Phase Network

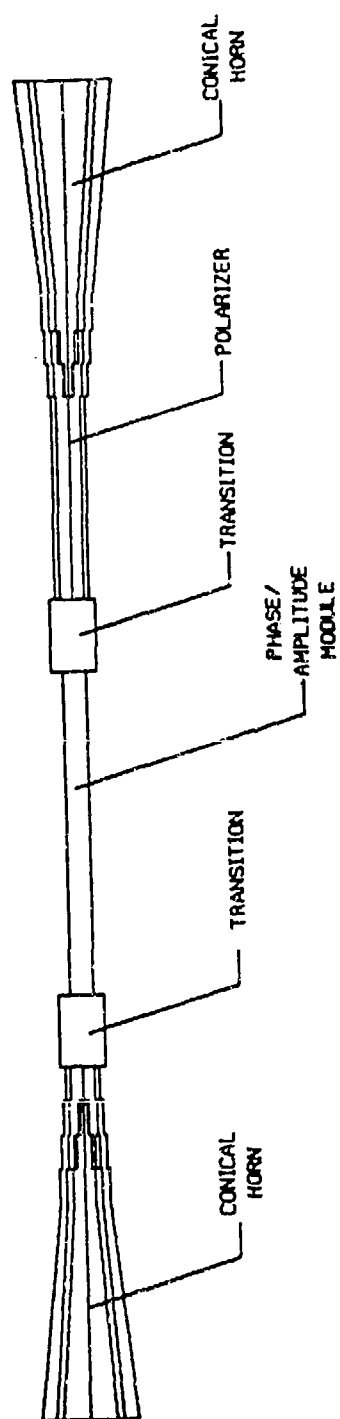


Figure 10. Beam Port Phase and Amplitude Element

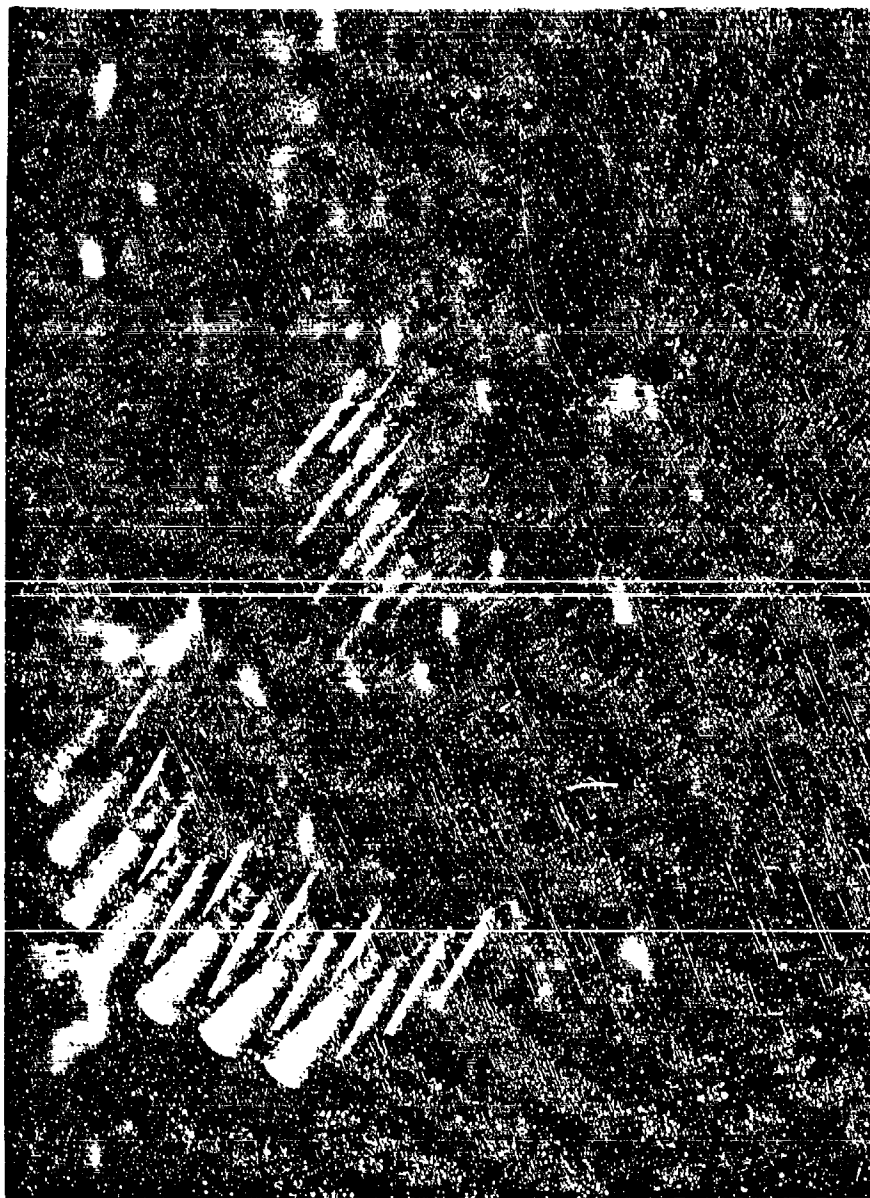


Figure 12. 37 Element Grouping of Phase and Amplitude Modules

3. LENS DESIGN

Several *uniform dielectric lenses* were considered and a variant of the lens originally considered by Shinn [1956] and more recently investigated by Rotman [1983,1984] was selected. This type of lens approximates the performance of an ideal *thin lens* which exhibits the property that the *coma error* is small in comparison to the *spherical error* [Cheston and Shinn, 1952]. The lens considered by Shinn has the property that the outer surface is spherical with the center coinciding with the focal point. Referring to Figure 12, the lens is designed by using Snell's law at the spherical surface (surface 2) and using the equipath condition for all rays. The more difficult problem is to determine the zone step locations. This is accomplished by the simultaneous solution of two coupled nonlinear equations.

A more generalized lens is realized by permitting the outer surface radius to assume other values. This generalized lens provides designs which are quite similar to more classical lenses such as the meniscus lens and the plano-convex lens. The generalized lens design is an exact duplication of the hyperbolic lens when the radius approaches infinity. Figure 13 illustrates the lens contours of several lenses considered in this study. It is clear that the lens approaches a thin spherical lens as the number of zone steps increases. However, an increase of the number of zone steps results in a decrease of the bandwidth of the lens since the zoning is exact only at a single frequency. For the present study, seven zones are normally used. An added benefit of zoning the lens is a decrease in the lens weight. Table 3 illustrates the weight and on axis thickness of a 34 inch generalized lens for various number of zones. A lens with seven zones is approximately a third of the unzoned weight and represents a significant weight advantage.

TABLE 3. *Generalized Lens Properties vs. Number of Zones*

Number of Zones	On Axis Thickness	Weight
1	5.353 in	98.34 lbs
2	4.906	83.02
3	4.459	70.94
4	4.013	60.11
5	3.566	50.54
6	3.119	42.25
7	2.673	35.26
8	2.226	29.59
9	1.779	25.26
10	1.333	22.28

$D=34.0$ in., $f/D=1.5$, Minimum Thickness= 0.375 in.,
 $R_o=0.85f$, Rexolite dielectric

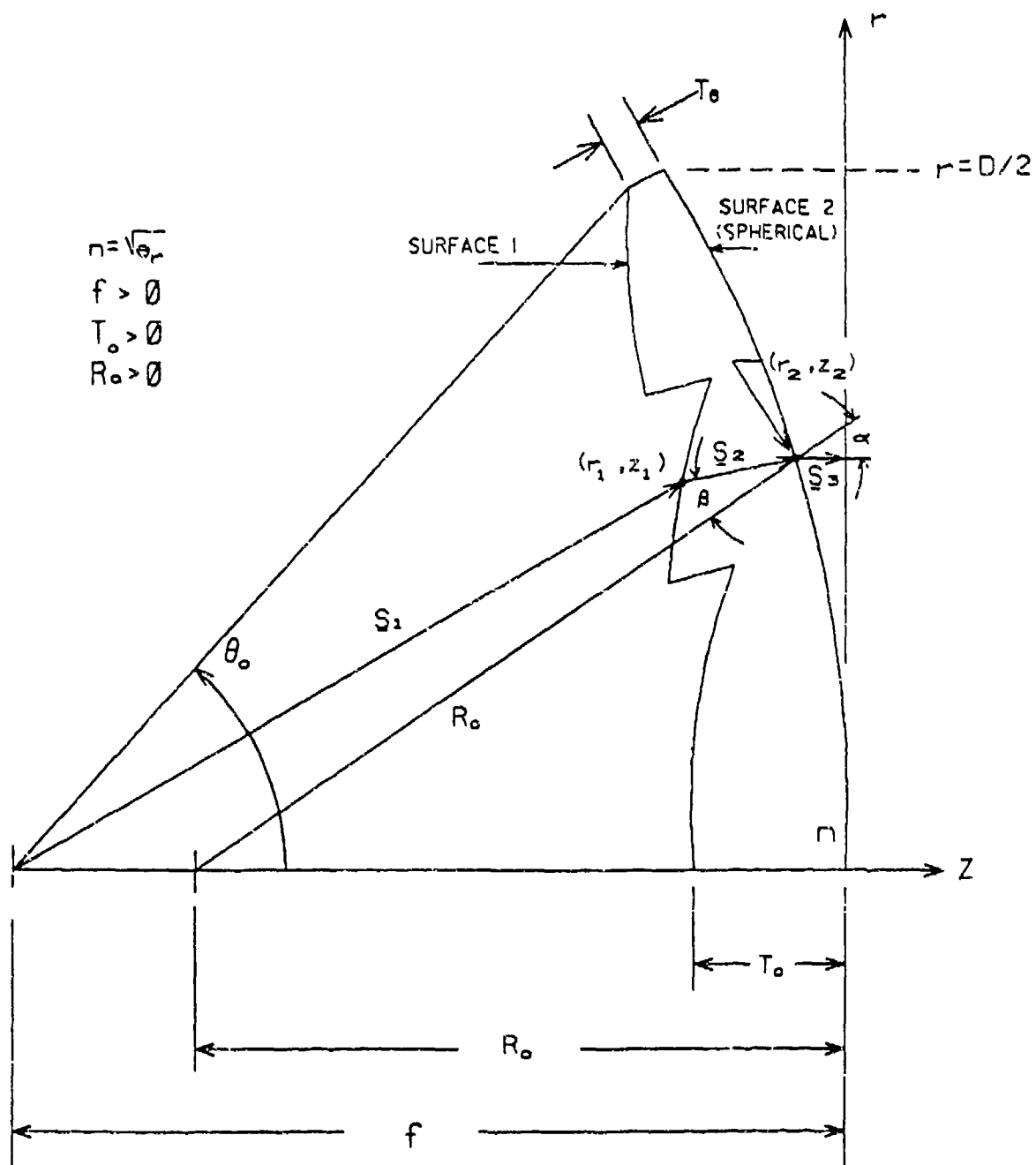


Figure 12. Lens Design Geometry

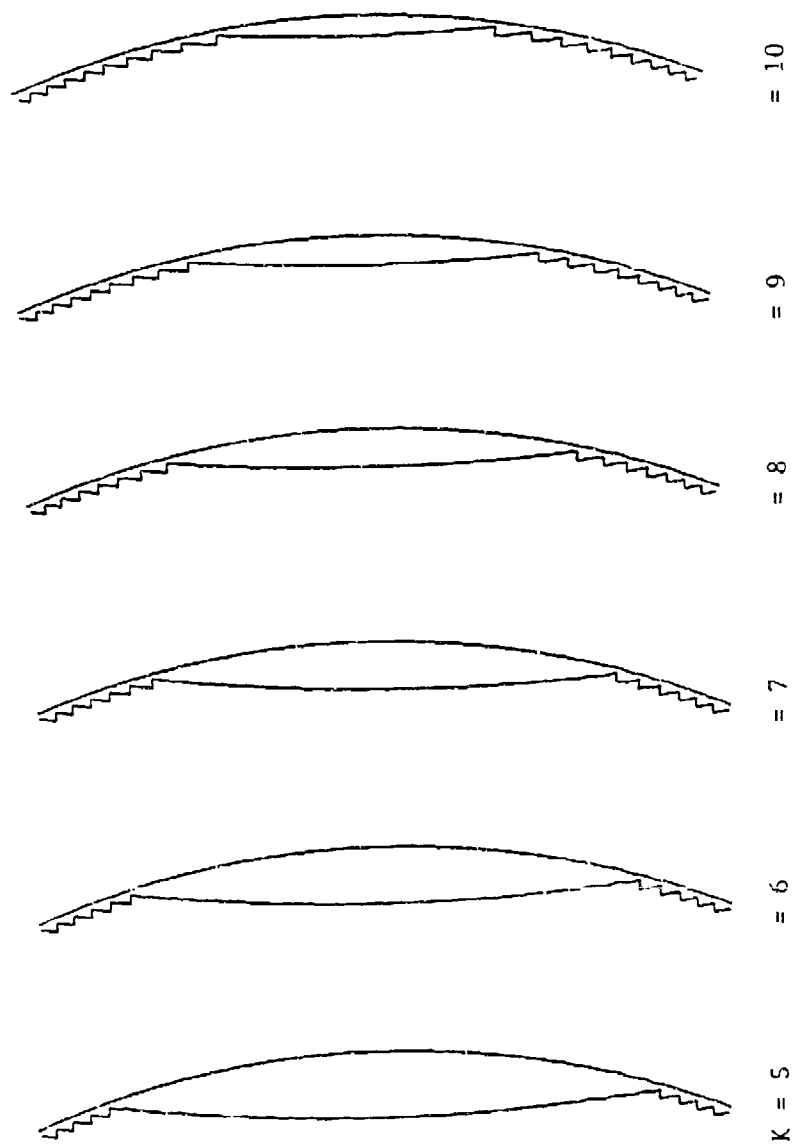


Figure 13. Generalized Lens Profile vs. Number of Zones K

4. PERFORMANCE ANALYSIS

Analysis Method

The analysis of the radiation properties of a large MBA involves: the prediction of a feed pattern, ray tracing from each feed through a large zoned dielectric lens to a planar aperture, and computation of the far field pattern using an FFT algorithm. Perhaps the most important element of the analysis is the ray tracing analysis. Referring to Figure 14, a projected aperture plane is defined with a square cell periodic grid. The ray tracing solution seeks the intercepts on both the inner and outer lens surfaces such that Snell's law is obeyed with the ray passing through the selected grid coordinates and the source point. This solution involves the simultaneous solution of two coupled nonlinear equations. The phase of the ray follows directly from : (1) the total path length with a consideration of the dielectric media along ray, and (2) the phase of the feed pattern. The amplitude is evaluated by the absolute feed pattern magnitude in the direction of the ray path and the proper treatment of the divergence factors [Lee, et. al., 1982; Deschamps, 1972] at each interface which includes the transformation of the two principal radii of curvature of the wavefront as it crosses dielectric boundaries. A scalar average of the Fresnel transmission coefficients for TE and TM polarizations is included at each interface. The loss tangent of the dielectric is included to properly account for dissipation for rays within the lens.

Feed Clusters

The use of a cluster of feeds with appropriate amplitude and phase excitations permits considerable flexibility by allowing: (1) alternate feed loci, (2) tailoring the secondary pattern characteristics such as sidelobes, and (3) adaptive nulling.

Three feed loci are considered: (1) a spherical surface having a radius equal to the lens focal length, (2) a compromise focal surface, and (3) a planar surface. A goal of the present study is to utilize planar surfaces where possible to ease interface difficulties associated with feed loci having a finite curvature. Figure 15 illustrates *single feed* patterns for a planar feed locus and a compromise feed locus at the edge of earth coverage using a 32.6 inch lens. (The feeds are pointed toward the lens apex.) The defocusing of the planar locus is quite evident while the compromise focal surface produces well focused patterns. The gain of the component beam on a planar focal surface is -1.1 dB below the compromise locus. (An additional gain reduction of 0.52 dB is incurred when the feeds are directed parallel with to the lens axis.) In order to overcome the planar surface defocusing, the performance of this same antenna with seven element hexagonal clusters is considered. Figure 16a illustrates the far field patterns at 8.6° scan for a seven element feed with a uniform amplitude and phase illumination. Figure 16b illustrates this same case except that the feed phases have been adjusted for cophased component beams. The compensation provided by the cluster is obvious.

Figure 17 illustrates the far field patterns of this cophased, seven element cluster with the outer six elements attenuated relative to the center element by various amounts. Sidelobe levels of better than -30 dB are achieved when the edge elements are approximately -12 dB relative to the center element.

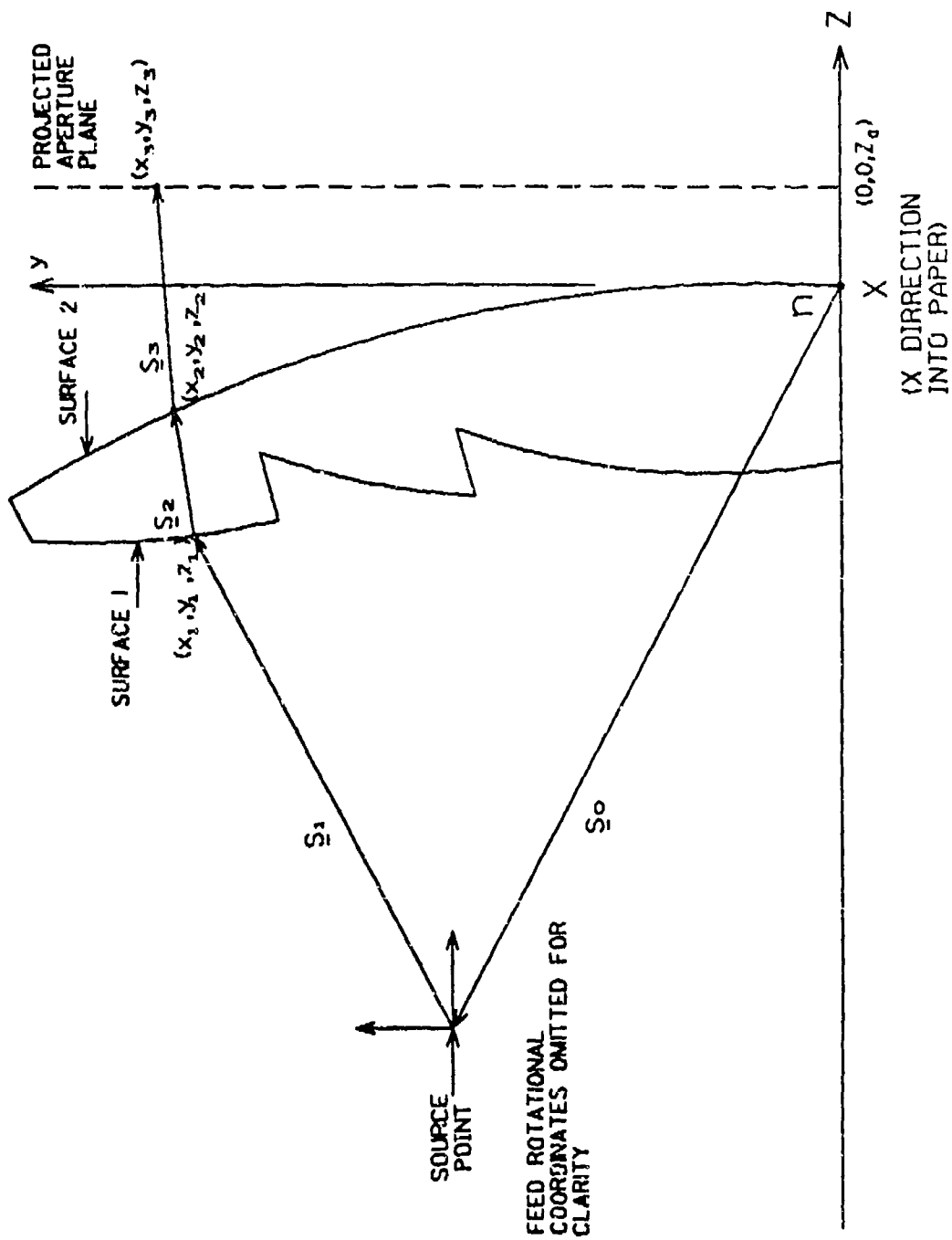
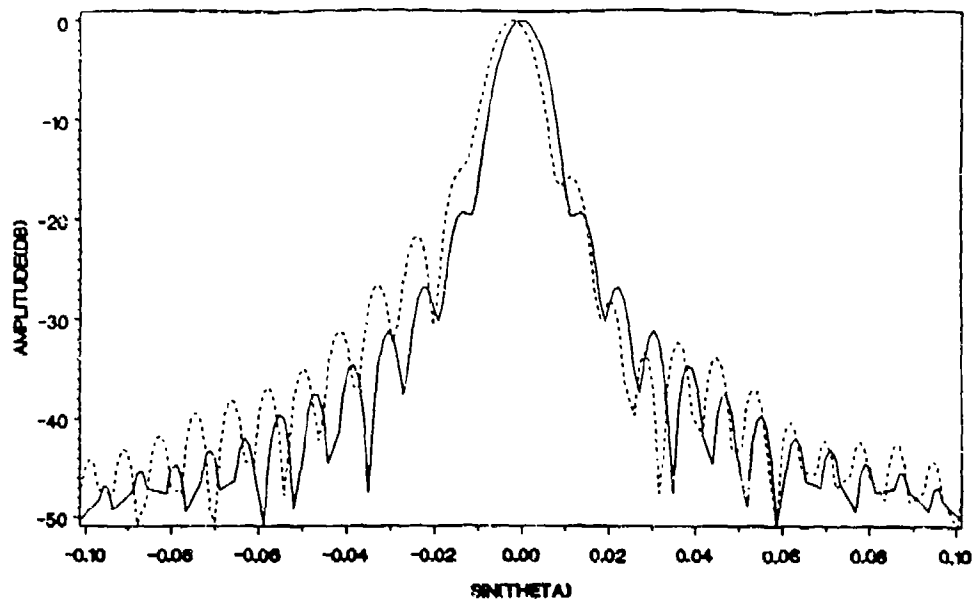
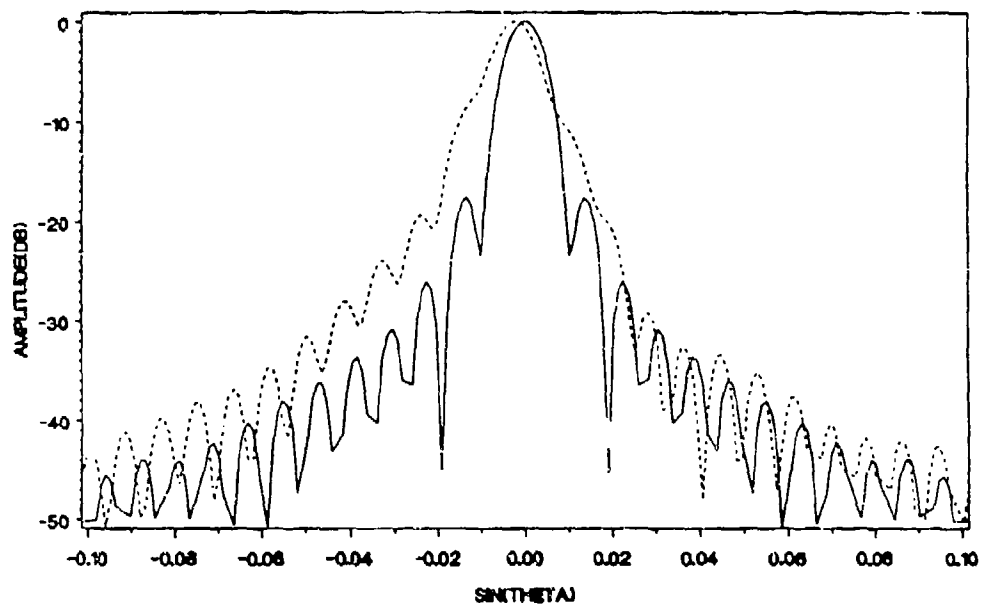


Figure 14. Ray Trace Lens Geometry

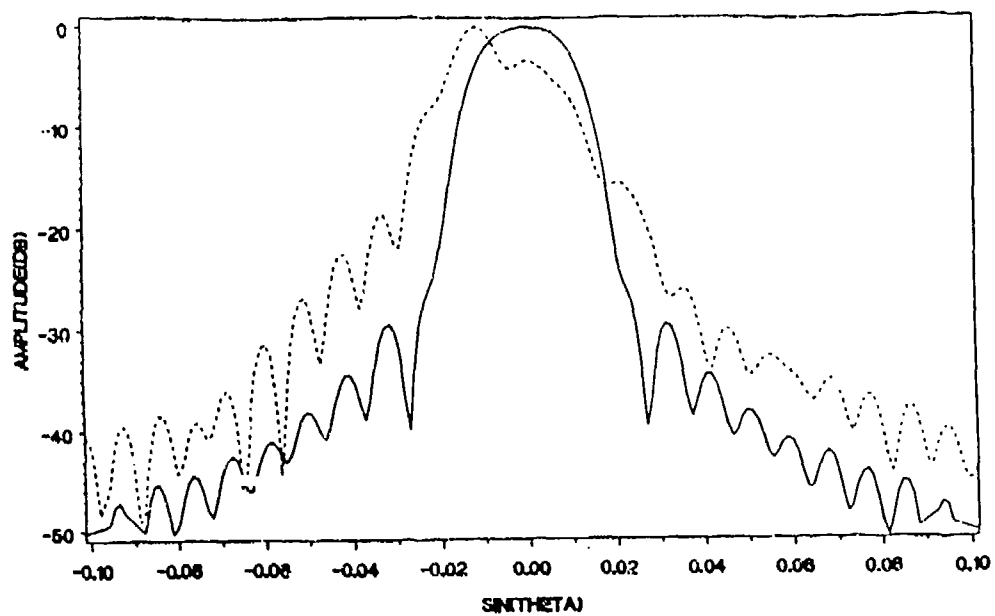


(a) Compromise Locus

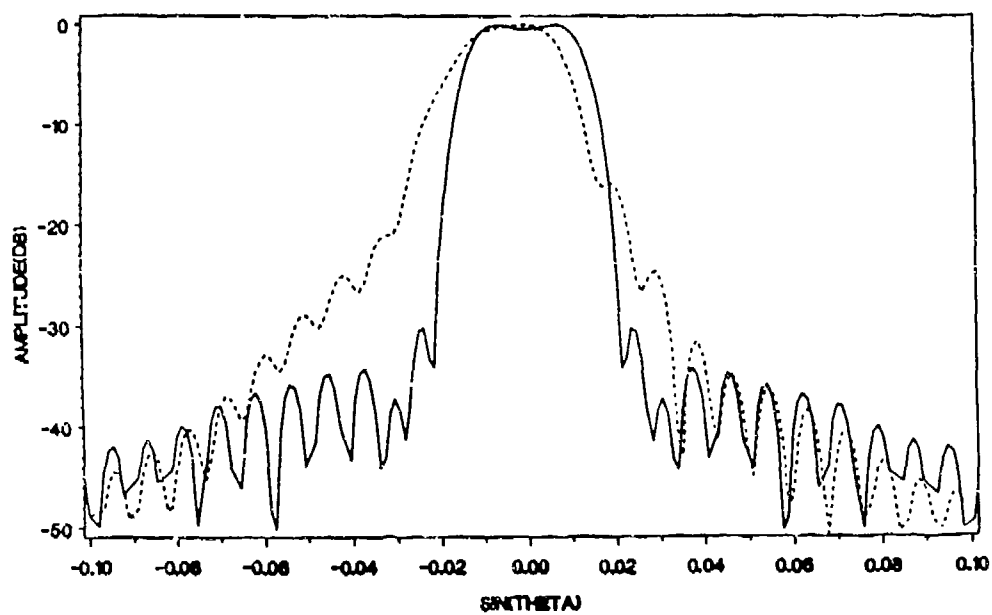


(b) Planar Locus

Figure 15. Feed Locus Examination



(a) No Phase Compensation



(b) Phase Compensation

Figure 16. Lens Patterns of a Uniform Amplitude Seven Element Cluster

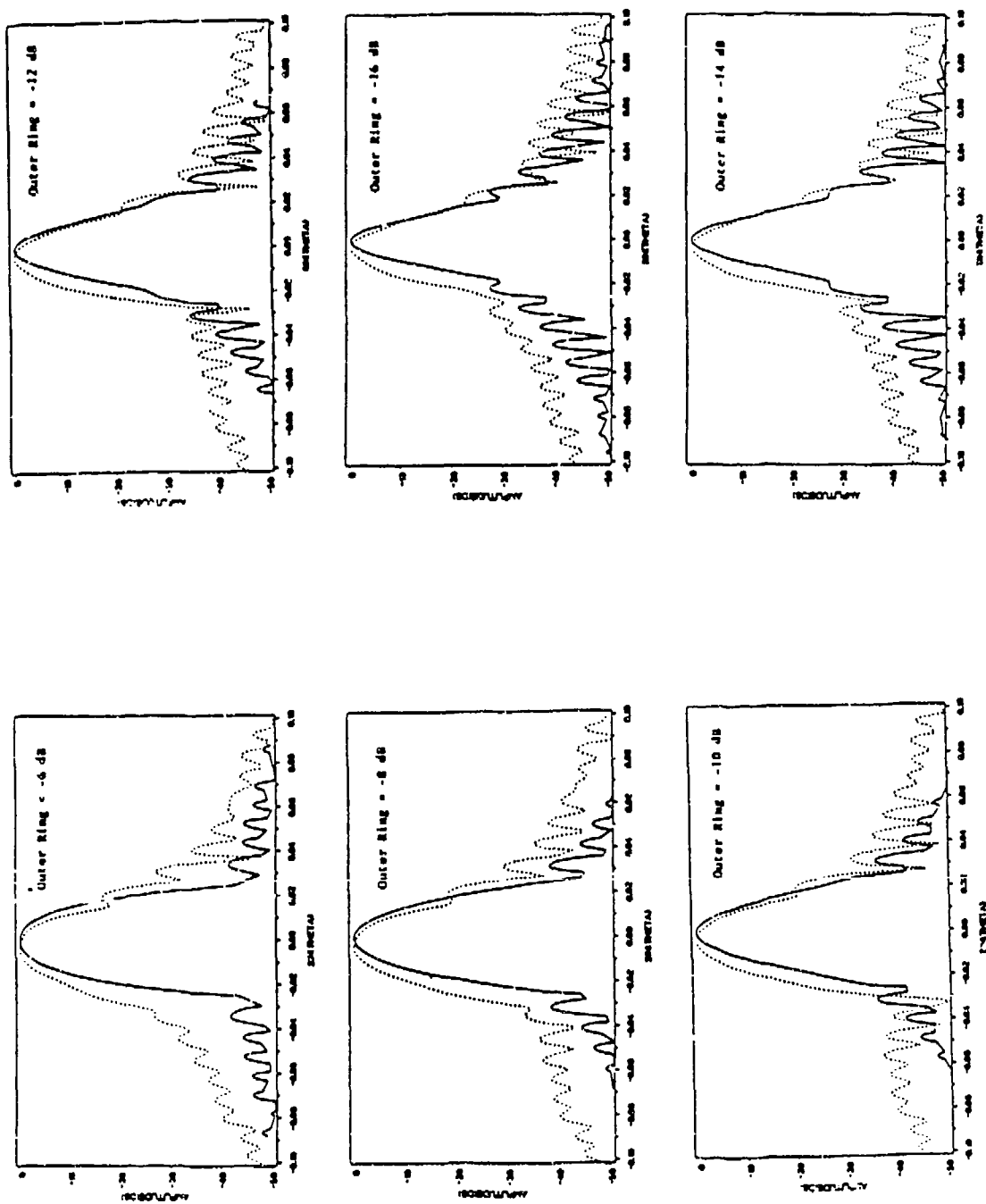


Figure 17. Lens Patterns of a Tapered Seven Element Cluster

Feed cluster control can also be used for adaptive nulling. The steady state weights in the presence of jammers are related to the quiescent (i.e. without jammers) weights via the channel covariance matrix [Fenn, 1982]. The eigenvectors (or eigenbeams) and eigenvalues of the covariance matrix are useful in interpreting the adaptive algorithm. Only the larger eigenvalues will produce adapted weights which vary significantly from the quiescent weights. The algorithm removes the projections of the interfering source eigenbeams from the quiescent weight vector, which results in a null in the antenna angular response in the direction of the interference. Alternately, the adaptive process may be viewed as forming beams in the direction of the jammers and subtracting the eigenbeams from the quiescent beam to form a null in the jammer direction. Figure 18 illustrates this process for the a large MBA with a seven element hexagonal cluster using a 34 inch diameter lens at 44.5 GHz. A user is assumed at the origin while a jammer is assumed at -0.2887° . The quiescent beam, the dominant eigenbeam (i.e. the largest eigenvalue), and the adapted beam are shown. It is clear that the dominant eigenbeam has a maximum in the direction of the jammer and that the adapted beam has a well formed null in the direction of the jammer.

5. BFN COMPARISON

The constrained BFN and the beam port array are compared with a number of considerations, including: (1) weight and size, (2) gain and noise temperature, (3) power requirements, (4) complexity and cost, (5) adaptive nulling, (6) reliability, and (7) robustness.

Weight and Size / Power Requirements

The weight of a satellite based antenna is one of its most critical properties, but even a lightweight antenna can have hidden weight penalties associated with the generation of power or the support structure of a large antenna. For this reason it is important to consider these parameters together.

Table 4 illustrates the estimated weight, power, and size of an 859 port antenna system.

TABLE 4. *Estimated Weight, Power, and Size of 859 Port MBA¹*

Approach	RF Weight	Elect. Weight	Total Power	Added System Wt ²	Total Weight	Size
Constrained	119.56	75.55	29.34	20.54	215.65	33 X 73
Beam Port	76.36	11.42	219.30	153.50	241.28	33 X 73

¹ Weight (lbs), Power (Watts), Size (inches)

² Weight attributed to prime power source at 0.7 lb/Watt

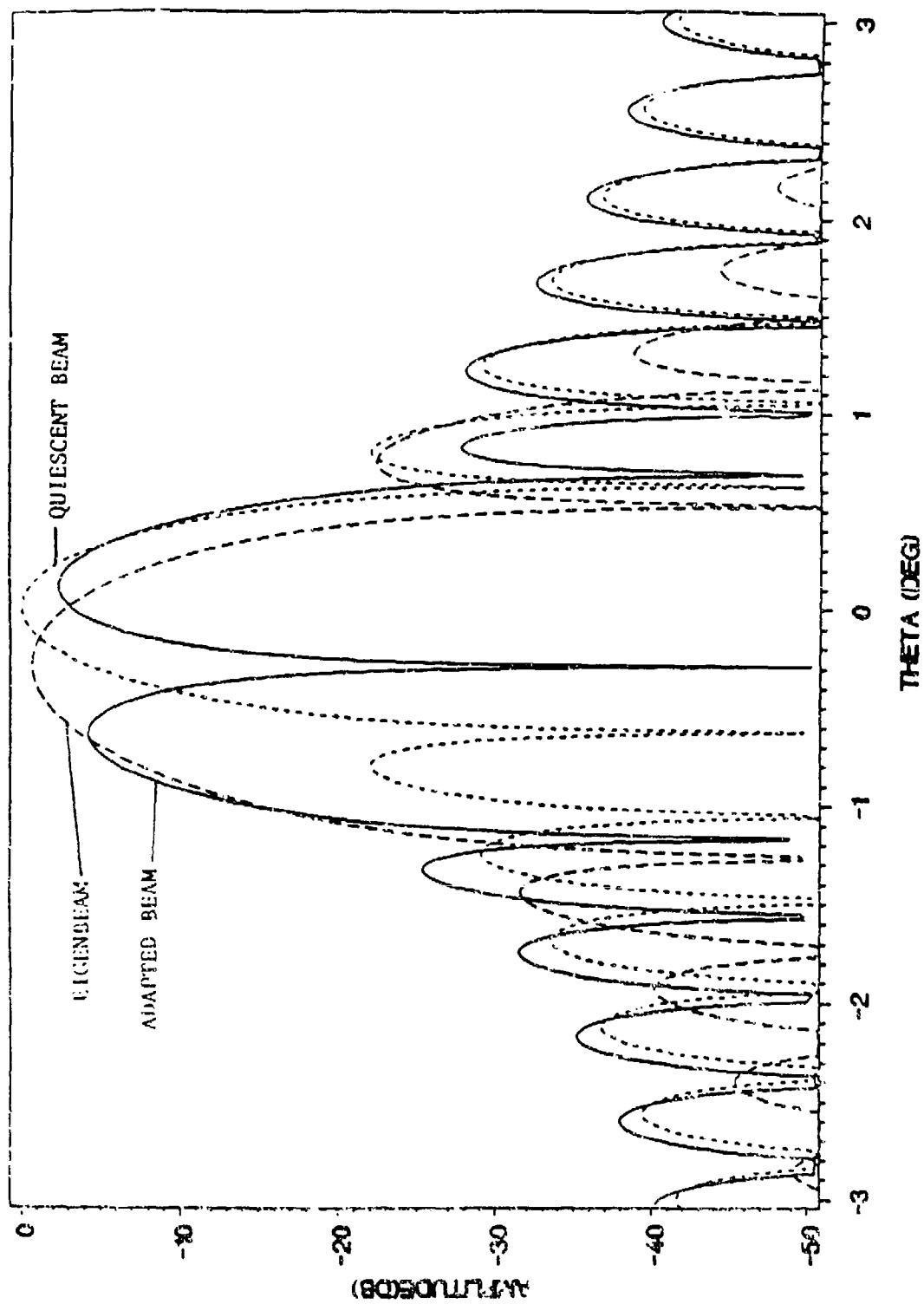


Figure 18. Adaptive Nulling with a Single Lens MBA

These estimates are based on a comprehensive examination of these antenna systems utilizing advanced state-of-the-art techniques. For the *constrained BFN* the estimate includes: waveguide, horns, polarizers, transitions, active switches, dummy switches, isolation switches, flanges, a 32.6 inch Rexolite dielectric lens, a seven port VPC network with 360° phase shifters, support structure, switch and VPC drivers (with full standby redundancy), central electronics (with full redundancy), and electronic enclosure weight (including EMP shielding). For the *beam port array* the estimate includes: horns, polarizers, transitions, phase and amplitude modules, a 32.6 inch Rexolite dielectric lens, a 511 element focused phased array feed, support structure, phase and amplitude module electronic drivers (with full redundancy), phased array drivers (with full redundancy), central electronics (with full redundancy), and electronic enclosure weight (including EMP shielding). The total hardware weight is 195 lbs for the constrained BFN and only 88 lbs for the beam port array. Hence, there initially appears to be a significant weight savings for the beam port concept. However, the power requirements of the beam port array are considerable in comparison to the constrained BFN, primarily due to the power associated with the phased array feed. This results in an increase in the estimated satellite weight by approximately 0.7 lb per Watt of the required power [Cummings, 1987]. When this *total system weight* is considered, the total hardware weight is 216 lbs for the constrained BFN and 241 lbs for the beam port array - a *different conclusion than originally anticipated*. This conclusion may vary dramatically if the possibility of solid state components are considered, however, the impact on the power supplies will still be significant.

Gain / Noise Temperature

The two antenna systems are identical in the selection of the dielectric lens, feed horns, and feed locus. Hence, the antenna gain relative to this radiating portion of the antenna does not distinguish the antennas. However, the insertion losses of the remaining beam forming network provide one basis for a quantitative tradeoff. The estimated insertion loss of the constrained BFN is 5.38 dB. For the beam port array, the estimated insertion loss is 9.4 dB near broadside and 10.6 dB at the edge of scan. (A large portion of the loss is associated with the coupling of the beam port array to the focused phased array — which is aggravated by the size of the beam port horn elements.) An alternative beam port array with a single horn feed was also examined — but exhibits an insertion loss of 22.1 dB at broadside and 25.5 dB at the edge of scan.

The use of low noise amplifiers (LNAs) can also be considered. The natural location for the LNAs for the constrained BFN is at the input to the seven channel VPC network and results in a loss of 1.93 dB ahead of the amplification. For either of the beam port concepts, the LNAs are considered ahead of the phase and amplitude control modules with only a loss of 0.2 dB ahead of the amplification. The properties of the LNA are assumed to be: 10 dB gain per stage and a 4 dB noise figure. Table 5 illustrates the noise temperature of the antenna systems based on the beam forming network loss and neglecting the antenna temperature. The system noise temperature is shown as a function of the number of LNA gain stages. Clearly, the beam port concept relies on the use of LNAs to achieve an acceptable result and is contrasted with the constrained BFN which can be used without LNAs. Note that single stage amplifiers will suffice for either the constrained BFN or the beam port array with the phased array feed. However, the beam port array

with a horn feed requires a two or three stage amplifier for satisfactory operation. (These choices are indicated in Table 5.) The prospects for the development of a multistage LNA at EHF with precise amplitude and phase tracking over the required temperature and frequency band are remote in the near future.

TABLE 5. *Noise Temperature Tradeoff*

Antenna System	No. Gain Stages	Temp ($^{\circ}$ K) ¹
Constrained BFN	0	719.9
	1	900.0 ←
	2	851.5
	3	846.6
BPA (Phased Array Feed)	0	3039.6
	1	775.4 ←
	2	503.0
	3	475.8
BPA (Horn Feed)	0	102605.9
	1	10732.0
	2	1498.7
	3	575.4 ←
	4	483.0

¹ ← indicates selected number of gain stages

A measure frequently used for defining the receiving properties of a system is the gain to temperature ratio, G/T , where T is the effective system temperature at some reference point and G is the gain prior to this reference. A nominal gain when a cluster is excited is 44 dB for the 859 port case when the outer ring is -10 dB relative to the center and a planar surface is used. Thus typical values of G/T are: 14.5 dB for the constrained BFN, 15.1 dB for the beam port array with a phased array feed. Without the use of LNAs, the resulting G/T ratios are 15.5 dB and 9.2 dB for the constrained BFN and beam port array, respectively.

Complexity / Cost

While the cost of any future system is subjective at best, the complexity is quite objective.

The 859 port *constrained BFN* has 1985 switches (1711 active switches including isolation switches), 19 phase shifters associated with the VPC amplitude and phasing network, and 7 LNAs at the input to the 7 port VPC network. This results in a total of 1730 control functions.

The 859 port *beam port array* has 1718 high precision phase shifters associated with the phase and amplitude control modules, 511 modest precision phase shifters associated with the focused phased array, and 859 bias switches for on/off control of the LNAs for added port isolation. This results in a total of 3088 control functions.

In addition, to the increased number of controls for the beam port array concept, the type of controls for this approach are also considerably more complex (i.e. an 8 bit phase shifter driver in comparison to a switch driver).

Assuming the hardware cost is approximately proportional to the number of controls, the cost of the beam port array is at least twice that of the constrained BFN. In a practical consideration, the cost differential could be even greater because of the added complexity of the phase shifters compared to the switches.

Adaptive Nulling

Adaptive nulling properties of the constrained BFN versus the beam port antenna are identical when the losses of the networks are not considered. However, there can be a significant difference in the implementation of the adaptive algorithm as well as differences due to the configuration of and the practical errors of the components.

For a seven port nulling algorithm, the constrained BFN requires the control of seven 360° phase shifters and six VPCs (another 12 phase shifters) - a total of 19 controls. The beam port array requires the control of 14 phase shifters and hence does offer some advantage.

The means of extracting an error signal are significantly different. Typically, directional couplers are used at the input of the VPC nulling network to extract the channel samples for a constrained BFN. The beam port array does not permit this method of obtaining a channel sample. Instead a dither of the desired channel can be used to modulate specific ports in amplitude and phase. The inherent simplicity of the dither method appears advantageous compared with the more complex structure of the VPC network used with a constrained BFN.

Reliability

The complexity of the large MBA is considerable in comparison to even the most complex MBA by today's standards. Hence, the issue of reliability is an important concern for either approach. Total standby redundancy has been assumed for all electronics for either approach — however, triple redundancy may be required for key components.

An interesting aspect associated with the reliability of a beam for a very high gain MBA is that finite beam failures can be tolerable. Since the antenna has a large number of beams with very close spacings, it may be possible to repoint the satellite only slightly and utilize other operational beams with only a slight degradation of antenna performance.

Robustness

In the present application, robustness refers to the ability of the antenna system to be designed for a wide variety of applications. In this sense, both antenna systems under consideration are quite robust. However, the beam port antenna allows additional robustness with regard to reconfiguration of the beam patterns since the central electronics can be sufficiently general as to allow increasing the cluster size and shape beyond a seven port hexagonal layout. This is not possible with the constrained BFN.

6. CONCLUSIONS

This paper has examined the general goal of achieving practical designs for large multiple beam antennas for EHF MILSATCOM. The two basic antennas under consideration are: a constrained BFN and a space feed antenna. The constrained BFN antenna represents a more traditional antenna concept using mature ferrite waveguide switches and waveguide feed networks. The beam port antenna represents an approach which potentially can offer weight and layout advantages. However, recent technology has made the constrained BFN attractive, even for a large MBA. In fact, a constrained BFN with several hundred feeds and seven port feed clusters is attainable with today's technology; and in particular, in terms of complexity, weight, and power consumption, a large constrained BFN is competitive with less capable concepts presently under consideration for EHF MILSATCOM.

The beam port concept with a focused phased array feed can offer equally acceptable microwave performance with less microwave hardware. However, with presently available electronic designs, the power consumption of the ferrite scanned phased array tends to make this approach less attractive than the constrained feed. With substantial advances in EHF LNA technology, the phased array could be replaced with a single horn, or the ferrite array replaced with a solid state MMIC array design that consumes less power. Given these advances, which may result from the current industry wide emphasis on MMIC, the space feed could offer significant advantages in terms of reduced weight and increased beam forming flexibility.

ACKNOWLEDGMENT

This work was performed under the sponsorship of Rome Air Development Center, Electromagnetics Directorate, Hanscom Air Force Base, under contract No. F-19628-86-C-0187 with Mr. John Strom serving as technical monitor.

REFERENCES

- T. C. Cheston and D. H. Shinn, "Scanning Aberrations of Radio Lenses," *Marconi Review*, Vol. XV, 1952, pp. 174-184.
- W. Cummings, Lincoln Laboratory, private communication, 1987.
- G. A. Deschamps, "Ray Techniques in Electromagnetics," *Proc. IEEE*, Vol. 60, No. 9, September 1972, pp. 1022-1036.
- A. J. Fenn, "Interference Sources and Degrees of Freedom in Adaptive Nulling Antennas," MIT Lincoln Laboratory Technical Report 604, 12 May 1982 (AD A116683).

- S. W. Lee, M. S. Sheshadri, V. Jamnejad, and R. Mittra, "Refraction at a Curved Dielectric Interface: Geometrical Optics Solution," *IEEE Trans. Antennas and Propagat.*, Vol. AP-30, No. 1, January 1982, pp. 12-19.
- J. F. Montgomery, D. L. Runyon, and J. A. Fuller, "Multibeam Lens Antenna for EHF SATCOM," *Electromagnetic Sciences, Interim Report to RADC*, Contract F19628-86-C-0187, May 1988 'RADC-TR-88-197 ADB129890L
- W. Rotman, "EHF Dielectric Lens Antenna for Satellite Communication Systems," MIT Lincoln Laboratory Report 620, 3 January 1983.
- W. Rotman, "Analysis of an EHF Aplanatic Zoned Dielectric Lens Antenna," *IEEE Trans. Antennas and Propagat.*, Vol. AP-32, No. 6, June 1984, pp. 611-617.
- D. H. Shinn, "The Design of a Zoned Dielectric Lens for Wide Angle Scanning," *Marconi Review*, Vol. XVIII, 1955, pp. 37-47.
- C. H. Tang and C. F. Winter, "Study of Use of Phased Array to Achieve Pencil Beam Over Limited Sector Scan," Raytheon Company, Final Report, AFCRL-TR-0482, July 1973. AD768618

MEASURED ANTENNA PERFORMANCE OF
AN EHF HYBRID SCAN ARRAY ANTENNA FOR
MILSATCOM APPLICATIONS

J. F. Pedersen

Hazeltine Corporation
Wheeler Laboratory
Greenlawn, NY 11740

ABSTRACT

Hazeltine has completed a contract to design an Advanced Development Model of an EHF Hybrid-Scan Array for potential application to airborne MILSATCOM terminals. This paper will present the design and electrical tests on the antenna assembly.

The antenna assembly includes: a dual-band aperture consisting of waveguide radiators with isolating filters to prevent coupling between receive-band and transmit-band radiators; a meander-line circular-wave polarizer; a conformal dual-band radome capable of passing circular polarized waves over a 70° range of incidence angles; a dual-band rotary joint and the associated electronics and phase shifters to stabilize and steer the antenna beam over nearly a hemisphere.

SECTION 1.0

INTRODUCTION

The task of providing high performance airborne platforms with SATCOM capability has involved one major conflict. Specifically, the user would like to have this communication capability with no antenna protrusion, for reasons relating to aircraft signature, drag, and blockage of other antennas. However, the need for near-hemispheric high gain coverage has required significant antenna protrusion and large radomes. Although conformal fully phased arrays are being developed, they are not presently viable candidates for a practical terminal.

Hazeltine has pursued the technology of hybrid scanning (electronic scanning in elevation and mechanical scanning in azimuth) as a cost-effective solution to the protrusion/gain trade-off¹.

At SHF, an exploratory model of a receive-only antenna² and an advanced development model of a flyable, full duplex antenna³ have employed a horizontal "turntable" aperture with electronic scanning from broadside to end-fire.

At EHF, however, end-fire scanning is not practical for the gain levels required. The EHF design concept uses a tilted array, which is located below the level of the fuselage (figure 1-1). The antenna array electronically scans the beam $\pm 35^\circ$ in elevation, while it rotates mechanically 360° in azimuth. It is protected by

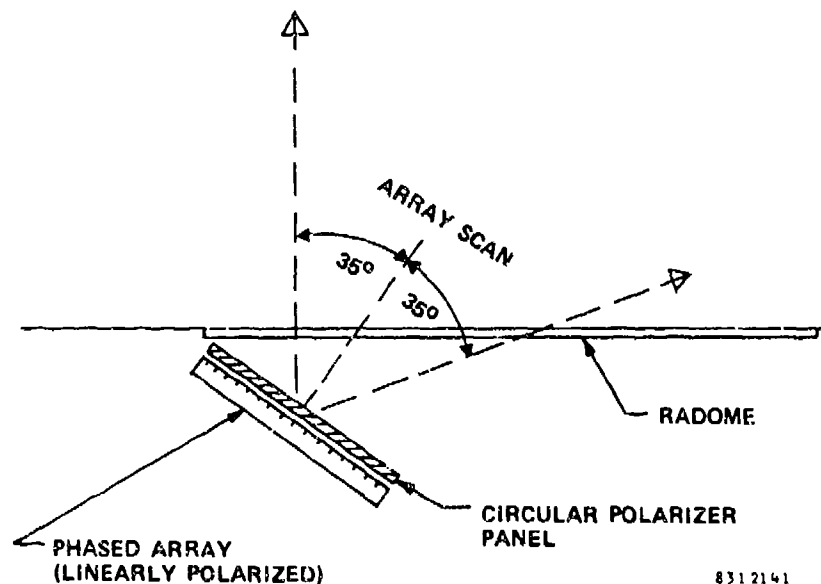


Figure 1-1. EHF Hybrid Scan Antenna Configuration With
Flush Radome

a radome that is contoured to the aircraft surface. The installation is flush, meeting performance criteria from zenith to 20° above the horizon⁴.

In addition to addressing the major antenna design issues, this program has also considered installation of the antenna on an aircraft such as the B1-B including preliminary structural analysis. This latter effort has been conducted by Electrospace Systems, Inc. (ESI) as a team member.

The realization of the design involves the development of several key components including:

- A dual frequency band radome, which must operate at 20 GHz and 44 GHz with circularly-polarized waves and with incidence angles ranging from 0° to 70°

- A dual frequency band aperture of interleaved 20 GHz and 44 GHz slot elements
- A dual frequency band polarizer, which must operate over a range of incidence angles from 0° to 35°

SECTION 2.0

DESIGN OF THE KEY COMPONENTS

2.1 RADOME

If the phased array were horizontal and flush with the aircraft surface, it could be protected from the environment by dielectric windows in the radiating elements or with a radome attached to the rotating radiating surface. However, with the internal location of the antenna, an independent radome is required that can be made flush with the aircraft surface.

The flush radome must operate at a small band of frequencies, about 20 GHz and 44 GHz, with circularly polarized waves and with incidence angles ranging from 0° to 70° . The radome must provide high transmission efficiency and minimum degradation of the axial ratio of circular polarization. Standard radome designs do not appear to be satisfactory. Electrically acceptable designs have poor mechanical strength, while radomes that are adequate mechanically have degraded electrical performance.

Acceptable electrical performance and adequate mechanical strength has been achieved by using a double-quarter wavelength

(at 20 GHz) dielectric sandwich with a shunt susceptance between the walls. The susceptance produces an effect that is large at 44 GHz and small at 20 GHz, giving independent control of the radome match angles. The computed performance of the radome is shown in figures 2-1a, 2-1b, 2-1c, and 2-1d. Figure 2-1a shows the reflection coefficient for H-plane incidence at 20 GHz and 44 GHz. Note that the match angles are nearly equal, providing low reflection at 20 GHz and 44 GHz over a wide range of incidence angles. Figure 2-1b shows the transmission phase difference between orthogonally polarized waves at 20 GHz and 44 GHz. Figure 2-1c shows a plot of axial ratio as a function of incidence angle. At 70° incidence and 44 GHz, the axial ratio is 3.5 dB; this is a result of an increase in the transmission phase difference at 70° shown in figure 2-1b. At all angles less than 70°, the axial ratio is significantly lower.

As shown in figure 2-2, the measured insertion loss of the 2-foot by 2-foot radome panel is less than 0.5 dB at 20 GHz and less than 0.75 dB at 44 GHz over the full range of incidence angles. The measured performance should be compared to the computed loss shown in figure 2-1d.

2.2 INTERLEAVED 20 GHZ, 44 GHZ APERTURE

Linearly polarized elements and a wave polarizer are used to achieve circular polarization. Separate elements are used for the

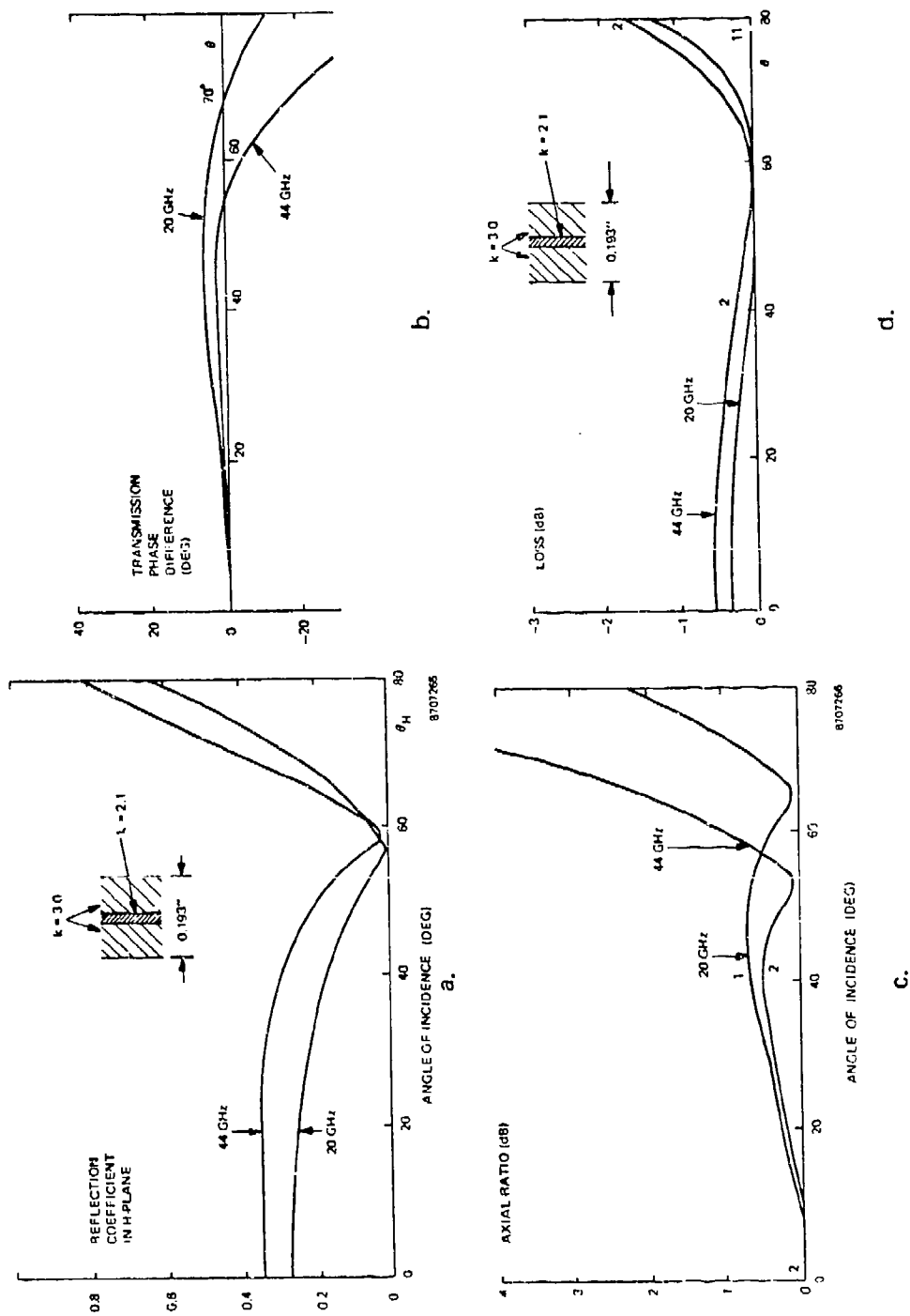


Figure 2-1. Computed Radome Performance

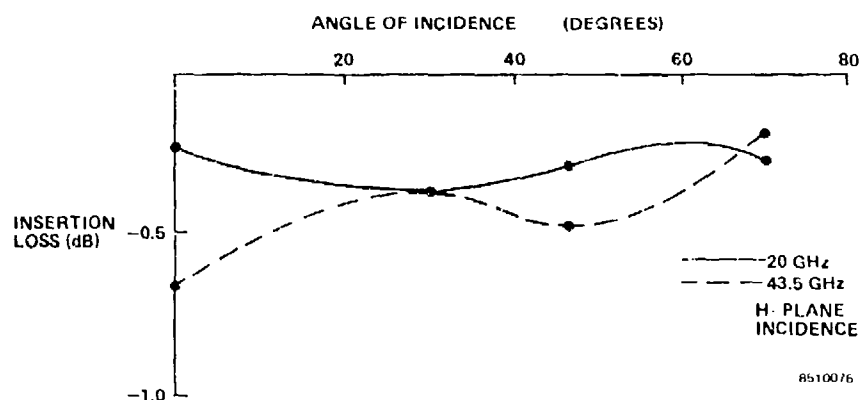


Figure 2-2. Measured Radome Insertion Loss as Angle
of Incidence

receive band and the transmit band. The elements are interleaved, forming a single aperture assembly.

The design of a dual-band array requires a technique for preventing the high band power from coupling into the low band radiator. This can be accomplished in two ways.

One method uses cross-polarized elements. Two possible arrangements of cross-polarized slots are shown in figure 2-3. In either arrangement, the net component of high band current flows along the length of the low band element. If the low band element is thin and below cut-off, it is not excited at the high band frequency.

To scan the array, a phase shift is introduced to each row of slots. A component of current can flow between rows of slots caused by this phase difference. The arrangement of slots shown in figure 2-3a does not couple to this current, and, therefore, it is the preferred arrangement of cross-polarized elements.

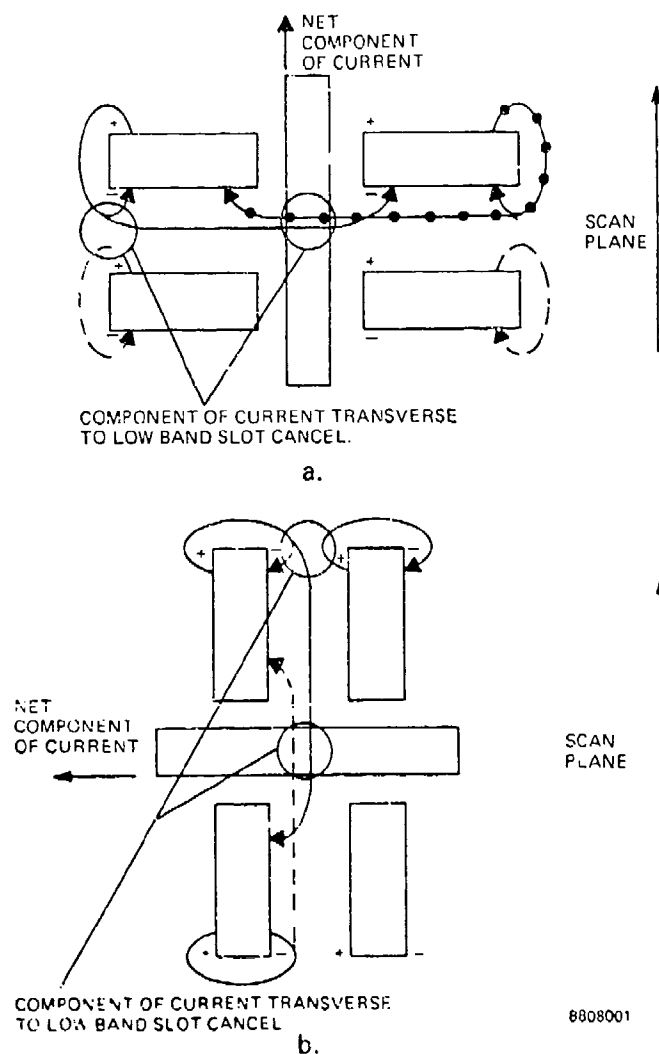


Figure 2-3. Two Arrangements of Cross-Polarized Slots Showing How High Band Currents Cancel Transverse to the Long Dimension of Low Band Slot

The second method of decoupling the low band radiator from the high band power is to use a filter that is internal to the low band element. Either cross-polarized or co-polarized elements may be used with this approach. The filter would be designed to put an effective short-circuit plane at the face of the low band element in both the fundamental TE_{10} and TE_{20} modes at the high

band frequency. The filter would also pass the low band frequency with small reflection loss.

The element spacing between rows of low band elements is determined by the scan requirements and the high band frequency. The preferred arrangement of cross-polarized elements has the long dimension of the low band element in the plane that has the smallest interelement spacing. Consequently, the low band element will be electrically small⁵. The low band element is also scanned in the H-plane, which reduces its radiation power factor further⁶. To increase the radiation power factor and maintain a low reflection coefficient, the low band element area must be increased. This results in a nearly square element rather than a thin element, which is desirable for minimal coupling. For these reasons, a co-polarized arrangement of slots with decoupling filters in the low band elements was selected for the antenna aperture.

The computed filter performance is shown in figure 2-4. Note the pass band and two reject bands in figure 2-4; one reject band corresponds to the fundamental high band waveguide mode while the second reject band represents the TE_{20} mode response.

Figure 2-4 shows the phase slope of the filter across its pass band. Since the filter's phase slope is not flat across the pass band, a shift in the center frequency of the filter caused by tolerances can introduce a phase error across the aperture. The

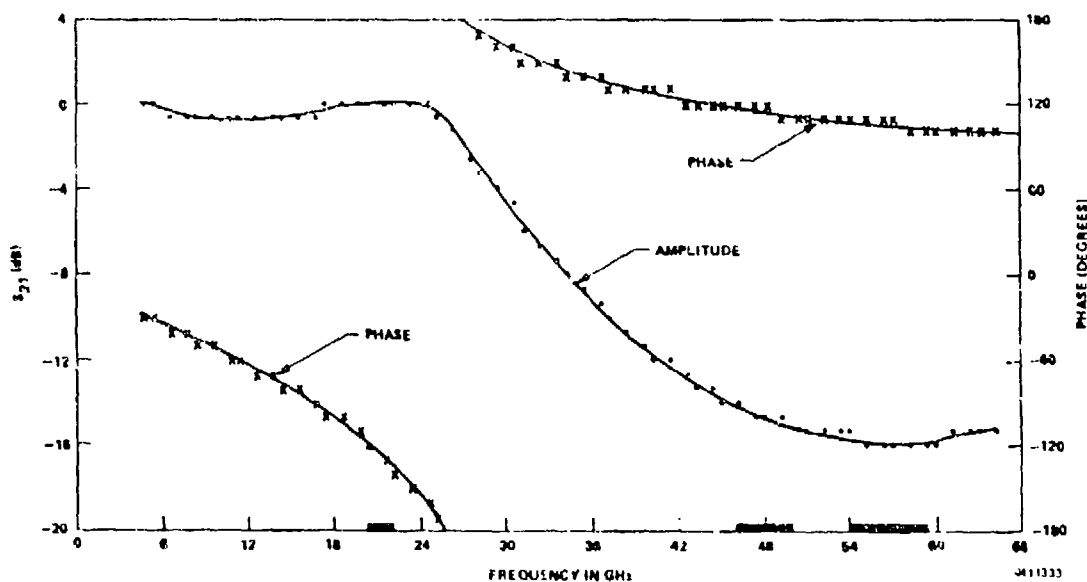


Figure 2-4. Reflection Loss vs Frequency of Isolating Filter

amount of phase error was evaluated as a random function of expected machining tolerances. The result is shown in figure 2-5 as a histogram. Each bin is approximately 1.5° wide; a total of 2000 trials were made with the number of trials indicated within each bin. The phase error introduced by the filter can produce error sidelobes at a -27 dB level. This error is acceptable since it is 5 dB below the design sidelobe level.

The computed filter performance was verified by fabricating a small section of the array. Coupling measurements and radiation pattern measurements were recorded with and without the filter in the low band element. Samples of these results are shown in the next four figures.

Figure 2-6a shows the coupled high band signal into the low band waveguide. It is at a maximum level of -5 dB in the TE_{10}


```

HIGH ( 0):
-104° ( 1):
      ( 9):*
      (36):*****
NOM   (94):*****
-109° (141):*****
      (247):*****
5% VARIATION ON (281):*****
Z AND LENGTHS (274):*****
2000 TRIALS    (284):*****
              (231):*****
. NUMBER OF SAMPLES (185):*****
WITHIN BIN        (104):*****
. EACH BIN=1.5°   ( 66):*****
      PHASE (DEG) ( 34):*****
              ( 10):*
              ( 3):
              ( 0):
-131° ( 0):
LOW   ( 0):

```

8808002

Figure 2-5. Histogram of Filter Phase

mode. Figure 2-6b shows the coupled signal with the filter. The coupled signal level has been reduced to -27 dB.

Radiation pattern measurements were also recorded. Sample results are shown in figures 2-7 and 2-8. Note the significant pattern degradation in figure 2-7 without the filter and the improvement shown in figure 2-8 with the filter. A control pattern is shown on each figure; it corresponds to a pattern of the high band array without the low band elements present.

2.3 POLARIZER

The circular polarizer converts the polarization of an incident wave for linear to circular at both 20 GHz and 44 GHz, over a range of incidence angles from 0° to ±35°.

An approach to designing a polarizer⁷ uses printed-circuit elements that introduce inductive and capacitive susceptance to an incident wave. A variation of this design⁸ uses inductive

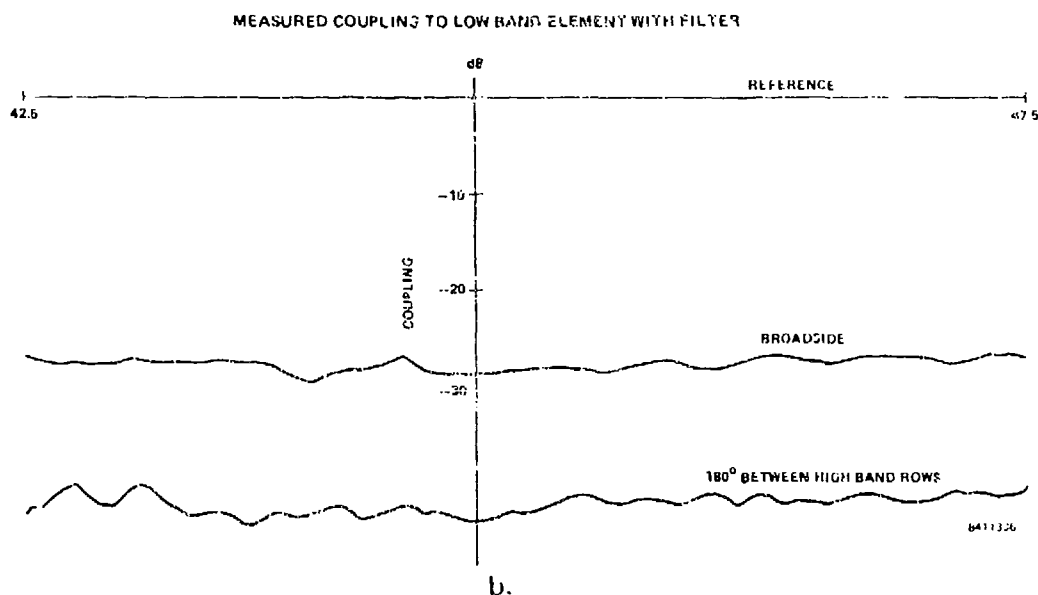
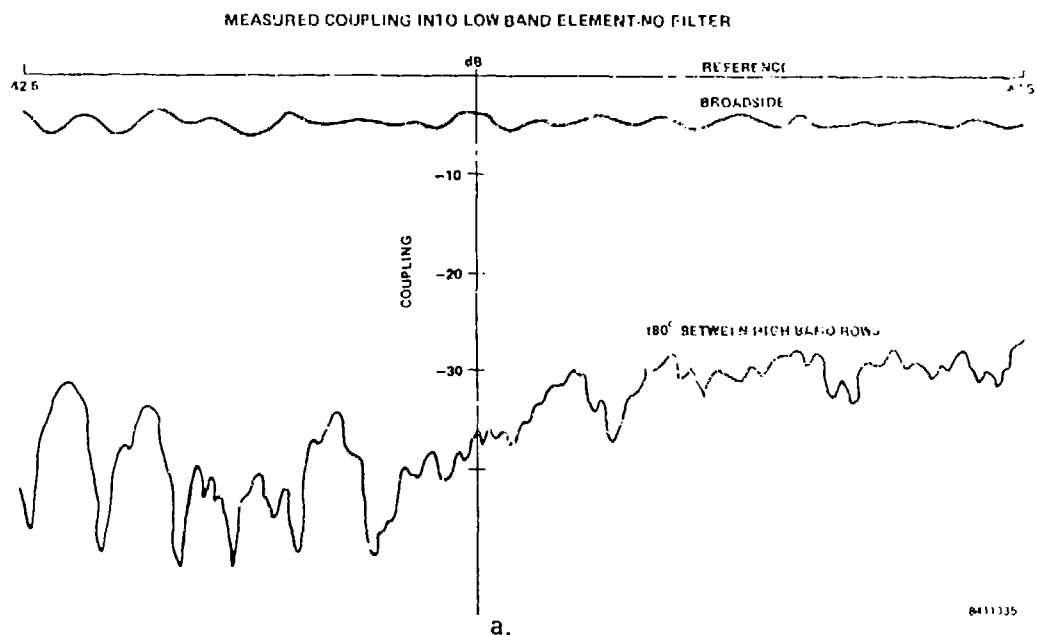


Figure 2-6. Coupled Signal

elements, which are serpentine rather than straight. This latter approach (a meander-line polarizer) was selected for the EHF polarizer.

The meander-line polarizer produces good circular polarization over a wide frequency range. This is accomplished by using

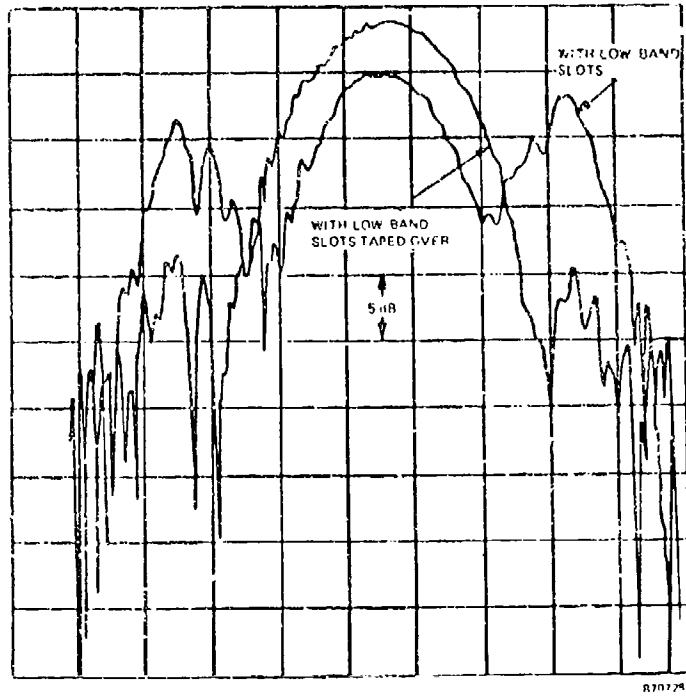


Figure 2-7. Measured Pattern - No Filter

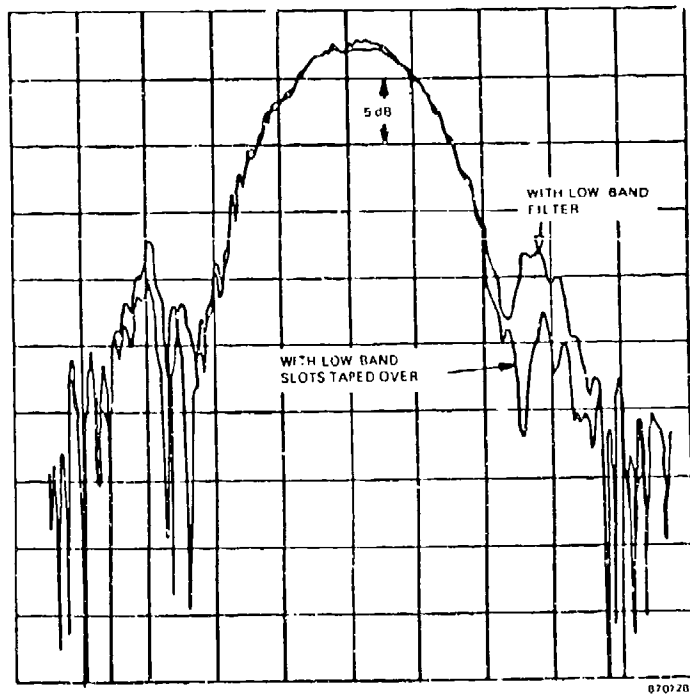


Figure 2-8. Measured Pattern - With Filter

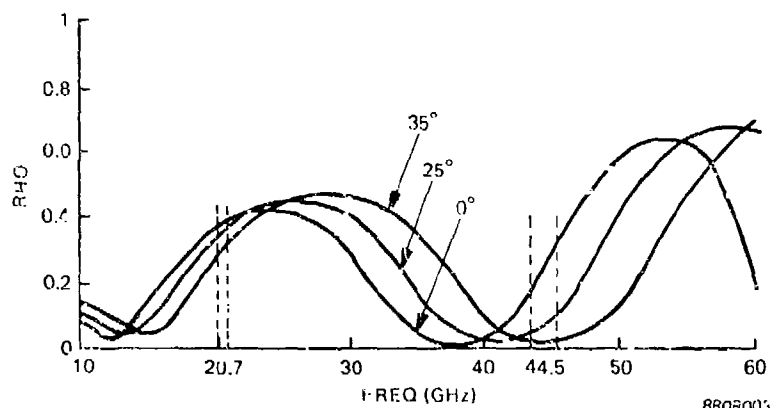
polarization-selective elements that have opposite frequency characteristics, thereby maintaining a nearly constant 90° phase shift over the frequency band.

There are several problems involved with the design of a circular polarizer for operation over a range of incidence angles. These include: the change of effective wavelength with incidence angle; the angle-sensitive behavior of the polarizer elements; and the geometric situation that precludes maintaining the desired 45° orientation of the polarizer elements relative to the polarization of the incident wave over the range of incidence angles.

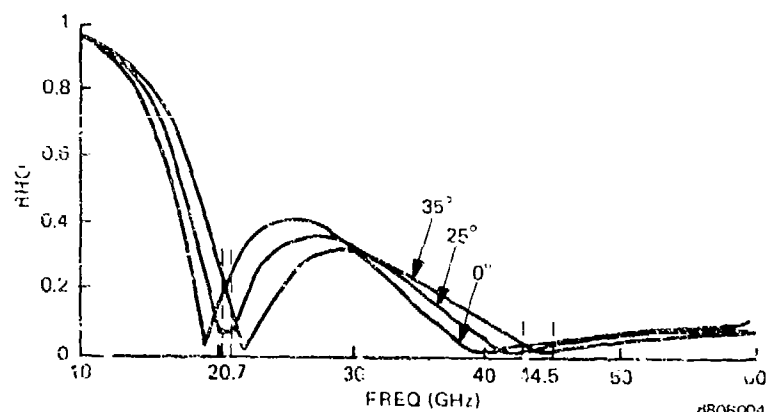
The last problem can be partially overcome by orienting the polarizer elements at an angle that deviates from 45° and that represents the best compromise over the range of incidence angle.

The requirement for a combination of both wide-band and wide-angle performance can be approached by designing the polarizer for operation at only the two 5-percent frequency bands, about 20 GHz and 44 GHz, rather than over the complete band between these frequencies.

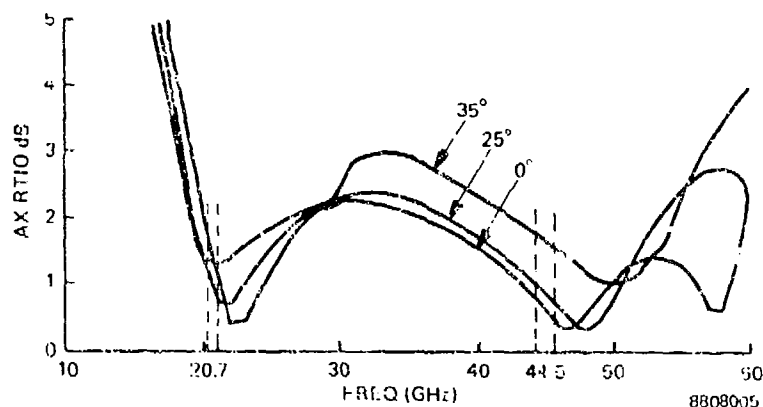
Figures 2-9a through 2-9c show the computed polarizer performance. Three curves are shown on each graph for three angles of incidence. The frequency bands of interest are noted on each figure. Figures 2-9a and 2-9b show the reflection coefficient of the principal polarizations. Figure 2-9c shows the resulting axial ratio of the polarizer. The measured axial ratio of the polarizer vs angle of incidence is shown in figure 2-10.



a.



b.



c.

Figure 2-9. Computed Polarizer Performance

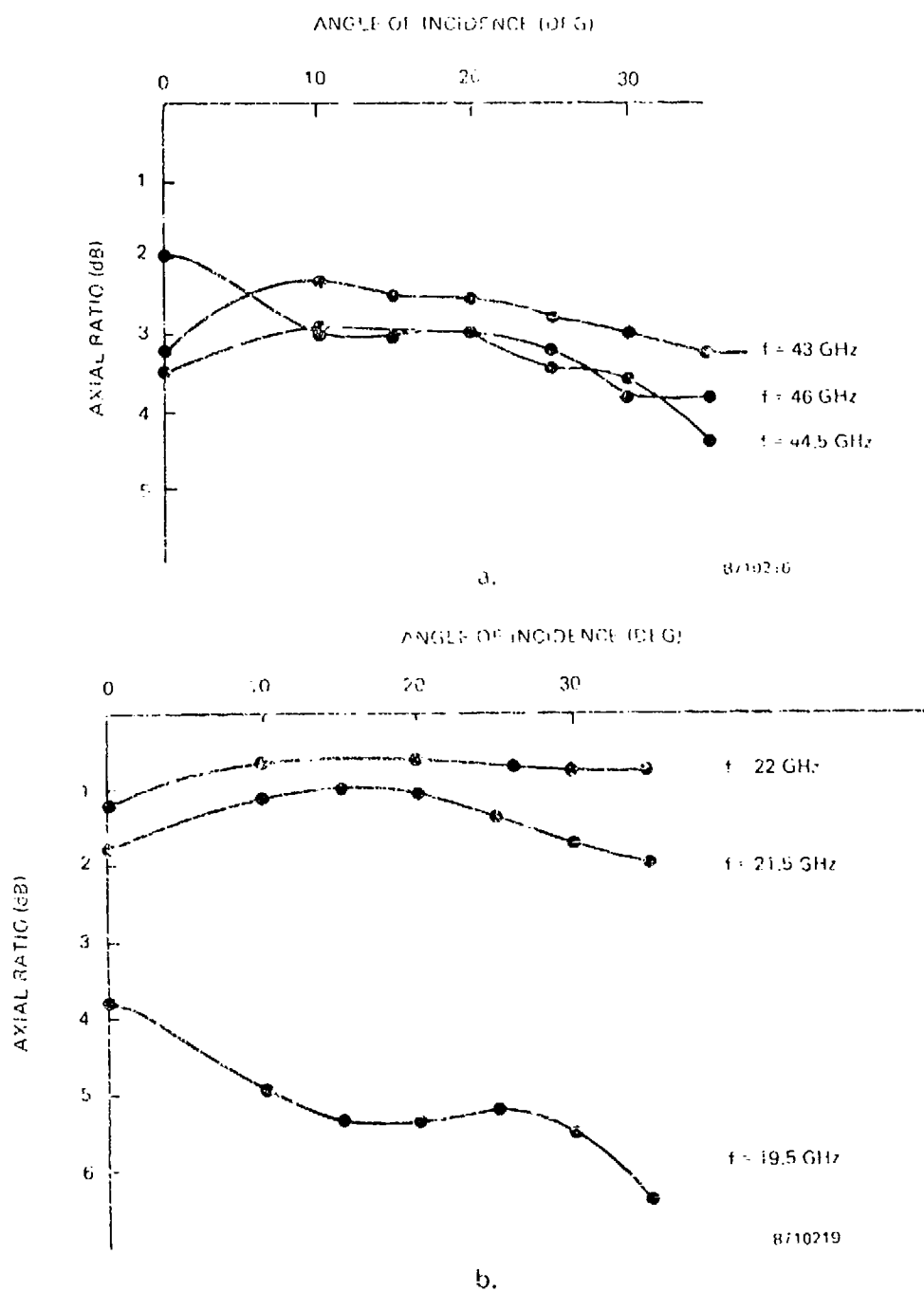


Figure 2-10. Measured Axial Ratio of Polarizer vs Angle of Incidence

2.4 POWER COMBINERS

For an array that scans in only one plane, the elements may be arranged in a rectangular grid. The element spacing in the plane of scan is smaller to prevent a radiating grating lobe. Even for a moderate scanning range (35°), the scan plane element spacing will preclude the use of standard waveguide as the feed. Stripline, suspended stripline, ridge waveguide, and reduced height waveguide are alternatives.

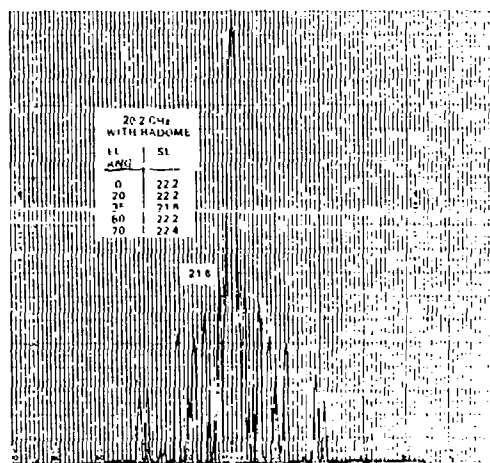
The antenna consists of many components connected in series. The dissipative loss is additive and it can be appreciable in total, especially at EHF frequencies. Effective control of the total antenna loss is required to achieve practical ERP and G/T levels. Since reduced height waveguide yields the lowest dissipative loss, all power combiners use this medium.

Sidelobe control was required for each principal plane of the array. In azimuth, the amplitude taper is achieved by using additional levels of equal (3 dB) splitters. The extra levels quantize the illumination in coarse 3 dB steps; however, the modest sidelobe requirement of -16 dB maximum in transmit and -22 dB in receive can be achieved by using this technique.

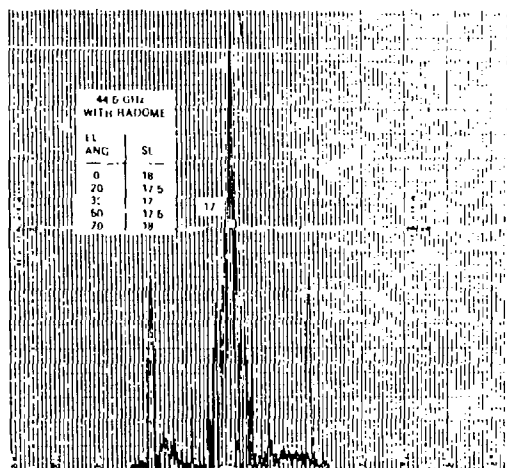
In elevation, a coarse approximation to the desired illumination will not yield these same sidelobe levels. This is because the array contains fewer rows of elements than elements per row.

As a result, nonequal E-plane waveguide dividers are used to derive the amplitude illumination in elevation.

Figure 2-11 shows measured azimuth patterns (nonscanning plane) of the array including radome at 35° elevation. Sidelobe levels as a function of elevation are shown tabulated in figure 2-11. Figure 2-12 shows typical measured patterns in the scanning of the array.

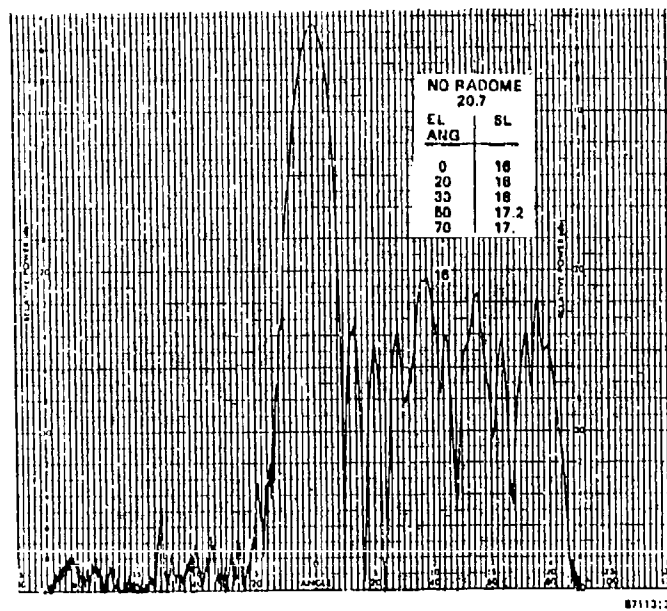


a.

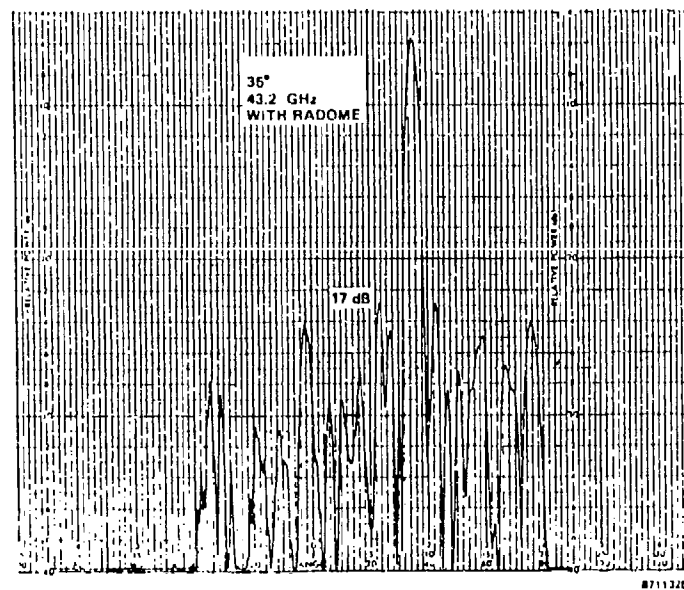


b.

Figure 2-11. Typical Measured Azimuth Plane Radiation Patterns



a.



b.

Figure 2-12. Measured Elevation Plane Patterns

SECTION 3.0

ARRAY CONSTRUCTION

Figure 3-1 is a photograph of the antenna pedestal. The pedestal consists of two housings - an inner housing that rotates and a stationary outer housing. The millimeter wave components, the electronics to control and stabilize the beam, and the phase shifter driver cards are assembled in the inner housing.

The stationary housing contains the motor stator and all power supplies needed to drive the electronics and phase shifters.

A blower, attached to the top of the inner housing, draws air up through the pedestal and exhausts the hot air through the array of holes at the periphery of the pedestal as seen in figure 3-1.

A slip ring routes control signals and power supply voltages between housings. A dual-band 20 GHz/44 GHz waveguide rotary joint (manufactured by Kevlin, Inc.) mounts inside the slip ring.

The beam is scanned electronically by using ferrite phase shifters, supplied by Electromagnetic Sciences, Inc.

A phase shifter assembly contains 16 phase shifters. Three assemblies (two 44-GHz and one 20-GHz) are arranged across the azimuth power divider, feeding the array in elevation. The driver cards are located in two bays and connect to the RF assembly by a flexible balanced strip transmission line.

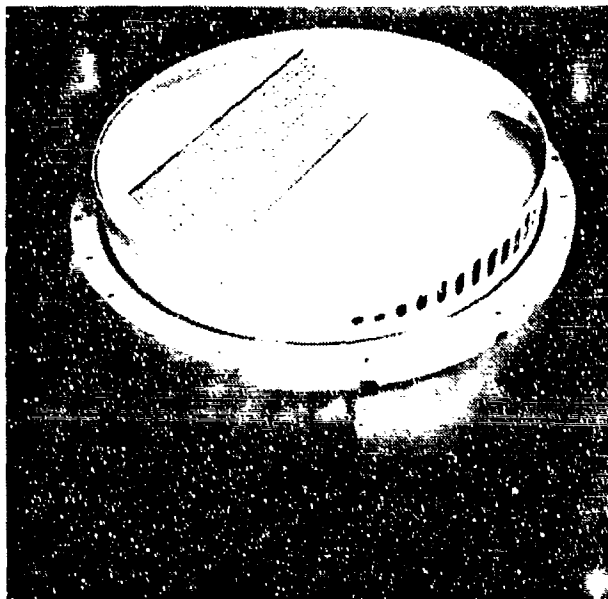


Figure 3-1. EHF Hybrid Scan Array

Reduced height waveguide power dividers are used for power distribution to the phase shifters and to the elements. The polarizer is mounted in a frame 0.25 inch in front of the array.

The radome for this program is a flat 2 foot by 2 foot panel mounted to a B-52 fuselage via an adaptor plate that conforms to the fuselage's cylindrical shape.

SECTION 4.0

CONCLUSIONS

Under this program, all the technologies required to provide a flush antenna system for an airborne MILSATCOM terminal have been reduced to practice. The array is a cost-effective solution for aircraft where a flush conformal array is needed.

SECTION 5.0

ACKNOWLEDGEMENT

This work has been sponsored by Rome Air Development Center under Contract F19628-81-C-0044. Appreciation is expressed to John McIlvenna, RADC/EEA, for his guidance during this program. Design concepts for the radome and polarizer were provided by P. W. Hannan. V. R. Milligan and W. P. Mordarski were instrumental in the designs of the array hardware.

SECTION 6.0

REFERENCES

- (1) Pedersen, J. F. (1988) Measured Performance of an EHF Hybrid Scan Array Antenna for MILSATCOM Applications. IEEE AP-S International Symposium, Vol 1, pp 192 - 195.
- (2) Maune, J. J. (1972) An SHF Airborne Receiving Antenna. USAF Antenna Research and Development, Twenty-Second Annual Symposium, pp 1 - 16.
- (3) Kelly, A. J., Pinck, E., Pedersen, J. F., Bogin, W. W. (1981) International Symposium Digest - Antennas and Propagation, Vol I, pp 186 - 190.

- (4) Kelly, A. J., Pedersen, J. F. (1984) EHF Hybrid Scan Array for Airborne SATCOM Terminals. Presented at IEEE Military Communications Conference (Oct).
- (5) Wheeler, H. A. (1947) Fundamental Limitations of Small Antennas. Proc/Re, Vol. 35, pp 1479 - 1484 (Dec).
- (6) Lopez, A. R. (1974) Wideband Dual-Polarized Element for a Phased Array Antenna. Technical Report AFAL-TR-94-242 (June)
- (7) Lerner, D. S. (1965) A Wave Polarization Converter for Circular Polarization. IEEE Trans. Antennas and Propagations, pp 3 - 7 (Jan).
- (8) Young, Robinson, Hacking (1973) Meander-line Polarizer, IEEE Trans. Antennas and Propagation, pp 376 - 378 (May)

TECHNIQUE TO MEASURE LARGE ANTENNA ARRAYS

Dr. Peter Franchi and Mr. Harvey Tobin
Rome Air Development Center
Electromagnetics Directorate
Hanscom Air Force Base
Lexington, Massachusetts 01731

ABSTRACT:

The measurement of one dimensional planar arrays that are electrically long is currently a difficult task. The accurate measurement of the antenna patterns is limited by large antenna range requirements for far field ranges, by the number of near field points that must be measured for near field probes, and by the great size and quality of the reflector/feed for compact ranges. This paper describes the use of quadratic and higher phase correction applied to the phased array.

The errors that result from this approach are analyzed as a function of range, antenna electrical length, sidelobe level and degree of correction. Both computer simulations and analysis are used to generate the limitations of this approach. Far field measurements made in the near field are currently planned.

INTRODUCTION:

The Air Force is currently investigating methods of mounting large lightweight phased arrays on the fuselages of long aircraft for long range airborne surveillance. Such arrays tend to be very long in one dimension, but moderate in size in the other. Because of the size of these antennas the measurement of their basic patterns is very difficult. For example the far field distance for a 10' x 100' aperture at C-band would be about 23 miles away, by the $2D/\lambda$ criteria for a very low sidelobe array the distance would be much greater if very little

pattern distortion is desired. Compact ranges for this size antenna require a massive high tolerance reflector and near field ranges would be extremely expensive. One technique to measure the far field patterns while using a conventional antenna range is based on the fact that in one dimension, the smaller one, the far field range is at a reasonable distance. For the other dimension the antenna is well within the Fresnel field, so an accurate pattern can only be found by putting in a phase correction over the aperture. Since this correction is only precisely correct at one angle, repeated corrections are therefore required to get a good approximation to the far field at infinity pattern. In this report the first two higher order correction factors are examined quadratic alone and quadratic and cubic. An analysis of the residual error is given and from that analysis, an estimate of the range of angles is over which a particular correction gives small addd error is found. That range of angles over which the pattern of infinity determines the number of resets of the phase shifters.

SIMULATION:

For the analysis a computer simulation was developed. This involved writing three individual computer programs. The first program generates the actual far field pattern, the result is shown in fig (1). Using the pattern as a reference a second program was written, using a modified expression which includes the correction factors. First the program was run including only the quadratic correction. This was performed for several different cases. First the distance R_0 are repeated. The program was then run including the third order correction and as with the quadratic correction the parameters R_0 and θ_0 are varied. To determine the degree of difference between the actual far field pattern and the pattern which include the correction terms another simulation was run. This program subtracts the actual far field values. This gives a measure of the error in adding the correction terms.

The results of the simulation for the quadratic term correction alone are presented in fig (2-5). These are for a 96 λ antenna. For the addition of the third order correction the results are shown in fig (6-9).

With the results of the computer runs a set of graphs have been developed. These graphs are a measure of how much error one can expect in applying this technique to a design.

Fig (10) shows how the error will vary with distance in applying the quadratic correction. (Fig 11) shows the effect of adding the third order correction. The graph represents how many times the phase shifter will have to be set in order to achieve a certain error margin.

ANALYSIS:

In order to estimate the residual error in using phase correction in the Fresnel field, several assumptions are made to derive the dominant error

forms. These assumptions include:

- 1) The $1/R$ amplitude term can be approximated by $1/R_0$, that the Fresnel distance chosen is large enough so that only the phase term contributes significantly to the residual error.
- 2) The type of patterns that concern us are low sidelobe patterns with Taylor illuminations or similar and beyond a small angular range these patterns have $\sin x/x$ behavior,
- 3) The quadratic phase error at the aperture edge is less than a radian.

The actual distance from the Fresnel field point to a point on the aperture is R . Since the array is in the near field in one dimension only the aperture can be treated as a linear array.

$$R = (R_0^2 + x^2 - 2xR_0 \cos \alpha)^{1/2} \quad (1)$$

where R is the distance from the near field point to the center of the array and x is the distance from the center of the array to any point on the array. For $R_0 \gg x$.

$$R = R_0 + \frac{x^2 - 2xR_0 \cos \alpha}{2R_0^2} + \frac{(x^2 - 2xR_0 \cos \alpha)^2 R_0}{8R_0^4} + \frac{(x^2 - 2xR_0 \cos \alpha)^3 R_0}{12R_0^6} - \frac{5(x^2 - 2xR_0 \cos \alpha)^4 R_0}{128 R_0^8} + \text{etc} \quad (2)$$

after combining terms

$$R = R_0 - x \cos \alpha + x^2 \left(\frac{1}{2R_0} - \frac{\cos^2 \alpha}{2R_0^3} \right) + x^3 \left(\frac{1}{2R_0^2} \cos \alpha - \frac{1}{2} \frac{\cos^3 \alpha}{R_0^3} \right) - x^4 \left(\frac{1}{8} \frac{\cos^3 \alpha}{R_0^3} - \frac{12}{16} \frac{\cos^2 \alpha}{R_0^4} + \frac{80}{128} \frac{\cos^4 \alpha}{R_0^5} + \dots \right) \quad (3)$$

Let $\psi = 90^\circ - \alpha$

$$R = R_0 - x \sin \psi + x^2 / 2R_0 \cos^2 \psi + x^3 / 2R_0^2 \sin \psi \cos^2 \psi - x^4 / 8R_0^3 (\cos^2 \psi (1 - 5 \sin^2 \psi)) \quad (4)$$

The Fresnel field expression $E(u)$ can be written as:

$$E(u) = k' \int_{-d/2}^{d/2} \frac{F(x') e^{jkR}}{R} dx' \quad (5)$$

$$\approx \frac{k'}{R_0} \int_{-d/2}^{d/2} F(x') e^{jkR} dx' \quad (6)$$

With $x' = \frac{D}{2} x$

and $u = \frac{kD}{2} \sin \psi$ For The Linear Term

$\beta = \frac{k \cos^2 \psi D^2}{8R_0}$ For The Quadratic Term

$\gamma = \frac{kD^3}{16R_0^2} \sin \psi \cos^2 \psi$ For The Cubic Term

and, $\alpha = \frac{kD^4}{128R_0^3} \cos^2 \psi (1 - 5 \sin^2 \psi)$ For the Fourth Order Term

$$E(u) = k \int_{-1}^1 F(x) e^{j(ux - \beta x^2 - \gamma x^3 + \dots)} dx \quad (7)$$

equation 7 can be approximated by

$$E(u) \approx k \int_{-1}^1 F(x) e^{j(ux - \beta x^2 - \gamma x^3)} dx \quad (8)$$

The actual far field Pattern is $E_0(u)$ where,

$$E_0(u) = k \int_{-1}^1 F(x) e^{jux} dx = g_0(u) \quad (9)$$

Since R_0 is chosen so that β are less than 1

$$E(u) \approx k \int_{-1}^1 F(x) e^{jux (1 - \beta x^2 - \gamma x^3)} dx \quad (10)$$

$$\begin{aligned}
 E(u) &\cong k \int_{-1}^1 F(x) e^{jux} dx - j\beta k \int_{-1}^1 F(x) x^2 e^{jux} dx - j\gamma k \int_{-1}^1 F(x) x^3 e^{jux} dx \\
 &= g_0(u) - j\beta k \int_{-1}^1 F(x) x^2 e^{jux} dx - j\gamma k \int_{-1}^1 F(x) x^3 e^{jux} dx
 \end{aligned}$$

Since,

$$\begin{aligned}
 \int_{-1}^1 x^k F(x) e^{jux} dx &= \frac{1}{(j)^k} \frac{dk}{du} \int_{-1}^1 F(x) e^{jux} dx \\
 &= g_0(u) - \frac{j\beta(2)}{-1} g_0(u) - \frac{j\gamma}{j} g_0^{(3)}(u)
 \end{aligned}$$

where $g^{(n)}$ represents the derivative to the n^{th} power the corresponding power pattern is $P(u) = E(u) E^*(u)$

$$\begin{aligned}
 P(u) &= |g_0(u) - g_0^{(3)}(u)|^2 + \beta^2 g_0^{(2)}(u)^2 + \text{higher order terms} \\
 &= g_0^2(u) + \gamma^2 g_0^{(3)}(u)^2 - 2\gamma g_0(u) g_0^{(3)}(u) + \beta^2 g_0^{(2)}(u)^2 + \text{higher order}
 \end{aligned}$$

Using the assumption that the ideal far field Taylor or similar far field Pattern can be approximated by

$$g_0(u) = \frac{a \sin u}{u} + \frac{bf(u)}{u^2} + \frac{cf(u)}{u^3}$$

So beyond small angle,

$$\begin{aligned}
 g_0(u) &\cong a \frac{\sin u}{u} \\
 g_0^{(2)}(u) &= a \left(\frac{-\sin u}{u} - \frac{2\cos u}{u^2} + \frac{2\sin u}{u^3} \right) \\
 g_0^{(3)}(u) &= a \left(\frac{-\cos u}{u} + \frac{3\sin u}{u^2} + \frac{6\sin u}{u^3} - \frac{6\sin u}{u^4} \right)
 \end{aligned}$$

$$E(u) \cong P_0(u) - P_0(u)$$

$$\begin{aligned}
 \sin^2 ua^2 & \frac{8\beta^2}{u^4} + \frac{6\gamma}{u^3} + \frac{\beta^2\gamma}{3ku^2} + \cos^2 ua^2 \left[\frac{4\beta^2}{u^4} + \frac{\beta^2\gamma}{u^2} \right] \\
 & + \sin u \cos ua^2 \left[-2\gamma u^2 \right]
 \end{aligned}$$

Comparison of terms indicates the $\frac{2\gamma}{u^2}$ term is the strongest. Simplifying further, the error envelope is:

$$E(u) \cong \frac{-2\gamma}{u^2} a^2 \quad \text{and} \quad \frac{a^2 8\beta^2}{u^4}, \quad \frac{a^2 4\beta^2}{u^4}$$

If quadratic phase error is removed, the $\frac{2\gamma}{u^2} a^2$ becomes the dominant term.

$$\beta' = \beta - \frac{kD^2}{8R_0}$$

$$\beta' = \frac{kD^2}{8R_0} (\cos^2 \Theta - 1) = -\frac{kD^2}{8R_0} \sin^2 \Theta$$

Without quadratic phase correction the dominant error term is proportional to $\cos^2 \Theta$ so the distortion is greatest at $\Theta = 0$. With the correction this error term becomes proportional to $\sin^2 \Theta$ and so is very small near $\Theta = 0$. As might be expected, this change results in the evaluation of the γ term as the dominant error. Examination of this expression gives the resulting error as a function of the array size, measurement distance and wavelength. This error is

$$E(u) \cong \frac{2a^2\gamma}{u^2}$$

and is the absolute resulting error. The normalized error or percentage error is

$$E(u) \cong \frac{E(u)}{g_0(u)} \cong 2\gamma$$

or,

$$\begin{aligned} E(u) &= \frac{kD^3}{8R_0^2} \sin \Theta \cos^2 \Theta \\ &= \frac{\pi D^3}{4 \lambda R^2} \sin \Theta \cos^2 \Theta \end{aligned}$$

This gives the residual error. If a ξ is also the acceptable error allowed by this measurement technique the minimum range for use of quadratic phase only is

$$R \geq \frac{D^3}{.3\lambda\xi}$$

For example if the maximum added error is .1db (.023) and ξ is .16', the

$$R = 30D^{3/2}$$

<u>D</u>	<u>R</u>	<u>$2D^2/\lambda$</u>
8'	1920'	3072'
16'	1920'	3072'
32'	5430'	12288'

If this range is too great the error can be reduced by using cubic phase correction repeated several times. This reduces the error around a limited angular range.

The normalized error is then,

$$E(u) = \frac{D^3}{\lambda R^2} (\sin \Theta \cos^2 \Theta - \sin \Theta_0 \cos^2 \Theta_0)$$

With an approximate range of 10° and the third order correction the range can be reduced by a factor of 8.

<u>D</u>	<u>R(cubic correction)</u>	<u>R(with quadratic only)</u>
8'	85'	680'
16'	240'	1920'
32'	680'	5430'

Over the full range of 180° the phase correction must be applied on the order of 9 times since the correction is double valued.

CONCLUSION:

The use of both quadratic and when necessary third order phase correction permits the accurate measurement of the far field pattern of very large phased

arrays at ranges much less than the normal far field distance. This technique applies only to arrays with one dimension much greater than the other and only when the statistical sidelobe behavior not the exact (with any particular phase shifter setting) is required.

REFERENCES:

- 1) Jull, E.V. (1962) "An Investigation of Near Field Radiation Patterns Measured with Large Antennas" APS Vol #4, AP-10
2. Sherman III, John, "Properties of Focused Apertures in the Fresnel Region." APS July 1962 Vol #4 AP-10.
3. Fahey, Micheal, Pierce, Thomas, Spaulding, William "Phased Array Focused In Near Field" Technical Report US army Missile Command Redstone Arsenal, Alabama.
4. Silver, Samuel (1949) "Microwave Antenna Theory and Design" McGraw Hill, New York pp 188-189.

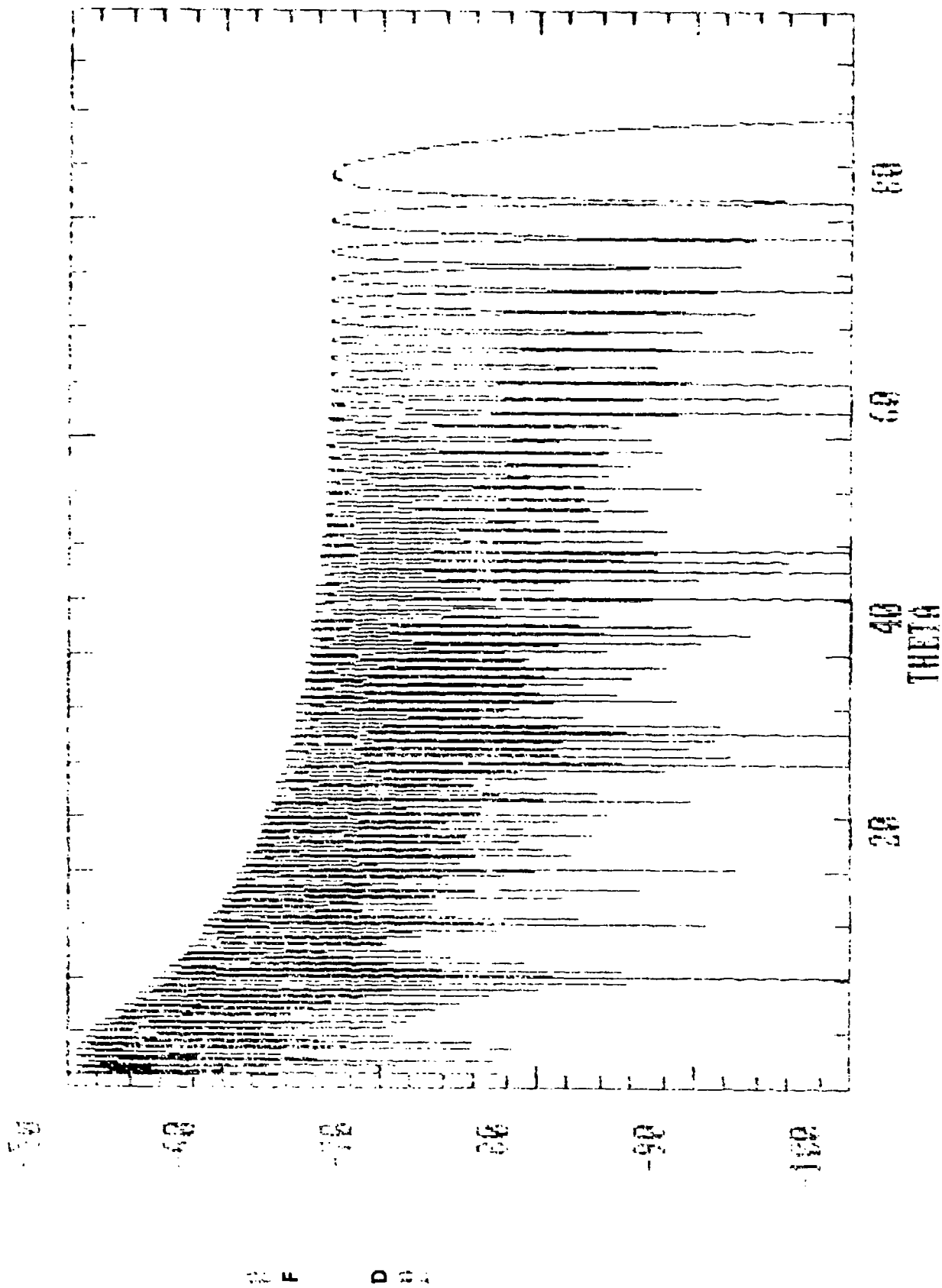


Fig.1 Actual Far Field

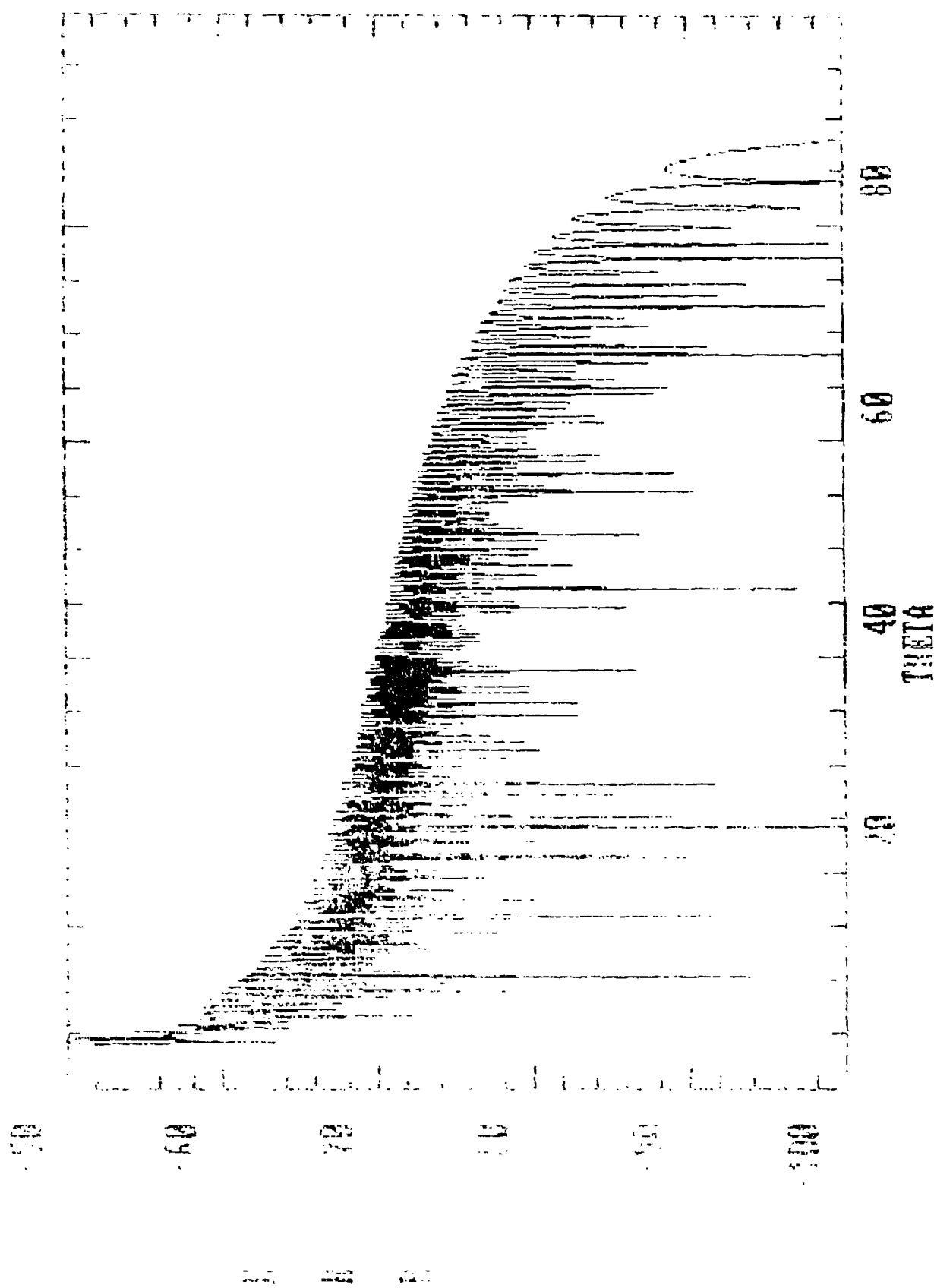


Fig.2 Quadratic Term $R_{0-1500} \approx 96\%$

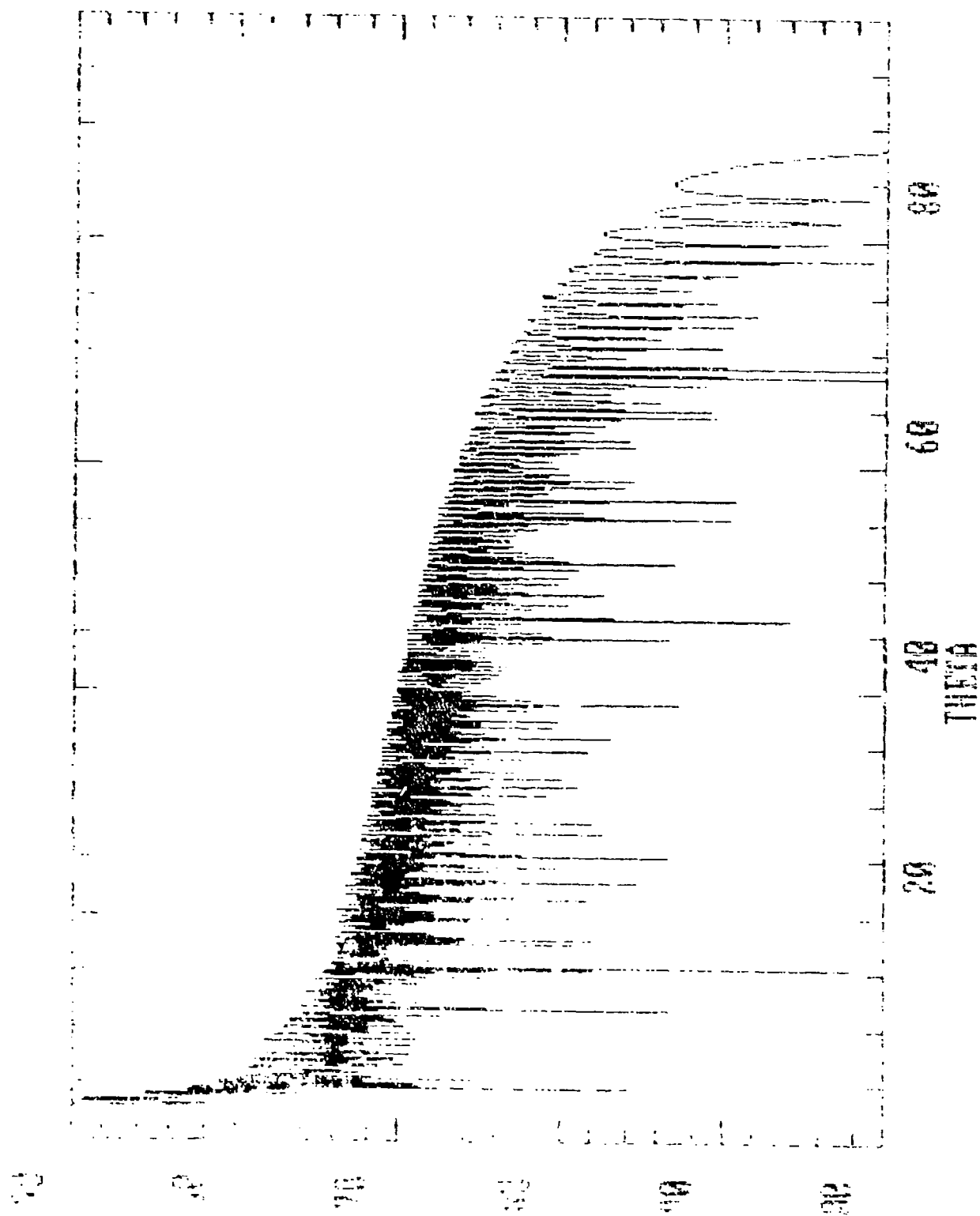


Fig.3 Quadratic Term $R_0=150^\circ-20^\circ$ 96λ

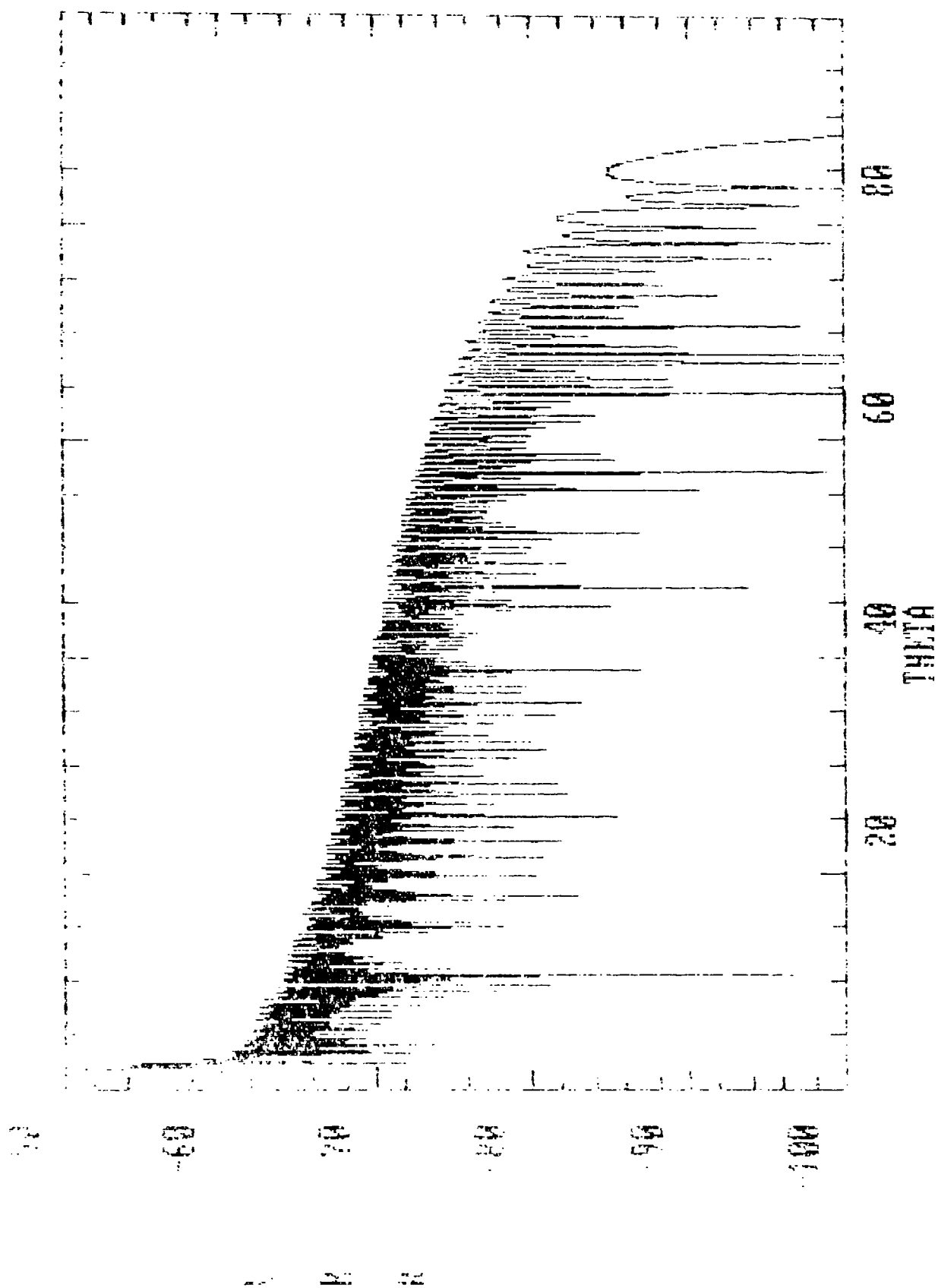


Fig.4 Quadratic Term $R_0=150^\circ \rightarrow 40^\circ \rightarrow 96^\circ$

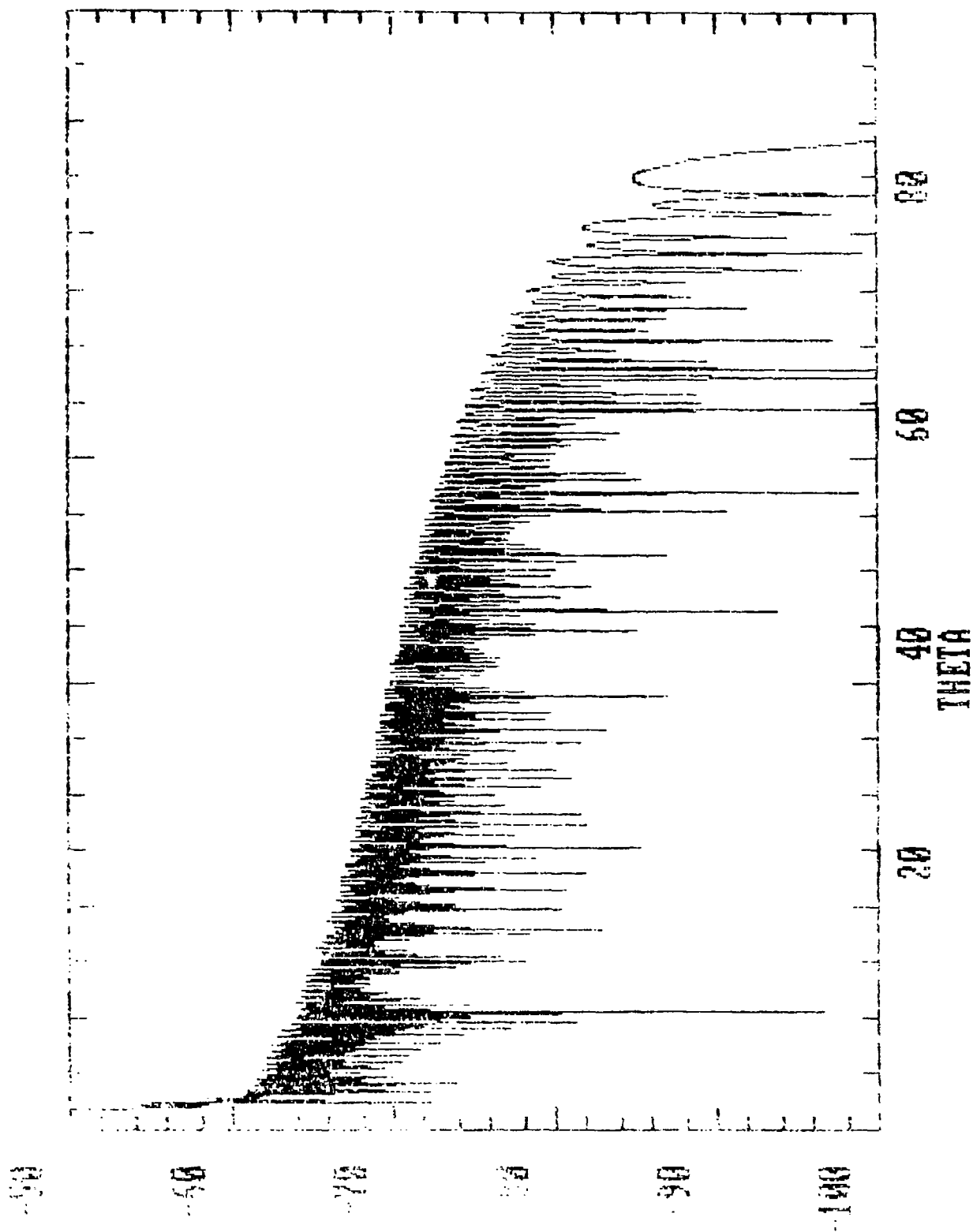


Fig. 5 Quadratic Term $Ro=150e80\ 96\lambda$

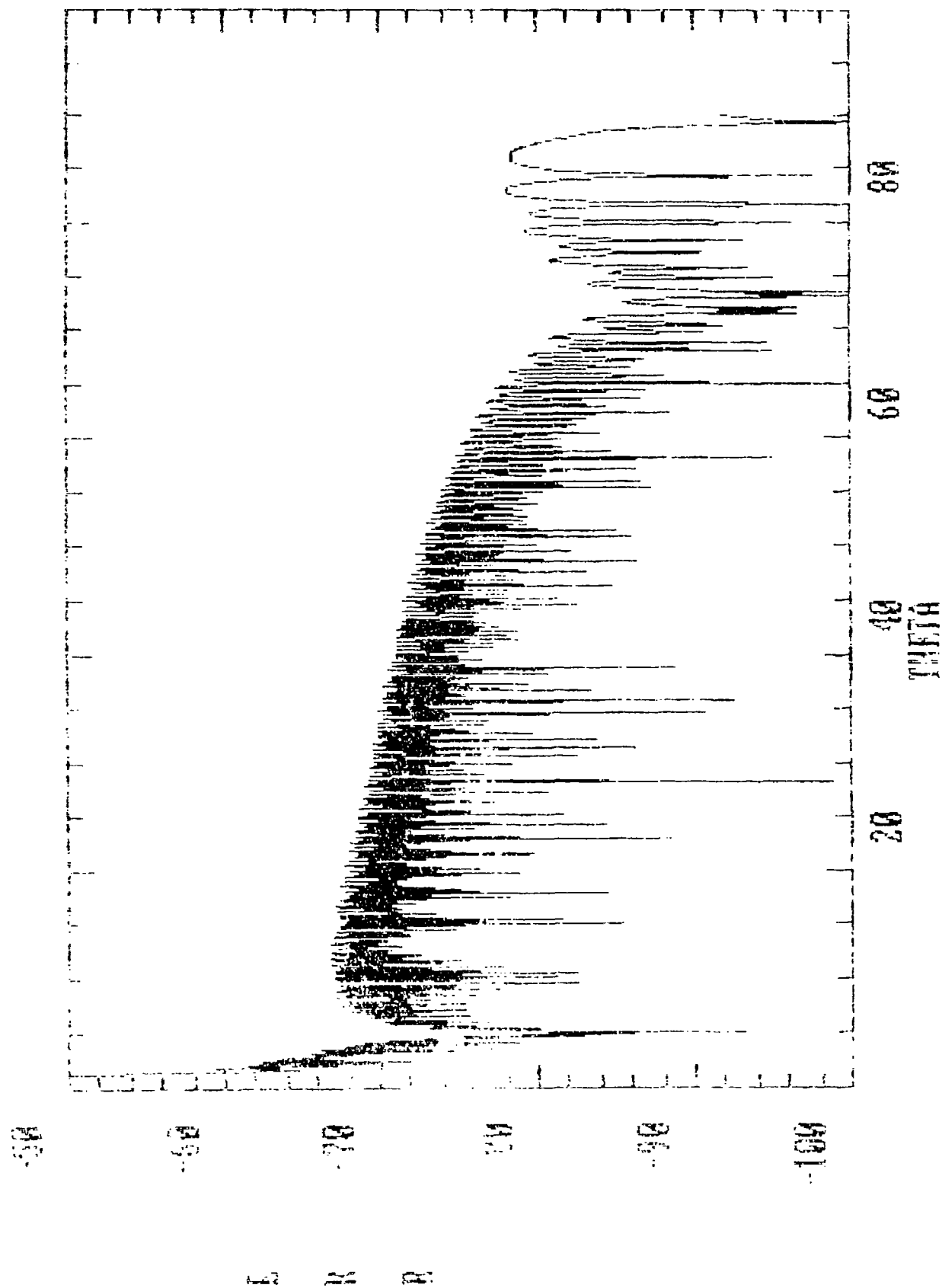


Fig.6 Third Order Term $R_0=150e-0^\circ 96\lambda$

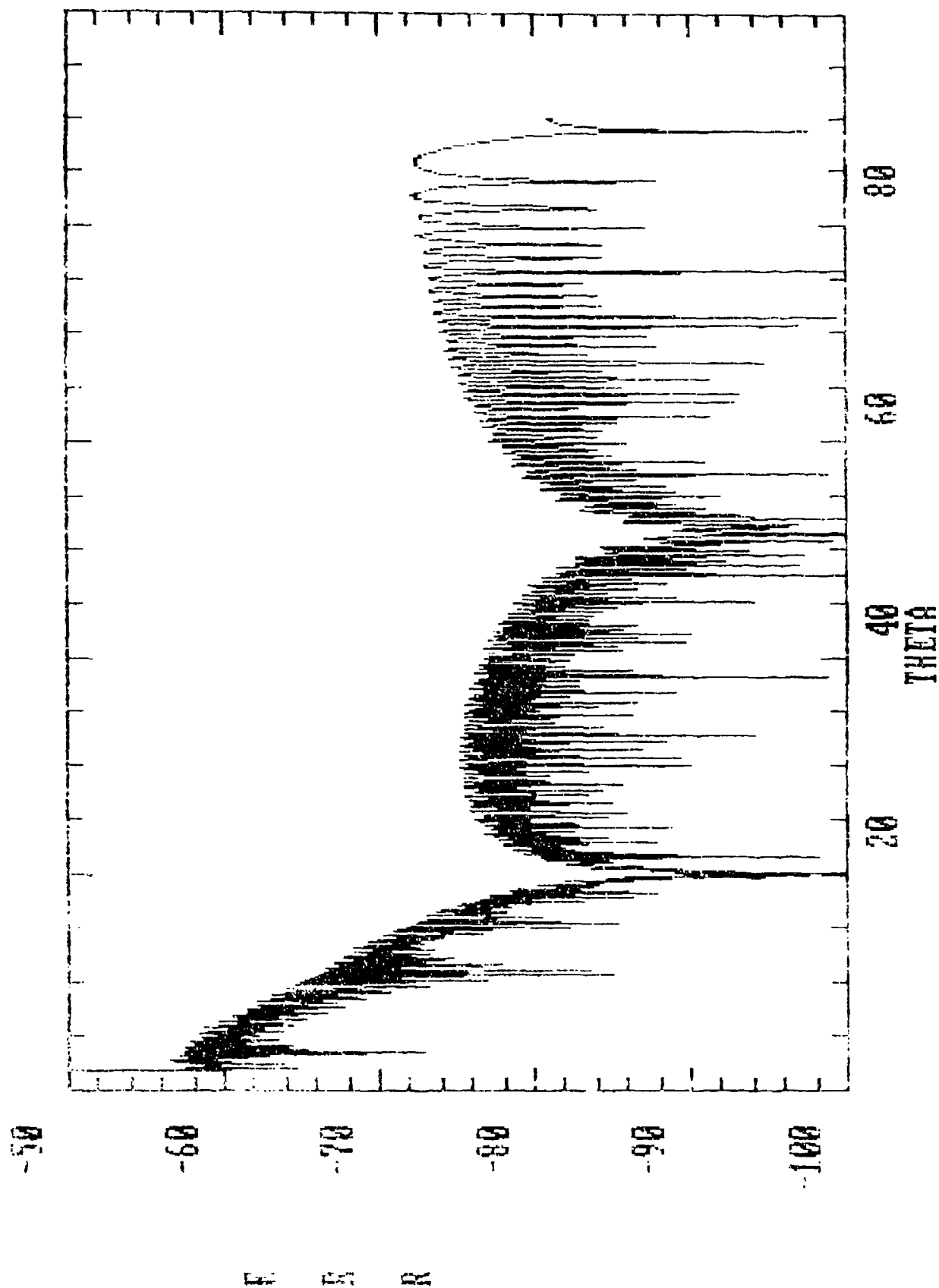


Fig.7 Third Order Term $R_0=150e^{20^\circ} 96\lambda$

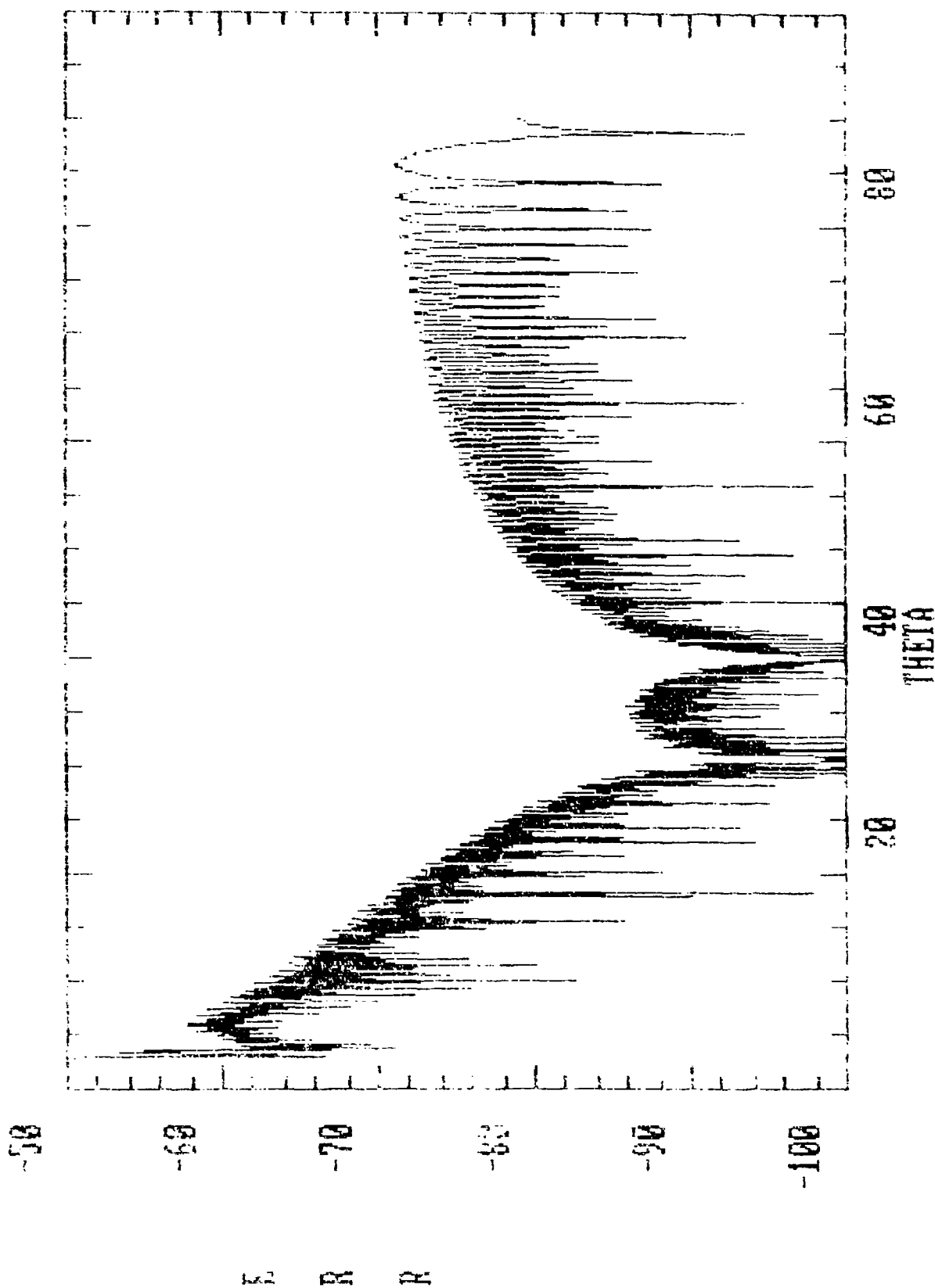


Fig.8 Third Order Term $R_0=150^\circ \pm 40^\circ$ 96°

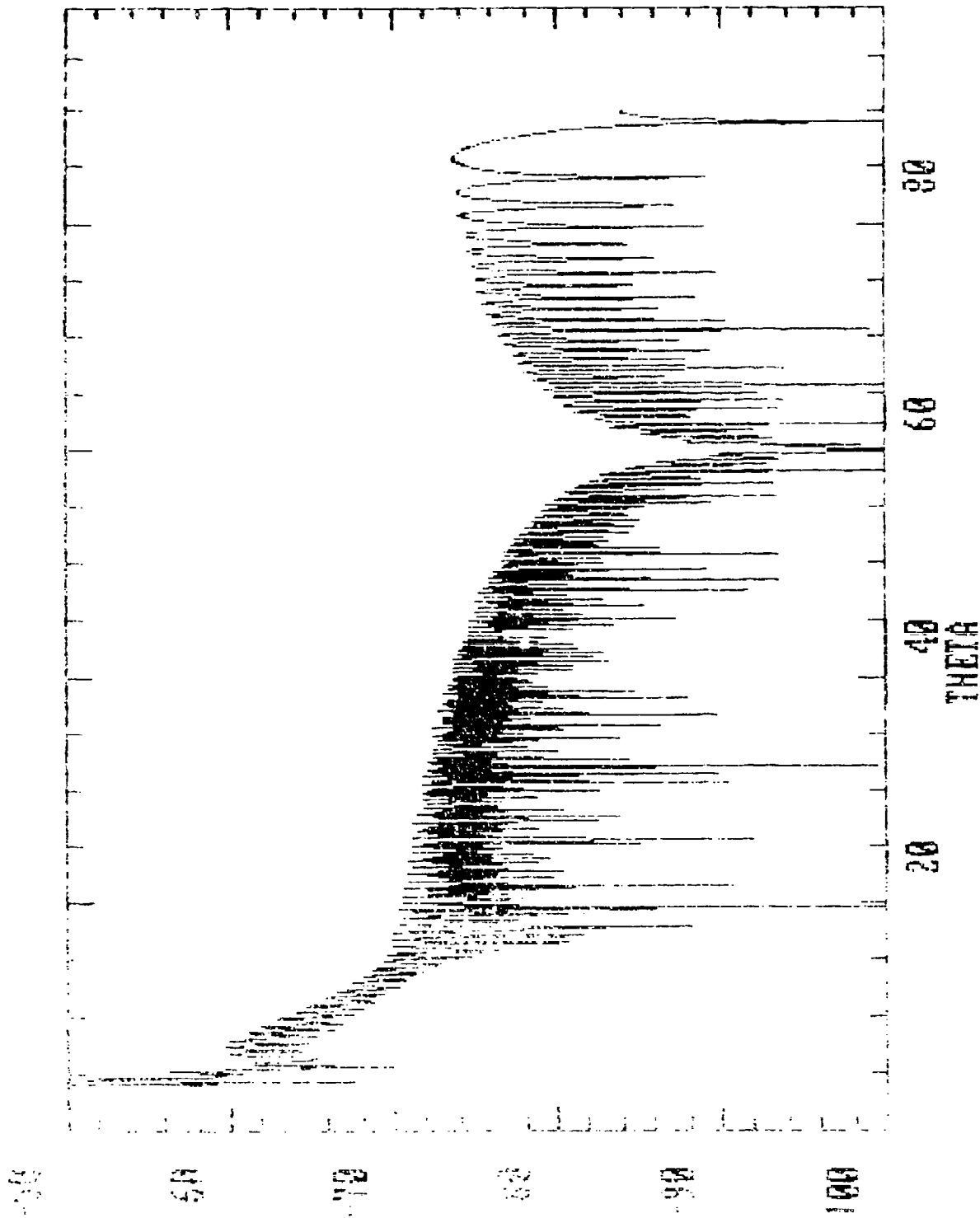


Fig.9 Third Order Term $Ro=150$

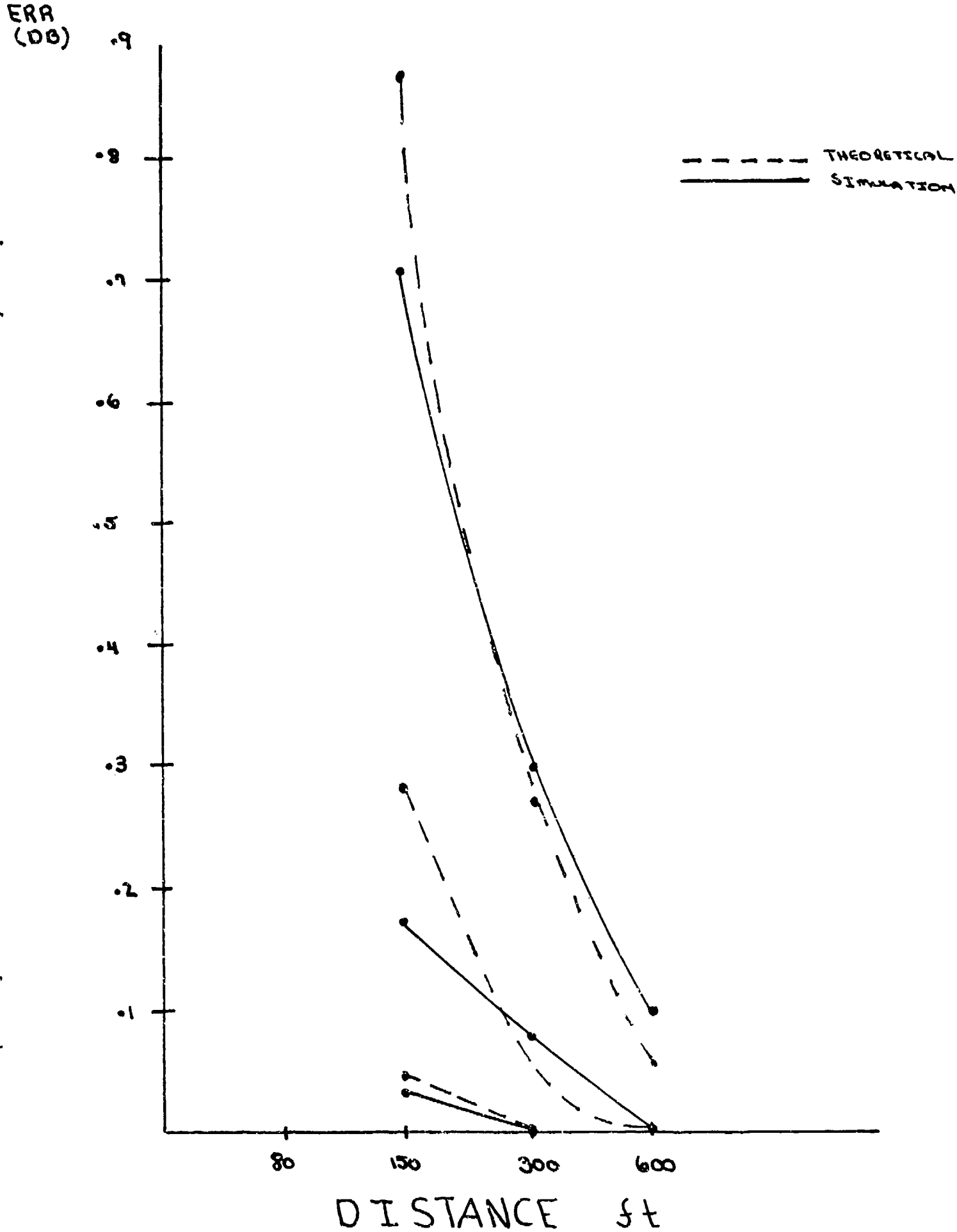


FIGURE 10: QUADRATIC ERROR RESULTS

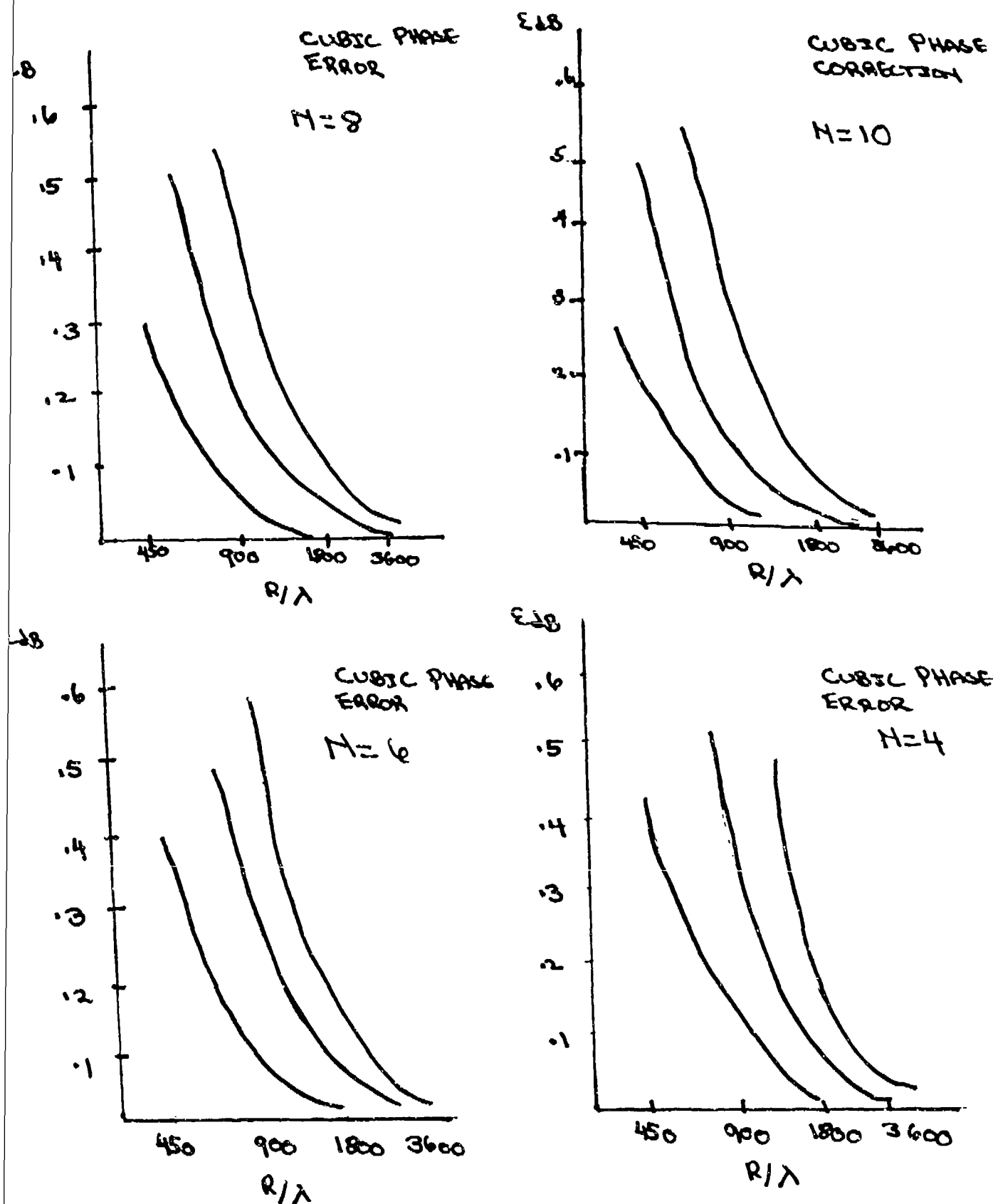


FIG. 11 AMOUNT OF PHASE SHIFTER CHANGE

N = PHASE SHIFTER SETTINGS.

R = DISTANCE (FT)

λ = WAVELENGTH

MATHEMATICAL MODEL OF A LARGE APERTURE FOCUSING ANTENNA

Thomas Smerczynski, RJO Enterprises, Inc. (IEEE Member)

Nathan Marchand, Marchand Electronics Laboratories (IEEE Member)

2nd Lt. Greg F. Smith, USAF RADC/EEV (IEEE Member)

Abstract - A methodology was developed using Holographic Metrology to study large aperture parabolic focusing antennas operating in the near field at 1-12 GHz. The methodology included the development of an algorithm characterizing the RF hologram. RF sources and reflections create the EMF phase and amplitude distribution across the aperture, which are used to calculate the RF hologram. The algorithm, as well, calculates the radial variation associated with intensity, a significant property when analyzing near field signals.

A computer model was developed to implement the algorithm, simulating an actual parabolic focusing antenna with an adjustable log-periodic dipole array feed. Extensive field tests were conducted and compared with output for various computer generated scenarios. Comparative analysis validated the use of the algorithm, proving the methodology successful.

I. INTRODUCTION

This paper describes the mathematical model used to determine the gain of very high frequency, large aperture antennas used for electromagnetic emission testing. The model was used to evaluate the gain at TEMPEST distances for a focusing parabolic reflector over a frequency range of 1.0 GHz to 12.4 GHz.

A computer model was established to replicate the mathematical model. The characteristics of a specified parabolic antenna with a log-periodic antenna at its focus were derived and integrated into the computer model as a test of accuracy and effectiveness.

The antenna under test was a 45-inch diameter Parabolic Focusing Antenna with an adjustable log-periodic dipole array feed. Field tests were performed at the Rome Air Development Center, Antenna Test Facility in Ipswich, Massachusetts. The results were compared to those obtained from the computer model, validating the algorithms mathematical model. Comparative data plots will be presented in the conclusion.

II. MODEL DESCRIPTION

Huygens was first to suggest that any wavefront could be regarded as an array of secondary sources and he postulated that the field of the secondary source should be entirely in the direction of the advancing wavefront. In addition, the Induction Theorem states that each secondary source is a combination of electric and magnetic current elements whose moments are respectively proportional to the magnetic and electric intensities tangential to the wavefront (Schelkunoff, pp. 357-358). What this means is that once we know the electromagnetic force phase and amplitude distribution across an aperture, we can determine by the radiation equations what the three dimensional radiated field distribution will be. When this is accomplished by using filters and lasers in the light frequency bands, the result is a hologram. Focusing to a point is a relatively simple application of these principles where the object is to obtain a three dimensional EMF pattern that converges to a point on the boresight vector line of an antenna.

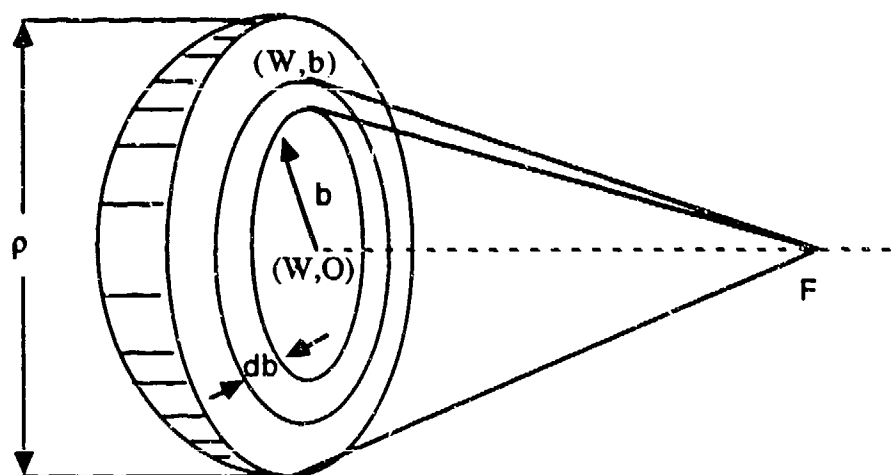


Figure 1 - Plane aperture of diameter " p " with a phase distribution that focuses the energy at the point F .

III. PARABOLA EQUATIONS

As shown in Figure 1, a plane circular aperture is illuminated by a point radiator at F, a point on the boresight WF of the aperture. The electromagnetic wave arriving at W, the center of the aperture, will lead in phase the EM wave arriving at b, the point on the aperture a distance b-O from the center. To bring into focus the radiator F it will be necessary to effectively match the phases in each differential portion of the aperture. In effect, it will be focusing on one element of a three dimensional, one color (frequency), hologram. The phases will be matched by means of a focusing parabola. (The parabola was used, even though it was not the optimum aperture for the task, because it was available to validate the model).

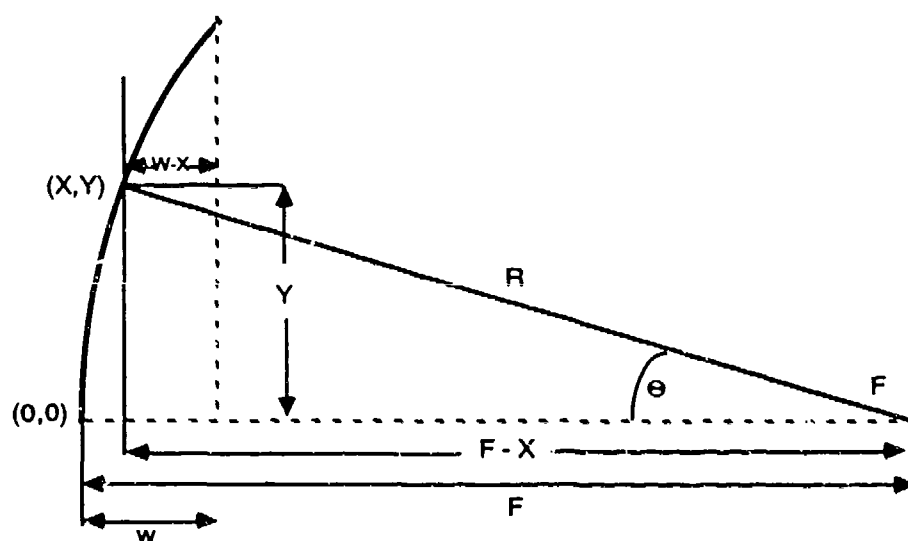


Figure 2 - Section through the center of a focusing parabola

From Figure 2 it can be seen that

$$(1) \quad (F-X)/R = \cos(\theta)$$

and

$$(2) \quad Y/R = \sin(\theta)$$

But for a parabola

$$(3) \quad F+W = R+W-X$$

or

$$(4) \quad R = F+X$$

Substituting Eq.4 into Eq.1 and solving for X

$$(5) \quad X = F \left[\frac{[1 - \cos(\theta)]}{[1 + \cos(\theta)]} \right]$$

Which can be reduced to

$$(6a) \quad X = F[\tan^2(\theta/2)]$$

Similarly, substituting Eq.5 into Eq.4 and solving for R

$$(6b) \quad R = F[\sec^2(\theta/2)]$$

And then using Eq.2

$$(6c) \quad Y = 2F[\tan(\theta/2)]$$

Thus the parabola is described in terms of F, a constant, the focal distance, and the variable, " θ ".

IV. MOVING THE TRANSDUCER

To vary the phase across the aperture, the transducer is moved out to B, the ray from the transducer at B, its new position, now makes an angle " Ψ " with horizontal. The new angle, " Ψ ", can be obtained in terms of " θ " by the following expression for its tangent.

$$(7a) \quad \text{TAN}(\Psi) = Y / (F+d-X) = \frac{2 F \text{TAN} \frac{\theta}{2}}{F+d-F \text{TAN}^2 \frac{\theta}{2}}$$

So that

$$(7b) \quad \Psi = \text{TAN}^{-1} \left[\frac{2 F \text{TAN} \frac{\theta}{2}}{F+d-F \text{TAN}^2 \frac{\theta}{2}} \right]$$

Also " β ", the angle the ray makes with the ray from " θ " is given by

$$(8) \quad \beta = (90^\circ - \Psi) - (90^\circ - \theta) = (\theta - \Psi)$$

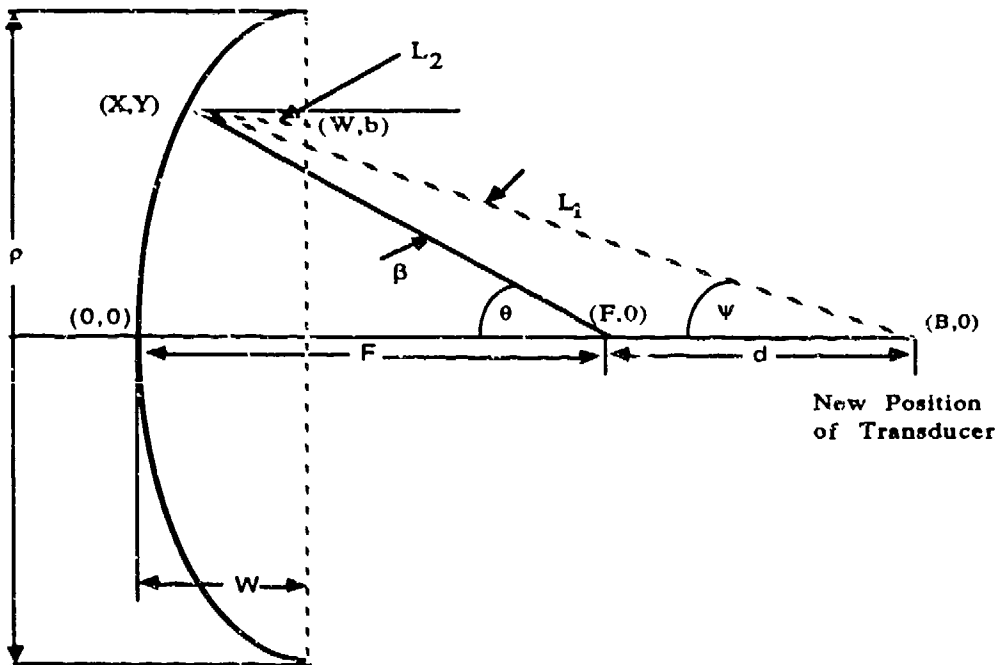


Figure 3 - Phase variation across the aperture when the transducer is moved an additional distance d out from F.

Using Snell's Equation which states that the angle of incidence equals the angle of reflection, the reflected wave, Xb, also makes an angle of " β " with the horizontal. Thus

$$(9) \quad \text{TAN}(\beta) = (Y-b)/(W-X)$$

And solving for b.

$$(10) \quad b = F\{[\text{TAN}(\theta-\Psi)][\text{TAN}^2(\theta/2)]+2\text{TAN}(\theta/2)\}-W\text{TAN}(\theta-\Psi)$$

In order to obtain the relative phase across the aperture, it is necessary to find the relative time delay. In free space, the distance delay is proportional to the time (or phase) delay. As a reference, the delay will be related to the normal distance delay of (F+D+W) as shown in Figure 4.

The relative delay, ΔL , for a transducer at the point B would be

$$(11) \quad \Delta L = L_1 + L_2 - (F+d+W)$$

Where

$$\text{COS}(\beta) = \frac{W-X}{L_2} = \frac{W-F\text{TAN}^2(\theta/2)}{L_2}$$

Or

$$(12) \quad L_2 = \frac{W-F[\text{TAN}^2(\theta/2)]}{\text{COS}(\beta)}$$

Thus

$$(13) \quad L_2 = \frac{W-F[\text{TAN}^2(\theta/2)]}{\text{COS}(\theta-\Psi)}$$

Where " Ψ " is shown in Eq. 7b.

$$(14) \quad \text{SIN}(\Psi) = Y/L_1$$

So that

$$(15) \quad L_1 = \frac{2F \tan(\theta/2)}{\sin(\Psi)}$$

Solving for " ΔL "

$$(16) \quad \Delta L = \frac{2F \tan(\theta/2)}{\sin(\Psi)} + \frac{W - F \tan_2(\theta/2)}{\cos(\theta - \Psi)} - (F + d + W)$$

Converting the distance to radians by, multiplying by $2\pi/\lambda$, and noting the phase variation in " ΔL " as " Φ ", we obtain:

$$(17) \quad \Phi = \frac{2\pi}{\lambda} \left[\frac{2F \tan(\theta/2)}{\sin(\Psi)} + \frac{W - F \tan(\theta/2)}{\cos(\theta - \Psi)} - (F + d + W) \right]$$

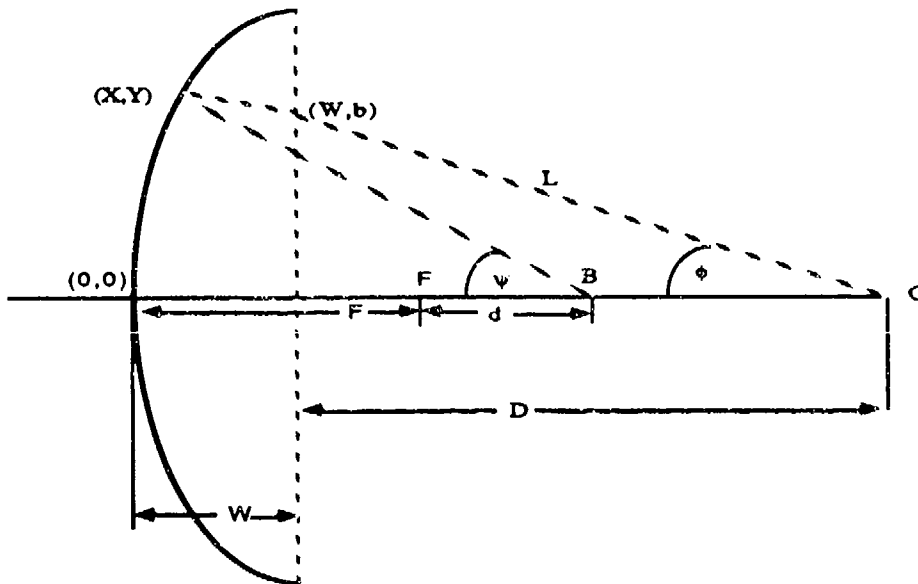


Figure 4 - Parabola focused on point C by moving the transducer from F to B.

V. TRANSDUCER EQUATIONS

As shown in Figure 4, the transducer is moved out to the point B, a distance d from the far field focusing point F, in order for the parabola to focus at the required point C, at distance D from the aperture plane. From the point C, the signal must travel a distance L to the aperture plane intercept (W,b). The angle the line L makes with the parabola normal is noted as " ϕ " so that:

$$(18) \quad L = D / (\cos(\phi))$$

However

$$(19) \quad \tan(\phi) = \frac{b}{D}$$

Using (10) and solving for " ϕ "

$$(20) \quad \phi = \tan^{-1} \{ [F/D] ([\tan(\theta - \Psi)] \tan^2(\theta/2) + 2 \tan(\theta/2)) - (W/D) \tan(\theta - \Psi) \}$$

Substituting into (18)

$$(21) \quad L = \frac{D}{\cos \{ \tan^{-1} [(F/D) ([\tan(\theta - \Psi)] \tan^2(\theta/2) + 2 \tan(\theta/2)) - (W/D) \tan(\theta - \Psi)] \}}$$

Again using the centerline distance of travel as the reference distance, the distance D is subtracted from L to get the relative phase variation to focus at the point C. Converting to radians, and calling this required phase variation "F" we get:

$$(22) \quad \phi = \frac{2\pi D}{\lambda} \left[\frac{1}{\cos \{ \tan^{-1} [(F/D) ([\tan(\theta - \Psi)] \tan^2(\theta/2) + 2 \tan(\theta/2)) - (W/D) \tan(\theta - \Psi)] \}} - 1 \right]$$

In order to have the antenna focus on the point C, the accumulative EM energy at the transducer should arrive, with the minimum phase difference, in all its components (This means that the energy arriving from each differential area on the aperture should add to the energy arriving from every other differential area with as little phase difference as possible). In other words, Φ plus Φ' should change as little as possible from one differential area on the aperture to the next. When this condition is met the antenna will effectively focus at the required point C.

VI. TRANSDUCER ANTENNA

To completely define the received vector, the relative amplitude of each differential radiated wave has to be determined. There are many possible transducer antennas, but since it was desirable to field test the methodology a log periodic dipole used with the antenna to be tested was used in the calculations. (Antenna Research Associates, Inc. antenna LPD-112/A). Referring to Figure 3, " Ψ " will vary with Y in accordance with

$$(23) \quad \text{TAN}(\Psi) = Y/(F+D-X)$$

or

$$(24) \quad \Psi = \text{TAN}^{-1}[Y/(F+D-X)]$$

Thus " Ψ " will have as its minimum

$$(25) \quad \Psi_0 = 0$$

Its maximum value will be its value at the edge of the dish (b equal to $\rho/2$). Calling this value " Ψ_p ",

$$(26) \quad \Psi_p = \text{TAN}^{-1}\{\rho/[2(F+D-X)]\}$$

Thus the relative amplitude used to determine the relative gain of the incident wave (effective amplitude) on the transducer is determined from the transducer pattern of width $2\Psi_p$. Since the pattern of a log periodic array is not omnidirectional but instead resembles a broadside dipole pattern, it was decided to use a cosine taper and define each frequency's taper by the available manufacturer's antenna pattern.

Actually, the E and H patterns were not similar nor exactly the cosine shape, but the differences were not significant enough to warrant the assumption of a complex taper. The major differences were above 10 Ghz, but even there the differences were less than 3 to 5 db.

Defining the Cosine taper in terms of the radial distance b:

$$(27) \quad \text{assumed Taper} = \cos(\pi b/Q)$$

Where Q is a constant for each taper and has to be determined from the log periodic antenna patterns. At b equal to zero the cosine is equal to one. At the edge of the dish where b is equal to $\tau/2$:

$$(28) \quad \cos(\pi \rho/2Q) = \frac{\text{Power at } \Psi_p \text{ (From the pattern)}}{\text{Power at } \Psi_o \text{ (From the pattern)}}$$

Thus the constant Q for a particular pattern is given by:

$$(29) \quad Q = \frac{\pi \rho}{2} \left[\frac{1}{\cos^{-1} \left[\frac{\text{POWER AT } \Psi_p}{\text{POWER AT } \Psi_o} \right]} \right]$$

Substituting into equation 27:

$$(30) \quad \text{TAPER} = \cos \left[\frac{2b}{\rho} \cos^{-1} \left[\frac{\text{POWER AT } \Psi_p}{\text{POWER AT } \Psi_o} \right] \right]$$

VII. WEIGHTING FUNCTIONS

The aperture distribution of assumed reradiators is circularly symmetrical such that a differential zone plate can be used for the differential reradiator. This yields a power weighting function, PWF, where:

$$(31) \quad \text{PWF} = 2\pi \left[\cos \frac{2b}{\rho} \right] \left[\cos^{-1} \left[\frac{\text{POWER AT } \psi_p}{\text{POWER AT } \psi_0} \right] \right] \text{ db}$$

As the transducer is moved farther away from the dish, the power also decreases with distance. (Refer to Figure 2). Let:

$$(32) \quad \delta_\theta = F + W$$

And:

$$(33) \quad \delta_\psi = F + W + d$$

Thus the power density correction factor, PDCF is given by:

$$(34) \quad \text{PDCF} = \delta_\theta^2 / \delta_\psi^2$$

The field intensity is also dependent on each differential reradiator in the aperture as well as the distance from each reradiator to the transducer. From Figure 4:

$$(35) \quad L = (D^2 + b^2)^{1/2}$$

And to account for the cosine taper that is being used, $\cos \Psi$ is incorporated where:

$$(36) \quad \cos(\Psi) = D/L = D / ((D^2 + b^2)^{1/2})$$

Taking the product to obtain the correction factor:

$$(37) \quad \cos(\Psi) = \frac{D}{(D^2 + b^2)^{1/2}} \cdot \frac{1}{(D^2 + b^2)^{1/2}}$$

Yielding:

$$(38) \quad \text{Pattern Intensity correction factor} = D / (D^2 + b^2)$$

VIII. INTEGRATION EQUATION

The relative differential intensity assumed to be reradiated from a differential zone plate, of width db , at the radial distance b from the center of the aperture is given by $dE\psi$ where P_0 is a constant determined by the feed antenna and the distances involved. Its value is unimportant in our case, because it will be canceled out when determining the relative antenna factor.

$$(39) \quad |dE\psi| = \frac{D}{D^2 + b^2} \left[\frac{\delta^2_\theta}{\delta^2_\psi} \left[\cos \left[\frac{2 b P_0 \cos^{-1} \left[\frac{\text{POWER AT } \psi_p}{\text{POWER AT } \psi_b} \right]}{\rho} \right] \right] \right] db \Bigg]^{1/2}$$

Integration can now be performed for the complete differential vector using the intensity from equation 39 and the phase angle, $\Phi + \Phi'$ from equations 17 and 22. Thus the field intensity at C, E_c , is given by

$$(40) \quad E_c = \int_0^{r_1} dE\psi / \Phi + \Phi'$$

In effect the phase is determined by the relative distances the signal travels from the point of origin to the transducer. The field intensity in the far field, E_f is obtained by assuming C in the far field. Similarly, the field intensity at one meter, E_a , is obtained by assuming C to be one meter.

The change in antenna factor is the ratio of the intensity received in the far field compared to the intensity received when the antenna is used at one meter. Thus, the change in antenna factor, (CAF), is given by:

$$(41) \quad CAF = 20 \log_{10}(E_f/E_n)$$

E_f is the relative intensity in the far field and E_n is the relative intensity at one meter.

IX. CONCLUSION

A final conclusion to this study is that the mathematical model for large aperture antennas, reconciled with the experimental work conducted on the antenna under test, demonstrates that the methodology is valid for determining the intensity for a given radial distance.

Figure 5 through figure 9 are plots comparing the field test data to the mathematical model output for a similar test scenario. The coordinates of the plots are gain (db) versus the point of focus (M). The results show remarkable resemblance given the fact that the model contained various approximations.

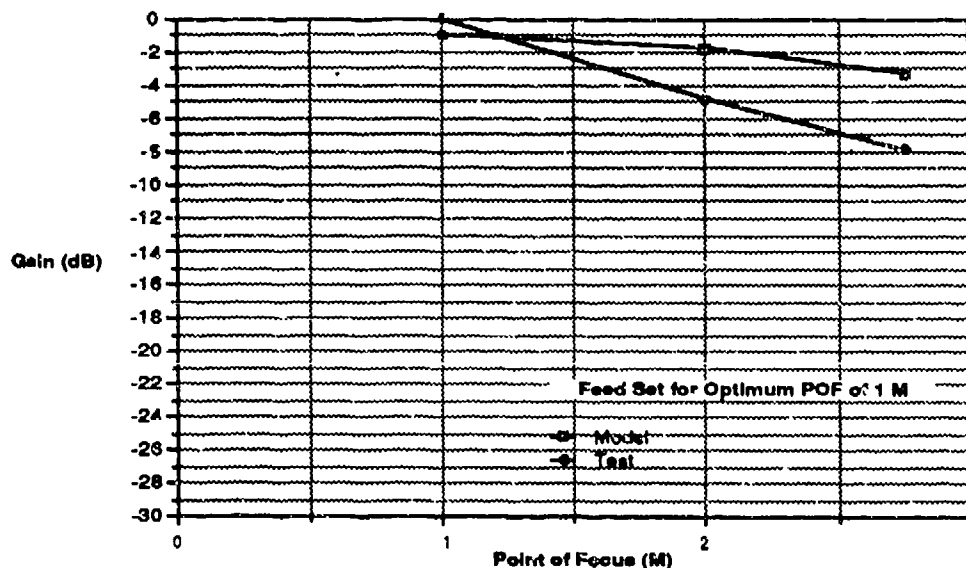


Figure 5 - Comparison of Test vs. Model at 2.6 GHz (S-Band)

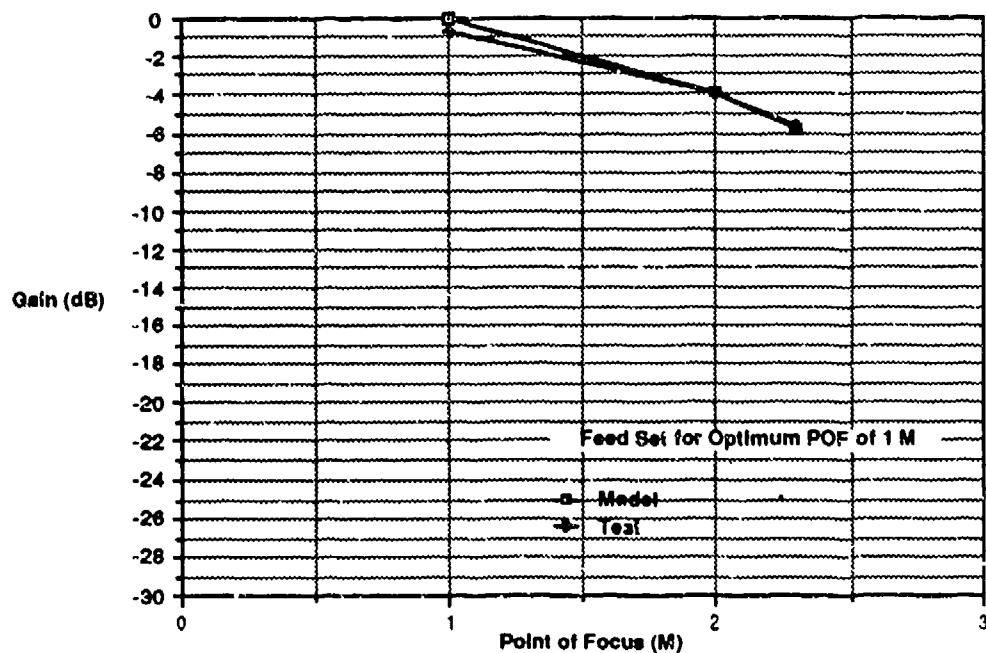


Figure 6 - Comparison of Test vs. Model at 4.0 GHz (S-Band)

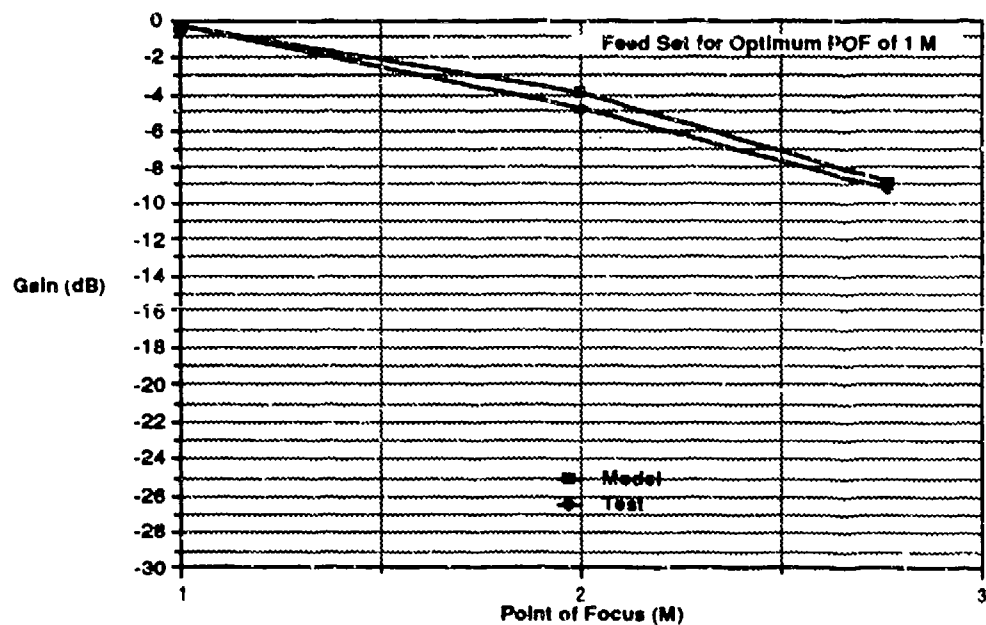


Figure 7 - Comparison of Test vs. Model at 4.0 GHz (C-Band)

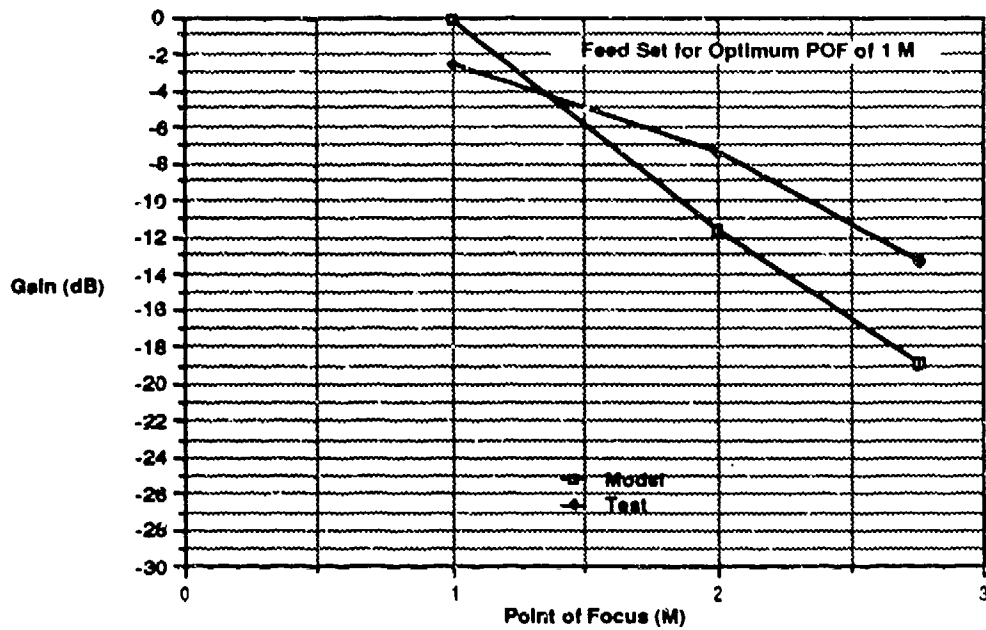


Figure 8. - Comparison of Test vs. Model at 6.0 GHz (C-Band)

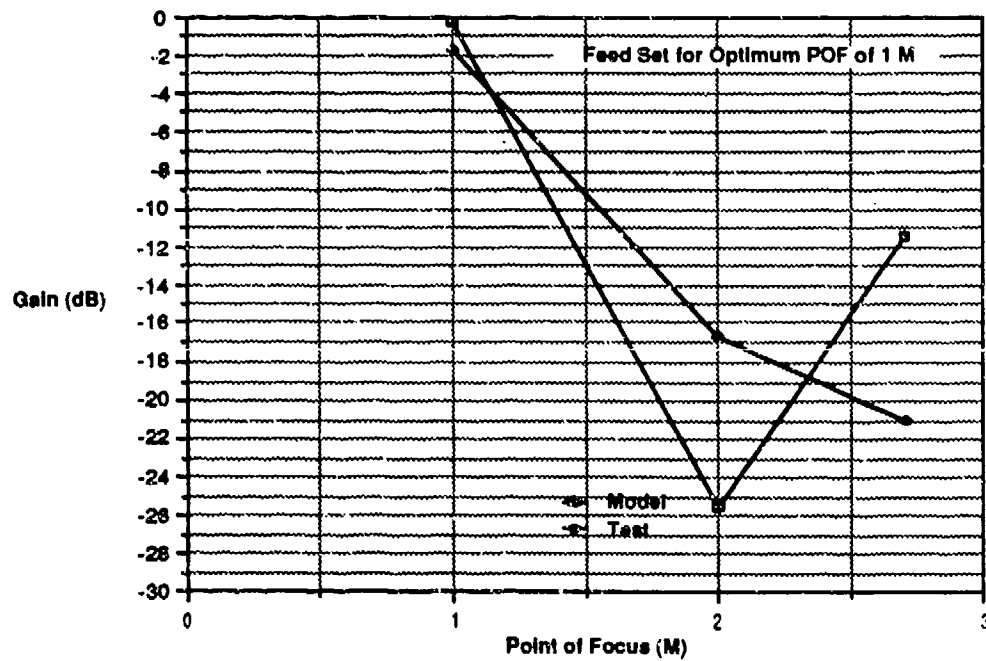


Figure 9 - Comparison of Test vs. Model at 8.0 GHz (C-Band)

This paper demonstrated that Holographic Metrology can be used to analyze the near field operator of large aperture antennas. Computer programs (see appendices A and B) for algorithms based upon this metrology can be formulated that describe the three dimensional (azimuth and elevation) distribution of sources and reflections that generate a specific aperture R.F. Hologram. The distribution obtained is unique.

References

1. Antenna LPD-112/A Product Literature, Antenna Research Associates, Inc., 11317 Frederick Ave, Beltsville, MD.
2. Kraus, J. D. Antennas, McGraw-Hill Book Company, Inc. 1950.
3. S.A. Schelkunoff, Electromagnetic Waves, D. Van Nostrand Company, New York, 1943.
4. Yariv, Amnon, Optical Electronics. CBS College Publishing. New York, 1985.

This work was performed under the auspices of USAF, RADC/EEV (Mr. Parker Vetrano), Hanscom Air Force Base, MA.

Brief Biographies

Thomas Smirczynski (S'85) received the B.S. degree in electrical engineering from Tufts University, Medford, MA. From 1985 - 1987 he served as a microwave antenna analyst for the Missile Systems Division of Raytheon Company, Bedford, MA. His experience is in advanced antenna system design, test, analysis and simulation for government applications.

He is currently employed by RJO Enterprises as a member of the Tactical Systems Group involved in TEMPEST antenna studies. Other projects include the design and installment of a digital microwave system for the Immigration and Naturalization Service (INS).

Nathan Marchand (A'39-M'44-SM'50-F64) was born in Shawinigan Falls, Quebec, Canada, on June 20, 1916. He received a B.S.E.E. degree from the College of the City of New York in 1937 and an M.S.E.E. degree from Columbia University in 1941.

He started his engineering career as a senior engineer with the ITT Federal Laboratories in 1941 and left full time employment in 1945 to start his own company. During World War II he introduced and taught courses in Microwave and Antenna Theory at Columbia University. After the war he joined the Graduate Faculty at the University as a lecturer in Electromagnetic Theory, Antenna Design, Frequency Modulation, and Television. He also taught Electromagnetic Theory and Transient Analysis at the Polytechnic Institute of Brooklyn.

As air travel grew he was a special consultant to the Air Navigation Development Board, the Airways Modernization Board, and the FAA on Air Traffic Control Communications. He also did a special study on Communications in the Air Traffic Control environment for the Special Assistant to the President for Aviation Facilities. He was also a member of the Radio Technical Commission for Aeronautics (RTCA) Special Committee 121 where he headed up the sub-committee on data communications for use by commercial aircraft.

From 1951 to 1954 he was an expert consultant to the US Air Force at Cape Canaveral (Kennedy) where he initiated basic improvements in tracking and telemetry.

From 1962 to 1966 he acted as technical advisor to the executive vice president of ITT Communications Systems in all matters concerning the design of the 480L Defense Communication System, the Deputy for Communications for the US Air Force and the Defense Communication Agency (DCA). He was a member of the Princeton Durbin committee to study the LOH helicopter and headed the subcommittee evaluating the avionics.

Since then, while under contract to the US Army and Air Force on various programs in electronic warfare, he was chairman of the special committee on the design and operation of the Micro-navigation and Position Location System (MNPLS) for the US Army Avionics Laboratories at Fort Monmouth and chaired the special committee that evaluated the TACFIRE program for the department of the Army. He was a member of the Standard Lightweight Avionics Equipment (SLAE) Task Force to determine how to reduce failure rates of SLAE radios. Just previous to that he had chaired a special committee that investigated and cleared up failure problems with the SLAE radios.

He also served as a consultant to Mitre Corporation on the Mitre study for the 1995 Air Traffic Control System.

He has done fundamental research in information theory. He was the organizer and first chairman of the Professional Group on Information Theory. As a staff member of the NYU-Medical Center he contributed to cardiac research and the application of electronic techniques to the diagnosis of heart disease.

He is a member of Eta Kappa Nu, Tau Beta Pi and Sigma Xi. In 1965 he was elected a fellow in the American Association for the Advancement of Science. He is a registered Professional engineer in the State of Connecticut and holds an Airman Certificate as a private pilot. At present he is president of Marchand Electronic Laboratories, Incorporated in Greenwich, Connecticut.

2nd Lt. Greg F. Smith (S 86) received the B.S. degree in electrical engineering from Norwich University in Northfield, Vermont. He is currently a candidate for the MSEE degree from the University of Lowell in Lowell, Massachusetts. In 1985, Greg performed a study of attenuation and refraction of millimeter waves in the earth's environment for the National Security Agency (NSA).

He is currently employed as a second lieutenant in the United States Air Force as a communications security engineer for the Rome Air Development Center. Present projects include the development of an optical analysis system, the study of EMI in the office environment and the development of portable field analysis systems.

APPENDIX A

```

!Parabola Program "TASRJO" - CORRECTION FACTOR
!UPDATED OCTOBER 27, 1987
!THIS PROGRAM VARIES THE LOCATION OF THE FEED
!"SMD" FOR A FIXED POINT OF FOCUS "D" - THE
!OUTPUT FILE GENERATED "ATE180" IS FORMATTED AS
!POWER INTENSITY VERSUS THE POINT OF FOCUS - THIS
!DATA FILE IS THEN INSTALLED INTO THE PLOT FILE
!"PLSMUZ"
!
!DEFINITION OF VARIABLES
!
!FREQ = FREQUENCY
!RTOD = RADIANS TO DEGREES
!DTOR = DEGREES TO RADIANS
!TFI = TWO*PI
!C = SPEED OF LIGHT
!TPIL = TWO - PI DIVIDED BY LAMBDA
!SMD = FEED LOCATION WITH RESPECT TO THE POF
!D = POINT OF FOCUS
!F = FOCAL POINT
!RHO = Y - INTERCEPT OF THE DISH
!W = X - INTERCEPT OF THE DISH
!CASE = FILE CONTAINING FEED DISTRIBUTION
!ATE180 = OUTPUT FILE CONTAINING INTENSITY
!VALUES FOR VARIOUS
!POINTS OF FOCUS AT A GIVEN FREQUENCY
!FACTOR = THE POWER INTENSITY
!POF = POINT OF FOCUS
!
CREATE BDAT "TV346",200,8
ASSIGN @Path2 TO "TV346"
ASSIGN @Path3 TO "CASE3"
C = 300000000
Tpi = 2*PI
Rtod = 180/PI
Dtor = PI/180
Freq = 1.2E+10
F = .50055
W = 6.61/39.37
RHO = 22.75/39.37
Lambda = C/Freq
Tpil = Tpi/Lambda
DIM Rhopwr (60)
Smd = .346
FOR X = 1 TO 60
    ENTER @Path3, X; Rhopwr (X)
NEXT X
D = .6787
FOR T = 1 TO 200
    Z = F+Smd
    Rel = 0
    Imag = 0
    Delt = F+W
    Delp = F+W+Smd
    Sqdt = Delt*Delt
    Sqdp = Delp*Delp
    Delsq = Sqdt/Sqdp
    Ref = Tpil*(F+Smd+W+D)
    N = 0
    Taper = 0
    Prime = 0
    Reffaz = 0
    Capphi = 0
    Tpwrrh = 0
    Relsq = 0
    Imagsq = 0
    Sumsq = 0
    Magpsi = 0
    Factor = 0

```

```

Db = .05
!
!ENTER LOOP TO CALCULATE THE POWER INTENSITY
!OVER THE ANGLE "THETA" AT A GIVEN POF
!
FOR Theta = 1.0 TO 60.0
    N = N+1
    Hlfeta = (.5*Theta)*Dtor
    Tanhlf = TAN(Hlfeta)
    Tansq = Tanhlf^2
    R = F/(COS(Hlfeta)^2)
    X = F*Tansq
    Y = 2*F*Tanhlf
    Psi = ATN((Y)/(Z-X))
    Psi = Psi/Dtor
    Beta = Theta-Psi
    Beta = Beta*Dtor
    Psi = Psi*Dtor
    B = F*(TAN(Beta)*Tansq+2*Tanhlf)-W*TAN(Beta)
    Wft = W-X
    Capphi = Tpil*((Y)/SIN(Psi)+(Wft)/COS(Beta))
    Bsq = B*B
    Dsq = D*D
    Bplsd = Bsq+Dsq
    Rdcomp = D/Bplsd
    Sqdb = SQR(Bplsd)
    Pprime = Tpil*(Sqdb)
    Reffaz = (Pprime+Capphi)-Ref
    Pwr = Rhopwr(Theta)
    Taper = Tpi*B*Db*COS((2*B/Rho)*ACOS(Pwr))
    Pwrtht = SQR(Taper*Delsq)*Rdcomp
    Tpwrrh = Tpwrrh+Pwrtht
    Intpsi = SQR(Taper*Delsq)*Rdcomp
    Rel = Rel+Intpsi*COS(Reffaz)
    Imag = Imag+Intpsi*SIN(Reffaz)
NEXT THETA
!
! EXIT "THETA LOOP" AND DETERMINE "FACTOR"
!
    Relsq = Rel*Rel
    Imagsq = Imag*Imag
    Sumsq = Relsq+Imagsq
    Magpsi = SQR(Sumsq)
    Factor = Magpsi/Tpwrrh
OUTPUT @Path2,T;Factor
D = D+.005
NEXT T
END

```

APPENDIX B

```

!THIS PROGRAM PLOTS THE OUTPUT FILE GENERATED
! FROM "TASRJO" - THE DATA IS PLOTTED AS
! POWER INTENSITY VESUS POINT OF FOCUS
ASSIGN @Path TO "ONE000"
INPUT "ENTER # OF DATA POINTS", Sata
INPUT "ENTER X - AXIS LENGTH IN METERS", Scat
DIM Dumy(200)
FOR X = 1 TO Sata
  ENTER @Path,X;Dumy(X)
NEXT X
PLOTTER US 705,"HPGL"
PEN 5
VIEWPORT 10,110,10,95
FRAME
AXES 4,10
CSIZE 4,.27
G = 8
Test = .1
MOVE 0,0
FOR X = 1 TO 5
  MOVE 1,G
  LABEL TEST
  TEST = TEST+.2
  G = G+20
NEXT X
Test1 = .4545
Testot = Test1
G = 9
FOR Y = 1 TO 11
  MOVE G,2
  LABEL Testot
  Testot = Testot+Test1
  G = G+11.5
NEXT Y
PEN 5
GRID 12,10
PEN 5
MOVE 70,80
CSIZE 4,.3
LABEL "INTENSITY"
MOVE 70,75
LABEL "AMP VS. METERS"
MOVE 70,70
LABEL "FREQUENCY = 1.0 GHZ"
MOVE 70,65
LABEL "POINT OF FOCUS IS OPTIMIZED FOR THE FAR
FIELD"
MOVE 0,0
FOR T=1 TO Sata
  Dumx = T*(133/Scat)
  Dumx = Dumx*(Scat/Sata)
  Dumy(T) = Dumy(T)*100
  DRAW Dumx,DUMY(T)
NEXT T
PEN 0
END

```

ABSTRACT

Reflector antennas on earth orbiting spacecrafts generally cannot be described analytically. The reflector surface is subjected to large temperature fluctuation and gradients, and is thus warped from its true geometrical shape. Aside from distortion by thermal stresses, reflector surfaces are often purposely shaped to minimize phase aberrations and scanning losses. To analyze distorted reflector antennas defined by discrete surface points, a numerical technique must be applied to compute an interpolatory surface passing through a grid of discrete points. In this paper, the distorted reflector surface points are approximated by two analytical components; an undistorted surface component and a surface error component. The undistorted surface component is a best fit paraboloid polynomial for the given set of points and the surface error component is a Fourier series expansion of the deviation of the actual surface points, from the best fit paraboloid. By applying the numerical technique to approximate the surface normals of the distorted reflector surface, the induced surface current can be obtained using physical optics technique. These surface currents are integrated to find the far field radiation pattern.

ANALYTICAL APPROXIMATION OF A DISTORTED REFLECTOR SURFACE DEFINED BY A DISCRETE SET OF POINTS

Roberto J. Acosta and Afroz A. Zaman

National Aeronautics and Space Administration
Lewis Research Center
Cleveland, Ohio 44135

1. Introduction

Reflector antennas in a space environment are subjected to continuous variation in temperature distribution, and are thus distorted from its true geometrical shape (typically parabolic, hyperbolic, elliptical, etc.). The distorted reflector surface has in general a very complicated shape and hence can not be represented with an analytical expression. The analysis of a distorted reflector antenna defined by a set of discrete surface points require the use of numerical techniques. Many numerical techniques for analyzing the performance of reflector antennas defined by a set of points have been extensively reported in the open literature (refs. 1-4). The most popular of these techniques represent the reflector surface either globally or locally by using polynomial splines (refs 5,6). The polynomial splines and other techniques require the surface points to be orderly labeled. This is an undesired characteristic because it can result in a nonunique approximation for the desired reflector surface. The order of the spline polynomial necessary to best fit the reflector surface points is in general unknown a priori, and therefore it involves a trial and error procedure for checking the accuracy of the interpolation.

The distorted reflector surface points can be best approximated by two analytical components, an undistorted surface component and a surface error component. The undistorted surface component is a best fit paraboloid polynomial for the given set of points and the surface error component is the deviation of the actual surface points from the best fit paraboloid. This residual error component is then described with a sinusoidal Fourier series expansion. This approximation technique is insensitive to the labeling of the reflector surface points and can describe the surface errors very accurately. Similar to a time signal the spatial spectrum of the surface error component is unique to the reflector under consideration. Therefore spatial spectra can be utilized as a performance index for comparing distortion profiles in reflector antennas.

2. Description of the Problem

The best analytical representation of the distorted reflector antenna surface that uniquely identifies the surface errors can be obtained as follows: the reflector surface points are separated into two components, a best fit paraboloid component and a sinusoidal Fourier series expansion of the residual (ref. 7). Figure 1 illustrates a conceptual layout of the problem under consideration.

In analyzing large reflector antenna performance it is necessary to accurately characterize the reflector surface points. Any deviation from its ideal geometry causes the antenna performance to degrade. The surface error component provides an independent performance index against which distorted reflector antennas can be compared. The surface error component by definition is a sinusoidal Fourier series expansion of the difference between the actual reflector surface points and the best fit paraboloid geometry. Information such as root mean square value (RMS), peak surface error and two-dimensional distortion profile can be calculated from the surface error component. Fourier coefficients in the series expansion represent the spatial spectrum that uniquely identifies the distorted reflector under study. The best fit paraboloid surface represents the reflector antenna surface in an average sense. When the surface error is zero the best fit paraboloid surface reduces to the ideal or the design surface geometry.

3. Numerical Results and Discussion

Figure 2 represents a block diagram of a computer simulation of the above stated problem. The reflector surface points are usually obtained from a holographic, photogrametric or any other surface detection technique. The computer algorithm was tested with known distortion profiles and TRASYS-SYNDA-NASTRAN (Ref.1) simulated thermal distortions superimposed into a reflector antenna geometry.

The distortion profiles considered for the simulation are described in Table 1 and the reflector geometry illustrated in figure 3. Case A in Table 1 describes a small ($\lambda/20$ or less) distortion profile and case B illustrates a large (in the order of several wavelengths) distortion profile. The frequency used for the simulation was 10 GHz. A set of equally spaced data points (100,100) were needed to generate the distorted reflector surface. The estimated surface errors and best fit paraboloid surface geometry are described in Table 2.

Figures 4(a) and (b) show the estimated surface profile corresponding to case A and case B and their respective far field radiation patterns. The results presented in table 2 are in good agreement with the

input distortion by Fourier coefficients in Table 2. It was found that the Fourier matrix had higher order coefficients with non zero values but they were one order of magnitude less than the lowest amplitude of the Fourier coefficient presented in Table 2.

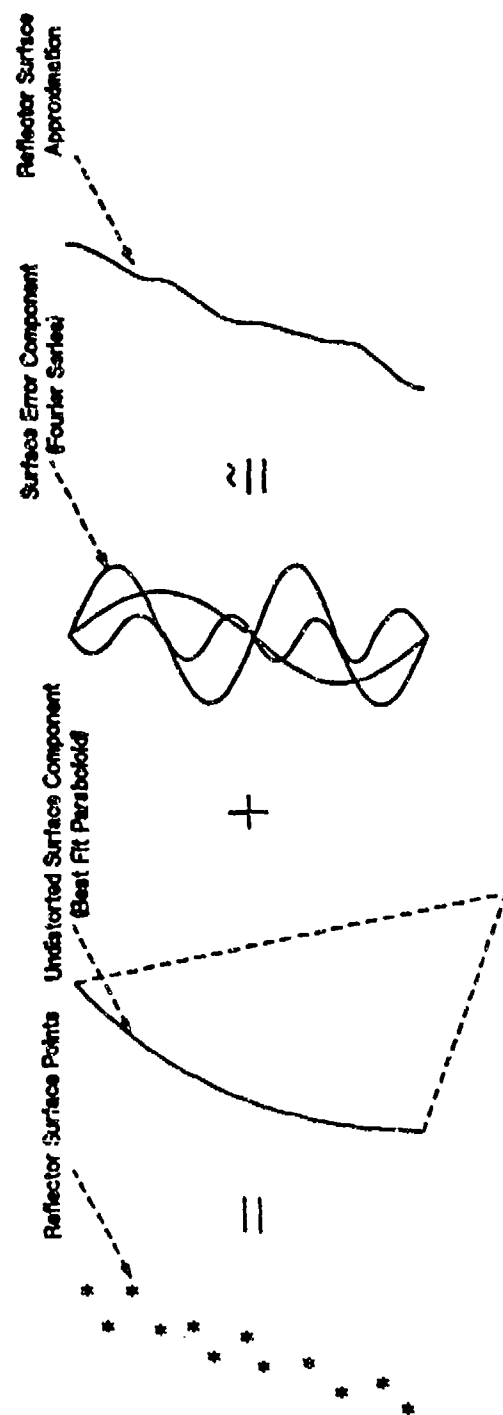
The technique was compared with results obtained by using a spline polynomial fit for approximating the distorted reflector surface points (ref . 1) In this case the distorted reflector surface points were obtained by simulating thermal deformation with a TRASYS-SYNDA-NASTRAN computer programs. In brief, TRASYS and SINDA are used to characterize the in-orbit thermal environment; NASTRAN calculates the thermally induced mechanical distortions. Figure 5 shows the temperature distribution on the reflector antenna surface for the case under consideration. The reflector geometry input to the thermal programs is presented in fig. 6. The frequency considered was 28.75 GHz and (100,100) surface points were used for the analysis. The far field radiation pattern corresponding to the thermal simulation case is presented in figure 7. The continuous line pattern corresponds to the polynomial spline algorithm and dotted line pattern corresponds to the best fit paraboloid and Fourier series expansion approximation. There are no major differences between the beam direction and sidelobe levels, indicating a good agreement between the two techniques. The best fit paraboloid and Fourier series algorithm was very slow: 3 hr. of c.p.u. time in an IBM 370 computer. The spline polynomial algorithm takes about 1/2 hr. on a CRAY XMP computer. The long computation can be justified as a trade-off to obtain vital information about the distorted surface characteristics. These are the amplitude spectra of the surface error, the distorted surface profile, RMS value and the largest deviation on the reflector antenna surface. These are not directly available from any of the other existing techniques.

4. Concluding Remarks

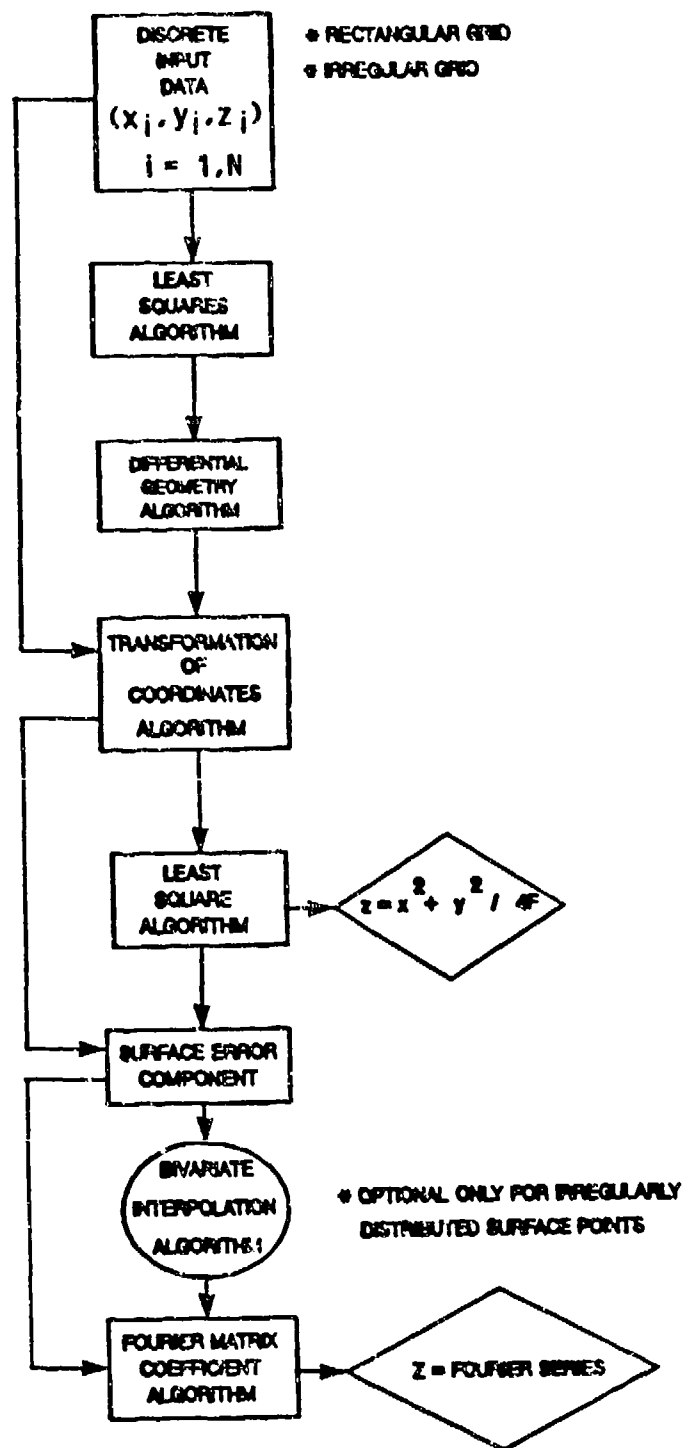
One advantage of the developed technique is that it can be easily implemented to any existing reflector antenna secondary pattern computational method. It can easily be extended to nonparabolic reflectors surfaces (spherical, planar, hyperbolic, elliptical, etc.) by modifying the least square polynomial approximation. In applications involving the fabrication and design of precision reflector antennas the technique can be used as a computer aided tool. Information such as the average focal length, a root mean square of the surface error, surface error profile and the amplitude spectra of the reflector antenna under consideration are easily accessible from the algorithm. One draw back of the algorithm is that it is slow. This can be improved by using a faster computer such as a CRAY and optimizing the computer codes.

REFERENCES

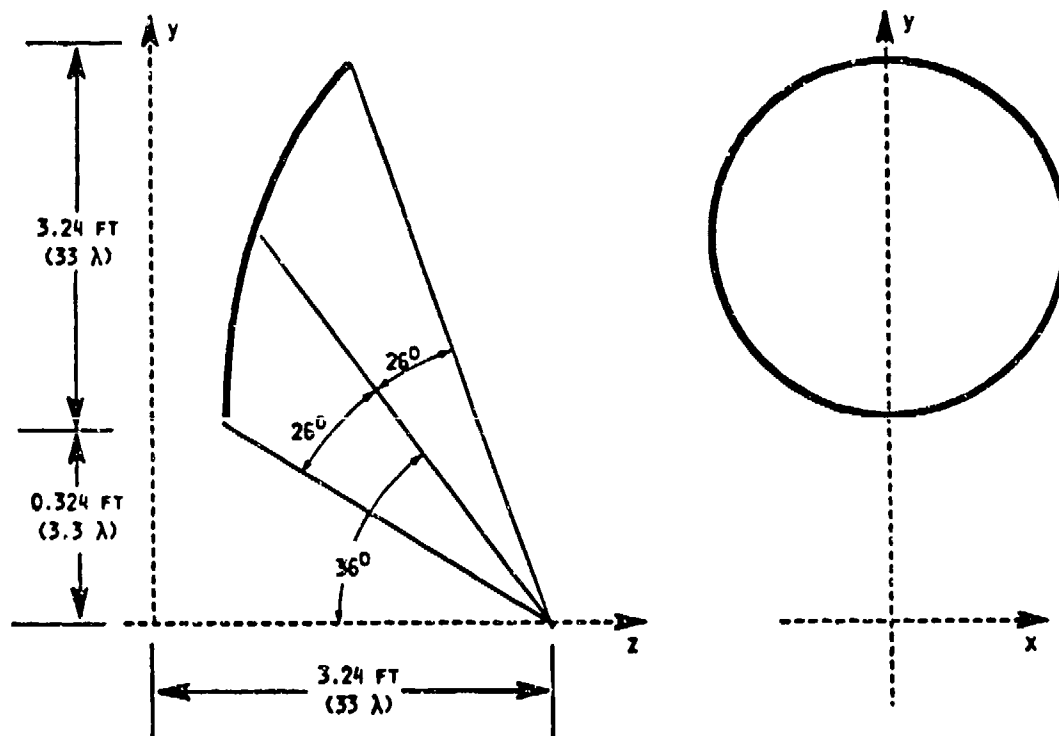
1. Steinbach, R.E.; and Winegar, S. R.: Interdisciplinary Design Analysis of a Precision Spacecraft Antenna 26th Structure, Structural Dynamics and Materials Conference, Part 1, AIAA, 1985, pp.704-712.
2. Ngai, E. C.; and Profera, C. E., Jr. : Application of Bivariate Interpolation to Antenna Related Problems. IEEE Trans. Antennas Propag., vol AP-32, no. 7, July 1984, pp.735-739.
3. Chan, K. K. and Raab, A. R.: Surface-Current Analysis of Distorted Reflector Antennas. IEE Proc., vol. 128, pt. H, no. 4, July 1981, pp. 206-212.
4. Lee , R. Q. and Acosta , R. : A Numerical Method for Approximating Antenna Surfaces Defined by Discrete Surface Points, NASA TM 87125, September 1985
5. DeBoor, C. : Bicubic Spline Interpolation. J. Mathematics and Phys., vol. 41, 1962, pp. 212-218.
6. Davies, W.A. : Splines for Electromagnetics. IEEE Trans. Antennas Propag., vol. AP-30, no. 4, July 1982, pp. 760-764.
7. Acosta , R. J. : Active Feed Array Compensation for Reflector Antenna Surface Distortions, NASA TM 100826, June 1988.



1 Distorted reflector surface points separated into an undistorted surface component and a surface error component.



2 Computer implementation for obtaining an analytical representation for a reflector surface defined by a set of points.



3 Offset parabolic reflector geometry

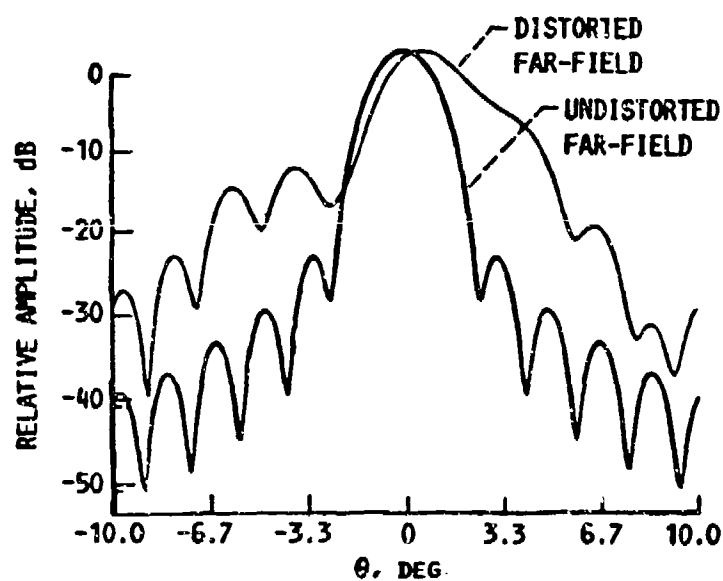
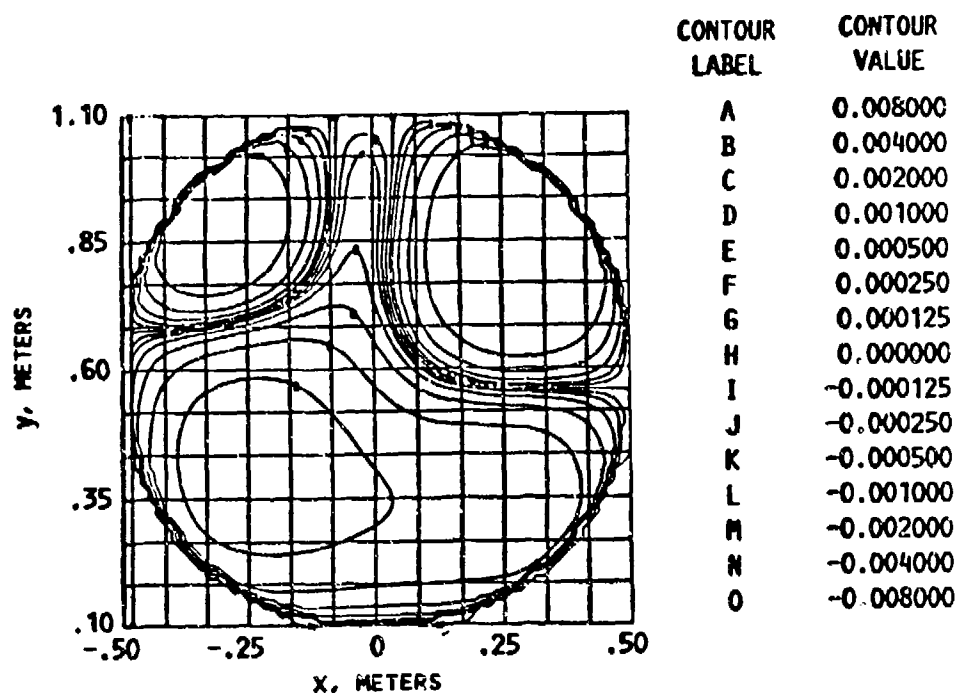
TABLE 1 - DISTORTION PROFILE PARAMETERS

	Fourier Coefficients (in wavelength)								
	d_{11}	d_{12}	d_{13}	d_{21}	d_{22}	d_{23}	d_{31}	d_{32}	d_{33}
Case A	+0.0500	+0.0700	-0.0300	+0.1500	-0.0040	+0.0900	-0.0033	-0.0083	-0.0310
Case B	+0.0300	+0.3000	-2.000	-3.000	+0.4000	+3.000	-1.000	+5.000	-0.3000

TABLE 2 - ESTIMATED DISTORTION PROFILE PARAMETERS

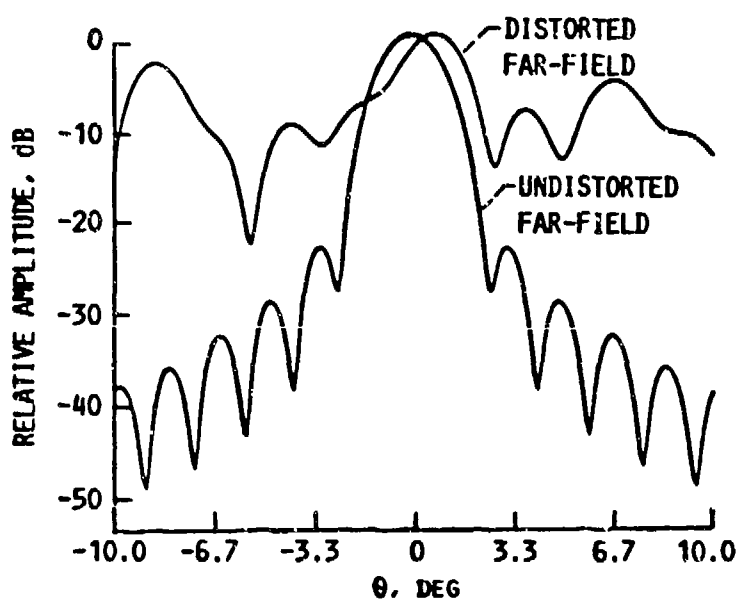
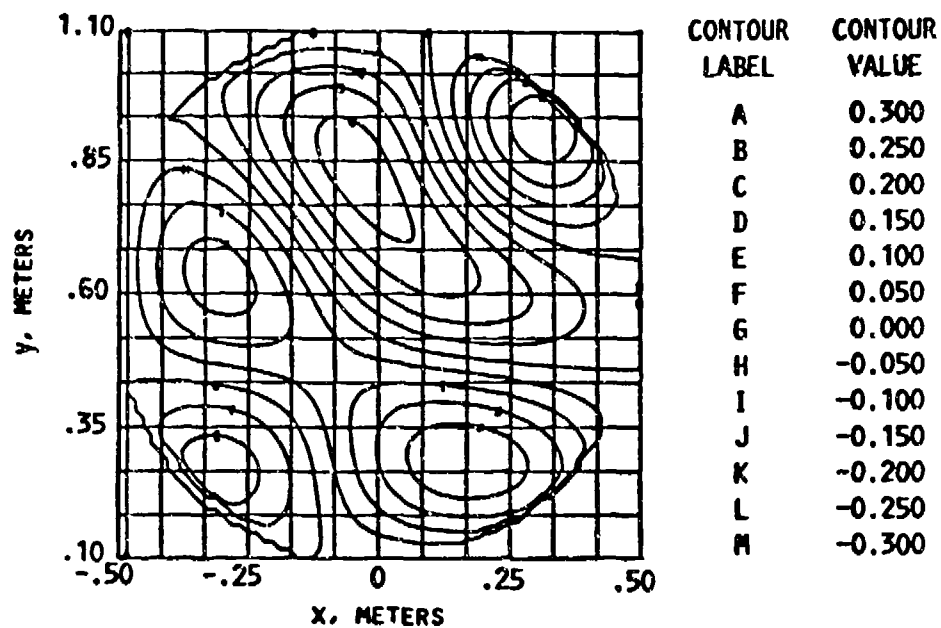
	Fourier Coefficients (in wavelength)								
	d_{11}	d_{12}	d_{13}	d_{21}	d_{22}	d_{23}	d_{31}	d_{32}	d_{33}
Case A	+0.0497	+0.0710	-0.0305	+0.1501	-0.0039	+0.0913	-0.0032	-0.0082	-0.0312
Case B	+0.0318	+0.2999	-1.998	-2.999	+0.4108	+2.988	-0.9999	+5.100	-0.2991

Estimated focal length:
Case A 3.290109 ft
Case B 3.313091 ft



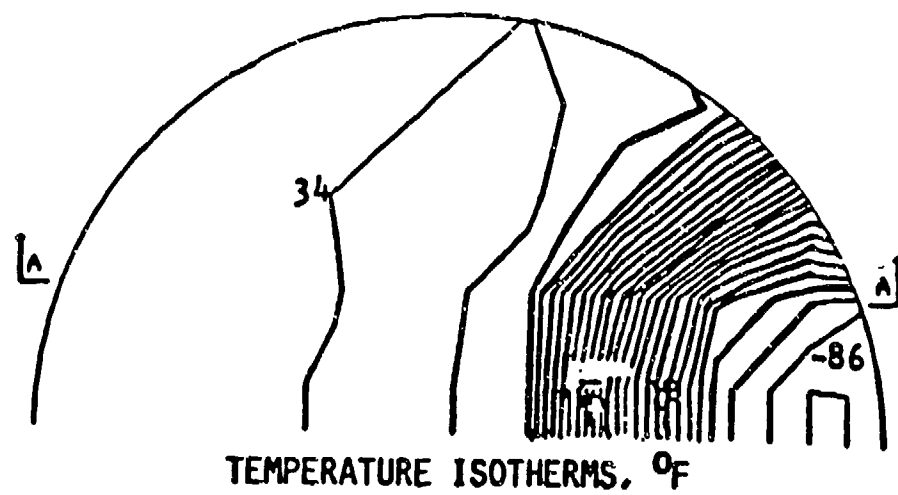
(a) Case A (small distortion profile).

4 E-plane radiation pattern and their estimated distortion profile.

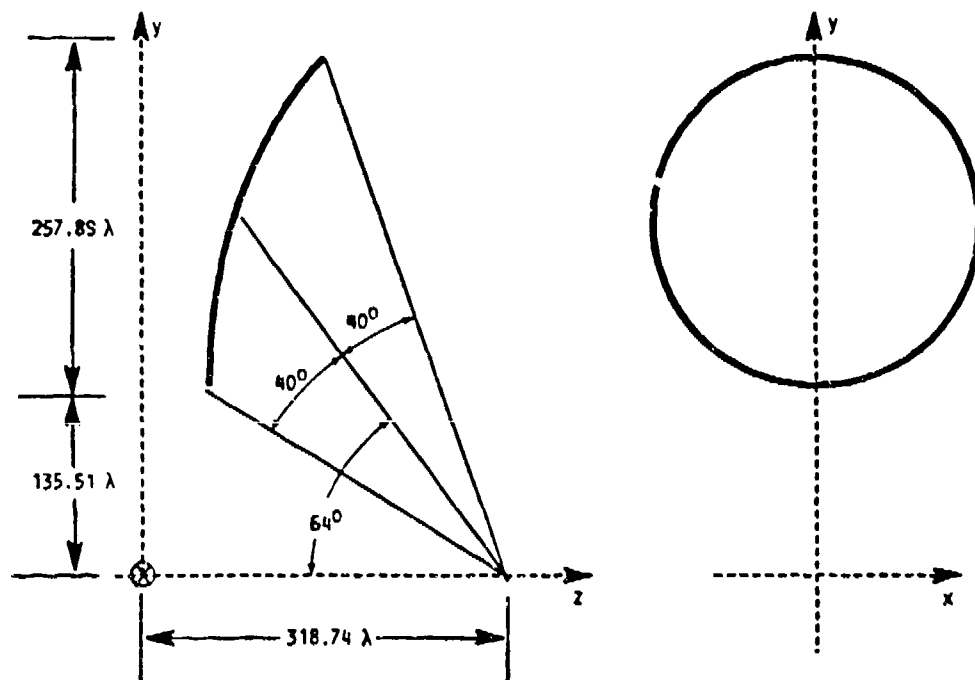


(b) Case B (large distortion profile).

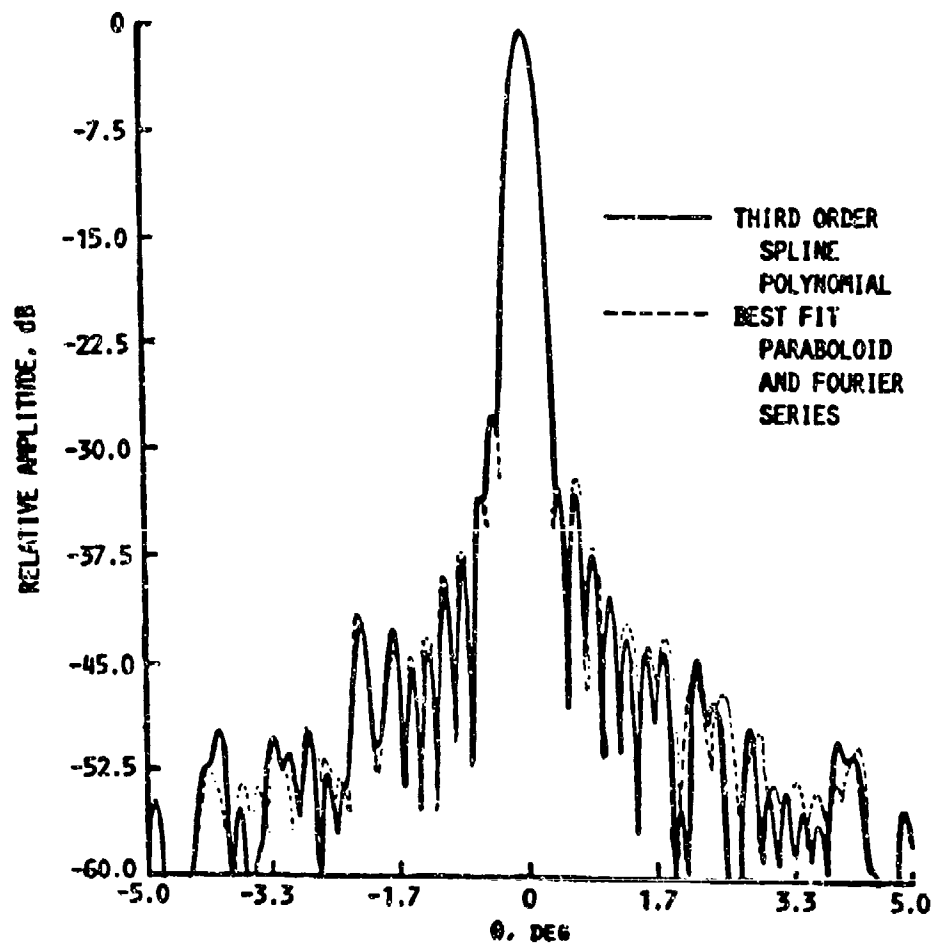
Fig. 4 - Concl.



5 Temperature distribution on the reflector surface



6 Offset parabolic reflector geometry



7 E-plane radiation pattern

THE FLEXIBLE ADAPTIVE SPATIAL SIGNAL PROCESSOR

RICHARD N. SMITH
ANTHONY M. GRECI
SALVATORE A. CAROLLO
DOROTHY JACKSON
EDWARD TOUGHLIAN

Rome Air Development Center
Griffiss Air Force Base, NY 13441-5700

ABSTRACT

This paper will describe the Adaptive Spatial Signal Processing Test Facility and some of the experimental results obtained using the facility. The test facility consists of an anechoic chamber, antenna pattern measurement equipment, and the Flexible Adaptive Spatial Signal Processor (FASSP).

Methods of implementing antenna arrays and spatially distributed RF signal/interference scenarios using the anechoic chamber are described. The use of antenna pattern measurement equipment to aid in the configuration of antenna arrays and positioning of signal/interference sources is also presented.

The capabilities of the FASSP are described. The different hardware modes of the FASSP and the methods of adaptive beamforming and nulling are described. Data from different arrays, scenarios, adaptive

algorithms and FASSP hardware configurations is presented.

The test bed has recently been enhanced by the addition of a systolic array processor. The function and capabilities of this adaptive processor will be described.

An effort to upgrade the test facility by employing optical fiber transmission lines is also discussed in the paper.

1. INTRODUCTION

In an effort to employ the interference suppression capabilities of adaptive antenna technology in military communications systems, many DoD labs have funded a large number of research and exploratory development efforts toward this end. For many applications of this technology, the specific design and development of an antenna array, signal processing hardware system, and algorithm to meet a specific user's needs is required. Although the interference suppression capability of such systems is impressive, many applications have not been implemented because they were not cost effective.

Over the years, RADC has attempted to reduce the development costs of adaptive antenna systems by

various means. In 1978, RADC purchased and installed an anechoic chamber and an antenna analyzer system. Significant cost savings on a number of adaptive antenna efforts was realized using this test facility. For the first time at RADC, antenna arrays could be designed and tested in a cost effective manner using the test facility.

The Flexible Adaptive Spatial Signal Processor (FASSP) was installed and integrated with the anechoic chamber and antenna analyzer in 1985, greatly enhancing the test facility. The flexibility of the FASSP hardware and the ability to program algorithms made the complete design and testing of adaptive antenna systems relatively inexpensive.

The Systolic Processor Array for Radar and Communications (SPARC) was delivered and integrated into the adaptive test facility in May of 1988. The impressive computational power of this digital processor performs a specific algorithm about 400 times faster than previously developed all-digital adaptive processors.

RADC is presently looking at the ways in which recent developments in photonics can enhance the adaptive test facility. A few efforts are planned to

explore optical links, optical beamforming and optical signal processors.

2. ANECHOIC CHAMBER AND ANTENNA PATTERN ANALYZER

The anechoic chamber was installed at RADC in the RF Lab in 1978. The chamber is rectangular in shape and can be used over a wide range of frequencies from 300 MHz to 10 GHz and above. The receive end of the chamber has a pedestal that can be rotated in azimuth or elevation either manually or under computer control. Antennas are mounted on the pedestal in the center of a 6 ft. diameter spherical quiet zone. The transmit end of the chamber is adjacent to an equipment room where interference sources and communications systems can be installed to implement many different test configurations.

The Scientific Atlanta measurement system provides a means of determining antenna/antenna-array patterns. The antenna analyzer system can be operated manually or automatically. For adaptive antenna array tests it is necessary to locate interference/communications sources at precise positions with respect to the array. A computer program can be used to predict the expected pattern of a given array based on the number of elements and

geometry of the array. A laser can be mounted on the pedestal and used to precisely locate a broadside CW source. Then the array can be installed on the pedestal and an actual pattern can be obtained using the CW source and the antenna analyzer system. The actual pattern and the predicted pattern can be compared. Once the two patterns agree, the actual pattern can be used to locate other sources for adaptive array testing (see figures 1 and 2).

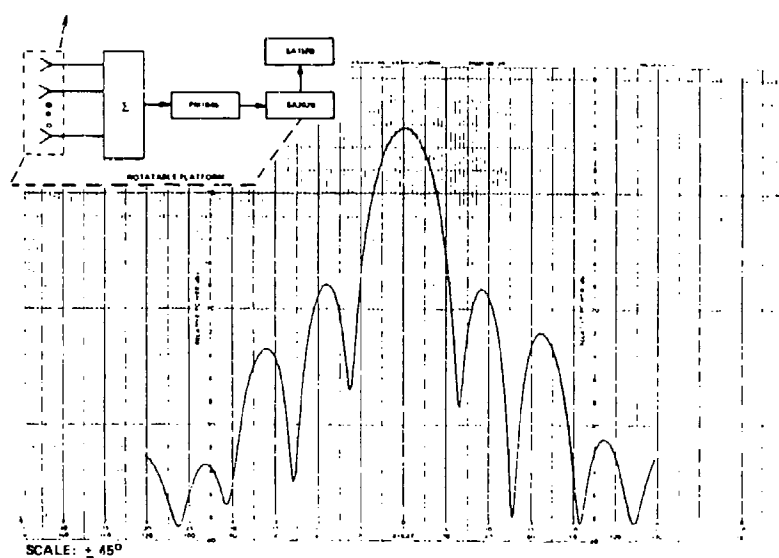


FIGURE 1 - ACTUAL ANTENNA PATTERN
(Four element linear horn array)

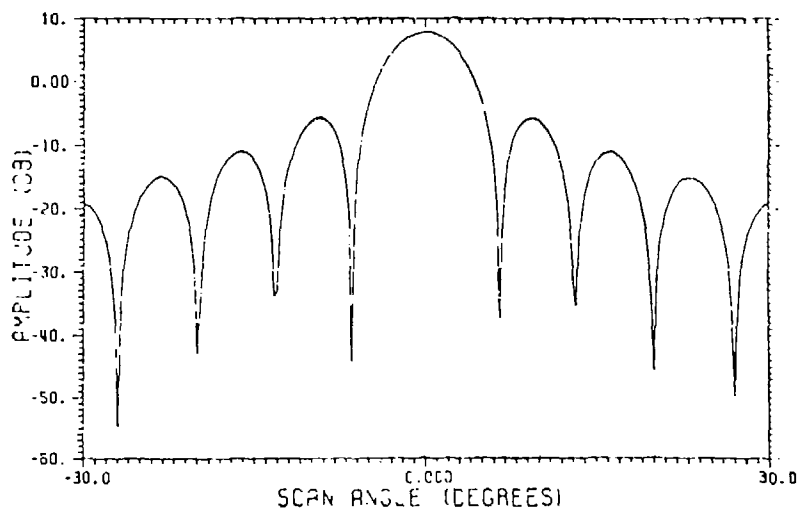


FIGURE 2 - COMPUTER GENERATED ANTENNA PATTERN
(Four element linear horn array)

3. FLEXIBLE ADAPTIVE SPATIAL SIGNAL PROCESSOR

Syracuse Research Corporation (SRC) installed and tested the FASSP in the RADC adaptive test bed in April of 1984. Essentially, the FASSP is a hardware/software reconfigurable/programmable analog and digital adaptive beamforming/interference-nulling processor. The FASSP has 12 SHF receivers which down-convert to an IF of 540 MHz. An IF interconnect panel allows 12 IF signals to be connected to any of the 12

analog and/or digital weighting modules. The baseband receivers down-convert the 26 real (13 complex) IF channels to baseband and, using eight bit sign magnitude A/D conversion, produce 26 real digital sampled data streams. All the adaptive data processing is done in an AP120B floating point processor and the digital weights are converted to analog, using D/A conversion, for application to the analog weighting modules or directly applied to the digital weighting modules. The whole process is under the control of an PDP11/44 DEC computer (see figure 3).

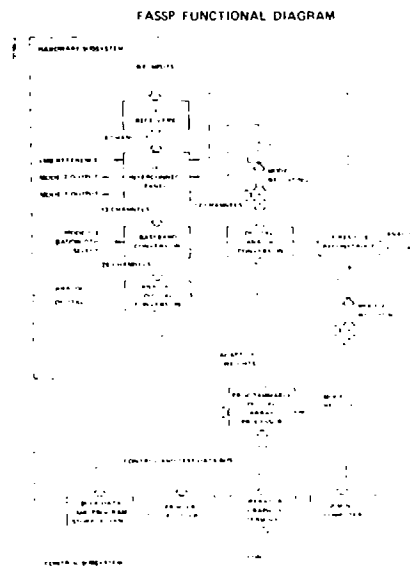


FIGURE 3

FASSP SPECIFICATIONS

1. Physical/Mechanical: Laboratory Environment, Commercial Cabinets, Semi-portable
2. Operating System: Software-Based, User Interactive
3. Adaptive Algorithms: Closed-Loop Gradient, Conjugate Gradient, Guided Random Search, Open-Loop Sample Matrix Inversion.
4. Number of Channels: 12 Adaptively-Weighted Channels, Derived From 6 RF Input Channels, Via Manually Patched Delay Lines
5. Operating Frequency Band: 7.0 to 8.5 GHz
6. Input Dynamic Range: -90 dBm to -20 dBm Total
40 dB Instantaneous
7. Adaptive Nulling Performance - Mode 1
40 dB Over 40 To 50 MHz Bandwidth (Closed-Loop)
20 dB Over 40 To 50 MHz Bandwidth (Open-Loop)
8. Adaptive Nulling Performance - Mode 2
40 dB Over 5 MHz Bandwidth (10 MHz Goal)
9. Convergence Speed: Suitable For Operation From A Scanning Antenna Pedestal, At 2 To 10 RPM

FIGURE 4

FASSP ALGORITHM PERFORMANCE

Definitions:	h = number of adaptive weights M = specified averaging interval (samples)
CFBSC:	Weight Update Interval: $87 + 15h$ microseconds Weight Update Rate (12 weights): 374 Hz (6 weights): 569 Hz Convergence Time: 10 to 100 updates
CGSC:	Weight Update Interval: $165 + 24h + 2h^2 + M(20 + 5h)$ Microseconds Assume $M = 100$ for gradient and residue estimates Weight Update Rate (12 weights): 176 Hz (6 weights): 173 Hz Convergence Time: 24 updates
SHSC:	Weight Update Interval: $223 + 9h + 7h^2 + 7h^3 + M(20 + 2h + h^2)$ microseconds Assume $M = 24$ for convergence Weight Update and Convergence Time: $223 + 42h + 11h^2 + 9h^3$ microseconds Weight Update Rate (12 weights): 56 Hz (6 weights): 350 Hz
IMSC:	Weight Update Interval: $127 + 43h + 10h^2 + h^3$ microseconds Weight Update Rate (12 weights): 264 Hz (6 weights): 1060 Hz Convergence Time: 24 weight updates
LRSP:	Weight Update Interval: $118 + 20h + M(23 + 5h)$ Microseconds Assume $M = 100$ for residue estimation Weight Update Rate (12 weights): 111 Hz (6 weights): 180 Hz Convergence Time: Indeterminate - Similar to CFBSC
Notes:	1. Mainlobe constraint and data recording options add slightly to the above times.

FIGURE 5

For a list of various performance specifications and available algorithms see the appropriate charts (see figure 4 and 5). The FASSP is capable of producing charts and graphs of antenna patterns, beamformer residue output power and Eigen vector/value analysis of the array correlation matrix (see figure 6).

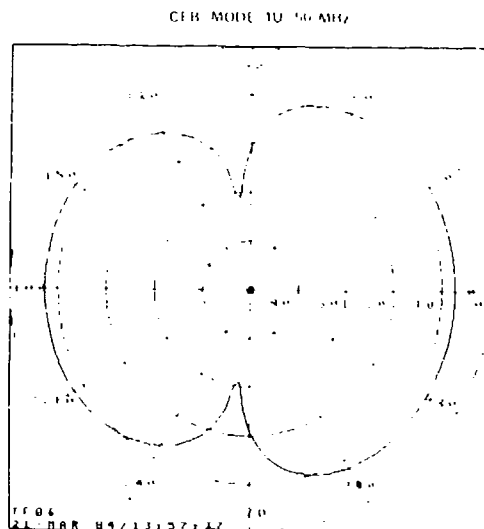


FIGURE 6

4. SYSTOLIC PROCESSOR ARRAY FOR RADAR AND COMM

The Hazeltine Corp. delivered to RADC the Systolic Processor Array for Radar and Communication

in the first quarter of 1988. Integration into the adaptive test facility and acceptance testing was completed in the second quarter of 1988 (see figure 7). SPARC is controlled, via an IEEE - 488 bus, through its interface by the same computer as the FASSP.

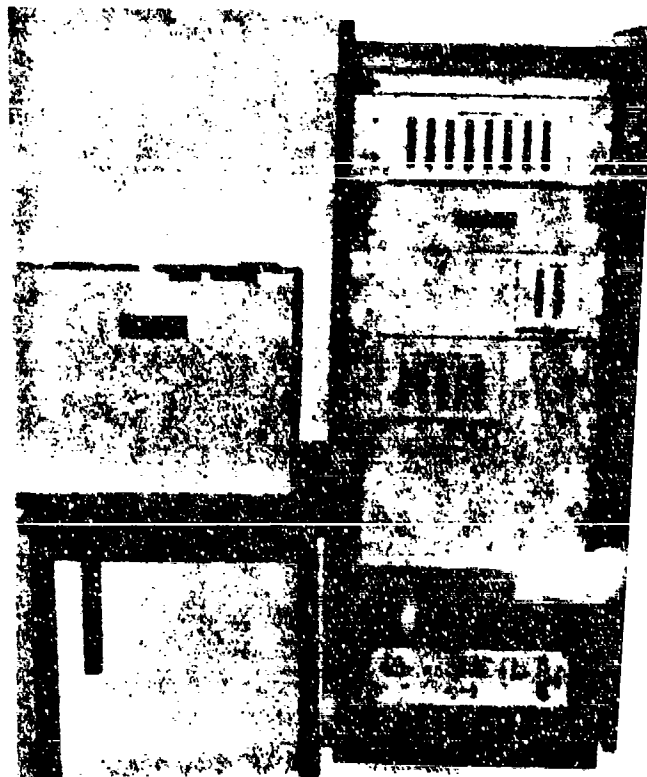


FIGURE 7 - SPARC

The processor is a linear systolic array which solves an $M \times 12$ system of equations by performing QR-factorization using Givens rotations.¹ The processor operates directly on the data which flows, in parallel, from the 12 complex channels of the FASSP through the SPARC interface to the SPARC processor. The SPARC solves the system of equations and provides a solution every 50 microseconds. The processor does all computation in 32 bit IEEE standard arithmetic but supplies the solutions/weights in 8 or 12 bit integer format.

Many of the SPARC parameters are programmable. Some of the parameters that can be selected are data source, batch or iterative mode, pilot vector, active elements and scaling for the integer weight output.

Using data from the 12 element array implemented in the anechoic chamber, the SPARC in concert with the FASSP can remove 11 spatially distributed interference sources from the residue output of the FASSP digital beamformer.

5. OPTICAL TECHNOLOGY APPLICATIONS

One of the reasons for upgrading the adaptive test facility by employing fiber optical transmission lines is to preserve the performance of the anechoic

chamber. Installation of the fiber optical cable will reduce the overall amount and size of existing cable and allow the removal of equipment now employed within the anechoic chamber to perform phased array antenna measurements. The FASSP receiver assembly will also be removed from the chamber.

There are some impressive advantages to fiber optical systems. Fiber optics offers very low, constant attenuation at all frequencies, bandwidths that are extremely wide, impervious to EMI and RFI, and the reduced size and weight of components to perform the same tasks.

A four element array will be constructed in the normal fashion to provide a means of comparison to a four element optically linked array (see figure 8). The components necessary for the four element link have been purchased and are being evaluated. The components will be assembled into links and time and phased matched as required by the beamforming/nulling adaptive process. The optically linked array will be evaluated in terms of noise figure, dynamic range, linearity, signal to noise and cancellation ratios and the antenna patterns of the arrays. These performance measures can be compared to the baseline standard

configured four element array.

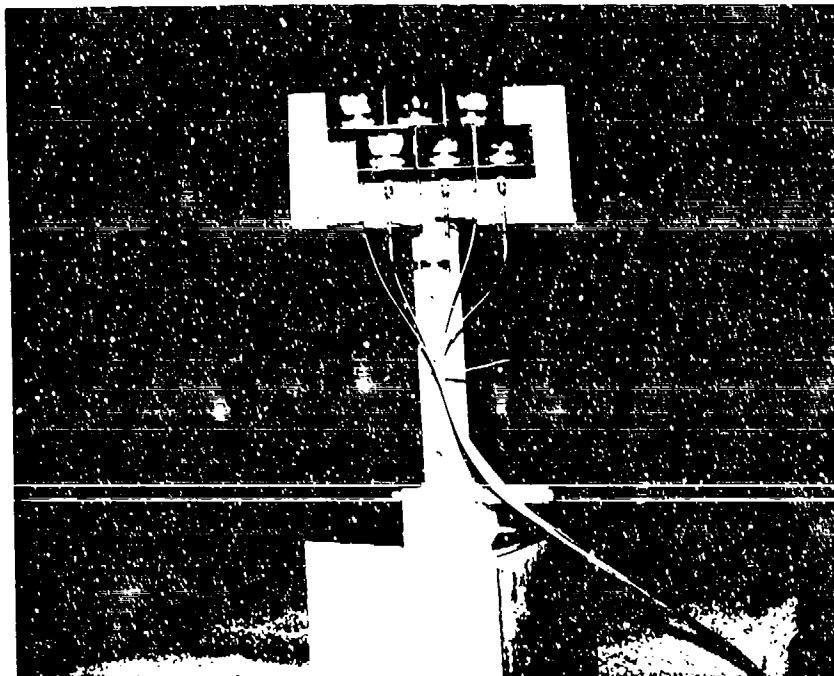


FIGURE 8 - SIX ELEMENT RECEIVE ARRAY

Design and development of an optical adaptive processor to be installed into the FASSP system is currently underway. The goal of this effort is to exploit the capability of optical technology in performing beamforming and nulling. The optical adaptive processor will be a digital system. It will be capable of performing digital beamforming and nulling with greater dynamic range than previously

developed analog optical systems. It also will be capable of performing the adaptive weighting and processing requirement much faster, using less power than its electronic counterparts with the same degree of accuracy. Design specifications for the optical adaptive processor to be installed in the FASSP include a processing bandwidth of 10 MHz, 4 degrees of freedom, and null depths of 40 dB with a goal for the weight update rate of 2.5 microseconds (see figure 9).

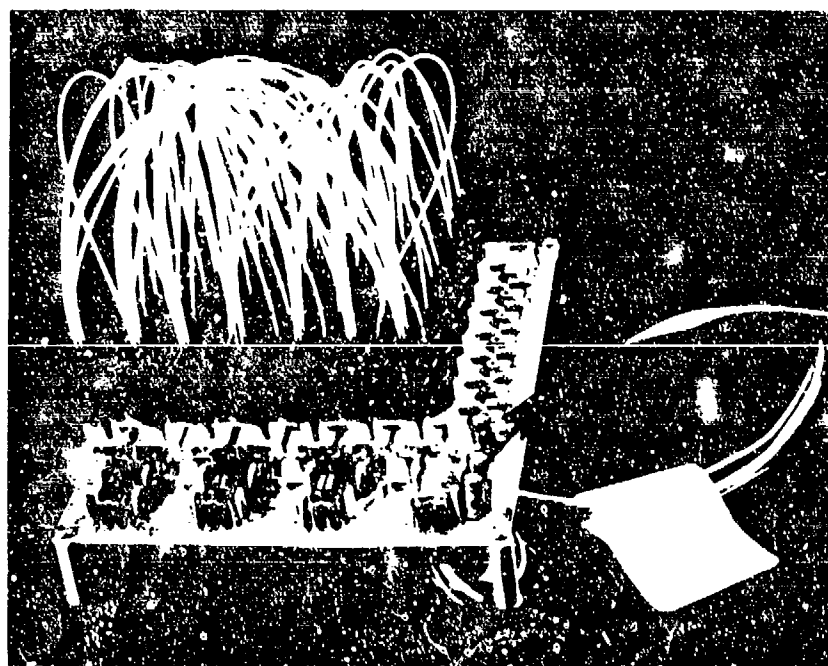


FIGURE 9 - OPTICAL LOOKUP TABLE

As a comparison of the performance of an optical processor against an electronic one, it has been estimated that if the same architecture were used for both types, the optical processor could achieve efficiencies of 9.15×10^{10} operations/sec. W, whereas the state of the art in GaAs would be limited to 8.9×10^8 operations/sec. W.²

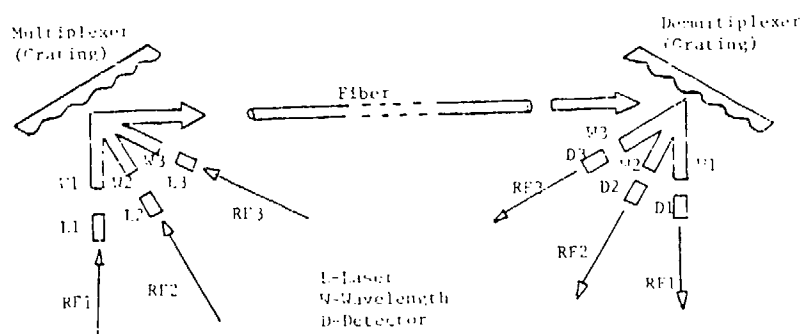


FIGURE 10 - OPTICAL MULTIPLEXER DEMULTIPLEXER

Wavelength Division Multiplexing (WDM) is a technique where each signal is assigned its own color (wavelength). The WDM system is relatively easy to implement with commercially available components. The

system includes (see figure 10) a laser diode transmitter for each signal, a multiplexer and demultiplexer (these are typically a grating which diffract each signal at a different angle as a function of its wavelength), optical fiber, and a photodetector receiver.

There are numerous system applications which would benefit by the WDM's high speed, compact and reliable system, and non-radiating and EMI impervious fiber transmission line. An immediate application at RADC is the anechoic chamber where the WDM system would eliminate the potentially RF radiating, 12 microwave cables, as well as its bulky preamplifiers and would result in a more accurate and efficient system.

WDM systems of 1500 signals are theoretically possible and work is progressing rapidly toward design and realization of these systems. When these systems become available it will become possible to control antenna arrays with hundreds of elements with a single WDM system.

6. CONCLUSIONS

Over the years the adaptive test facility has been upgraded many times and will continue to be

upgraded in the future. The facility has been a cost effective tool for adaptive antenna system design. Development efforts for beamforming/interference-suppression for satellite communications, radar and antenna array designs have made use of this facility to reduce design and development costs.

7. REFERENCES

- ¹ McWhirter, J. C., (1983) "Recursive Least-Squares Minimization Using a Systolic Array", Real Time Signal Processing VI, Proceedings of SPIE, Vol. 431.
- ² Gotzoulis, A. P., (1988) "A Comparison of Optical and Electronic Position Coded Lookup Tables", SPIE, Vol 881, Optical Computing and Nonlinear Materials, p204.

A RAPID, ACCURATE TEST METHOD FOR MEASURING ELECTRICAL PHASE LENGTH

By George J. Monser

**RAYTHEON COMPANY
Electromagnetic Systems Division
Goleta, California 93117**

ABSTRACT

This paper first presents an overview of the types of errors present in phase length measurements. Next, a minimum-error test method is formulated. The first test results using this test method are included, demonstrating accuracies on the order of ± 3 electrical degrees at 18 GHz. Measurement time using currently available ANAs is accomplished in less than 1/2 minute when run in the reflective, time-domain mode.

Key words: phase length measurements, minimum-error test method

1.0 INTRODUCTION

For optimum performance of advanced multibeam phased-array systems, the design criteria of electrical phase must be satisfied since any deviations from these criteria result in a reduction of system radiated power (Figure 1), beam-broadening, beam-steering errors, and higher sidelobes (Figure 2). Because all of these factors are considered

undesirable, it was necessary to devise a test method for accurately measuring phase lengths. And, since a number of parts were to be measured, a test method was needed that required minimum test time.

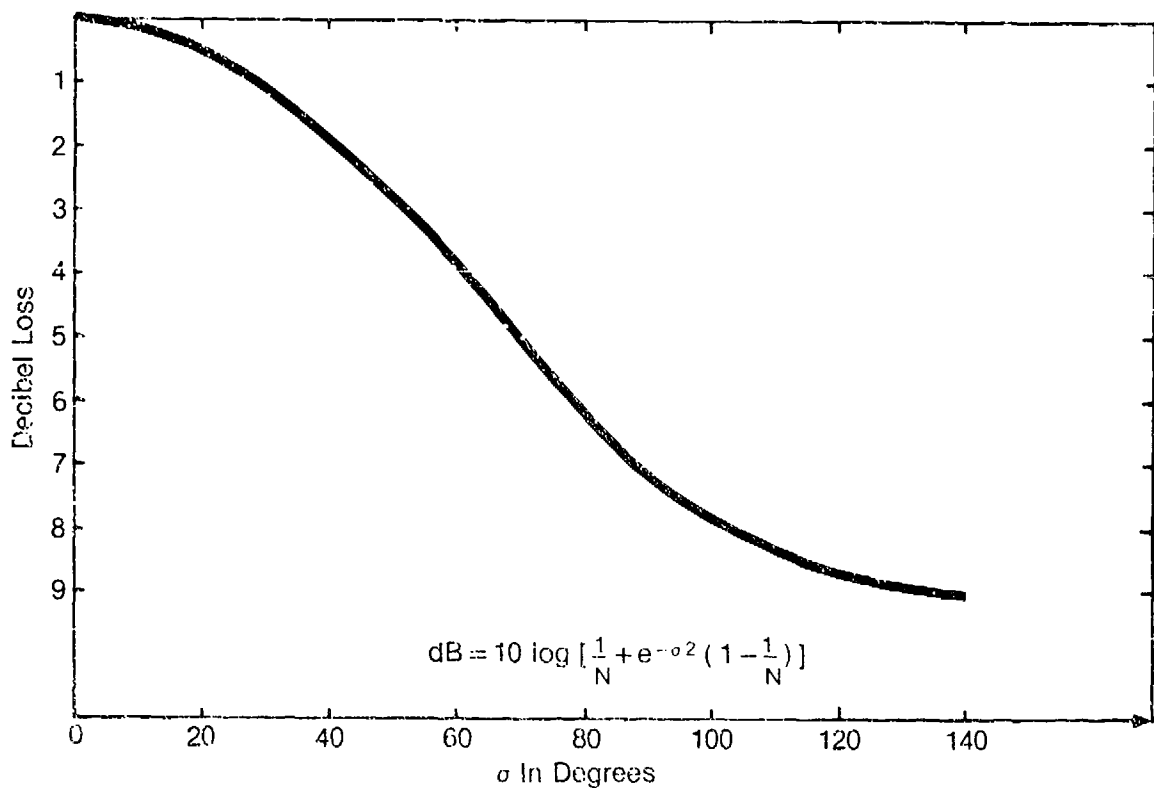


Figure 1. Transmitter with Eight TWTs Degradation with Phase Error (Gaussian Distribution)

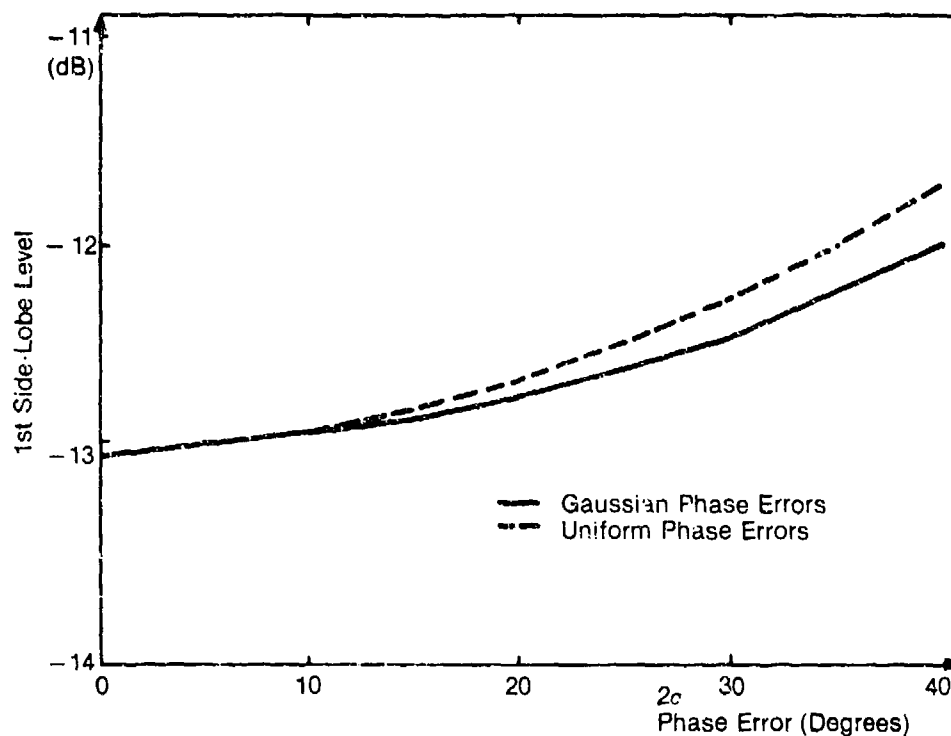


Figure 2. Small Array (N Equals 10) First Side-lobe Level versus Phase Error

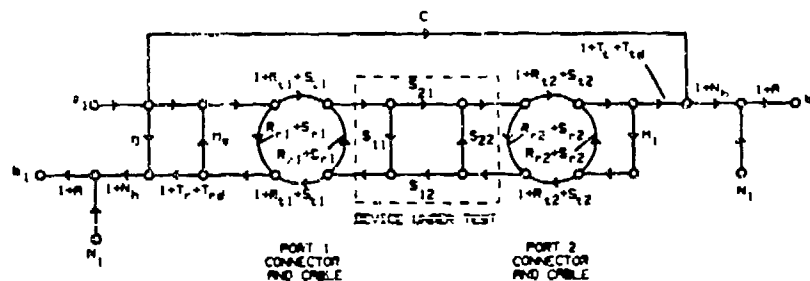
This paper presents an overview discussion of the types of errors present in phase-length measurements; considers the test options, and then formulates a fast, minimum-error test method.

2.0 REDUCING ERROR SOURCES

Figure 3 illustrates the system flow and errors to be considered. (Figure 3 is based on Hewlett-Packard 8510 General Information, pp 1-89.)

Random errors are typified by connector-mating uncertainties

and flexure (bending) effects when cables are tested. Machine errors are those resulting from internal errors. They can be combined in RSS fashion to specify analyzer's proficiency. Under controlled conditions, without regard to mating uncertainties, this RSS error represents the best tolerance to which a phase measurement can be made.



Total Reflection Phase Uncertainty (E_{rp})

$$E_{rp} = \sin^{-1}(V_r/S_{11}) + T_{id}(\text{phase}) + 2S_{11}$$

where

$$V_r = S_r + \sqrt{W_r^2 + X_r^2 + Y_r^2 + Z_r^2}$$

$$S_r = \text{Systematic Error} = (D + S_{r1}) + T_r S_{11} + (M_s + S_{r1}) S_{11}^2 + (M_1 + S_{r2}) S_{21} S_{12} + A S_{11}$$

$$W_r = \text{Random low-level noise} = 3N_1$$

$$X_r = \text{Random high-level noise} = 3N_h S_{11}$$

$$Y_r = \text{Random Port-1 repeatability} = R_{r1} + 2R_{r1} S_{11} + R_{r1} S_{11}^2$$

$$Z_r = \text{Random Port-2 repeatability} = R_{r2} S_{21} S_{12}$$

$$T_{id} = \text{Phase stability with temperature} = [0.1 + 0.01 \times f_{GHz}] \times \Delta^\circ C$$

$$S_{r1} = \text{Port 1 cable transmission stability} = [0.05] \times f_{GHz}$$

Figure 3. System Flow and RSS Errors

Systematic errors are typified as bias effects. For example, for a phase measurement relying on comparison to a reference channel cable, the difference in temperatures between the test and reference channels produces a bias error. In addition, a bias error will exist in converting

electrical length to physical length if the velocity of light used in the computation is not corrected for local ambient conditions.

The correction for calculating the speed of light relative to local ambient conditions requires knowledge of temperature, humidity, and air pressure. Given these values, and using an NBS-furnished equation, a correction can be effected.

Connector-mating uncertainties can be reduced by using precision connectors and adapters. Flexure uncertainties in cable tests can be avoided using a cable-holding jig.

Using a frequency synthesizer locked to an ultra-stable source minimizes the frequency error so that the remaining error is associated to the errors in determining time delay. It has been found that the best results are achieved by linearizing the network analyzer over the widest bandwidth (i.e., 2 to 18 GHz is typical).

Following linearization and transformation, the machine is commanded to measure the distance difference between reflection from a short at the output and then from the same short positioned at the end of the cable-under-test.

Errors in the resulting measurement include the intrinsic network analyzer error and the uncertainty errors associated with connecting to the cable-under-test.

3.0 TEST METHOD

Looking at the two choices for measuring electrical length, it appears that less error is incurred in a reflection-type measurement (see Table 1).

Figure 4 shows a simplified schematic of the test configuration used to automatically determine the electrical length of the cable. Either network analyzer can be programmed and used to find the time delay to a short at the end of the cable-under-test. Internal to the network analyzer, the measurement is performed in the frequency domain and the value is then converted to time delay. A final computation is made to determine electrical length,

$$\text{Electrical Length} = 360 \times F \times T \quad (1)$$

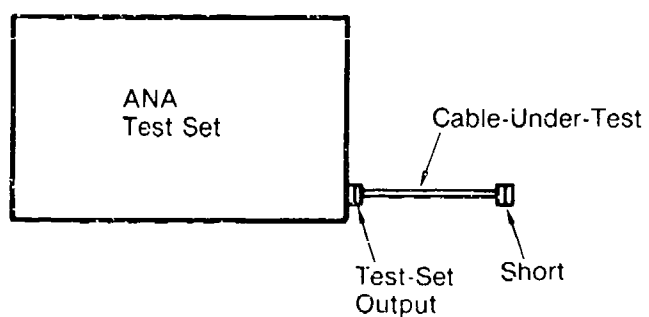
where:

F = Frequency in GHz

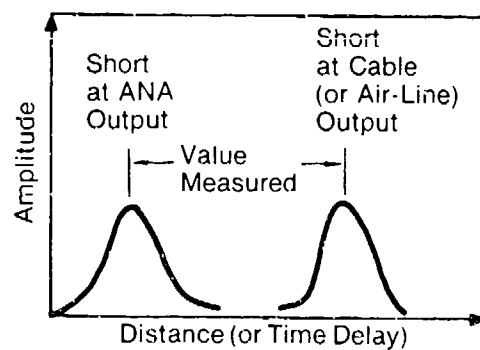
T = One-way cable delay in
nanoseconds

TABLE 1. MEASUREMENT CHOICES

	Transmission	Reflection
Requires the fewest number of adapters		X
Permits measurement without distorting the cable		X
Transits through the cable $N=2$, averaging effect		X



(a) Test Schematic



(b) Illustrative Measurement

Figure 4. Measurement Concept

Rather than attempting to quantify each error and computing an RSS error, the following method was used:

- 1. First, using beadless air lines, the mechanical length is accurately found.**
- 2. Next the electrical length is computed from these dimensions, taking into account local ambient temperature, humidity and pressure which slightly affect the speed-of-light to be used in computing length.**
- 3. The air line is then measured using the network analyzer.**
- 4. Results are then compared.**
- 5. The connection and measurement (steps 2 through 4) are then repeated several times to determine a quasi-probable error (many more measurements over a time span are required to obtain a statistical probable error).**

Following the above calibration, the electrical length for the cable is measured, first from J1 to J2 and then from J2 to J1. Next, an average electrical length is computed. Following the test, the calibration intactness is re-verified with the air line.

4.0 TEST RESULTS

Two sets of results are given.

4.1 AIR LINE MEASUREMENTS

Following the above procedure, air lines were tested at both Hewlett-Packard and Wiltron. First the mechanical lengths were determined. Next the lengths were determined using the respective ANAs. Values found by each ANA measurement were then corrected for local ambient conditions. Table 2 shows the results.

TABLE 2. AIR LINE RESULTS

Vendor	First Article (Beadless Air Lines)	Measured Mechanical Length (MM)	Measured Length By ANA (MM)	Corrected ANA Measurement (MM)
A	7.5 CM	74.930 ± 0.013	75.064	75.044
B	10.0 CM	100.012 ± 0.013	100.040	100.008

- Vendor **A** results = 0.11% milli-meters or about 2.5 electrical degrees at 18 GHz
- Vendor **B** results = 0.028 milli-meters or about 0.6 electrical degrees at 18 GHz
- Repeat test for vendor **A** showed 1.5° at 18 GHz

The difference for Vendor A showed 0.114 mm, which is about 2.5 electrical degrees at 18 GHz. The difference for Vendor B showed 0.028 mm, which is about 0.6 electrical degree at 18 GHz. In addition, similar measurements were performed by a cable manufacturer using Vendor A's equipment. The resulting error was 1.5 electrical degrees at 18 GHz.

An interesting fact is that for stainless steel airlines of a nominal length of 7.5 cm, a temperature change of $\pm 3^{\circ}\text{C}$ changes the length about ± 0.1 electrical degree at 18 GHz.

4.2 CABLE MEASUREMENTS

Following the air line tests, the electrical lengths for four 0.141 mm semi-rigid cables were determined by each manufacturer. Table 3 shows the results.

From this tabulation it may be observed that the electrical lengths agree within 6 electrical degrees, or approximately 0.1 percent. The final operation is to find the mechanical length for the above cables.

TABLE 3. CABLE RESULTS

Vendor	Test Article (0.141 Semi- Rigid Straight Cables)	Measured Time Delay In Pico- Seconds	ANA Calculated Electrical Length In Degrees At 18 GHz
A	1	1665.053	5395
A	2	1667.598	5403
A	5	1667.368	5402
A	6	1665.198	5397
B	1	1666.644	5400
B	2	1667.644	5403
B	5	1668.644	5406
B	6	1667.644	5403

Observe that the electrical lengths agree within 6° or approximately 0.1 percent.

The following expression relates the variables,

$$\text{Electrical Length} = 360^\circ \times L / \lambda \times \sqrt{e} \quad (2)$$

where:

L = Physical Length

λ = Wave Length = C/F

e = Dielectric Constant

C = Velocity of Light

F = Frequency

In using equation (2) both λ and L must be in consistent units, and accurate knowledge of the dielectric constant (as it exists in the cable) is required. This can be found by testing a long, known length of cable and computing the phase velocity, which is $1/\sqrt{\epsilon}$. In addition, the speed of light should be corrected for air temperature, humidity, and pressure.

For example, in a vacuum, the speed of light is given as:

$$C = 2.997928 \pm 0.000004 \times 10^{10} \text{ CM/Second}$$

(Physics and Chemistry Handbook)

Using an NBS computation, the effective dielectric constant of air is found to be 1.000649 for 760 mm pressure, 50 percent humidity, and 20°C.

Thus the speed of light used in equation (2) should be multiplied by,

$$\frac{1}{\sqrt{\epsilon_{\text{AIR}}}} = 0.9996757$$

Finally, the frequency must be accurately known, and frequency stability maintained throughout tests.

5.0 CONCLUDING REMARKS

- 1. A reliable and fast test method for accurately determining electrical length has been described.**
- 2. By rigorously following the procedure, the electrical lengths can be found to within ± 3 electrical degrees, provided connector uncertainties do not exceed ± 2 electrical degrees.**
- 3. In tests with both analyzers, it was found that the phase length measurement time was under 1/2 minute.**

2-D MICROWAVE IMAGING OF AIRCRAFT

Bernard D. Steinberg
Valley Forge Research Center
The Moore School of Electrical Engineering
University of Pennsylvania
Philadelphia, PA 19104

ABSTRACT

Because of the long wavelength of microwave radiation, the imaging of targets requires very large antennas. This paper describes three methods of imaging aircraft from the ground with microwave radar with quality suitable for aircraft target recognition. The imaging methods are based upon a self-calibration procedure called adaptive beamforming (ABF) that compensates for the severe geometric distortion inherent in any imaging system that is large enough to achieve the high angular resolution necessary for two-dimensional target imaging. The signal processing algorithm is described and X-band (3 cm) wavelength experiments demonstrate its success on commercial aircraft flying into Philadelphia International Airport.

1. INTRODUCTION

This paper describes three methods of imaging aircraft from the ground with microwave radar with quality suitable for aircraft target recognition. Illustrations are shown in the upper portions of Figure 1-3. Plan-view drawings of the airplanes are included to facilitate comparison. The imaging methods are based upon a self-calibration procedure called adaptive beamforming (ABF) that compensates for the severe geometric distortion inherent in any imaging system that is large enough to achieve the high angular resolution necessary for two-dimensional target imaging.

The lower portions of the figures illustrate the failure of conventional electronic scanning to form useful images; in all three cases the distortions in the microwave apertures grossly exceed the

tolerances stipulated by diffraction theory. The same data sets were used to form the upper and the lower images in each experiment. ABF was introduced only when the upper images were being formed. It is evident from the ease of target recognition from these images that the procedure phase-corrected the radar echos and thereby compensated for the distortions in the apertures. The result (upper) is high resolution, diffraction-limited imagery from which length and wing span can be measured, the sweep of the wings observed, the question of whether or not there are engines in the wings answered, and so forth. In short, target classification becomes possible.

2. ADAPTIVE BEAMFORMING

ABF is a data adaptive feedback control procedure that adjusts the complex weight vector in a large phased array so as to compensate for geometric and electrical distortion in the system. The control information is derived from measurements of the complex radiation field from the targets being imaged.

2.1 Dominant Scatterer Algorithm

The basic procedure assumes that there exists somewhere in the field of view of the imaging system a point-like scatterer or source having large radar cross-section or source strength. A corner reflector proves to be an excellent target for the beamforming procedure. The theory governing the requirements on its characteristics is published^{1,2}. There it is shown that the physical size of

the source can be no larger than $\lambda R/2L$, where λ is the wavelength, R is the radar-to-target distance and L is the size of the imaging aperture; and that its echo strength must exceed the total backscatter from all the other scatterers in its range bin by at least 4 dB. Such a target or source radiates a nearly spherical wavefront, which induces a simple phase variation across the array. Provided that the array is linear or planar, the phase variation is linear if the target or the source is in the far field, or approximately quadratic when the source is in the near field. Deviations from such simple behavior indicate geometric distortion in the array, electrical mistunings, or wavefront distortion due to turbulence in the propagation medium.

Figure 4 models the problem². A transmitter in the upper right launches a short RF pulse toward a point scatterer. The reradiation illuminates the receiving phased array with a spherical wavefront. The array is shown distorted in two dimensions: the antenna elements are displaced from a datum line denoting the location of the array, and the spacings between the elements are not equal. Thus the phases of the signals received by these elements are not those determined by the distances from the point target to the intersections of a periodically sampled straight line (the array) and a circle (cross section of the spherically expanding wave). Instead, the measured phases are altered by the displacements of the antenna elements from their design positions. The phase-error tolerance is smaller than

one-tenth of a wavelength if the gain of the array is to be maintained to within about one dB, and smaller still if reasonable control is to be exercised over the side radiation pattern^{3,4}. The tolerable distortion, therefore, is very small. Similarly small are the allowed mistunings in the receiver channels (not shown) behind each antenna element or the phase distortion in the wavefront induced by variations of the refractive index of the propagation medium.

Adaptive beamforming compensates for this problem in the following manner: The amplitudes of the echoes from the point target, as measured in the receivers, are little perturbed by the geometric errors in the array or the electrical errors in the receivers. Phase information, on the other hand, is substantially destroyed when the displacements of the antennas exceed a small fraction of the wavelength. The signal processor uses the fact that the variance of the amplitude of the echoes from the point target, as measured in the receivers, is small: it searches in range for that range bin, called the reference range, in which the echoes have the smallest amplitude variance. Corrections are easily made to the array by phase shifting all the signals received from the point scatterer at the reference range to a common phase. This process is called phase conjugation^{5,6} and is schematically indicated by the feedback network in the lower right of the figure. A superior correction is a complex weight at each location that is the complex conjugate of the received signal. This correction results in a radiation pattern that

is approximately the matched spatial-filter response of the system to the target or source^{7,2}. This means that the magnitude of the radiation pattern closely follows the modulus of the reflection profile, in the transverse or azimuth direction, of the point-like scatterer. In this way, a very narrow beam is formed from a large, distorted antenna array provided that the adaptive beamforming target driving the process reradiates like a point source. A corner reflector has been found to emulate such a target very well.

Table 1 describes the algorithm. Following compensation for known gain variations in the antenna elements (step 2), the system searches through range for that range bin in which the normalized variance of the amplitudes of the echoes across the array is the smallest (step 3). It designates that range bin as the reference bin and calls its range R_0 . It then conjugates the phases at R_0 to form the weight vector, phase shifts all echoes by the weight vector (steps 4 and 5), focuses the array at all ranges (step 6), and scans the array in azimuth to form the two-dimensional image (steps 7 and 8). This algorithm is sometimes called the minimum variance algorithm (MVA) and sometimes the dominant scatterer algorithm (DSA).

2.2 Reference Target of Opportunity

In imaging aircraft from the ground, it is not possible to implant an artificial target such as a corner reflector in the general area of the target. Nor can it be assumed that point-like targets of opportunity will be in the neighborhood of the airplane. Hence the procedure depends upon the existence of one or more

TABLE 1. STEPS IN RADIO CAMERA IMAGING (FROM [27],[23])

Step		
1	Measure and store complex envelopes of echo samples	$V_{in}e^{j\psi_{in}}$
		range bin \nearrow ← element number
2	Correct amplitudes by dividing by element pattern estimate \hat{f}_n	$A_{in}e^{j\psi_{in}}$
3	Find R_0 such that $A_{0n} \approx A$, all n	$Ae^{j\psi_{0n}}$
4	Phase rotate at R_0 by phase conjugate in relation to reference element, $\exp j(\psi_{0i} - \psi_{0n})$	$Ae^{j\psi_{0n}}$
5	Phase rotate at all range elements	$A_{in}e^{j(\psi_{in} - \psi_{0n} + \psi_{0i})}$
6	Focus at each range R_i	$A_{in}e^{j(\psi_{in} - \psi_{0n} + \psi_{0i} + (kx_n^2/2)(1/R_i - 1/R_0))} \triangleq B_{in}$
7	Phase shift linearly with angle	$B_{in}e^{-jkx_nu}$
8	Sum at each range element	$\hat{s}_i(u) = \sum_{n=1}^N B_{in}e^{-jkx_nu}$

suitable reflectors on the aircraft itself.

It is evident that the smaller the range cell, the larger the probability that a range bin containing a single dominant reflector exists. 100 experiments on approximately 30 aircraft were conducted to determine the statistics. Data were taken at X-band ($\lambda = 3$ cm) at the Valley Forge Research Center of the University of Pennsylvania. The aircraft, flying at distances from 3 to 30 km from the laboratory, were primarily commercial airplanes flying into the Philadelphia International Airport; some were military aircraft associated with the Naval Air Station in Willow Grove, PA. When the range cell was 1 m, a suitable beamforming source was available in approximately 80% of the experiments. When the range cell was increased to 3 m, the success rate dropped to approximately 25%⁸. A 1 m range cell was employed in the imagery shown in Figures 1-3.

2.3 Efficacy of Adaptive Beamforming

Figures 1-3 show the crucial importance of adaptive beamforming in large imaging systems. Their lower portions show imagery from the same data sets without the self-calibration procedure. The image of each such unphase-corrected echo sequence is a hopeless jumble of pixels.

3. SPATIAL RADIO CAMERA

The term "radio camera"⁹ was introduced to capture the idea of a picture-taking instrument at radio or radar wavelengths. It is characterized by an aperture large enough to provide the desired azimuthal or transverse resolving power but, because of its large size, is intrinsically distorted beyond the tolerance permitted by diffraction theory. Compensation is provided by the adaptive beamforming procedure.

3.1 32-Receiver Experiment

A bistatic radar configuration was employed in the experiment that produced the aircraft image of Figure 1. The X-band transmitter radiated a 1 kw peak-power pulse of 7 ns duration. The range cell, therefore, was 1 m, and the radiated and received bandwidth was 150 MHz. The antenna was a 1.2 m paraboloid mounted on a mechanically steerable pedestal. The receiving array consisted of 32 X-band receivers deployed on a laboratory roof in an irregular line. The receiver spacings were approximately 1 m. The size of array, therefore, was approximately 1000 times the wavelength. Diffraction

theory teaches that the beamwidth of a diffraction-limited antenna is (in radians) about the reciprocal of its size as measured in wavelengths^{3,10}. After ABF, which converted the system from a highly irregularly placed set of antennas to a diffraction-limited phased array, the radiation pattern that was formed exhibited a beamwidth of 10^{-3} rad or 1 mr, as expected. At the nominal target distance of 3 km, the transverse dimension of the resolution cell was 3 m. The receiver cabinets were propped up on cinder blocks to an elevation of approximately 30°. Each cabinet had a horn antenna 19 x 14 cm and a horizontal beamwidth of 12°. The pointing angles and pattern orientations differed somewhat from receiver to receiver.

Each antenna in the receiving array received a modulated RF wave consisting of the echoes of targets and clutter from the transmitted pulse. The receivers were fully coherent in the sense that all oscillators were frequency-and phase-locked to a 120 MHz master oscillator in the system. Its waveform is frequency-multiplied several times to provide the transmitter RF and the required local oscillator waveforms. The received RF waveforms were detected in each receiver, coherently quadrature demodulated, sampled at a 200 megasample per second rate and each quadrature sample was converted to an 8-bit digital word.

3.2 Signal Processing

The sampled and stored data are the complex field amplitudes received by the antennas and measured in the receivers. The function of the signal processor is to transform these data into an image. The large size of the aperture precludes the possibility that it is undistorted. As a consequence, the argument of each measured complex field amplitude is in error by the altered phase delay from scatterer to antenna due to the misplacement of each antenna from its design position. The adaptive beamforming algorithm described earlier corrects this error. Without such correction the measured phases are garbled and the resulting image is a jumble of pixels. The lower picture in Figure 1 is an example.

4. TEMPORAL RADIAL CAMERA (ISAR + ABF)

Synthetic aperture radar (SAR)^{11,12,13,14} was a monumental invention of the early 1950's. Deviations from nonaccelerating flight due, for example, to wind gusts distort the synthetic aperture. Measurements can be made within the airplane with pendulums or other inertial devices to note the instantaneous acceleration of the platform, from which the instantaneous vector deflection from straight line flight can be calculated. In turn, these measurements can lead to phase corrections made in the local oscillator of the receiver or in the data set to correct for the aperture distortions. In this way, SAR systems are able to compensate for deviations from straight line, constant speed flight.

Not so with inverse synthetic aperture radar (ISAR), however. Although the concept was a product of the same decade, the problem of phase compensation is intrinsically more complicated and has delayed ISAR's application. In contrast to SAR the aircraft is the target and the radar is on the ground or on some arbitrary platform. The target motion is used to synthesize an extended aperture which can then image the airplane. As a consequence, the radar has no means for obtaining the mechanical measurements of instantaneous aircraft position and correcting the radar data accordingly. This is exactly what adaptive beamforming can do, however. Thus radio camera processing is directly applicable to ISAR. Time replaces the spatial dimension. That is, the radar waveform received as a result of the n th transmission (of N) is treated in the signal processor as if it were the n th antenna element in an array of N antennas.

Figure 2 shows an airplane imaged in this fashion. The aircraft is a Boeing 727 flying at 3.2 km from VERC. The same antenna and transmitter described in the earlier section were used for this ISAR experiment. Only a single receiver was employed, however, and it was driven by the same 1.2 m dish used for the transmitter. The radar was operated in a conventional monostatic fashion. The pulse length, as before, was 1 m. The lower portion of the figure shows the image from the same data sequence without the phase corrections introduced by adaptive beamforming. As before, the image is useless when phase compensation for the geometric distortion is not applied.

5. SPATIAL-TEMPORAL RADIO CAMERA (COMBINED ISAR AND RADIO CAMERA)

Because the same signal processing is applied to both the spatial and the temporal systems, it is not unreasonable to assume that they may be combined into a common spatial-temporal imaging system.

Figure 5 illustrates the procedure with two receivers. A transmitter is colocated with one receiver. The target is an airplane. Synthetic apertures are formed by each receiver. The combined data from the two antennas form the total data set. Adaptive beamforming compensates for flight path deviations in each of the synthetic apertures, and also compensates for the unknown jump in phase between the two data sequences. The upper image of Figure 3 was formed in this manner. The two receiving antennas were 25 m apart, the aircraft was flying at approximately 250 knots transverse to the line-of-sight, the interpulse period was 2.5 ms and the number of pulses integrated was 85. The radar wavelength was 3 cm.

7. SUMMARY

Microwave radar has now matured to the point where aircraft free of a clutter background can be imaged in two dimensions with sufficient resolution to recognize the target. While the experiments were performed from the ground, there is nothing in the nature of the techniques described in this paper to preclude their applicability to airborne or space platforms. High resolution in the range dimension requires a large bandwidth. For example, 150 MHz is

needed to achieve one meter in range. Such bandwidth can be achieved with existing design procedures and components.

The same is not true in the orthogonal dimension, however. High angular or cross-range resolution requires an aperture, so huge as to be intrinsically distorted, often making it impossible to form a highly directive main lobe.

Electrical distortion (primarily phase errors) will accrue through mistunings, impedance mismatches and component drift with age and temperature. A self-calibrating technique called adaptive beamforming (ABF) successfully overcomes such distortion and correctly reconstructs the main beam properties. Such an instrument is called a radio camera. The same procedure compensates for flight-path distortion in airborne targets that are in the clear, thereby permitting ISAR imaging to work satisfactorily. Because the signal processor is the same in the two systems, the combination of ISAR and ABF is called a temporal radio camera. Further, because the same adaptive beamforming procedure solves both problems, they may be combined to form highly thinned, huge imaging arrays. Figures 1-3 demonstrate the quality currently being achieved by these three imaging configurations.

VIII. ACKNOWLEDGMENTS

The entire staff of the Valley Forge Research Center has participated in the program leading to the demonstrated results. Most notable for their contributions are the late Dr. S. Hassan

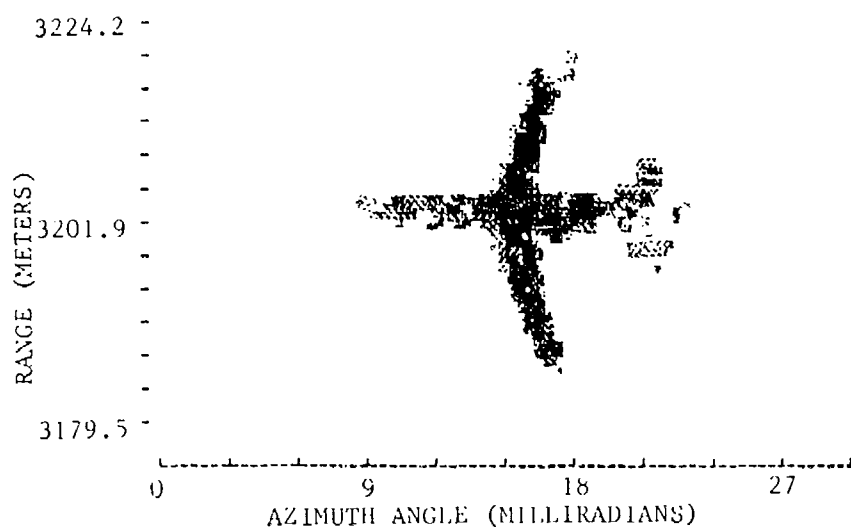
Taheri, Donald Carlson, William Whistler, Todd Seeleman and Walter Borders. Special thanks and deep appreciation is reserved for the many years of support from the Army Research Office, the Office of Naval Research, the Air Force Office of Scientific Research and the Rome Air Development Center (Hanscom Field); and to Sperry Corporation (now UNISYS) for the farsighted research funding of the ISAR-ABF project.

9. REFERENCES

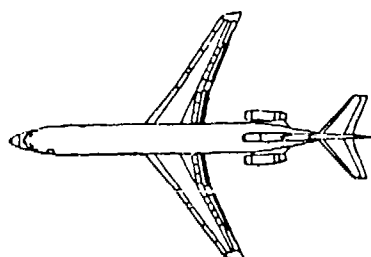
1. B. D. Steinberg, "Properties of Phase Synchronizing Sources for a Radio Camera," IEEE Trans. Antennas and Propagation, AP-30(6), Nov. 1982, pp. 1086-1092.
2. _____, Microwave Imaging with Large Antenna Arrays: Radio Camera Principles and Techniques, John Wiley and Sons, Inc., New York, 1983.
3. _____, Principles of Aperture and Array System Design, John Wiley and Sons, Inc., New York, 1975.
4. S. H. Taheri and B. D. Steinberg, "Tolerances in Self-Cohering Antenna Arrays of Arbitrary Geometry," IEEE Trans. Antennas and Propagation, AP-24(5), September 1976, pp. 733-739.
5. E. D. Sharp and M. A. Diab, "Van Atta Reflector Array," IRE Trans. Antennas and Propagation, AP-8, July 1960, pp. 436-438.
6. R. C. Hansen, "Communications Satellites Using Arrays," Proc. IRE, 49, June 1961, pp. 1066-1074.
7. B. D. Steinberg, "Radar Imaging from a Distorted Array: The Radio Camera Algorithm and Experiment," IEEE Trans. Antennas and Propagation, AP-29(5), Sept. 1981, pp. 740-748.
8. D. Carlson, "Preliminary Study of ISAR Amplitude Statistics," Valley Forge Research Center Quarterly Progress Report No. 52, Jan.-June 1987, pp. 1-3.
9. B. D. Steinberg, "Design Approach for a High Resolution Microwave Imaging Radio Camera," Journal of the Franklin Institute, Dec. 1973.
10. E. A. Wolff, Antenna Analysis, John Wiley and Sons, New York, 1966.
11. D. E. Sunstein, "Some Physical Aspects of Extensive Area Clutter," Symposium on Radar Reflection Studies, Research and Development Board, Washington, D. C., 27, 28 September 1950. This is the earliest paper disclosing the concept. The first flight test was in 1952 in an Air Force program called Atran, in which an L-band radar with a dipole antenna demonstrated a

2° azimuth beamwidth. The next year a group from the Control Systems Laboratory of the University of Illinois produced X-band maps of the Florida Keys with SAR processing.

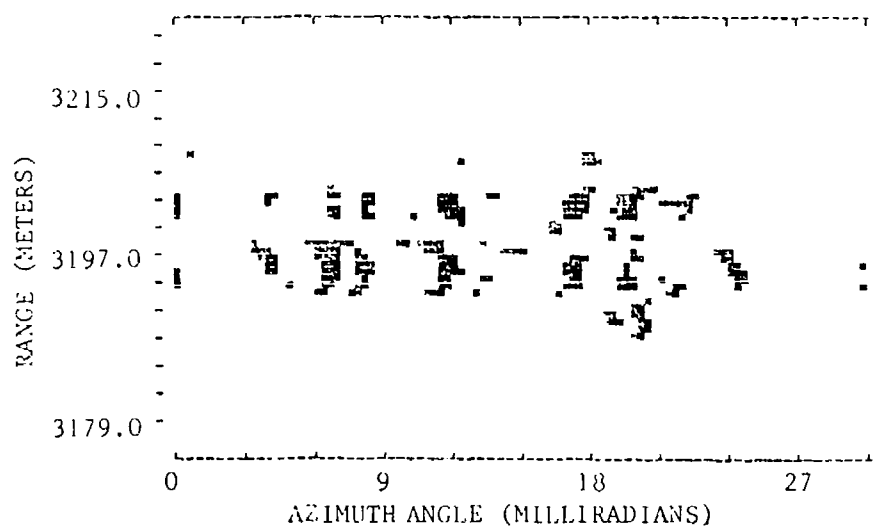
12. C. W. Sherwin, J. P. Ruina, D. Rawcliffe, "Some Early Developments in Synthetic Aperture Radar Systems," IEEE Trans. Mil. Electron., No. 1, MIL-6, 1962, pp. 111-115.
13. L. J. Cutrona, "Synthetic Aperture Radar," Chapter 23, Radar Handbook, M. I. Skolnik, Ed., McGraw-Hill, New York, 1970.
14. D. R. Wehner, High Resolution Radar, Artech House, Norwood, MA, 1987.



(a)
WITH ADAPTIVE
BEAMFORMING

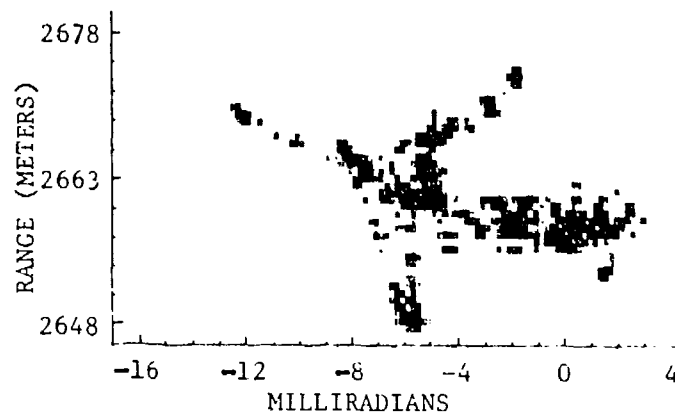


(b)
PLAN VIEW DRAWING
OF AIRCRAFT

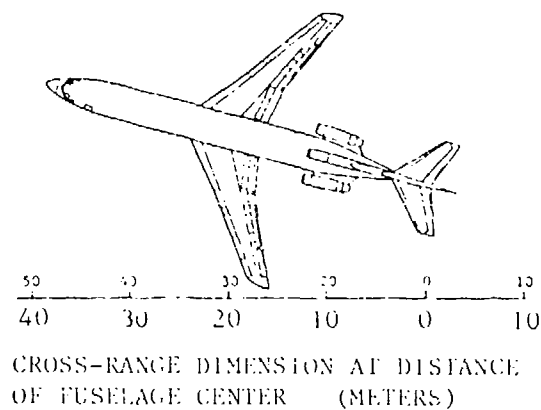


(c)
WITHOUT ADAPTIVE
BEAMFORMING

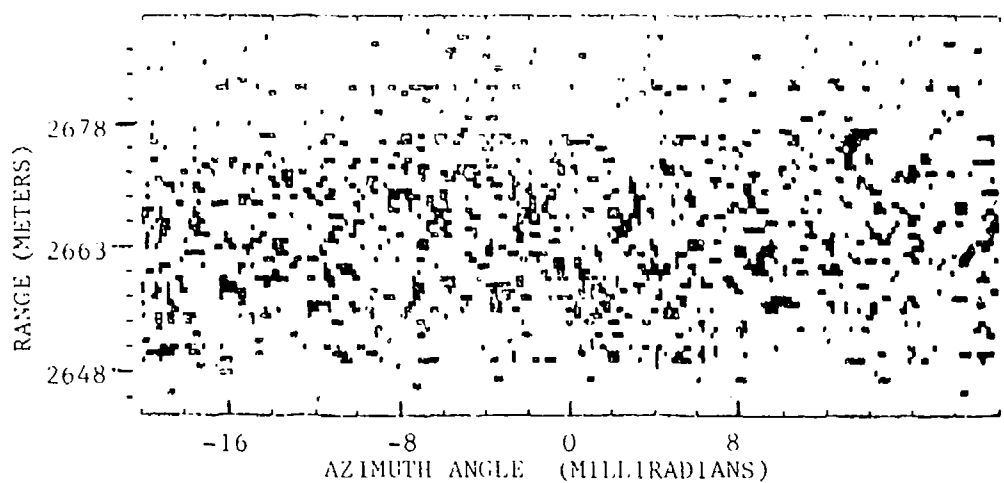
FIGURE 1. MICROWAVE IMAGE OF BOEING 727 OBTAINED WITH 32m X-BAND RADIO CAMERA. AIRPLANE IS FLYING AT DISTANCE OF 3.2 Km FROM VALLEY FORCE RESEARCH CENTER.



(a)
WITH
ADAPTIVE
BEAMFORMING

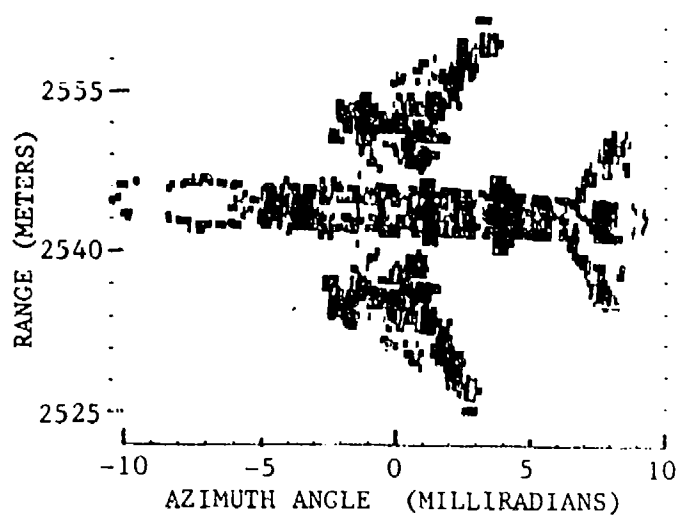


(b)
PLAN VIEW
DRAWING OF
AIRCRAFT

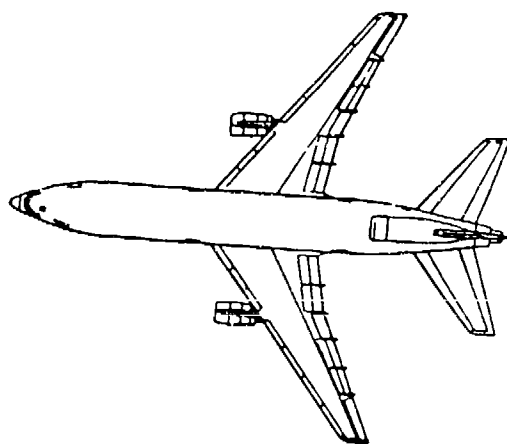


(c)
WITHOUT
ADAPTIVE
BEAMFORMING

FIGURE 2. MICROWAVE IMAGE OF BOEING 727 OBTAINED AT X-BAND WITH MONOSTATIC RADIO CAMERA. AIRPLANE IS FLYING AT DISTANCE OF 2.7 Km FROM VALLEY FORGE RESEARCH CENTER



(a)
WITH ADAPTIVE
BEAMFORMING



(b)
PLAN VIEW DRAWING
OF AIRCRAFT



(c)
WITHOUT ADAPTIVE
BEAMFORMING

FIGURE 3. MICROWAVE IMAGE OF LOCKHEED L-1011 OBTAINED WITH X-BAND RADIO CAMERA CONSISTING OF TWO-ELEMENT INTERFEROMETER PLUS INVERSE SYNTHETIC APERTURE PROCESSING. THE AIRPLANE IS FLYING AT A DISTANCE OF 2.5 Km FROM VALLEY FORGE RESEARCH CENTER.

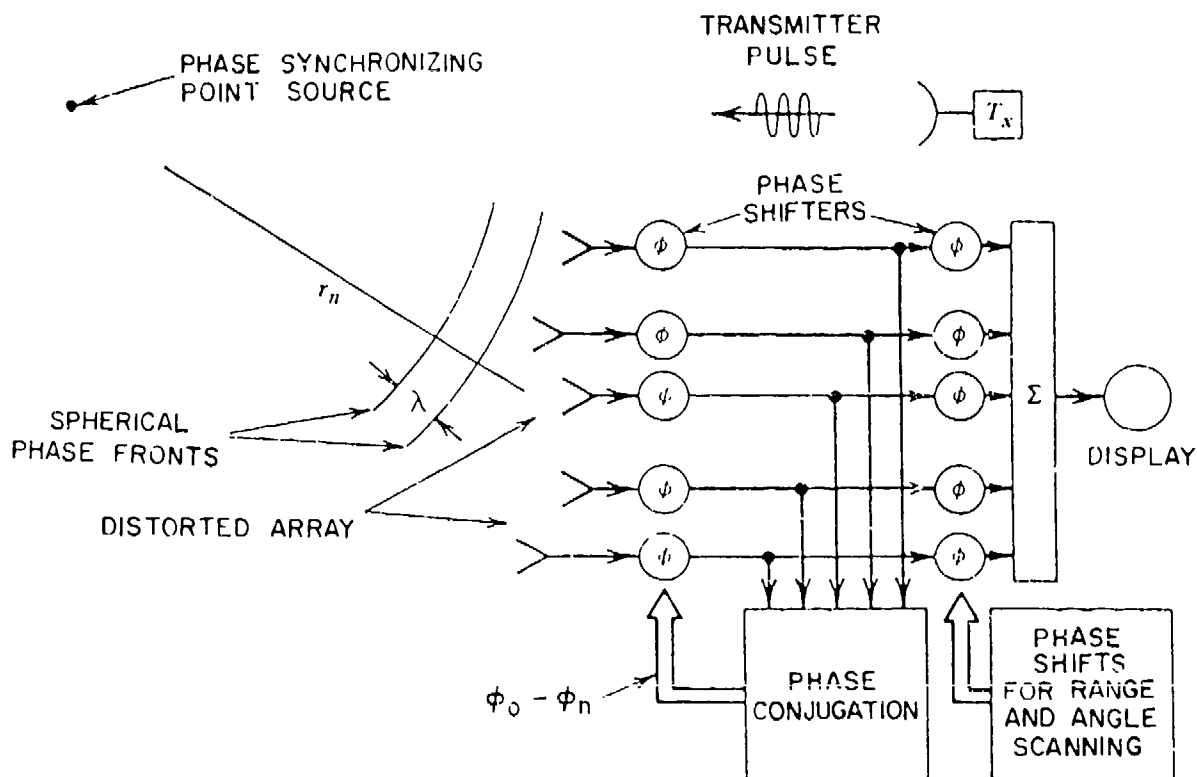


FIGURE 4. THE DISTORTED ARRAY SAMPLES THE WAVEFRONT AT IRREGULAR INTERVALS. MEASURED PHASES ARE IN ERROR BECAUSE OF DISPLACEMENTS OF ANTENNA ELEMENTS FROM THEIR DESIGN POSITIONS. ADAPTIVE BEAMFORMING COMPENSATES FOR THESE ERRORS.

ϕ_n IS THE MEASURED PHASE IN THE n th RECEIVER CHANNEL AT DISTANCE r_n .
 $\phi_0 - \phi_n$ IS THE CONJUGATE PHASE RELATIVE TO A FIXED REFERENCE PHASE.

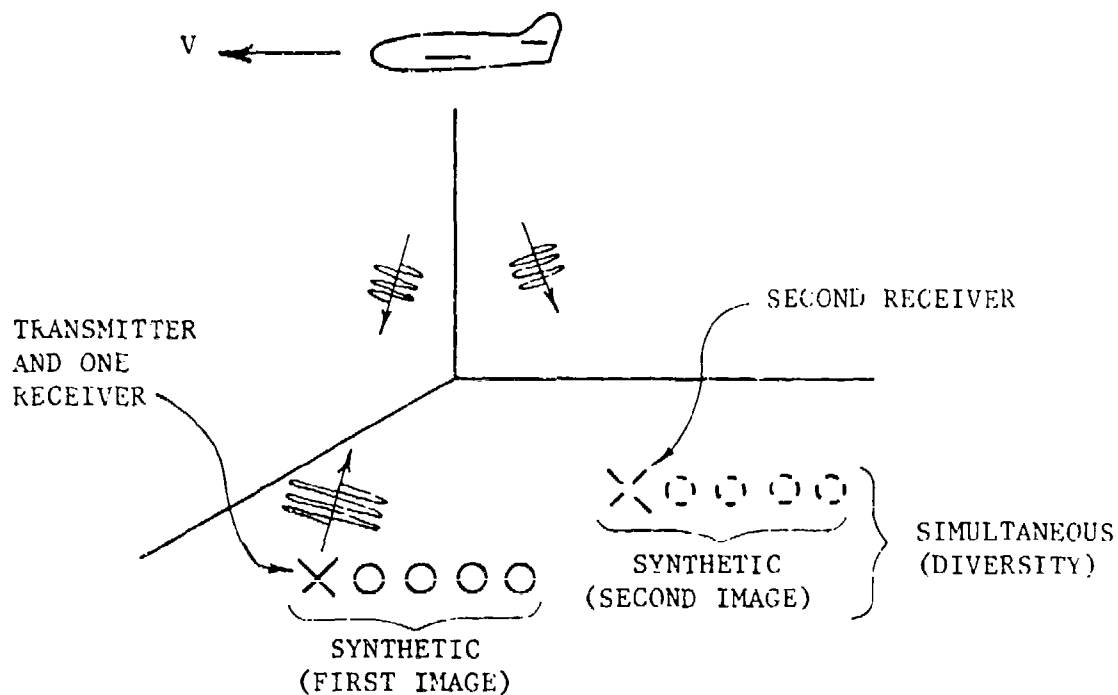


FIGURE 5. SPATIAL-TEMPORAL RADIO CAMERA. TWO OR MORE RECEIVERS FORM SYNTHETIC APERTURES SIMULTANEOUSLY. ADAPTIVE BEAMFORMING PERMITS THE DATA TO BE COMBINED TO REMOVE GRATING LOBES AND PROVIDE FINER RESOLUTION. IN ADDITION, THE INDIVIDUAL IMAGES ARE COMBINED FOR DIVERSITY ENHANCEMENT.



MISSION of Rome Air Development Center

RADC plans and executes research, development, test and selected acquisition programs in support of Command, Control, Communications and Intelligence (C³I) activities. Technical and engineering support within areas of competence is provided to ESD Program Offices (POs) and other ESD elements to perform effective acquisition of C³I systems. The areas of technical competence include communications, command and control, battle management, information processing, surveillance sensors, intelligence data collection and handling, solid state sciences, electromagnetics, and propagation, and electronic, maintainability, and compatibility.